Strain-Tuning of Periodic Optical Devices: Tunable Gratings and Photonic Crystals

by

Chee Wei Wong

S.B. Mechanical Engineering, University of California at Berkeley, 1999
A.B. Economics, University of California at Berkeley, 1999
S.M., Massachusetts Institute of Technology, 2001

Submitted to the Department of Mechanical Engineering
in partial fulfillment of the requirements for the degree of

Doctor of Science

at the

MASSACHUSETTS INSTITUTE OF TECHNOLOGY

August 2003

©Massachusetts Institute of Technology 2003. All rights reserved.

Author . . . .
Department of Mechanical Engineering
August 20, 2003

Certified by . . . .
Sang-Gook Kim
Ester and Harold E. Edgerton Associate Professor of Mechanical Engineering,
Commmittee Chair

Certified by . . . .
George Barbastathis
Ester and Harold E. Edgerton Assistant Professor of Mechanical Engineering

Certified by . . . .
Lionel C. Kimerling
Thomas Lord Professor of Material Science and Engineering

Accepted by . . . .
Ain A. Sonin
Chairman, Department Committee on Graduate Students

Strain-Tuning of Periodic Optical Devices:
Tunable Gratings and Photonic Crystals

by
Chee Wei Wong

S.B. Mechanical Engineering, University of California at Berkeley, 1999
A.B. Economics, University of California at Berkeley, 1999
S.M., Massachusetts Institute of Technology, 2001

Submitted to the Department of Mechanical Engineering
on August 20, 2003, in partial fulfillment of the
requirements for the degree of
Doctor of Science

Abstract

The advancement of micro- and nano-scale optical devices has heralded micromirrors, semiconductor micro- and nano-lasers, and photonic crystals, among many. Broadly defined with the field of microphotonics and microelectromechanical systems, these innovations have targeted applications in integrated photonic chips and optical telecommunications. To further advance the state-of-the-art, dynamically tunable devices are required not only for demand-based reconfiguration of the optical response, but also for compensation to external disturbances and tight device fabrication tolerances.

In this thesis, specific implementations of strain-tunability in two photonic devices will be discussed: the fundamental diffractive grating element, and a photonic band gap microcavity waveguide. For the first part, we demonstrate high-resolution analog tunability in microscale diffractive optics. The design concept consists of a diffractive grating defined onto a piezoelectric-driven deformable membrane, microfabricated through a combination of surface and bulk micromachining. The grating is strain-tuned through actuation of high-quality thin-film piezoelectric actuators. Device characterization shows grating period tunability on the order of a nanometer, limited by measurement uncertainty and noise. The results are in good agreement with analytical theory and numerical models, and present immediate implications in research and industry.

For the second part, we generalize the piezoelectric strain-tunable membrane platform for strain-tuning of a silicon photonic band gap microcavity waveguide. Additional motivation for this strain-tuning approach in silicon photonic crystals lies in: (a) the virtual absence of electro-optic effects in silicon, and (b) the ability to achieve tuning with low power requirements through piezoelectric actuation. Compared to current thermo-optics methods,

piezoelectric actuation affords faster and more localized tuning in high-density integrated optics. The small-strain perturbation on the optical resonance is analyzed through perturbation theory on unperturbed full 3D finite-difference time-domain numerical models. Device fabrication involves X-ray nanolithography and multi-scale integration of micro- and nano-fabrication methods. Experimental characterization achieved dynamically-tunable resonances with 1.54 nm tunable range (at 1.55 μm optical wavelengths), in good agreement with theory. This is the first demonstration of strain tunability in photonic crystals and contributes to the development of smart micro- and nano-scale photonics.

Sang-Gook Kim
Title: Ester and Harold E. Edgerton Associate Professor of Mechanical Engineering, Commmittee Chair

George Barbastathis
Title: Ester and Harold E. Edgerton Assistant Professor of Mechanical Engineering

Lionel C. Kimerling
Title: Thomas Lord Professor of Material Science and Engineering

Acknowledgments

First and foremost, I thank Professor Sang-Gook Kim, my thesis advisor, for providing the invaluable opportunity for me to explore the scope of this research. His words of wisdom and encouragement at critical times is a lesson learnt and a lesson never to forget. His emphasis on setting the objectives in research has taught me to see things in a different light. I also thank Professor George Barbastathis for his humor and quick insights. His willingness to work with students and his guidance as a friend and mentor is heart-felted and another exemplary example of leadership in the academia. "Patience, Luke", he says. I am immensely grateful to Professor Lionel Kimerling who, despite his busier-than-normal-MIT-professor schedule, provided both stimulating queries and strong encouragement in all aspects of this research. I am also thankful to Professor Alan Epstein and Dr. Stuart Jacobson who have taught me to be swift, directed and yet general in perspective towards scientific research.

The two major components of my doctoral research would never have been possible, if not for several people and their research laboratories. Steven Johnson, with the Joannopoulos Research Group, provided a clarity into photonic crystals, in addition to generously assisting in theory and numerical experiments. Pete Rakich, whom I first met coincidentally at a conference and with Professor Erich Ippen's Optics and Quantum Electronics Group, was great (and fun!) to work with and provided much experience and insights to the physical experiments.

The people in the NanoStructures Laboratory has also been instrumental in my development. In particular, I would like to thank Professor Hank Smith for graciously allowing me to work in his laboratory and to interact with his students and staff. These people have been entirely unselfish and volunteered their valuable time: Minghao Qi, who have worked with me in the after-hours (i.e. 3 am) and single-handedly answered most of my queries, Todd Hastings, Euclid Moon, Jim Daley, Dario Gil, Juan Ferrera, Jo-Ey Wong, Jimmy Carter, Tim Savas and Mark Mondol. All of them, in one form or another, have been able to interrupt their work and aid on my processing at an instance's notice. I am impressed with the high-level of cooperation in this laboratory and will strive to do the same, either for other students or in my own endeavors.

It has been a joy to work with many of the users and staff in Microsystems Technology Laboratories. Notably, Kurt Broderick, Paul Tierney, Joe Walsh, Vicky Diadiuk and Marty Schmidt provided a strong support network amidst the ger-zillons things they were charged to deliver. From the fabrication team of the MIT Microengine Program, Dennis Ward, Yoav Peles, Norihisa Miki, Linh Vu Hol, Ravi Khanna and Hongwei Sun provided endless comic relief in the strictly-work-only cleanrooms.

From the Micro- and Nano-Systems Laboratory, Yongbae Jeon provided much experience and agility of mind in the thin-film piezoelectric microfabrication; in a yoda-like fashion: "It's

the mind", he says. In the office, it is also a pleasure to work alongside Stanley Jurga, whose ever-so-helpful mindset constantly amazes me. Yong Shi, Kehan Tian, Wenyang Sun, Arnab Sinha, Greg Nielson, Wei-Chuan Shih, Nick Conway and Raj Sood provided much interesting interactions, academically and socially.

The group of friends I have developed at MIT and Boston, both within and outside the office, made this endeavour ever more worthwhile. My buddies, Keng Hui Lim and Eng Sew Aw, have a great sense of humor that resonates with our work and adventures. Shayan Mookherjea is an inspiring friend with a magical touch - I wish him well. Simon Nolet, with that Canadian tongue for maple, and Xue'en Yang are excellent to hang out with and pleasant to meet amongst the blurry faces along the infinite corridor. Bryan Crane, Tracey Ho, Ji-Jon Sit, Ben Leong, Allen Miu, Andy Wang, Sanith Wyesinghe, Dilan Seneviratne, Chiang Juay Teo, Kai Wang, George Siu, Poh-Boon Phua and Sriram Krishnan are some of the fantastic people I had the chance to meet, in unexpected ways in this fantastic place.

The opportunity and motivation to pursue this work would not have been possible *at all* if not for the direct unwavering support of my parents, Chee-Yann, and Maggie Chang. I am very fortunate to receive their unconditional love. This leadership, regardless of my efforts and progresses, has provided a strong incentive for me to excel in my work. I hope, and will continue to strive, to do the same for them. This thesis is thus dedicated to my family.

To my father who taught me the way of life, to my mother who guides us with her love, to Maggie who made our lives so wonderful, and to my brother, the comedian in our group, and hence the strongest of us all.

大路在前须分明认去

一肩担下当努力将来

Contents

1 Introduction **23**
1.1 Background And Motivation 23
1.2 Brief Review Of Tunable Diffractive Gratings 25
1.3 Brief Review Of Photonic Crystals And Tunable Methodologies 27

2 Design Of Analog Tunable Diffractive Gratings **29**
2.1 Concept Of Device 29
2.2 Micro-Electro-Mechanical Design 31
2.2.1 Piezoelectric theory 31
2.2.2 Analytical thin-film piezoelectric design 32
2.2.3 Finite-element piezoelectric modeling 36
2.2.4 Membrane structural and energy considerations 39
2.3 Optical Grating Design 43
2.3.1 Diffractive gratings theory 43
2.3.2 Efficiency, deviation and resolving power 43
2.4 Specific Applications Of Analog Tunable Diffractive Gratings 47
2.4.1 Thermal compensation and wavelength-selective switching for Optical Add/Drop Multiplexers 47
2.4.2 Dynamic dispersion compensation 48
2.5 Summary 51

3 Microfabrication And Experiment Of Analog Tunable Diffractive Gratings **53**
3.1 Microfabrication 53
3.1.1 Overall process flow and design permutations 54
3.1.2 Electrodes processing 55
3.1.3 PZT processing 56
3.1.4 Diffractive gratings 60
3.1.5 Device release 62
3.2 Electrical Characterization 63
3.2.1 Variation of electrode sizes 66
3.2.2 Water-immersible active cantilever characterization 66
3.3 Device Demonstration - Mechanical 68

3.3.1 Membrane and cantilever deflections . . . 68
3.3.2 Microvision analysis . . . 70
3.3.3 Vibration and noise characterization . . . 73
3.4 Device Demonstration - Optical . . . 75
3.5 Summary . . . 77

4 Design Of Strain-Tunable Photonic Band Gap Microcavity Waveguide 79
4.1 Background . . . 79
4.2 Strain-tuning Platform For Microphotonics . . . 81
4.3 Concept And Design Of Microcavity Waveguide . . . 83
4.3.1 Dielectric slab waveguide . . . 83
4.3.2 The microcavity waveguide . . . 85
4.3.3 Design thoughts . . . 89
4.4 Perturbation Theory On Maxwell's Equations For Shifting Material Boundaries 91
4.4.1 Finite-difference time-domain results . . . 93
4.4.2 Mechanics of circular hole deformation . . . 96
4.4.3 Perturbation analysis . . . 99
4.5 Other Considerations . . . 103
4.5.1 Photoelastic Pockels effect . . . 103
4.5.2 Bending losses in waveguide . . . 103
4.5.3 Limiting strain and stress concentration . . . 104
4.6 Summary . . . 106

5 Nanofabrication And Experiment Of Strain-Tunable Photonic Band Gap Microcavity Waveguide 107
5.1 Nanofabrication . . . 107
5.1.1 Overall process flow and integration considerations . . . 108
5.1.2 PZT processing for integrated microactuators . . . 110
5.1.3 X-ray nanolithography for microcavity waveguide . . . 112
5.1.4 Tunable membrane platform release . . . 115
5.2 Experiment . . . 117
5.2.1 Measurement setup . . . 117
5.2.2 Waveguide loss characterization . . . 118
5.2.3 Membrane mechanical measurements . . . 120
5.2.4 Static microcavity measurements . . . 120
5.2.5 Dynamic strain-tunable microcavity measurements . . . 124
5.3 Summary . . . 128

6 Conclusions 129
6.1 Looking Back . . . 129
6.2 Looking Forward . . . 131
6.2.1 Tunable diffractive gratings explorations . . . 131

6.2.2 Microphotonic elements for the strain-tunable platform 132
6.2.3 Tunable microcavity waveguide explorations 134
6.2.4 Summary 136

A Fabrication Details Of Analog Tunable Gratings 137
A.1 Detailed process of analog tunable gratings 137
A.2 Mask layout and design summary of analog tunable gratings 141

B Other Design Considerations Of The Photonic Band Gap Microcavity Waveguide 143
B.1 Design considerations on high-contrast dielectric waveguide losses 143
B.2 Effects of variation on primary photonic crystal design 145
B.3 Computational scheme for strain-perturbation on microcavity waveguide . . 146

C Fabrication Details Of Photonic Band Gap Microcavity Waveguide 147
C.1 Detailed integrated process flow of strain-tunable photonic band gap microcavity waveguide 148
C.2 Mask layout of strain-tunable photonic band gap microcavity waveguide . . . 154
C.3 Optimized RIE conditions for high-contrast dielectric waveguide 155
C.4 Electron beam lithography for microcavity waveguides 158

Bibliography 161

List of Figures

1-1 Digital tunable gratings: (a) Grating Light Valve schematic [1, 137], (b) Polychromator schematic [49, 135]. 26
1-2 Current analog tunable gratings: (a) Rhomboidal heatuator schematic [167], (b) Variable blazed gratings [10]. 26
1-3 Sampling of photonic crystals: (a) Radially symmetric one-dimensional photonic structure serving as omnidirectional reflecting mirrors in an optical waveguide [58], (b) Two-dimensional photonic band gap defect mode laser [116], (c) Three-dimensionally periodic dielectric layered structure with omnidirectional photonic band gap [67]. 27

2-1 Actuation concept of analog and digital tunable gratings. The analog design permits analog control of diffraction angle. 30
2-2 Design schematic of double-anchored deformable membrane, driven via thin-film piezoelectric actuators. The gratings, defined on top of the membrane, are tuned progressively along with the membrane. 30
2-3 Design schematic of (a) double-anchored perforated membrane, (b) free cantilever with gratings. 31
2-4 (a) Hysteresis in field-induced strain curves, (b) Strain creep characteristics. Adapted from Uchino [150]. 32
2-5 Nomenclature of closed-form solution with loaded cantilever end [157]. 34
2-6 Theoretical membrane displacement against applied voltage for various d_{31} and L parameters. The linear response, without spontaneous polarization transition, is assumed in this analysis for sufficiently small electric fields. . . 34
2-7 Theoretical membrane strain against: (a) t_{pzt}/t_{mem} ratio and, (b) L/L_{mem} ratio, in our design space. 35
2-8 Finite element mesh of analog tunable grating, depicting x-axis displacement. For illustration, film thickness in the z-direction are exaggerated 100X and z-displacement is exaggerated 2X. 36
2-9 Finite element mesh of analog tunable grating, depicting y-axis displacement. 37
2-10 Finite element mesh of analog tunable grating, depicting membrane Mises stress concentration regions. 37
2-11 Finite element mesh of analog tunable grating, depicting z-axis displacement. 38

2-12 Comparison of analytical and CoventorWare Finite-element models. 38
2-13 Membrane Mises stress and displacement profile under 100 kPa load, with 350 MPa residual stress in PZT and -300 MPa residual stress in thermal oxide. The displacement is exaggerated for clarity. 40
2-14 Harmonic response of double-anchored membrane: (a) first three modes for damping coefficient b of 1×10^{-4}, (b) solid line is with b of 1×10^{-2}, and dotted line is with b of 1×10^{-4} but with a L_{pzt} of 200 μm. In all cases, the loading amplitude is 400 pN. 42
2-15 Normalized spectral intensity of binary phase grating. 44
2-16 Diffraction efficiency comparison: (a)with as-fabricated ridge height for various orders, (b)with as-fabricated fill factor for the first order. 45
2-17 Normalized spectral intensity of binary phase grating, with 16.71 mrads bow in grating flatness, in comparison with an optically-flat binary phase grating. Both spectra are based on the as-fabricated fill factor and step heights. . . . 46
2-18 Normalized spectral intensity of the first diffracted order, against different maximum vertical deflections in the membrane bow. Multiple maxima peaks appearing due to bow in the grating flatness. 46
2-19 Optical Add/Drop Multiplexers elements in a DWDM ring network. 48
2-20 Grating pair setup for: (a) chromatic dispersion compensation, (b) polarization mode dispersion compensation. 49
2-21 Chromatic dispersion compensation for various grating periods using grating pair setup illustrated in Figure 2-20a. 50
2-22 Polarization dispersion compensation for various grating periods using grating pair setup illustrated in Figure 2-20b. 51

3-1 Microfabrication process flow of the analog tunable grating. The process consists of five masks and involves both surface and bulk micromachining. . . 54
3-2 Patterned bottom electrodes, fabricated via evaporation and lift-off, for subsequent PZT processing. 2 μm minimum linewidths are used for both the perforated membrane design and contact pad separation. 56
3-3 X-ray diffraction results of the fabricated PZT films, for different bottom adhesion and diffusion barrier materials and processing conditions. The four lines depicted (from top down) are: PZT/Pt/Ti/SiN_x, PZT/Pt/Ti/SiO_2, PZT/Pt(annealed)/Ta/SiO_2, PZT/Pt/Ta/SiO_2. XRD measurement courtesy of Y.-B. Jeon. 57
3-4 SEM of annealed PZT film: (a) grain size uniform at approximately 100 nm (top surface view of film; picture courtesy of Y.-B. Jeon.), (b) side profile of PZT film, detailing bottom electrode and fabricated film thickness. 57

3-5 AFM images of PZT film surface: (a) PZT surface on top of opened Pt/Ti bottom electrode gap, with PZT film in contact with SiO_2, (b) PZT surface next to Pt/Ti gap, (c) PZT surface on top of Pt/Ti bottom electrode, (d) schematic of AFM imaging location. AFM imaging and figure construction courtesy of Y.-B. Jeon. 58
3-6 Wet-etched PZT on patterned bottom electrode. 59
3-7 SEM cross-section of wet-etched PZT profile, showing undercut. 59
3-8 Top optical microscope view of wet-etched PZT shape, with thin 1 μm OCG 825 resist. The undercut is on the order of 50 μm. 59
3-9 SEM of fabricated binary diffractive grating. SEM courtesy of Y.-B. Jeon and A. Garratt-Reed. 60
3-10 Top-view of completed thin-film processing of devices, prior to KOH release: (A) cantilever design, (B) double-anchored membrane design, (C) perforated membrane design, (D) close-up on the multi-layer structure. 61
3-11 Released membrane after KOH bulk micromachining and RIE release. The bow at the membrane edges is observable from the out-of-focus regions, extending approximately 20 μm into the membrane. 62
3-12 Optical profilometry on membrane before RIE release and after KOH bulk micromachining, depicting membrane profile before final release. 63
3-13 Polarization electric field (expressed as applied voltage) hysteresis curve for completed device. Ferroelectric properties were unaffected after KOH bulk micromachining and RIE release. 64
3-14 Dielectric constant and dielectric loss frequency response of PZT film in completed device. 64
3-15 Fatigue cycling results of PZT film, under a 5 V 19.6 μs rectangular pulse. The second set of cycling is done on the same device and polarization is the value investigated. 65
3-16 Measured dielectric constant for various electrode sizes for a single wafer. Figure courtesy of Y.-B. Jeon. 66
3-17 Left: Design schematic of water-immersible piezoelectric cantilever. Right: Side profile of fabrication process. Figure courtesy of Y.-B. Jeon. 67
3-18 Polarization properties of PZT film in air and water: (a) hysteresis characterization, (b) fatigue analysis. Figure courtesy of Y.-B. Jeon. 68
3-19 Probe station setup with a completed double-anchored membrane design. The bright region in the center of the figure is the diffractive grating region. . . . 69
3-20 Probe station setup with a completed free cantilever. Uneven flatness in the gratings region, due to unbalanced residual stresses, can be visually observed. 69
3-21 Measured period change against applied voltage for two different device designs. Both results match with the analytical model for a single set of material properties and with a single fitted d_{31} coefficient at -100 pC/N. 71

3-22 Uniformity of membrane strain under actuation. A uniformity variation of 16% (defined as the standard deviation over the averaged value) is measured. The error bars depict the maximum and minimum values of the measurements. 72
3-23 Dynamic response of double-anchored membrane, with first modal (out-of-plane bending) resonance at 14.1 kHz. 73
3-24 Double-anchored membrane displacement under 14.1 kHz excitation. The figure segments show the displacements for different time-steps of one oscillation. 74
3-25 Comparison of deformable membrane against an unreleased grating device, for characterization of ambient noise floor effects. Up to the first modal resonance of 14.1 kHz, there is no discernable difference within the resolution of the instrument. 74
3-26 Schematic of setup for optical centroid measurements. 75
3-27 First order diffracted angular change against applied voltage obtained by optical image centroid processing and mechanical motion measurements. The optical measurement is corrected for tilt in the membrane through the finite-element mechanical model and is the main source of uncertainty. 76

4-1 Schematic of microcavity waveguide. 81
4-2 Strain-tuning platform for microphotonics. Consisting of thin-film piezoelectric actuators and a double-anchored membrane, this design is general for various microphotonic components of interests. 82
4-3 Finite-element model of membrane strain: (a) in-plane strain profile, along length of PZT, (b) variation of membrane strain against Si membrane thickness. 83
4-4 Band structure of dielectric slab waveguide with embedded holes. Computation courtesy of Johnson [65, 68]. 86
4-5 Photonic band gap transmission spectrum of microcavity waveguide. Computation courtesy of Johnson [65]. 88
4-6 Interpolated $\mathrm{E}_{real,\hat{z}}$ field for one unit cell of the photonic crystal waveguide. The columns are from a coarse 3D FDTD computation by Johnson [65]. The interpolated result is the surface defined by the columns. 94
4-7 (A) Unperturbed interpolated $\mathrm{E}_{real,\hat{z}}$ field (color plot) at middle slice of waveguide, (B) Energy density distribution (color plot) at same middle slice. Design parameters are $a_d = 1.50a$, $w = 1.19a$, $t_{Si} = 0.44a$, air-cladded Si "air-bridge" waveguide, and with 4 holes on each side of cavity. Resonance found at 0.2625 c/a and Q at 180. 95
4-8 Example of interpolated $E_{||}$ and $D_{\perp}$ profiles along one hole circumference of the photonic crystal waveguide. The x-axis is the discretized points (total of 360) along the hole circumference. 95
4-9 Nomenclature of circular hole deformation. 96
4-10 Shape profile of holes under perturbed non-dimensional stress (S/E) of 0.2 . 98
4-11 Hole material displacements for perturbed non-dimensional stress (S/E) of 0.2 . 98

4-12 Schematic depicting the summation over the entire photonic crystal waveguide. Translation and ellipticity effects of the microcavity and holes are both required. The field plotted is $E_{x,}$ (real) at the middle slice of the waveguide. 99
4-13 Change in resonant frequency against mechanical strain for 2D perturbation computation. The mechanical strain effects is divided into: (1) change in the defect size, (2) change in the lattice constant, and (3) ellipticity of the holes. For a +0.2% strain (tensile), a 8.67 nm (0.56%) increase in the resonance wavelength is expected. 100
4-14 Change in resonant frequency against mechanical strain for a 3D perturbation computation. For a +0.2% strain (tensile), a 8.46 nm (0.55%) increase in the resonance wavelength is computed. 101
4-15 Perturbed transmission from 0.2% applied strain in comparison with the original transmission. 102
4-16 Finite-element mesh of microcavity waveguide, showing bow in the waveguide. For a loading stress of 140 MPa (0.1% strain), there is a 16 nm relative out-of-plane displacement for the 8 μm region of waveguide investigated. Displacement is amplified for visual clarity. 104
4-17 Finite-element mesh of microcavity waveguide, under 200 MPa loading stress. The maximum interface stress, between the Si device layer and oxide, is $\sim$ 810 MPa. 106

5-1 Fabrication process flow schematic of strain-tunable photonic crystal waveguide. 109
5-2 Topview of processed results for defining thin-film piezoelectric actuators: (a) Pt/Ti bottom electrode patterned with lift-off, (b) wet-etched patterned PZT, (c) wet-etched patterned PZT (annealed) at higher magnification, and (d) Pt/Ti top electrode patterned with lift-off and oxide layer etched in preparation for XeF_2 etching to release membrane. 110
5-3 Polarization electric field (expressed as applied voltage) hysteresis curve for completed actuators for the microcavity waveguide. The PZT film was etched before annealing in a wet-etchant. 111
5-4 Intermediate steps of X-ray processing: (a) transfer of pattern from mask into PMMA, (b) Cr lift-off to form hard mask for Si plasma etching. 112
5-5 Aligned X-ray nanolithography with Cr hard-mask defined on Si mesa before waveguide etch. 113
5-6 SEM of completed microcavity waveguide under 20,000X magnification. . . . 114
5-7 Stitching error in electron-beam writing of X-ray mask, as reflected in discrete kinks in resultant waveguide. In this particular SEM, the stitching error is approximately 125 nm. 115
5-8 Double-anchored oxide membranes released by front-side XeF_2 isotropic etching: (a) optical micrograph, (b) SEM image. 116

5-9 Schematic of waveguide characterization setup in the MIT Optics and Quantum Electronics Group. Setup permits measurement range from 1430 to 1610 nm with laser diodes, full polarization control, 10 nm sample stage resolution, and high resolution confocal signal collection. Figure courtesy of P. T. Rakich [124]. 117
5-10 Imaged views of microcavity waveguide in operation: (a) exit view of waveguide depicting proper coupling into waveguide and low-loss transmission through waveguide, and (b) top view of guidance into a waveguide with radiation losses from the holes and at the microcavity. 118
5-11 (A) Comparison of Microvision [34] measured strain against FE model estimates, (B) top view of deformable membrane under the Microvision system, (C) x-axis displacement estimates under the FE model. 120
5-12 Normalized transmission of static microcavity waveguide. The measured spectrum is low-pass filtered to remove high frequency measurement noise. Measured device dimensions are listed in Table 5.1. 121
5-13 Measured resonances for microcavity waveguides with different defect length a_d. Design I has $a_d = 1.50a = 648$ nm. Design II has $a_d = 1.52a = 662$ nm. . 123
5-14 Experimental setup with positioned lensed fibers for input and output coupling, imaging optics, and electrical probes for the integrated PZT microactuators. 124
5-15 Strain-tuned resonance of the microcavity waveguide at 0 V and 16 V, in tension. A trust-region nonlinear least squares fit is used to generate the Lorentzians. 125
5-16 Comparison of strain-tuned microcavity resonance against modeling predictions. 126

6-1 Inclusion of the diffractive grating with an atomic force microscopy tip for metrology applications. Top-view schematic shown. 131
6-2 Design concept for localized strain, to perturb the elongated holes for dynamic tuning of Q for a 2D photonic band gap defect mode laser. 133
6-3 Vertical displacement of dielectric slab to perturb the field at the microcavity. Electrostatic capacitors plates with feedback control or piezoelectric actuators could be used to control the displacement. 134

A-1 Detailed process conditions for analog tunable gratings (I). 137
A-2 Detailed process conditions for analog tunable gratings (II). 138
A-3 Detailed process conditions for analog tunable gratings (III). 139
A-4 Detailed process conditions for analog tunable gratings (IV). 140

A-5 Mask layout for a single chip with analog tunable gratings: (A) Test element for 2 μm diffractive gratings lift-off, (B) Device: free cantilever with gratings, (C) Test element for Pt top electrode, (D) Test element for Pt-PZT-Pt structure, (E) Device: double-anchored membrane with gratings, (F) Test element for PZT-Pt structure, (G) Test element for backside KOH, (H) Device: perforated double-anchored membrane with gratings, (I) Test element for Pt bottom electrode. 141
A-6 Summary of design matrix for analog tunable gratings. Shown also are the locations of the chips on a wafer. A water-immersible active cantilever is also included in the design and fabrication. 142

B-1 Waveguide losses, from mode extension into substrate, against buried oxide insulator thickness for various waveguide geometries as calculated by Foresi [32]. 144
B-2 Quality-factor Q against the number of holes on each side of the microcavity, as calculated by Fan [27]. 145
B-3 Summary of computation scheme for strain-perturbation on microcavity waveguide for a given perturbation. 146

C-1 Detailed process conditions for strain-tunable photonic band gap microcavity waveguide (I). 148
C-2 Detailed process conditions for strain-tunable photonic band gap microcavity waveguide (II). 149
C-3 Detailed process conditions for strain-tunable photonic band gap microcavity waveguide (III). 150
C-4 Detailed process conditions for strain-tunable photonic band gap microcavity waveguide (IV). 151
C-5 Detailed process conditions for strain-tunable photonic band gap microcavity waveguide (V). 152
C-6 Detailed process conditions for strain-tunable photonic band gap microcavity waveguide (VI). 153
C-7 Mask layout with mirror-symmetrical (horizontal and vertical) segments A,B,C, and D on the wafer. The five different chips in each segment, as labeled, are: (a) strain-tunable photonic crystal, (b) DONS device 1, (c) DONS device 2, (d) Nanoservo, and (e) water-immersible cantilever. The space layout on the mask is designed to be compatible with the X-ray masks. 154
C-8 Etch conditions: CF_4 / O_2 at 13.5 / 1.5 sccm ; 20 mtorr; 400 V DC bias. Etch rate: 52 nm/min. 155
C-9 Etch conditions: CF_4 / O_2 at 13.5 / 1.5 sccm ; 20 mtorr; 300 V DC bias. Etch rate: 36 nm/min. 156
C-10 Etch conditions: CF_4 / O_2 at 13.5 / 1.5 sccm ; 10 mtorr; 300 V DC bias. Etch rate: 20 -26 nm/min. 157

C-11 Variation in electron beam exposure dose, through different beam scanning frequencies, on the microcavity waveguide geometry. SEM shows profile after Cr lift-off with PMMA. Design details in the electron beam layout are listed in Figure C-12, page 159. 158
C-12 Design matrix of microcavity waveguide for electron beam lithography. . . . 159

List of Tables

3.1 Analog Piezoelectric Tunable Grating Parameters. 70

4.1 Microcavity Waveguide Design Parameters. 87

5.1 Specific measured dimensions of microcavity waveguide with transmission spectrum shown in Figure 5-12. 122

Chapter 1

Introduction

Nothing tends so much to the advancement of knowledge as the application of a new instrument. The native intellectual powers of men in different times are not so much the causes of the different success of their labours, as the peculiar nature of the means and artificial resources in their possession.
—Sir Humphrey Davy, 1778-1829.

This chapter summarizes the background and motivation for this thesis work. A brief review of literature specific to the tunable gratings and photonic crystals of interest is presented.

1.1 Background And Motivation

The advent of microelectronics has permitted significant advances in microelectromechanical systems (MEMS) and microphotonics. The ability to make devices at micrometer and nanometer length-scales has opened up new application spaces and challenged our physical understanding and intuition. In the field of micro- and nano-scale optics, there exist innovations and discoveries in optical microelectromechanical systems and photonics crystals. We pursue here these two major fields based on one generalized concept – that of *strain-tuning of periodic structures* to achieve modulation of the optical responses.

In optical microelectromechanical systems (Optical MEMS), there is significant attention on micromirror arrays, both as beam steering in optical telecommunication networks [6, 95, 108, 111] and compact, reliable projection display systems [75, 152, 52]. As optical networks evolve, the need for active tuning of network components – such as laser sources and wavelength add/drop filters – is emphasized, based on the following demands:

I. usage-based reconfiguration of network components for overall network adaptivity and reliability,
II. active compensation against external disturbances such as thermal and stress-induced fluctuations, material dispersions and absorptions, and

III. device trimming to achieve or relax tight production tolerances in high bandwidth optical and optoelectronic devices.

An immediate example of dynamically tunable network components is the phalanx of MEMS-based tunable vertical cavity surface emission lasers as reconfigurable laser sources [14, 151].

In the corresponding realm of micro- and nano-photonics, there exits a spectrum of devices, ranging from Bragg grating waveguides, high Q microcavities [3], microring resonators [98] to nanolasers [26, 53] among the many. In particular, a new class of materials has emerged that affords complete control on the flow of light [62, 161, 63]. Termed as photonic crystals, they are the optical analog of electronic semiconductor materials, possessing *photonic* band gaps which prevent light from propagating in certain directions with specified energies. This is achieved through designing the structure of these periodic crystals to affect the properties of photons, in much the same way as semiconductor lattices affect the properties of electrons. The same demands of dynamic reconfiguration, active compensation, and device trimming for practical implementations of photonic crystals bring about the necessity of active tuning for photonic crystals.

Current methods for tuning Current methods for tuning include electro-optic and thermal effects. While the electro-optic (Pockels and Kerr effects) method is commonly used and has response times on order of GHz or more, it typically requires high voltages and is virtually absent in silicon optical devices. With active III-V materials, the wavelength tuning range $\Delta\lambda$ is typically on order of 0.05 nm [99] and reported up to 0.26 nm [83]. In polymeric electro-optic materials, the tuning range is reported up to 6.6 pm/V [123].

Thermal actuation is also a commonly employed tuning method. However, thermal tuning – either through direct thermal expansion or with charge carriers or with liquid crystals – generally requires high power (mW per active device) and has response times on order of kHz. Furthermore, with thermal tuning, it might be difficult to achieve localized tuning, within the order of 10 μm spatial dimension, for individual devices in high-density integrated optical circuits. Following from these generalizations, we will elaborate, in Section 1.2 and 1.3, on the current specific tuning methods for each of our two implementations.

The generalized case for piezoelectric strain-tuning We propose the generalized concept of strain-tuning with integrated piezoelectric microactuators with the following benefits:

I. low power consumption (order of nW) and low voltages (order 5 volts),

II. ultra-fine control with MHz dynamic response,

III. localized tuning, with negligible cross-talk, for integrated optical circuits, and

IV. compact integration of microactuators.

The low power consumption and voltage requirements per active device is significantly smaller than thermal actuators, due in part to the high energy density piezoelectric microactuators [56]. Piezoelectric actuators are also commonly used for ultra-fine displacements, such as in positioning atomic force microscope tips, through control of the input voltage.

The response times can achieve MHz modulation, although this is significantly slower than electro-optic methods. The tuning is also easily localized as individual devices can be designed to be physically separate with its neighbouring devices. Compared to electrostatic actuators, piezoelectric actuators permit compact integration possibilities.

The trade-off is the added complexity in device micro- and nano-fabrication to include the integrated piezoelectric films. In addition, a moving part is often involved in order to have active localized strain only at the individual devices, as opposed to the whole substrate. A control loop may also be required to maintain the tuning; however, the power expended is small compared to power dissipated for controlled-temperature environments in current optical devices [1].

In this thesis, thus, we present the generalized concept of strain-tuning to periodic optical structures. In particular, we present two implementations: (I) a fundamental diffractive grating element, and (II) a photonic band gap microcavity waveguide. We begin with a literature review in each of the two implementations.

1.2 Brief Review Of Tunable Diffractive Gratings

Digital tunable gratings – with discrete reconfigurability – have successfully been advanced in Optical MEMS. For example, the Grating Light Valve [1, 137] shown in Figure 1-1a switches between a reflective micromirror and a diffractive grating through control of every alternate grating beam, with primary targeted applications in high-end projection systems. In addition, the Polychromator [49, 135] illustrated in Figure 1-1b modulates the grating period with individual control of the gratings beams for applications in high-resolution miniaturized spectroscopy. Inter-digitated cantilevers for a deformable diffraction grating has also been reported for scanning probe microscopy applications [104]. In all three devices, the grating elements are deflected out of the grating plane to modulate the optical spectrum. The resolution is then defined by the width of a microfabricated grating beam, on the order of a micrometer.

Analog tunability on gratings was reported via the following mechanisms:

Thermal actuation through thermal expansion of one or more derived grating structures, such as shown in Figure 1-2a, with preferential expansion in the direction of the grating period. Reported diffraction angle modulations ranges from 1 to 35 mrads [130, 167].

Bulk strain actuation through bulk piezoelectric material, magnetic actuators, and motion of a seismic mass on fiber Bragg gratings [92, 76, 122, 60, 140]. These gratings are applied in an erbium-doped fiber amplifier module, or as a channel-switching add/drop multiplexer for wavelength division multiplexing.

[1] A back-of-the-envelope calculation for power dissipation with natural convection gives an estimate of 0.3 W for a 5 ^{o}C differential temperature in a controlled environment.

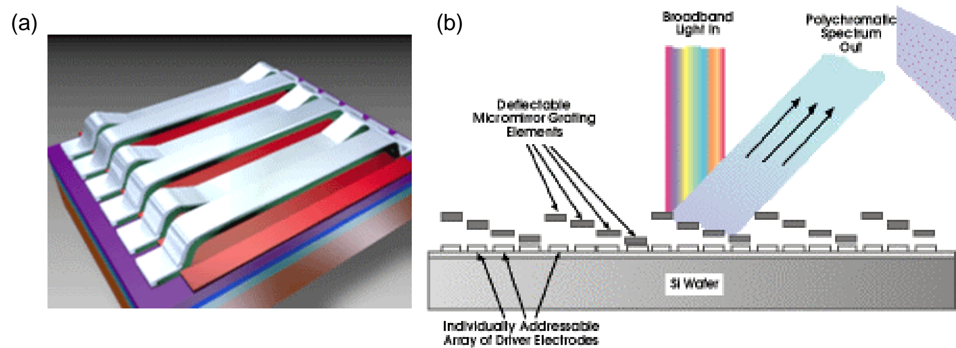

Figure 1-1: Digital tunable gratings: (a) Grating Light Valve schematic [1, 137], (b) Polychromator schematic [49, 135].

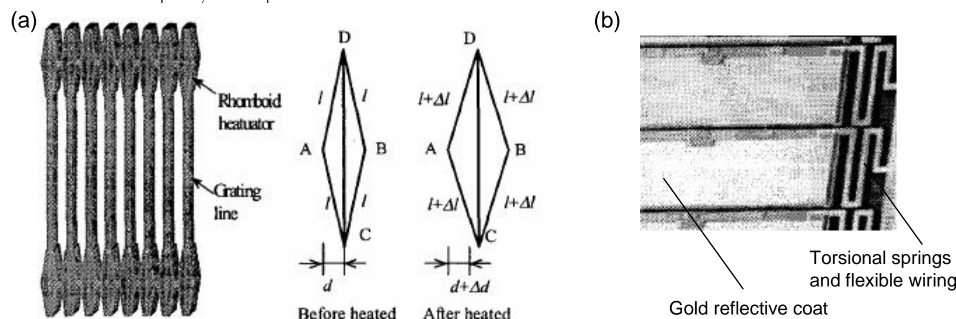

Figure 1-2: Current analog tunable gratings: (a) Rhomboidal heatuator schematic [167], (b) Variable blazed gratings [10].

Vertical electrostatic actuation through capacitance plates that include grating structures [130, 156]. The phase relationship between the vertically-movable grating is modulated with respect to a fixed grating on the substrate, resulting in control of the diffracted order intensities.

Blazed electrostatic actuation through rotational motion of blazed gratings such as illustrated in Figure 1-2b. The deflection of the diffracted orders are reported up to ± 44 mrads [10].

Compared to the current implementations, we propose a method of strain-tuning to achieve tunability with a resolution on the order of 1 μrad and range up to several hundred μrads. Our device concept thus trades deflection range for angular resolution. The theoretical design of this device is presented in Chapter 2, wherein the piezoelectric mechanical design, optical design, and specific applications of the device are discussed. Chapter 3 presents the fabrication results and experimental analyses – electrical, mechanical and optical – on the piezoelectric analog tunable grating.

1.3 Brief Review Of Photonic Crystals And Tunable Methodologies

The early 1990s saw an emergence of fascinating work on 1-dimensional, 2-dimensional and 3-dimensional photonic crystals, in both theoretical proposals and experimental demonstrations [161, 63, 62, 116, 97, 154, 114]. A sampling is shown in Figure 1-3. These spatially periodic structures typically consist of high dielectric contrast media, wherein absorption is minimized and scattering designed at the interfaces, to produce many of the same phenomena for photons as the atomic potential does for electrons. These characteristics are theoretically captured exactly through Maxwell's equations. Applications, through the ability to control the flow of light with photonic band gaps, range from low-threshold semiconductor lasers [116], high efficiency light-emitting diodes, novel optical fibers, high-Q optical resonators and filters, negative refractive index material and superlens [102], theoretically proposed all-optical transistors [138, 64], and many others.

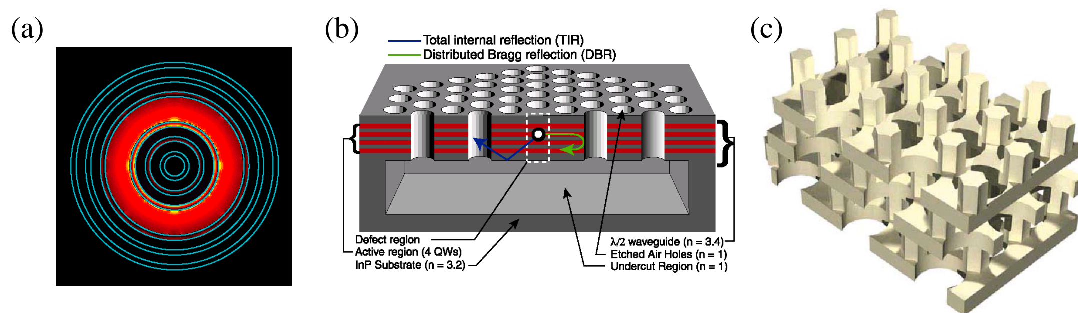

Figure 1-3: Sampling of photonic crystals: (a) Radially symmetric one-dimensional photonic structure serving as omnidirectional reflecting mirrors in an optical waveguide [58], (b) Two-dimensional photonic band gap defect mode laser [116], (c) Three-dimensionally periodic dielectric layered structure with omnidirectional photonic band gap [67].

While most of the theoretical and experimentally demonstrated photonic crystals are not tunable, several mechanisms for tunability have been proposed:

Electro-optic effect through the application of an electric field to change the refractive index of a compound semiconductor material [28], with the typical range of modulation of the refractive index less than 0.1%.

Charge-carrier effect through variations in concentraton of free carriers for photonic crystals with semiconductor constituents. This is achieved through temperature or doping modulation. For example, Halevi and Ramos-Mendieta suggest tuning of the band gap with temperature variations more than order 20 ^{o}C [40], although absorption needs to be considered for high levels of doping. The typical range of modulation of the refractive index less than 0.1%.

Liquid crystal tuning through infiltration of an optically birefringent nematic liquid crystal into void regions of an inverse opal photonic band gap material. Specifically, Busch and John [11] theoretically suggests the application of electric fields to reorientate the axis of nematic liquid crystals relative to the photonic crystal backbone. Yoshino *et. al.* reports thermal tuning with liquid crystals, with an order 13 nm red-shift in wavelength for a 45 ^oC temperature difference [165] in an opal structure. These developments suggest the possibility of tuning up to 2% by application of heat or an external electric field.

We here propose strain tuning of photonic crystals as another mechanism to modulate the optical response, for the generalized reasons brought up in Section 1.1. This is especially relevant for silicon microphotonic integrated circuits where the electro-optic effects are vanishingly small. Strain tunability, in addition, has recently seen theoretical discussions in modulating the photonic band gap such as reported by Kim et. al. [74], controlling the polarization from a photonic crystal laser [115], and tuning the quality factor Q of a nanocavity defect laser [155].

Specifically, we focus on the implementation of a strain-tunable microcavity, a 1-dimensional photonic crystal embedded in a silicon waveguide. This development is made possible based on collaborative work first reported by Foresi, Fan and Lim [33, 27, 94]. Chapter 4 describes the concept of the device, along with perturbation analysis on finite-difference time-domain results and mechanical displacement computations. Other considerations, such as photoelastic Pockels effect, are also described. Chapter 5 describes the micro- and nano-scale integrated processing and presents experimental results of the strain-tunable microcavity waveguide. Chapter 6 summarizes the results and conclusions of both the analog tunable diffractive gratings and the strain-tunable microcavity waveguide, along with suggestions for future explorations.

Chapter 2

Design Of Analog Tunable Diffractive Gratings

But soft! What light through yonder window breaks?
It is the East, and Juliet is the sun!
Arise fair sun, [...] .
– W. Shakespeare (1565 - 1616).

We propose analog control over the diffraction angle of a tunable MEMS grating, with resolution at 1 μrad up to a range of 300 μrads. Compared with other tunable grating implementations such as the Grating Light Valve [1, 137], the Polychromator [49, 135] and several others (Section 1.2), our device concept has ultra-fine angular resolution. Specific high resolution applications include external cavity tunable lasers, thermal compensators for wavelength multiplexers-demultiplexers, and miniaturized spectrometers. This chapter discusses the piezoelectric, mechanical and optical designs on the analog tunable grating, achieved with thin-film piezoelectric actuators for fine resolution.

2.1 Concept Of Device

Analog tunability of the diffractive grating is achieved by lateral actuation forces on the grating structure. This is illustrated in Figure 2-1 wherein the grating period is progressively increased, resulting in control over the diffracted angles. The binary phase grating, created on a membrane, deforms along with the supporting membrane when mechanically strained by thin-film piezoelectric actuators as shown in Figure 2-2. The piezoelectric actuators, a lead zirconate titanate (PZT), is located at the ends of the membrane and are capable of producing sufficient force to deform the membrane up to 0.3% strain, or equivalently, a 0.3% diffracted angle change. The analog tuning is a linear response to the applied voltage due to the small strain range of less than 1%. The fine voltage control of the piezoelectric actuators permit a theoretical resolution of 1 μrad.

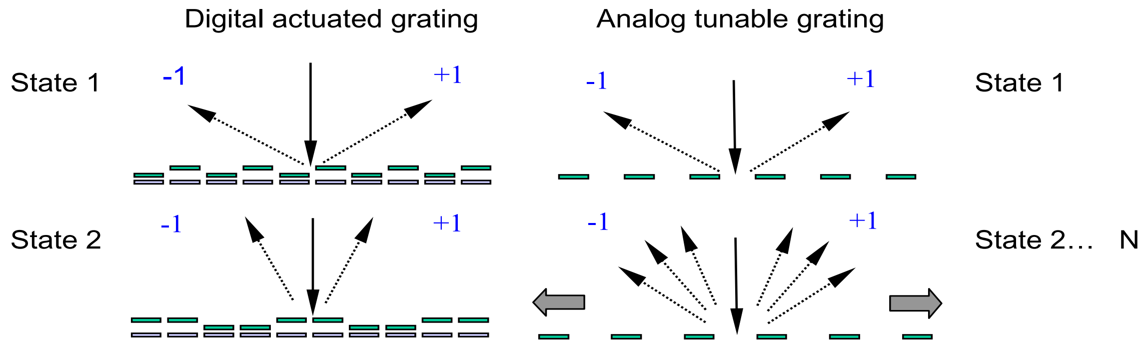

Figure 2-1: Actuation concept of analog and digital tunable gratings. The analog design permits analog control of diffraction angle.

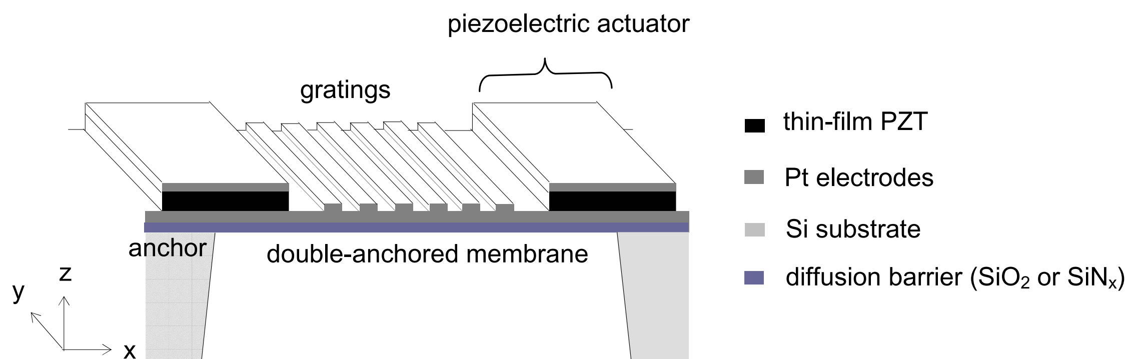

Figure 2-2: Design schematic of double-anchored deformable membrane, driven via thin-film piezoelectric actuators. The gratings, defined on top of the membrane, are tuned progressively along with the membrane.

A more compliant grating structure, such as a double-anchored perforated membrane design, would allow a larger grating period displacement per unit actuation force. The design is shown in Figure 2-3a. There is, however, increased difficulty in fabricating the beams with bulk micromachining. Another possibility for increased grating period displacement is a free cantilever design with a grating structure defined on top of the cantilever, as shown in Figure 2-3b; however, out-of-plane bending due to unmatched residual stresses or actuation of the cantilever bimorph will significantly affect the optical response. The designs are discussed further in Section 2.2.2. An alternate method of lateral tuning of the grating period involves using electrostatic comb-drives on an accordion-like grating structure [134, 159].

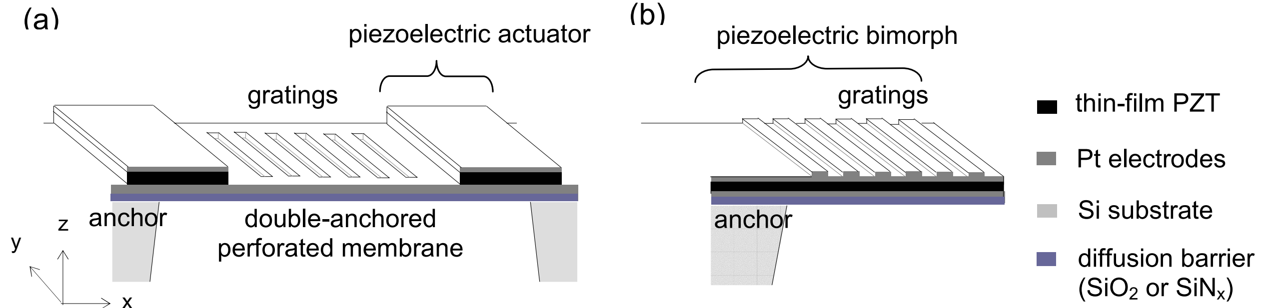

Figure 2-3: Design schematic of (a) double-anchored perforated membrane, (b) free cantilever with gratings.

2.2 Micro-Electro-Mechanical Design

2.2.1 Piezoelectric theory

In 1880 Pierre and Jacques Currie [21] discovered surface electric charges on certain crystals when subjected to mechanical stress. Rapidly, they proved experimentally the converse of this effect, namely mechanical deformation under an applied electric field. This phenomenon of electrical charge and mechanical deformation coupling was termed as piezoelectricity by Hankel [41] and reviewed historically by Cady [12]. A brief review of early development of PZT transducers can be found in Lee [87].

A motivation to employ thin-film piezoelectric actuators is the large power density achievable in this class of contractile materials. Studies on piezoelectric ceramics report power densities greater than 1000 W/kg [149], on the order of shape memory alloys, magnetostrictive actuators and conducting polymers [56, 57, 5], while approximately an order of magnitude large than muscles [56] and two orders of magnitude larger than electrostatic actuators [113]. A drawback is the small strain viable in piezoelectric materials (typically ranging up to 0.1%, depending on the ceramic composition), though mechanical amplifiers have increased the effective strain 8 to 10 times [141]. The expected power consumption is also low (on the order of 10 nW) due to the high resistivity and low voltage requirements of the piezoelectric film.

The piezoelectric coupling between electric field and stress can be expressed as [131]

$$\epsilon_I = \sum_J S^E_{IJ}\,\sigma_J + \sum_j E_j\,d_{jI} \quad (2.1)$$

$$D_i = \sum_J d_{iJ}\,\sigma_J + \sum_j \varepsilon^{\sigma}_{ij}\,E_j \quad (2.2)$$

where $i, j \in$ [1,2,3] and are indices of electric constituents, $I, J \in$ [1,...,6] and are indices of mechanical constituents, ϵ_I the mechanical strain, S^E_{IJ} the compliance matrix at constant

electric field, σ_J the mechanical stress, E_j the applied electric field, ε_{ij} the dielectric permittivity, d_{iJ} the strain-electric-field piezoelectric coupling coefficient. A detailed discussion can be found in Uchino [150]. For ceramic piezoelectric actuators, d_{31} can typically range from -2 to -100 pC/N. In addition, there are polymer piezoelectric actuators [42, 71], another class of piezoelectric transducers, that could provide a larger strain, although the piezoelectric properties (such as d_{31} and the electromechanical energy coupling factor k_{31}) are typically smaller.

In addition, Figure 2-4a illustrates the hysteresis in piezoelectric materials, due to nonlinear strain changes from polarization reorientation in an external electric field. Strain creep, shown in Figure 2-4b with time as the horizontal axis, is also expected due to depoling, and asymptotically approaches a final steady value [150]. To maintain a desired strain precisely, therefore, a passive mechanical latch or active control would prove desirable.

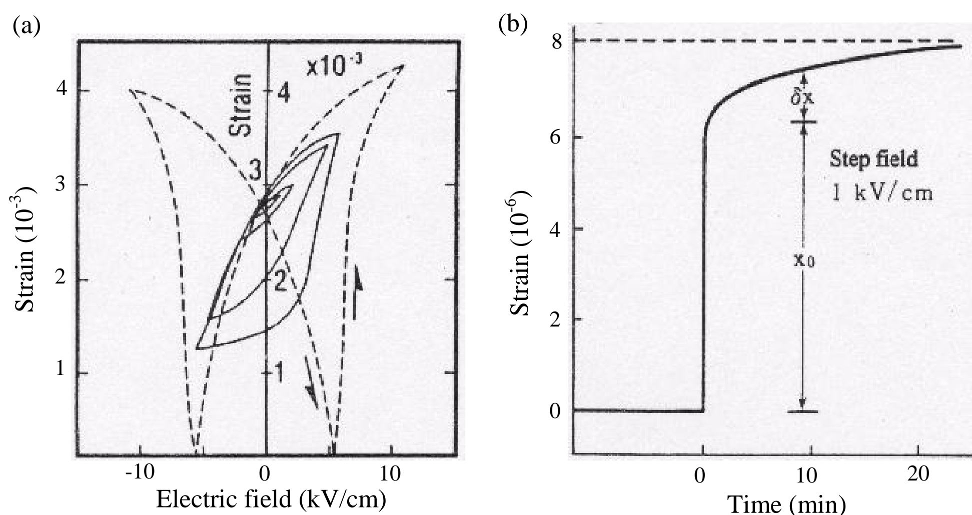

Figure 2-4: (a) Hysteresis in field-induced strain curves, (b) Strain creep characteristics. Adapted from Uchino [150].

2.2.2 Analytical thin-film piezoelectric design

An analytical model for multiple-layer cantilever devices – applicable to thin-film micromachined devices – was introduced by DeVoe and Pisano [23]. Alternate methods for modeling include lumped-element modeling [1] or variational approaches with large piezoelectric coupling coefficients for dynamic analysis [39, 50]. Weinberg developed a closed-form solution and a static model which could account for built-in axial forces at the end of a cantilever [157]. The latter work forms the basis of our model to design the deformation in our double-anchored membrane. The modeling assumptions are the following:

[1] This is presented in Senturia [131], Section 21.5.2 .

- Plane strain in beam, such that the Young's modulus $E \rightarrow \frac{E}{1-\nu^2}$ and $d_{31} \rightarrow d_{31}(1+\nu)$
- No-slip between the layers
- Static equilibrium of cantilever
- Beam thickness sufficiently smaller than beam radius of curvature
- Small piezoelectric coupling, such that $\frac{d_{31}^2 E}{\varepsilon} < 1$

In particular, the position of the cantilever end $[z_L, \theta_L, x_L]$ and the generated charge Q can be expressed as

$$\begin{bmatrix} z_L \\ \theta_L \\ x_L \\ Q \end{bmatrix} = \begin{bmatrix} \frac{kL - tanh\ kL}{Pk} & \frac{1-\frac{1}{cosh\ kL}}{P} & 0 & \frac{1-\frac{1}{cosh\ kL}}{P} M_v \\ \frac{1-\frac{1}{cosh\ kL}}{P} & \frac{k\ tanh\ kL}{P} & 0 & \frac{k\ tanh\ kL}{P} M_v \\ 0 & 0 & \frac{1}{k_x} & \frac{F_v}{k_x} \\ \frac{1-\frac{1}{cosh\ kL}}{P} M_v & \frac{k\ tanh\ kL}{P} M_v & \frac{F_v}{k_x} & C \end{bmatrix} \times \begin{bmatrix} F_L \\ M_L \\ P \\ V \end{bmatrix} \tag{2.3}$$

where

$$M_v = \frac{\sum_j \frac{d_{31j} E_j A_j (z_m - z_j)}{\varepsilon_j}}{\sum_j \frac{t_j}{\varepsilon_j}} = \text{the torque per unit voltage across electrodes,} \tag{2.4}$$

$$F_v = \frac{\sum_j \frac{d_{31j} E_j A_j}{\varepsilon_j}}{\sum_j \frac{t_j}{\varepsilon_j}} = \text{the axial force per unit voltage,} \tag{2.5}$$

$$k_x = \frac{\sum_i E_i A_i}{L} = \text{the axial stiffness of the stack,} \tag{2.6}$$

$$C = \frac{\varepsilon b L}{t} = \text{capacitance of the electrodes,} \tag{2.7}$$

with L the PZT length, E_j the Young's modulus of layer j, A_j the cross-sectional area of layer j, z_m the neutral axis for torque inputs, and t the thickness of the layer between the electrodes. The nomenclatures used in the modeling is illustrated in Figure 2-5. The subscript i denotes layers in the stack, while the subscript j denotes only the layers between the electrodes.

Specifically, we note that P is the externally applied axial force through the neutral axis. Taking symmetry through the center of the membrane, P must match the axial force, $P_{membrane}$, from the remainder of the membrane, to the right of the piezoelectric actuator. To model the deformation in our double-anchored membrane, an initial guess of the deformation was first computed and iteratively solved to have P equal to $P_{membrane}$ within a defined tolerance.

The design variables are the following: (1) PZT length L, (2) membrane length L_{mem}, (3) PZT thickness t_{pzt}, (4) membrane (platinum and silicon oxide) thickness t_{mem}, (5) piezoelectric dielectric coefficient d_{31}. Of these, L and L_{mem} are the design parameters to vary for

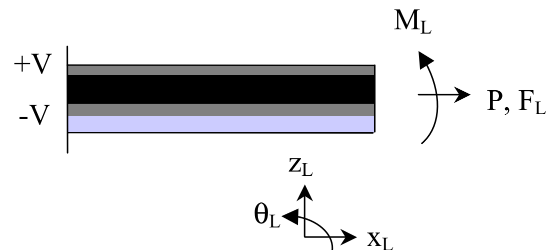

Figure 2-5: Nomenclature of closed-form solution with loaded cantilever end [157].

devices on a single wafer. The d_{31} coefficient is a key parameter obtained from device fabrication quality, while the layer thickness are generated from actual fabrication constraints and optimizations.

The predicted total membrane displacement as a function of applied voltage against various d_{31} and L parameters are plotted in Figure 2-6 for comparison. The values of L_{mem}, t_{pzt} and t_{mem} used in this plot are 300 μm, 0.5 μm and 0.27 μm respectively. The linear response against applied voltage, without spontaneous polarization transition, is assumed in this analysis for sufficiently small electric fields. As PZT length L is increased, there is more displacement (and strain) in the membrane; likewise, as the d_{31} coefficient is increased, there is more displacement. For L at 200 μm and d_{31} at -100 pC/N, a membrane in-plane displacement of 187.4 nm is predicted.

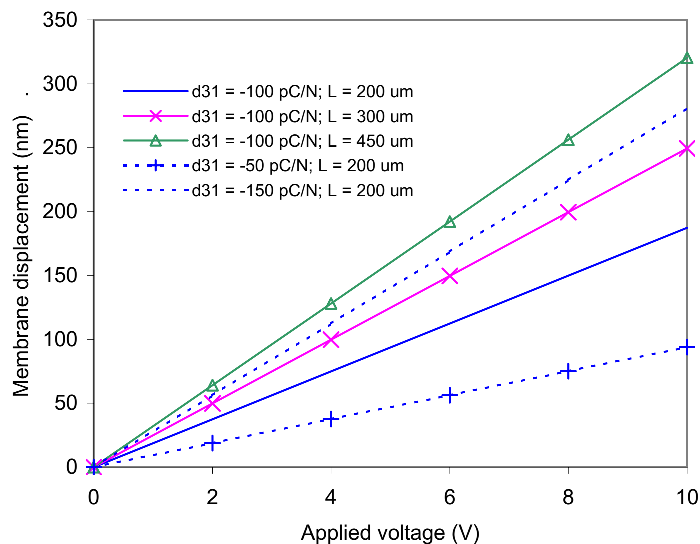

Figure 2-6: Theoretical membrane displacement against applied voltage for various d_{31} and L parameters. The linear response, without spontaneous polarization transition, is assumed in this analysis for sufficiently small electric fields.

Design space To investigate the membrane strain (or the piezoelectric actuation axial force) against various parameters, Figure 2-7 shows the membrane strain versus nondimensional PZT thickness, t_{pzt}/t_{mem}, and nondimensional PZT length, L_{pzt}/L_{mem}, in our design space. As expressed in Equation 2.5, the piezoelectric axial actuation force per unit voltage is solely dependent on d_{31}, the width of the actuator, and Young's modulus of PZT, and not a direct function of t_{pzt} as t_{pzt} cancels out for a structure with a single piezoelectric layer. d_{31}, however, is dependent on t_{pzt} [160] and the specific relationship dependent on the fabrication process.

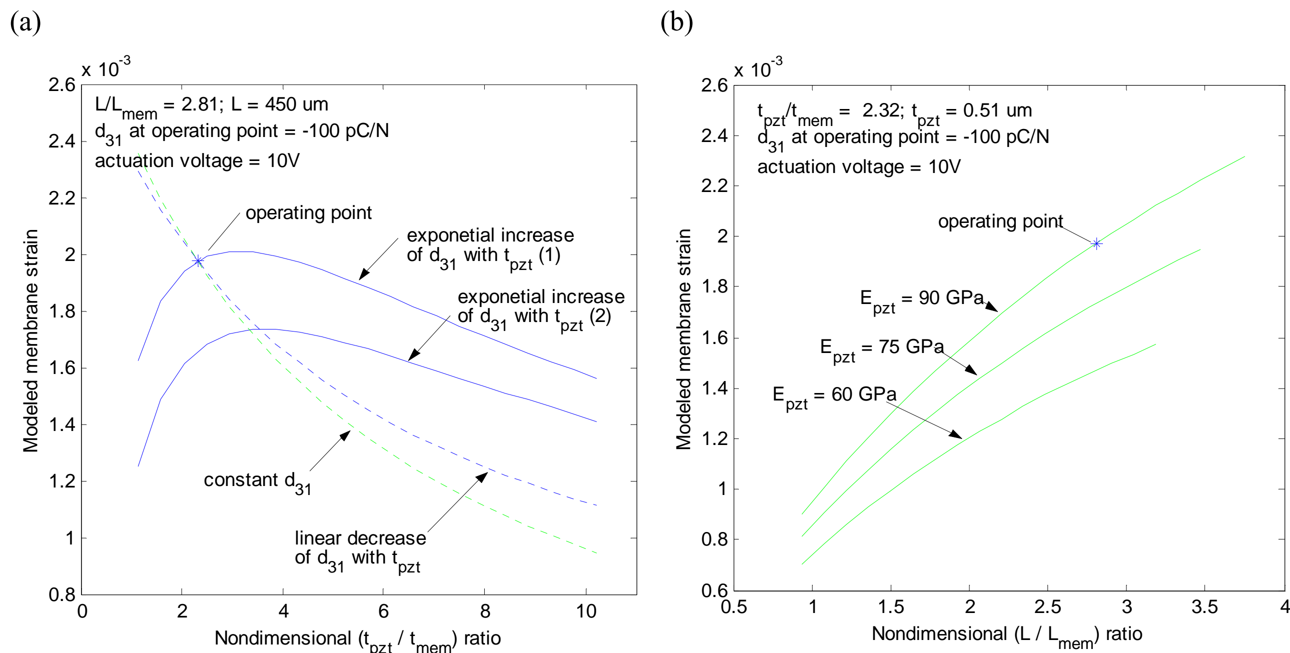

Figure 2-7: Theoretical membrane strain against: (a) t_{pzt}/t_{mem} ratio and, (b) L/L_{mem} ratio, in our design space.

For a nonlinear relationship between d_{31} and t_{pzt}, the resultant membrane strain against nondimensional PZT thickness is shown as the solid lines of Figure 2-7a for two different exponential relationships, labeled as (1) and (2) in the Figure. For small t_{pzt} values (such as 0.25 μm), as t_{pzt} is increased, there is an increase in the d_{31} coefficient and hence increase in the membrane strain. For larger t_{pzt}, the increase in d_{31} saturates. The increase in t_{pzt} then contributes more to the increased stiffness in the actuator (than the increase in d_{31}), thereby resulting in a decrease in the overall membrane strain. The dashed lines in Figure 2-7a shows the situation if d_{31} stays constant for all t_{pzt}, and if d_{31} is a linear increasing function with increasing t_{pzt}.

The ratio of PZT length to membrane length serves as an linear length amplification factor, pushing the membrane strain above 0.1%. Figure 2-7b shows the membrane strain as the PZT length to membrane length ratio is increased. Too large a ratio is not viable due to fragility of the membrane during fabrication. Also shown in Figure 2-7b are plots for

various PZT Young's modulus. A larger PZT Young's modulus with respect to the membrane modulus (fixed at 95 GPa with a 0.33 Poisson ratio) brings about a larger membrane strain, due to the increased relative stiffness of the actuators. In general, the ratio[2] of (PZT axial stiffness / membrane axial stiffness) needs to be on order unity or larger in order to effect strains above 0.1% for a fixed (L/L_{mem}). Depending on d_{31} and the Young's modulus, typical piezoelectric actuation axial forces per unit voltage range from 0.5 - 2 mN/V for a 300 μm wide thin-film actuator designed for our devices[3].

2.2.3 Finite-element piezoelectric modeling

While the analytical model provides an excellent estimate on the grating deformation, a finite-element solution provides insight into more subtle details such as characteristics of possible bow in the grating, stress concentration regions and modal responses of the deformable membrane.

The finite-element modeling is created through CoventorWare^{TM}. A right-hand coordinate system is used, with the x-axis defined along the membrane length, the y-axis along the membrane width, and the z-axis upwards from device substrate to the thin-films. Membrane deformation, with the piezoelectric thin-films, is computed through coupled linear solutions of the electric field potential and the mechanical displacement; that is, this assumes sufficiently small electric fields without spontaneous polarization transition of the piezoelectric material.

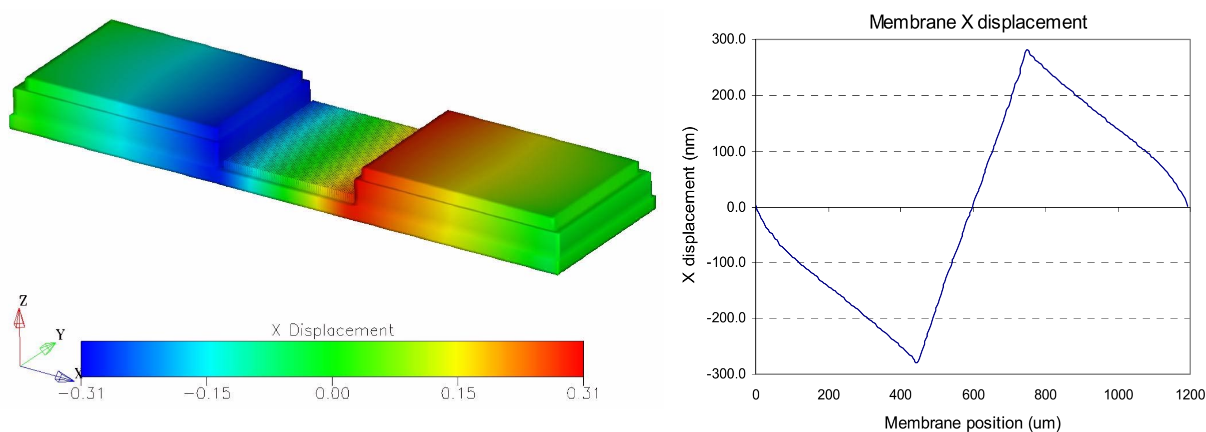

Figure 2-8: Finite element mesh of analog tunable grating, depicting x-axis displacement. For illustration, film thickness in the z-direction are exaggerated 100X and z-displacement is exaggerated 2X.

[2]The axial stiffness k_{axial} is defined as $\frac{EA}{L}$ with A the cross-sectional area.

[3]This axial force is in agreement with Weinberg [157] from which our model is originally derived, and serves as order-of-magnitude check. Though piezoelectric energy density is more often the reported parameter [56, 84], our interest here is the actuation force to deform the membrane.

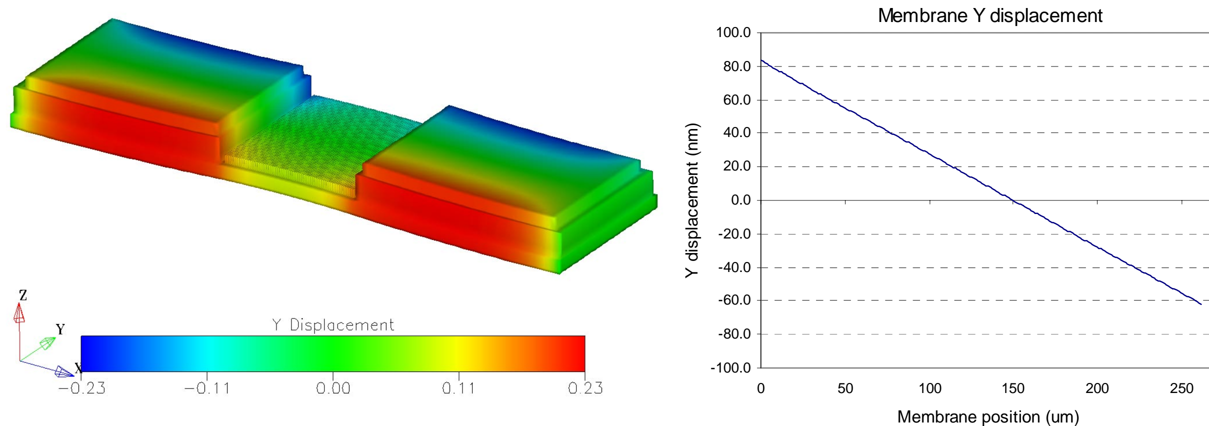

Figure 2-9: Finite element mesh of analog tunable grating, depicting y-axis displacement.

For a d_{31} of -128 pC/N and 10 V applied to both actuators, our numerical model predicts a maximum x-axis displacement of 280 nm at the end of each 450 μm actuator (as shown in Figure 2-8), corresponding to a 0.197% strain in the membrane. The strain is linear in the membrane and, at 10 V, gives a 7.89 nm grating period change for 4 μm grating period. Moreover, there is Poisson contraction in the y-axis, with a maximum of 83 nm across the gratings and 226 nm across the membrane at 10 V, as displayed in Figure 2-9. The Mises stress concentration of 220 MPa (at 10 V actuation) is seen at the membrane edge attachment to the silicon base anchor (Figure 2-10), and suggests inclusion of fillets to prevent membrane breakage during actuation.

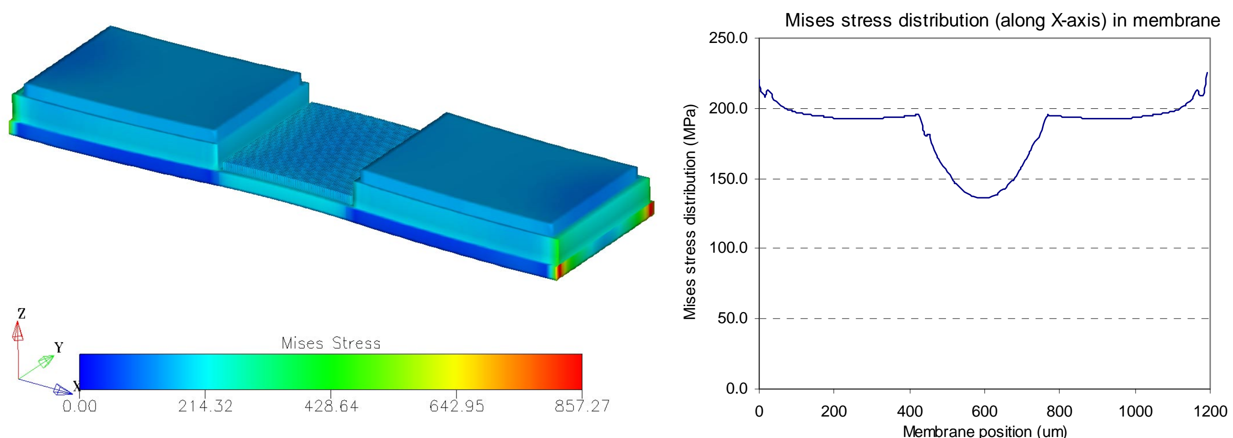

Figure 2-10: Finite element mesh of analog tunable grating, depicting membrane Mises stress concentration regions.

Moreover, the finite-element model also predicts a 1.941 μm rise in the grating center across a 282 μm grating size as seen in Figure 2-11 in the x-direction. For ease of reference in this work, we chose to define the grating bow angle as $\tan^{-1}$(grating center rise height/grating

half-size); this gives us an estimated grating bow angle of 16.71 mrads. There is also a slight

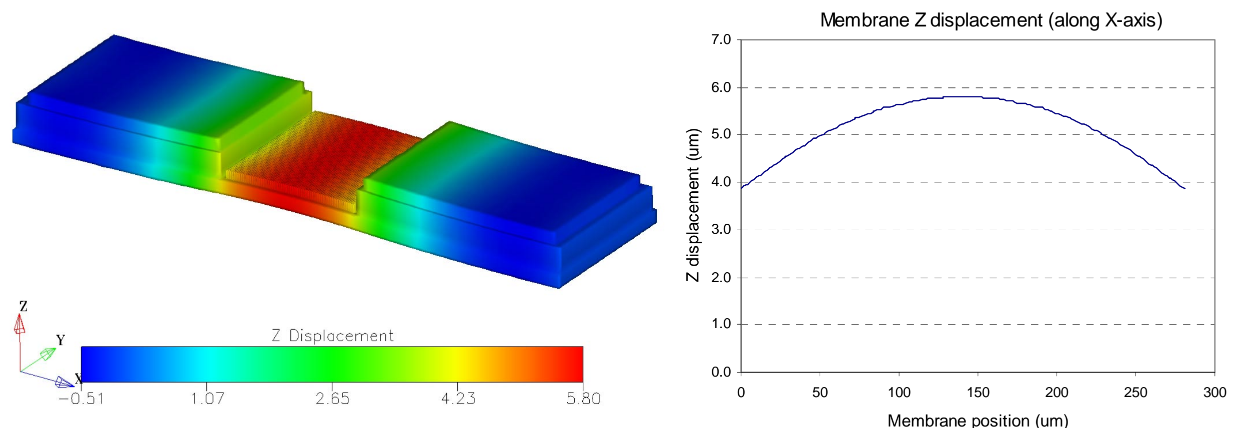

Figure 2-11: Finite element mesh of analog tunable grating, depicting z-axis displacement.

Figure 2-12 shows the comparison between analytical and finite-element models. Material properties, device dimensions and designs are entirely consistent between the models. There is only fair agreement between the models, with about 23% discrepancy between the theoretical predictions, most probably due to the out-of-plane motion captured by the finite-element mesh. A corrected d_{31} at -128 pC/N for the finite-element model predicts (within 1%) the displacement for the analytical model with d_{31} at -100 pC/N.

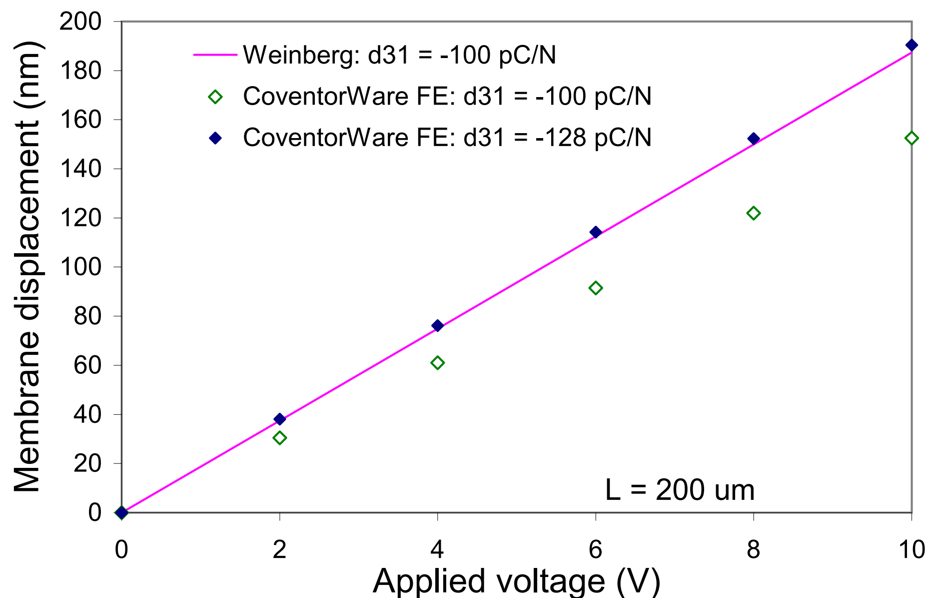

Figure 2-12: Comparison of analytical and CoventorWare Finite-element models.

2.2.4 Membrane structural and energy considerations

Residual stress effects Residual stress strongly affects the bending stiffness and mechanical resonance of our double-anchored membrane. While analytical solutions of plates and membranes under various loading conditions are presented in Timoshenko [144], we employ a combined variational technique and finite-element computations to understand the effects of residual stress. A plate or membrane clamped on four sides under uniform loading exhibits the following stiffness functional form, extending from Senturia [131]:

$$k_{eff} = C_r \sigma_o H \ + \ C_b \frac{EH^3}{(1-\nu^2)L^2} \ + \ C_s f_s(\nu) \frac{EH}{(1-\nu)L^2} \ c_1^2 \tag{2.8}$$

where coefficients C_r, C_b, C_s and $f_s(\nu)$ are to be determined from finite-element numerical simulations of structural deflections, c_1 the deflection at the plate or membrane center, H the membrane thickness, L the membrane length, ν the Poisson ratio, E the Young's modulus, k_{eff} the effective stiffness ($= \frac{PL^2}{c_1^2}$), P the applied uniform load, and σ_o the residual stress. The functional form is determined from a variational solution for an appropriate trial function to the double-anchored structure, while the numerical coefficients are determined from finite-element computations.

From our particular device geometry, the residual stress contribution (the first term) dominates over the bending contribution (the second term) in Equation 2.8. That is, the residual stress induced bending energy dominates over the intrinsic bending energy. Similarly, the stiffness of a double-anchored narrow beam under uniform loading possesses the same functional form to Equation 2.8 with the absence of the $\frac{1}{(1-\nu^2)}$ and $\frac{1}{(1-\nu)}$ terms. Thus, the residual stress directly affects out-of-plane deflection of our membrane and its resonant frequency. For large deflections (such that $c_1 > H$), nonlinear amplitude-stiffened Duffing spring effects appear, as seen in the third term of Equation 2.8, to further modify the deflection and resonance response.

Finite-element simulations are performed to capture specific numerical values of C_r, C_s and $f_s(\nu)$ for our designed double-anchored membrane. With C_b is assumed to be zero [96], C_r is found to be $\sim$ 0.6, $C_s \sim 21.2$, and $f_s(\nu)$ at (0.5 - 0.5 $\times$ ν) when fitted to the finite-element simulations. We note that determination of C_s and the form of $f_s(\nu)$ are arbitrary since only the product is of concern. Equation 2.8 can also be recast as:

$$\frac{PL^2}{Hc_1} = C_r \sigma_o \ + \ C_s f_s(\nu) \frac{E}{(1-\nu)L^2} \ c_1^2 \tag{2.9}$$

where if $\frac{PL^2}{Hc_1}$ is plotted against c_1^2, the film residual stress and biaxial modulus can be found from the line-intercept and the slope respectively. The membrane profile with 350 MPa residual stress (tensile and causing the structure to shrink) in PZT and -300 MPa residual stress (compressive) in the thermally-grown silicon oxide under 100 kPa load is shown in Figure 2-13. The Mises stress distribution is relatively uniform within the grating region

and the PZT actuator region, with the maximum stress at the anchor support region.

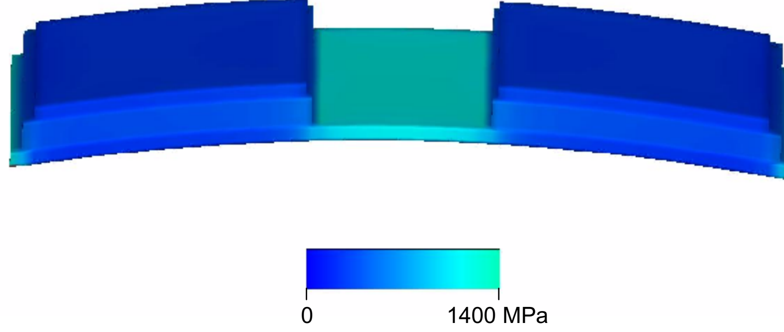

Figure 2-13: Membrane Mises stress and displacement profile under 100 kPa load, with 350 MPa residual stress in PZT and -300 MPa residual stress in thermal oxide. The displacement is exaggerated for clarity.

Variational technique for elastic strain energy The above variational technique to gauge residual stress effects can be further implemented for large amplitude deflections in the double-anchored membrane. For large out-of-plane deflections, the in-plane strains need to account for both in-plane and out-of-plane displacements as given by [144, 131]

$$\epsilon_x = \frac{du}{dx} + \frac{1}{2}\left(\frac{dw}{dx}\right)^2 \tag{2.10}$$

$$\epsilon_y = \frac{dv}{dy} + \frac{1}{2}\left(\frac{dw}{dy}\right)^2 \tag{2.11}$$

$$\gamma_{xy} = \frac{du}{dy} + \frac{dv}{dx} + \left(\frac{dw}{dx}\right)\left(\frac{dw}{dy}\right) \tag{2.12}$$

where u is the in-plane displacement in the direction towards the two fixed ends, v the in-plane displacement perpendicular to u, w the out-of-plane displacement. x is the in-plane axis towards one of the fixed ends, y the in-plane axis perpendicular to x, z the out-of-plane axis, ϵ_x and ϵ_y the strains in the x and y directions respectively, and γ_{xy} the shear strain in the xy-plane. The $\frac{1}{2}\left(\frac{dw}{dx}\right)^2$, $\frac{1}{2}\left(\frac{dw}{dy}\right)^2$ and $\left(\frac{dw}{dx}\right)\left(\frac{dw}{dy}\right)$ terms account for axial stretching. To respect the boundary conditions of the double-anchored membrane, we use the following approximate trial functions:

$$\hat{w} = \frac{c_1}{2}\,(1 + \cos\frac{2\pi x}{L_1})\,(1 + \cos\frac{\pi y}{L_2}) \tag{2.13}$$

$$\hat{u} = c_2\,\sin\frac{2\pi x}{L_1}\,\sin\frac{\pi y}{L_2} - z\,\frac{d\hat{w}}{dx} \tag{2.14}$$

$$\hat{v} \;=\; \frac{c_3}{2}\, \sin\frac{\pi y}{L_2}\, (1+\cos\frac{2\pi x}{L_1}) \;-\; z\, \frac{d\hat{w}}{dx} \tag{2.15}$$

where L_1 and L_2 is the membrane length in the x and y directions respectively. The $z\,\frac{d\hat{w}}{dx}$ and $z\,\frac{d\hat{w}}{dx}$ terms account for bending.

In addition, for a plane-stress scenario, the piezoelectric coupled stresses is expressed as [39]

$$T_1 \;=\; -\, d_{31}E\,\mathbf{E} + E\epsilon_x \tag{2.16}$$
$$T_2 \;=\; -\, d_{31}E\,\mathbf{E} + E\epsilon_y \tag{2.17}$$
$$T_6 \;=\; G\,\gamma_{xy} \tag{2.18}$$

where $\mathbf{E}$ is the electric field in the z direction, E the isotropic Young modulus, and G the shear modulus. The elastic strain energies are then given by

$$W \;=\; \int_{vol} [\, \frac{E}{2(1-\nu^2)}\, \left(\epsilon_x^2+\epsilon_y^2+2\nu\epsilon_x\epsilon_y\right) + \frac{G}{2}\,\gamma_{xy}^2 \,]\, dxdydz \tag{2.19}$$
$$W_{residual} \;=\; \int_{vol} \sigma_o\,(\epsilon_x+\epsilon_y)\, dxdydz \tag{2.20}$$
$$W_{piezo} \;=\; \int_{vol,piezo} \frac{1}{2}\,\mathbf{S}^T\mathbf{T} = \int_{vol,piezo} \frac{1}{2}\,(\epsilon_x T_1+\epsilon_y T_2+\gamma_{xy}T_6)\, dxdydz \tag{2.21}$$

where W is the elastic strain energy including both bending and axial stretching, $W_{residual}$ the residual stress strain energy, W_{piezo} the piezoelectric coupled electromechanical strain energy, ν the Poisson ratio, and σ_o the residual stress, $\mathbf{S}^T$ the transpose of the strain vector, and $\mathbf{T}$ the stress vector.

The constant terms c_1, c_2 and c_3 terms are found with the variational solution, of minimizing the total elastic strain energy and external work done with respect to c_1, c_2 and c_3. As mentioned earlier (on page 39), residual stress is the dominant term in our designed double-anchored membrane. After some lengthy algebra, the various contributions to the elastic strain energy W, to first-order, can be summarized in the following functional forms:

$$\text{bending term in } x = f(c_1^2, \frac{1}{L_1^3}, L_2, H^3) \tag{2.22}$$

$$\text{bending term in } y = f(c_1^2, L_1, \frac{1}{L_2^3}, H^3) \tag{2.23}$$

$$\text{axial stretching term in } x = f(c_1^4, \frac{1}{L_1^3}, L_2, H) \tag{2.24}$$

$$\text{axial stretching term in } y = f(c_1^4, L_1, \frac{1}{L_2^3}, H) \tag{2.25}$$

$$\text{cross-coupling term in } xy = f(c_1^2, \frac{1}{L_1^3}, L_2, H^3) \tag{2.26}$$

$$\text{shear term in xy-plane} = f(c_1^2, \frac{1}{L_1}, \frac{1}{L_1}, H^3) \tag{2.27}$$

where H is the membrane thickness. Again, we observe the cubic dependence of the bending terms on H and the linear dependence of the axial stretching terms on H – as consistent with the earlier Equation 2.8. Looking at the bending and axial stretching terms for our particular design parameters (such as the tunable microcavity waveguide as described in Chapter 4 and Chapter 5), the most susceptible (least energy) mode is the bending mode in x. This is followed by axial stretching in x, bending mode in y, and finally, axial stretching in y. This coincides with our intuitions; the first bending mode experiments are described in Section 3.3.3.

Vibration and harmonic analysis Harmonic excitations of the double-anchored membrane is carried out in the finite-element model, where a device quality Q at 0.1 (and damping coefficient b of 1×10^{-4}) is used with a loading amplitude of 400 pN. Since the device is bulk-micromachined with no surface underneath membrane, there is negligible squeeze-film effects. For device L_{pzt} at 450 μm, the first three resonant modes are found to be 10.62 kHz, 11.09 kHz and 18.76 kHz respectively. The corresponding Bode responses are illustrated in Figure 2-14a. The first resonant mode is a vertical out-of-plane membrane deflection; the second mode tilt in the membrane; the third mode a higher-order vertical deflection. We note the nonlinear Duffing amplitude-stiffening in the third resonance mode. Figure 2-14b shows the response with b of 1×10^{-2} and the response for a shorter device L_{pzt} at 200 μm where the first resonant mode is higher at 18.22 kHz. To design for operation at higher frequencies, L_{pzt} can be decreased and the thickness H of the membrane increased for the same material properties.

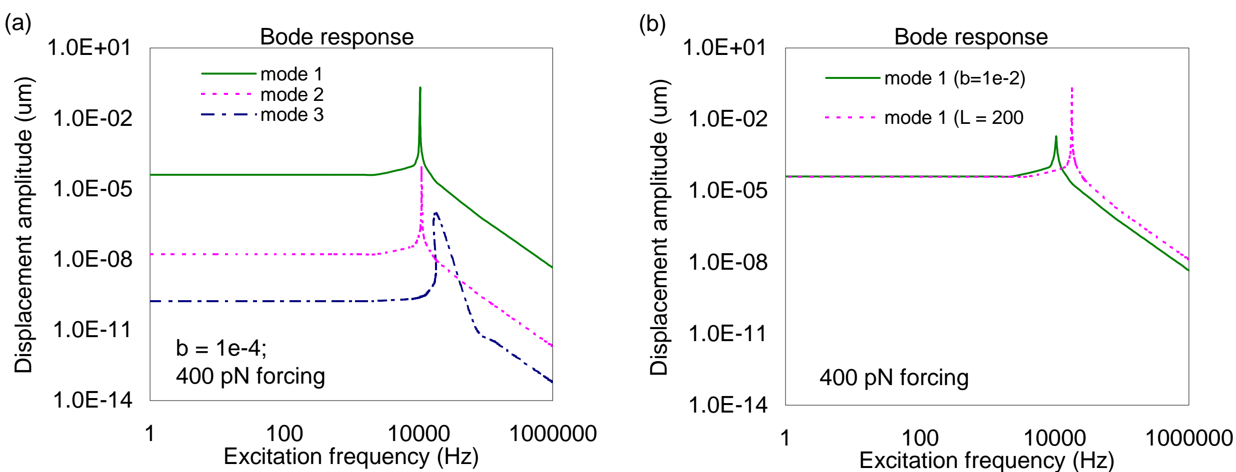

Figure 2-14: Harmonic response of double-anchored membrane: (a) first three modes for damping coefficient b of 1×10^{-4}, (b) solid line is with b of 1×10^{-2}, and dotted line is with b of 1×10^{-4} but with a L_{pzt} of 200 μm. In all cases, the loading amplitude is 400 pN.

2.3 Optical Grating Design

2.3.1 Diffractive gratings theory

A grating structure consists of periodic elements that has the effect of producing periodic modifications in the phase or amplitude of the incident beam. In the simplest form, the generated interference pattern can be expressed in the grating equation. For example, the mth diffracted angle at normal incidence can be found as

$$\Lambda\ \sin\theta_m = \Lambda\ \sin\theta_i + m\ \lambda \tag{2.28}$$

with Λ the grating period, θ_m the diffracted angle, θ_i the incident angle, m the diffracted order ($\in [0, \pm 1, \pm 2, ...]$), and λ the wavelength. For analog tuning in the grating period such that $\Lambda\ \rightarrow\ \Lambda + \Delta\Lambda$ and incident angle perpendicular to the grating, Equation 2.28 can now be modified into

$$\Delta\theta_m = \frac{m\lambda\Delta\Lambda}{\Lambda^2} \tag{2.29}$$

where $\Delta\theta_m$ is the change in the diffracted angle and $\Delta\Lambda$ the grating period change. A small Λ would serve as a quadratic amplification factor in $\Delta\theta_m$. A more detailed Fourier description for a 50% fill-factor binary phase grating within a finite rectangular aperture can be cast as

$$\Psi(u,v) = \frac{e^{i2\pi z/\lambda}\ e^{i\pi(u^2+v^2)/\lambda z}}{i\lambda z}\ \mathcal{F}\{e^{[j comb(dx)*\frac{\lambda}{4}rect(\frac{dx}{2})]} rect(ax)rect(by)\} \tag{2.30}$$

where $\Psi(u,v)$ is the optical field in the Fraunhofer regime and under the paraxial approximation. The terms used are λ as the incident wavelength, z the propagation distance, $\mathcal{F}\{\ \}$ the Fourier transform notation, *comb*( ) the comb operation, *rect*( ) the rect operation, a and b the finite aperture lengths at the object plane with coordinate (x,y) respectively. The terms $e^{i2\pi z/\lambda}\ e^{i\pi(u^2+v^2)/\lambda z}$ in the numerator are the linear phase and the parabolic phase factors respectively, and the term $i\lambda z$ is a constant of propagation. This Fourier representation is useful for examining optical efficiencies under microfabrication deviations and device actuation conditions.

2.3.2 Efficiency, deviation and resolving power

From Equation 2.30, the calculated intensity ($|\Psi(u,v)|^2$) is normalized with the maximum intensity from the zeroth order. The spectral intensity from a binary phase grating is illustrated in Figure 2-15. A binary amplitude grating, also included in the set of designed devices, will have first-order diffraction efficiency a quarter of the binary phase grating, as half of the incident field is lost in the amplitude grating.

In actual fabrication, however, the fill factor – chosen as the percentage of ridge height to groove height – is not at 50% nor is the step height at quarter-wavelength. As measured from the actual fabricated gratings (in Section 3.1.4), the dimensions are revised with the resulting

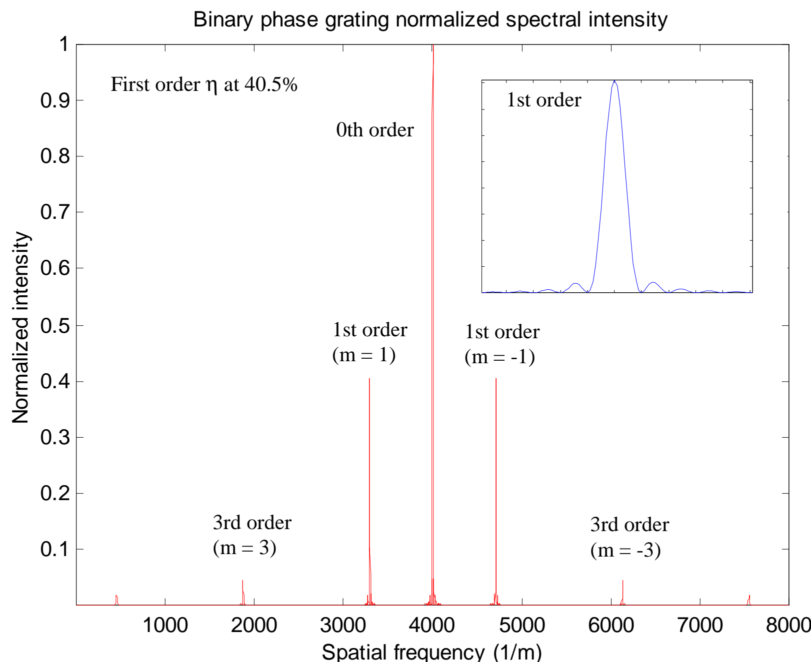

Figure 2-15: Normalized spectral intensity of binary phase grating.

diffraction efficiency shown in Figure 2-16 for each of the two effects. The cumulative effect, of a 42% fill factor and 1.2π step height phase delay, decreases the first-order diffraction efficiency to 21.5% (normalized with maximum intensity in this spectral). A trapezoidal shape profile of the binary grating could further decrease the diffraction efficiency [119]. Iterated fabrication optimizations for the grating beam form factor will improve the efficiency.

Moreover, with the grating bow predicted in the finite-element solution (Section 2.2.3), we investigate its effects on the diffraction spectra. A parabolic fit in the phase delay (as suggested in the membrane z-displacement) is included in the transmission function. Figure 2-17 shows the resultant spectral in comparison with an optically-flat binary phase grating. A 16.71 mrads bow in the grating flatness is used. Both spectra are based on the as-fabricated fill factor and step heights. We observe a spatial spreading out of the energy, although the total diffraction efficiency remains relatively unvaried at 20.3% for an ideal grating and 16.8% (for the as-fabricated 42% fill factor and 1.2π step height phase delay). The membrane bow also distorts the first diffracted order response, as shown in Figure 2-18 where spectrum at the Fourier plane for the first order is plotted for different maximum vertical deflections in the membrane bow. The membrane bow contributes approximately an additional 56% shift in the first diffracted order, compared with the same grating period actuation on an ideal flat grating. This additional shift needs to be taken into account in the optical design of piezoelectric tunable gratings for specific optical telecommunication devices and miniaturized spectrometers.

To reduce membrane bending, residual stress in the membrane could be controlled through a silicon nitride (instead of silicon oxide) diffusion barrier with variable silicon ra-

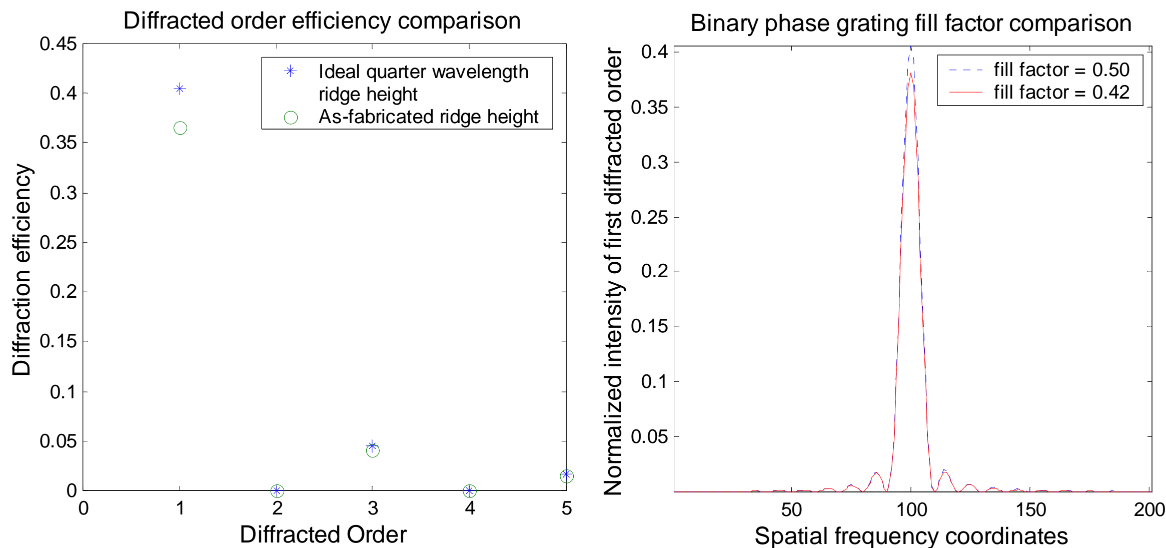

Figure 2-16: Diffraction efficiency comparison: (a)with as-fabricated ridge height for various orders, (b)with as-fabricated fill factor for the first order.

tio. In addition, the membrane thickness could be increased for a cubic increase in bending stiffness, while trading-off a linear decrease in axial stiffness in the small-deflection regime. Other design possibilities include: (1) designing the PZT actuators as continuous between the left and right actuators (which will reduce bending at the expense of grating period change), (2) having a sliding guide on top of the membrane to prevent out-of-plane deflection, (3) locating the piezoelectric actuators on the same plane as the neutral axis of the multimorph membrane. The latter could perhaps be fabricated by filling a trench in a thick Pt membrane with PZT.

Spectral resolving power [4] of the grating can be described by a criteria [5] first proposed by Rayleigh [125]. The resolving power $\frac{\lambda}{\Delta\lambda}$ is

$$\frac{\lambda}{\Delta\lambda} = \frac{mW}{\Lambda} = mN \tag{2.31}$$

where W is the total grating size ($\sim L_{mem}$ in the nomenclature given in Section 2.2.2) and N the number of grating grooves. For our microfabricated grating (Λ at 4 μm and W at 282 μm), $\frac{\lambda}{\Delta\lambda}$ is 70.5 for the first order, which gives $\Delta\lambda$ at only 9 nm for λ at 632.8 nm. A grating with more periods and using the higher-orders, if possible, will be necessary to improve the resolving power.

[4]The term “resolving power” is a property of the grating, whereas “resolution” – the smallest change of wavelength detectable – is a function of both the grating and the instrumentation.

[5]Rayleigh proposed two patterns of equal intensity to be just resolved when the principal intensity maximum of one pattern coincides with the first intensity minimum of the other.

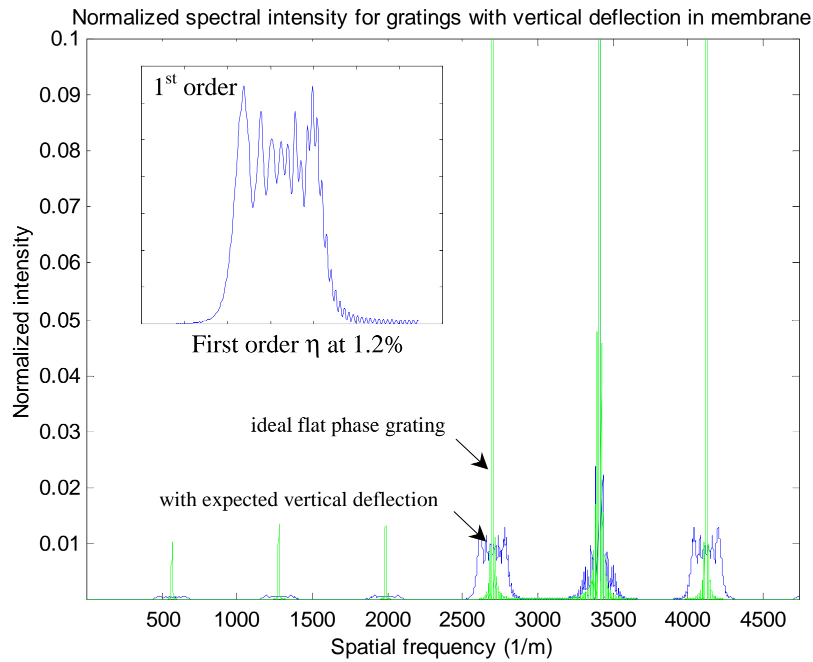

Figure 2-17: Normalized spectral intensity of binary phase grating, with 16.71 mrads bow in grating flatness, in comparison with an optically-flat binary phase grating. Both spectra are based on the as-fabricated fill factor and step heights.

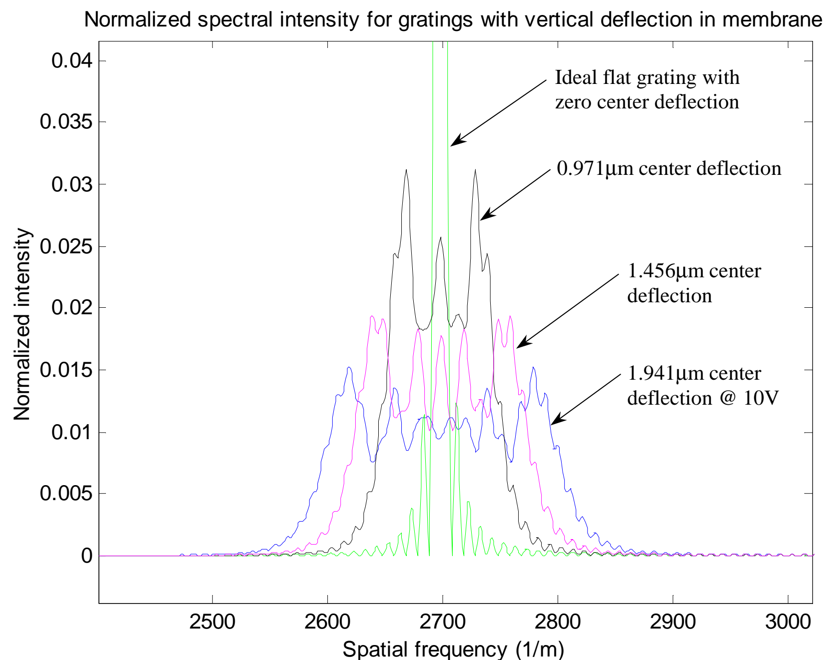

Figure 2-18: Normalized spectral intensity of the first diffracted order, against different maximum vertical deflections in the membrane bow. Multiple maxima peaks appearing due to bow in the grating flatness.

2.4 Specific Applications Of Analog Tunable Diffractive Gratings

The ease of high-resolution grating period control through electrically-excited piezoelectric actuators has brought about several applications to mind; we cite here two specific applications: (1) thermal compensation for optical network channel add/drop multiplexers, and (2) dynamic compensation of polarization and chromatic mode dispersion. Other possibilities include miniaturized spectrometry, optical strain gauges [9, 13, 132], and tunable external cavity lasers.

2.4.1 Thermal compensation and wavelength-selective switching for Optical Add/Drop Multiplexers

The double-anchored membrane has a Biot number of 2×10^{-9} in the thickness of the membrane and 1×10^{-5} in the membrane length-wise direction. This suggests the conduction resistance is significantly less than the convection resistance; that is, without the presence of heat generation, the temperature distribution is uniform within the grating membrane. With a thermal expansion coefficient of $8.8\times10^{-6}\ K^{-1}$, a ΔT of 2.8 ^{o}C leads to a 0.1 nm change in a 4 μm grating period. A temperature variation of -5 ^{o}C to 80 ^{o}C would therefore suggest a strain of 2 to 5×10^{-4}. This is the actuation range needed to compensate for thermal effects and is achievable in our device. For small-amplitude displacement, a feedback controller unit could be implemented to compensate for creep in both the PZT actuators and the metallic (Pt) membranes [6].

The piezoelectric-actuated tunable gratings could also perform wavelength-selective switching for a small number of 100 GHz C-band channels, whether for wavelength add/drop filters or tunable external cavity lasers [7]. An schematic illustration of the wavelength add/drop nodes in an optical network is shown in Figure 2-19. The number of channels that can be switched can be derived simply from the grating equation (Equation 2.28) which, when modified for a change in wavelength λ, gives the change in diffracted angle as

$$\Delta\theta = \frac{m}{d}\,\Delta\lambda \tag{2.32}$$

The wavelength range $\Delta\lambda$ for a certain operating frequency is related by

$$\Delta\lambda = \frac{\lambda^2\Delta f}{c} = \frac{c\Delta f}{f^2} \tag{2.33}$$

[6] While we expect the metallic creep to be small for low-temperature and low-stress operation, a Si or SiO_2 membrane, with Pt metallization, could also be used to reduce transient [25] and steady-state creep.

[7] Thermally-actuated gratings have been suggested and demonstrated for wavelength-selective switching in the industry.

For a 100 GHz channel (or $\Delta\lambda$ of 0.8 nm) in dense wavelength division multiplexing (DWDM) optical networks, this translates to a $\Delta\theta$ of 2×10^{-4} rads, for our current grating device design and employing only the first-order. From this, Equation 2.29 then suggests a required grating period change $\Delta\Lambda$ of 2.06 nm for each channel. Given the theoretical $\Delta\Lambda$ of 7.89 nm at 10 V in our membrane design, we estimate this first device design could possibly be sufficient to switch $\sim$ three 100 GHz channels.

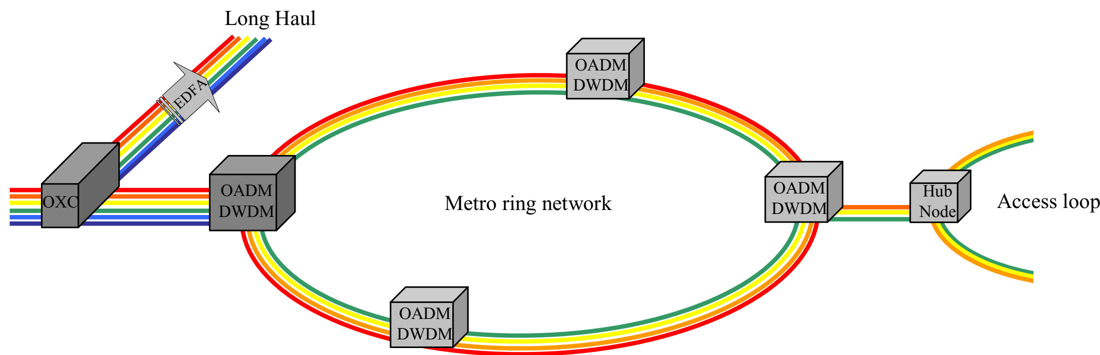

Figure 2-19: Optical Add/Drop Multiplexers elements in a DWDM ring network.

Careful packaging is also necessary to make this device a viable commercial product. At the chip packaging level, examples of considerations include cost-efficient electrical wire-bonding to the piezoelectric actuators, isolation of external disturbances such as vibration and electrical noise to the device, and negligible thermal gradients imposed on the grating. At the product packaging level, examples of considerations include alignment of optical elements, modularity of supporting optical components, electronic driving circuitry and feedback module, and on-board calibration schemes.

2.4.2 Dynamic dispersion compensation

Tunable gratings also has applications in dynamic compensation for chromatic and polarization mode dispersion in optical fibers, through use of a grating pair for pulse compression [147] or varying the differential optical path lengths between the polarization modes.

Chromatic dispersion Pulse spreading occurs in a dispersive fiber due to the fact that different frequency components travel have different group velocities. In normal dispersion fibers ($\frac{d^2\beta}{d\omega^2} > 0$, where β is the propagation constant of the guided mode), the pulse broadens for frequencies above a critical frequency and fiber length [44]. Typical dispersion values for single-mode fibers are on order of 17 ps/nm-km; that is, a 10 Gbps pulse (100 ps pulse width) will spread 17 ps from its mean after traveling for 1 km. A system with anomalous dispersion ($\frac{d^2\beta}{d\omega^2} < 0$) is required to recompress the pulse. Fiber Bragg gratings with anomalous dispersion have been investigated with dispersions up to -100 ps/nm suggested [35], while

liquid-crystal phase modulators have been used for arbitrary pulse shaping, such as demonstrated by Weiner [158]. Another convenient artificial realization for pulse compression is a grating pair. Figure 2-20a illustrates such a setup for chromatic dispersion compensation. The dispersion is expressed by [44]

$$\frac{d^2\phi}{d\omega^2} = -\frac{(1/\omega^2)(\lambda/\Lambda)(2\pi g/\Lambda)}{[1-(\sin\theta_i - \lambda/\Lambda)^2]^{3/2}} \tag{2.34}$$

where ϕ is the phase shift through the grating pair, g the perpendicular distance between the gratings, and θ_i the incidence angle. Only the first-order diffraction is used. For gratings with variable period Λ, the dispersion compensation is calculated from Equation 2.34 and shown in Figure 2-21 for various grating period changes. For a grating period change of 10 nm, the tunable dispersion compensation provides the range – up to order of -100 ps/nm – needed in deployed fibers. The anomalous dispersion is also strongly dependent on the incidence angle. Figure 2-21 is based on a grating incidence angle of 18.0^o, Λ of 1 μm before actuation, incident wavelength of 1.3 μm, and a gap g of 10 cm between the grating pair. For a larger tunable dispersion compensation range, the incidence angle can be further decreased. Response time is limited by the mechanical resonance frequency, on order of kHz to MHz. The fallback is the low efficiency: for binary transmission gratings, the ideal two-pass efficiency using a single first-order diffraction beam is 16.4% (or 7.9 dB loss), although other grating configurations are possible.

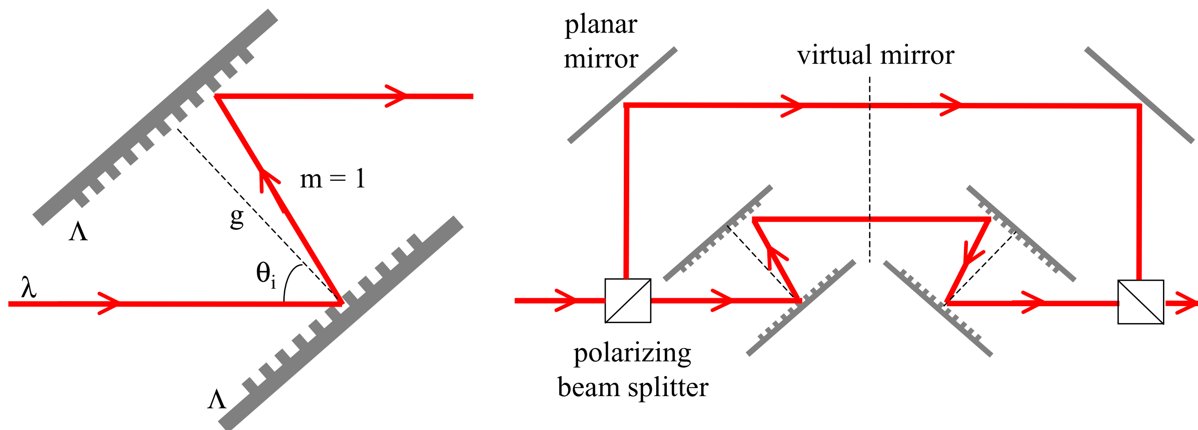

Figure 2-20: Grating pair setup for: (a) chromatic dispersion compensation, (b) polarization mode dispersion compensation.

Polarization Mode Dispersion “Single-mode” fibers support two orthogonally polarized HE_{11} modes [164]. In an ideal fiber, these modes are degenerate. However, because of loss of circular symmetry, the two modes have different group velocities due to fiber birefringence. The random perturbations, both intrinsic (during manufacturing) and extrinsic, of the birefringence lead to random coupling between these modes, which results in pulse dis-

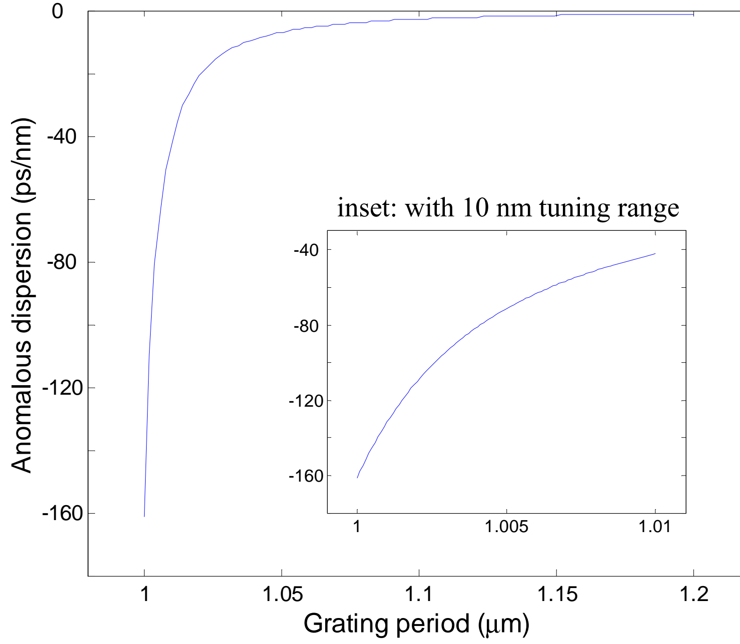

Figure 2-21: Chromatic dispersion compensation for various grating periods using grating pair setup illustrated in Figure 2-20a.

tortion [37, 70]. Typical polarization mode dispersions (PMD) range from 0.1 to 1 ps/$\sqrt{km}$ for the mean differential group delay and accumulated dispersions up to 100 ps between nodes, at this time of writing.

Figure 2-20b shows the grating pair element setup to vary the optical path length for one polarization. The beam output then is combined back with the other unperturbed polarization. The change in the optical path length, in free space, $\Delta_{path\ length}$ for a variable grating period is expressed geometrically as

$$\Delta_{path\ length} = 2\left[-\frac{g}{cos(\phi_1+\delta\phi)} + \frac{g}{cos\ \phi_1} + l\ sin\ \theta_i\right] \tag{2.35}$$

$$\text{with}\quad l = g\ (tan(\phi_1+\delta\phi) - tan\ \phi_1) \tag{2.36}$$

where θ_i is the incidence angle, g the perpendicular distance between the gratings, ϕ_1 the first-order diffracted angle, and $\delta\phi$ the change in the diffracted angle.

The result with the tunable gratings is as shown in Figure 2-22, where the gratings are designed to compensate for 100 ps of dispersion. This specific calculation is for a gap g of 10 cm, incident wavelength of 1.3 μm, and a grating period of 4 μm. A diffracted angle change of 400 μrads corresponds, and varies linearly, to a grating period change of 4.9 nm on a 4 μm period for the first diffraction order, as described previously in Equation 2.29. The PMD compensation is linear with respect to the diffraction angular change, or grating period change, due to the small angular changes involved. The dispersion compensation is

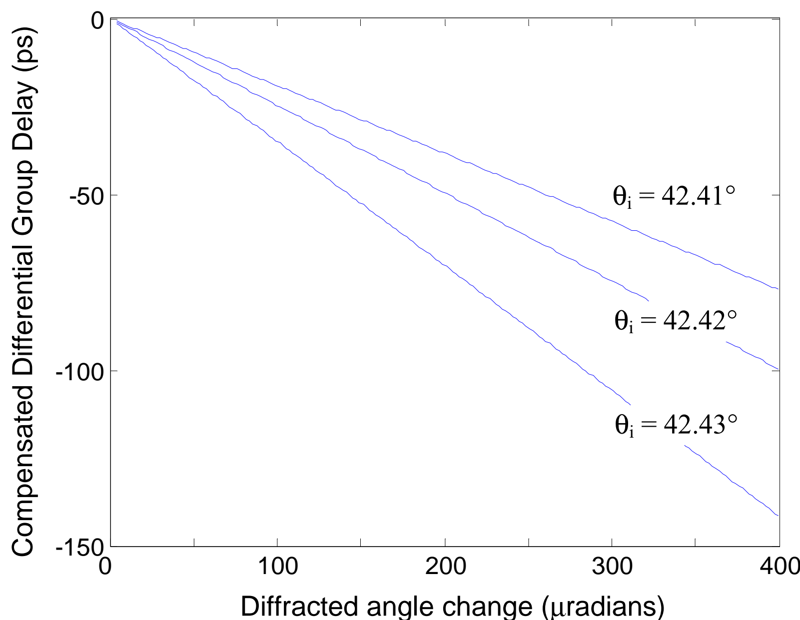

Figure 2-22: Polarization dispersion compensation for various grating periods using grating pair setup illustrated in Figure 2-20b.

also strongly dependent on the incident angle. The fallback of the system are: (1) the low efficiency, as in the chromatic dispersion setup, in the required four passes at the gratings, and (2) the need to position the incident angles to precision within 0.01^o.

2.5 Summary

This chapter begins with a conceptual description of analog tunable gratings, enabled by thin-film piezoelectric microactuators. Different designs are considered and modeled analytically. Through the analytical model, the effects of various design parameters on the grating period displacement are investigated and mapped onto the design space. A finite-element model is built, not only as a confirmation of the analytical model, but also to provide an estimate of the out-of-plane displacement and the resonance modes. The effects of membrane bow is then mapped onto the optical domain. The optical model is also used to consider effects of a non-ideal binary phase reflection grating. We then end with a discussion on specific applications, such as thermal compensation and wavelength-selective switching for optical add/drop multiplexers, and dispersion compensation in optical fibers.

The next chapter will present the fabrication process of the piezoelectric-actuated analog tunable gratings. Experimental results, including electrical characterizations, mechanical demonstrations, and optical measurements will be presented in comparison with theory.

Chapter 3

Microfabrication And Experiment Of Analog Tunable Diffractive Gratings

Physics constitutes a logical system of thought
which is in a state of evolution... The justification of the system
rests in the proof of usefulness of the resulting theorems
on the basis of sense experiences, where the relations of the latter to the former
can only be comprehended intuitively.
—A.E., Out of my later years.

This chapter presents the microfabrication and experimental results on the analog tunable gratings driven via thin-film piezoelectric actuators. In the microfabrication section, the processes detailed include PZT fabrication, diffractive gratings lift-off and electrode material optimization. In the experimental section, electrical, mechanical, and optical measurements are analyzed and discussed. Measurements of a water-immersible piezoelectric cantilever are also presented.

3.1 Microfabrication

The features in this device are defined invariably with optical lithography. Following patterning, the features are either surface micromachined (via lift-off or reactive ion etching (RIE)), or bulk micromachined via potassium hydroxide (KOH) etching [81, 103]. This combination of surface and bulk micromachining presents hurdles in material selectivity and fragility of thin-film membranes, but is chosen to prevent issues of stiction of the large deformable membrane. The microfabrication is completely carried out in the Microsystems Technology Laboratories at MIT.

3.1.1 Overall process flow and design permutations

The essential steps of the fabrication process are summarized in the process side profile shown in Figure 3-1. First, a 200 nm dry thermal oxide is grown as a diffusion barrier to PZT. Next, a 200 nm silicon nitride layer is deposited via PECVD on the backside and then patterned to serve as a hard mask for an eventual KOH backside etch. (Although low-stress LPCVD silicon nitride, via control of silicon composition, is preferred to control the residual stress in the composite membrane and for less pitting during KOH, the particular machine was not available during the device fabrication.) A 200 nm Pt layer, with 20 nm Ti adhesion layer, is then evaporated on the substrate and patterned via lift-off to create the bottom electrode. To expedite the process and to maintain repeatability, Pt RIE was not used. Sol-gel PZT is then spun-on in repeated individual steps, with each coating about 60 nm, and annealed to create a high-quality PZT layer with 0.5 μm thickness. The condition, cleanliness, and fabrication recipe, of the Pt/Ti bottom electrode is key to the PZT quality. PZT hillock and crack formation issues were resolved with process experimentation of the Pt/Ti bottom electrode and PZT fabrication conditions. Alternatives such at Pt/Ta and nitride as the diffusion barrier were investigated and found not to be as effective as the Pt/Ti/SiO_2 combination.

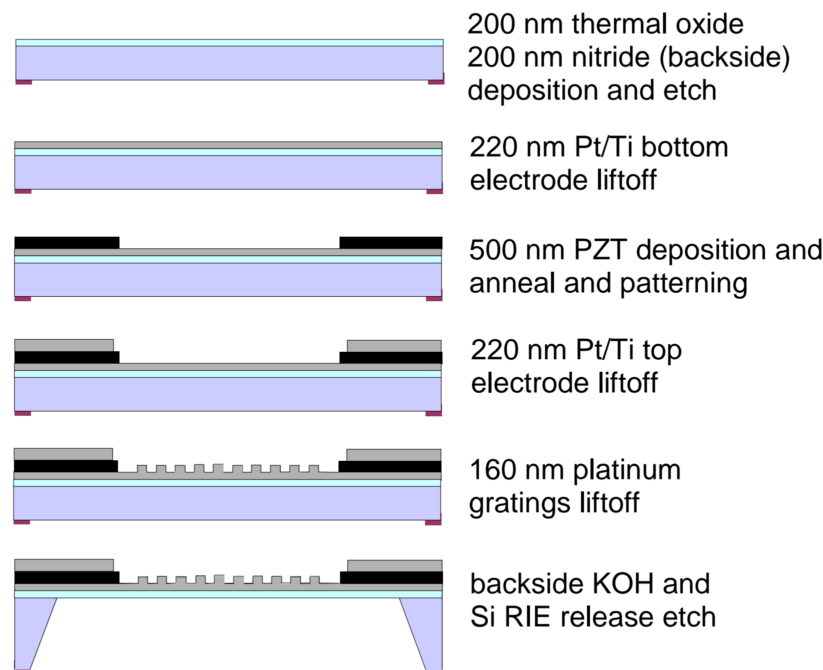

Figure 3-1: Microfabrication process flow of the analog tunable grating. The process consists of five masks and involves both surface and bulk micromachining.

After PZT deposition, we next employ a modified HF:HCl wet-etch recipe to pattern the PZT [101]. Wet-etching is faster and more economical than dry-etching, although the undercut in the PZT layer has to be controlled (as further discussed in Section 3.1.3). The top

electrode is then deposited with a second 220 nm Pt/Ti evaporation and lift-off procedure. The diffractive grating is next separately created [1] with a 158 nm Pt lift-off with 2 μm minimal linewidth features. The wafer is then etched from backside with a 445 μm KOH etch, using Apiezon wax W for the wafer frontside protection. The wax is coated with the wafer heated on a hot plate and, after the KOH etch, removed with a trichloroethylene solvent. The membrane is finally released with an approximately 5 μm Si RIE from the backside. The detailed process steps and conditions are listed in Appendix A.1 for reference. To complement the process flow, Appendix A.2 shows the projection lithography mask layout for a single chip.

As discussed in Section 2.2.2, the PZT length L and the membrane length L_{mem} – or the ratio of $\frac{L}{L_{mem}}$ – are the design parameters to vary for devices in one wafer. In our specific mask, two $\frac{L}{L_{mem}}$ ratios of 1.33 and 3.00 are used. The membrane width is kept at 300 μm for a square grating optical aperture and, since the theoretical piezoelectric design deemed sufficient force from the PZT actuators, there was no need to increase the width beyond 300 μm. Variations in the grating period, at 2 μm and 4 μm, are also included. To prevent issues of electrical shortage between the top and bottom electrodes during wire bonding ("punch through" of the PZT), separated contact pads on the bottom electrode are designed so that in the event of a "punch through", there will still be no electrical shortage. Variations in the contact pad sizes are also designed, since a larger contact pad would be easier to probe, though more susceptible to electrical shortage with the larger PZT area (as measured in Section 3.1.3). A water-immersible active cantilever design is also included in the fabrication masks. Appendix A.2 summarizes the design permutations and also the chip locations on one wafer.

3.1.2 Electrodes processing

The Pt/Ti top and bottom electrodes are processed via resist lift-off. Resist AZ5214-E is used with image-reversal techniques, with optimization in the resist thickness, exposure and baking times (as detailed in Appendix A.1) to create 2 μm minimum linewidths in the bottom electrode as shown in Figure 3-2. While sputtering is the preferred technique to create bottom electrodes with stronger adhesion, evaporation was used due to availability and compatibility of the machine at the desired Class 100 cleanroom. Lift-off, instead of RIE, is also used to pattern the electrodes. The quality of the evaporation, the cleanliness of the bottom electrode after lift-off, and the size of the separation gap in the bottom electrode are essential control parameters in preventing subsequent PZT hillocks and cracks.

[1] Although both the grating and top electrode depositions are made up of Pt and are consecutive processes, the two depositions are kept separate to allow for differences in the grating step height (needed at quarter-wavelength of incident light) and the top electrode step height (kept at 200 nm as a conservative estimate) in this process demonstration.

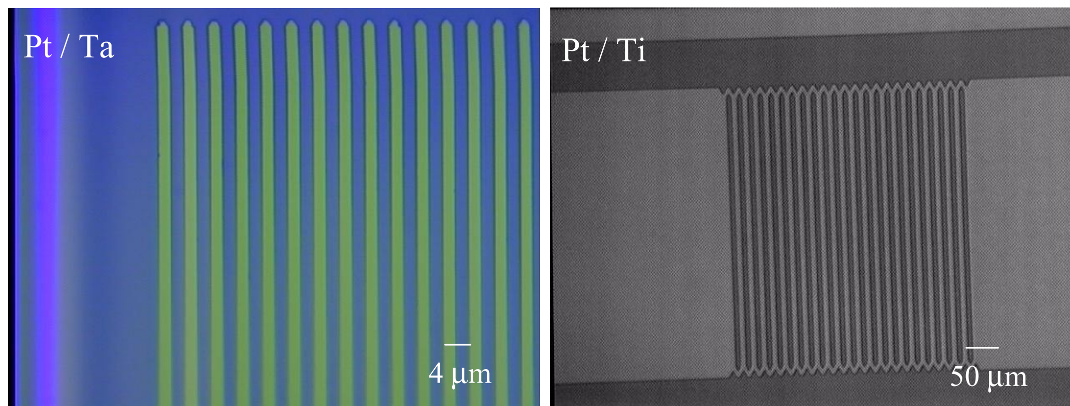

Figure 3-2: Patterned bottom electrodes, fabricated via evaporation and lift-off, for subsequent PZT processing. 2 μm minimum linewidths are used for both the perforated membrane design and contact pad separation.

3.1.3 PZT processing

Sol-gel PZT material[2] is first spun-coated (500 rpm for 3 sec, followed by 1500 rpm for 30 sec) on the Pt/Ti bottom electrode. Pyrolysis is then carried out on a hot plate at 150 ^{o}C for 3 mins and then a second hot plate at 350 ^{o}C for 5 mins. Each spin-coating is approximately 60 nm. To make a 0.25 μm layer, a one-time annealing at 700 ^{o}C for 15 mins is carried out after 4 spin-coatings. To make a 0.5 μm layer, two separate annealings are used, each after a 0.25 μm PZT layer (4 spin-coatings with 4 pyrolysis) is deposited. The first annealing lasts 1 min at 700 ^{o}C and the second annealing lasts 15 mins at the same temperature.

Figure 3-3 shows the X-ray diffraction (XRD) results over different bottom adhesion and diffusion barrier materials and processing conditions. For the adhesion layer, both Ti and Ta were tried. While Ti is the stronger adhesion material, it is highly susceptible to KOH attack. Ta is less susceptible to KOH (if kept under low temperature, approximately 100 ^{o}C, processing to prevent formation of Ta silicide), but is a poorer adhesive material between Pt and the diffusion barrier. Upon PZT annealing, there were significant hillocks in the PZT film with a Pt/Ta bottom electrode. The XRD results in Figure 3-3 show the presence of the pyrochlore phase. We attempted annealing the Pt/Ta bottom electrode before PZT deposition to improve the adhesion between Pt and SiO_2, but the fabricated PZT film still showed hillocks and, as seen in Figure 3-3, the presence of the pyrochlore phase. The Pt/Ti bottom electrode works best for the fabricated PZT film. A SiN_x diffusion barrier is also experimented, as the residual stress in the nitride can be varied (via control of Si composition in SiN_x), possibly to complement the tensile PZT residual stress. The actual devices fabricated and tested eventually had a SiO_2 diffusion barrier because the variable-composition nitride deposition tool was not functional during the device fabrication period.

[2]Mitsubishi PZT sol-gel with 15% PZT(118/52/48) A6 Type.

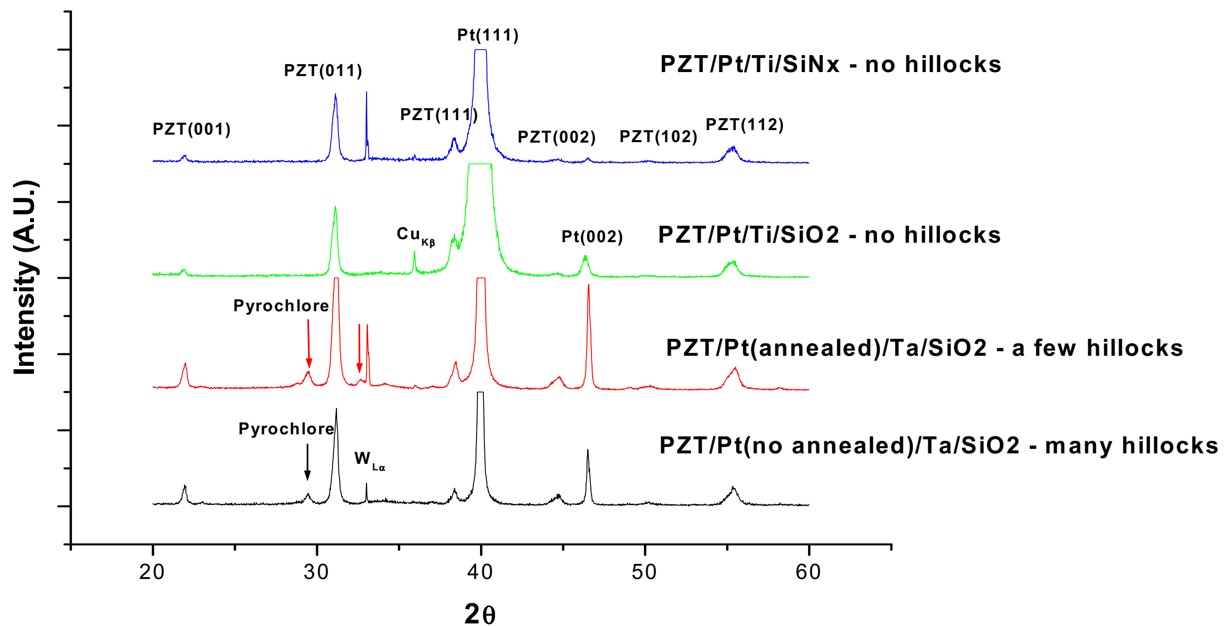

Figure 3-3: X-ray diffraction results of the fabricated PZT films, for different bottom adhesion and diffusion barrier materials and processing conditions. The four lines depicted (from top down) are: PZT/Pt/Ti/SiN_x, PZT/Pt/Ti/SiO_2, PZT/Pt(annealed)/Ta/SiO_2, PZT/Pt/Ta/SiO_2. XRD measurement courtesy of Y.-B. Jeon.

Figure 3-4a shows an SEM on the annealed PZT film grain size. The grain size is uniform across the surface, with average grain size of approximately 100 nm. Figure 3-4b shows the side profile of the PZT film, detailing the bottom electrode and the fabricated film thickness.

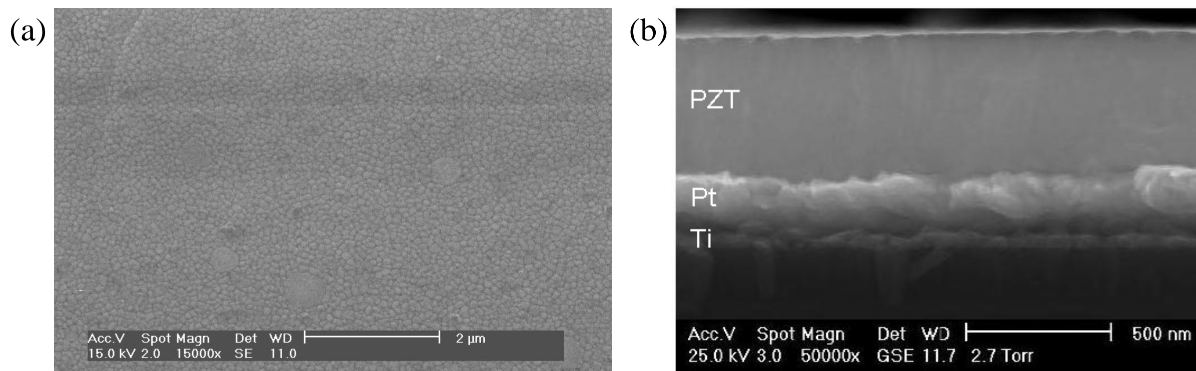

Figure 3-4: SEM of annealed PZT film: (a) grain size uniform at approximately 100 nm (top surface view of film; picture courtesy of Y.-B. Jeon.), (b) side profile of PZT film, detailing bottom electrode and fabricated film thickness.

In addition, the PZT film surface above an opened Pt/Ti bottom electrode gap is illustrated in Figure 3-5. Some parts of the Pt/Ti bottom electrode are opened (in 2 μm gaps), via lift-off and thus exposing the SiO_2, to prevent possible electrical shortage at the contact pads and, secondly, to allow for a water-immersible active cantilever design. Figure 3-5a shows the AFM image immediately above the opened Pt/Ti bottom electrode, where the PZT film is in contact with the SiO_2 diffusion barrier. We observe that the film surface is relatively smooth here, suggesting a different composition of the film on top of a Pt/Ti bottom electrode as shown in Figure 3-5c.

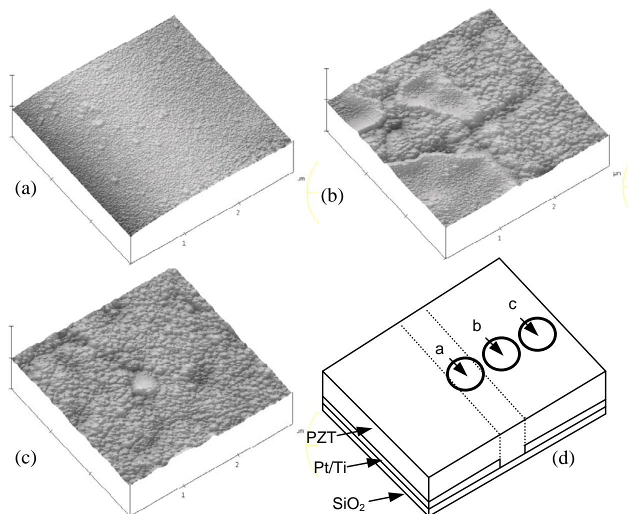

Figure 3-5: AFM images of PZT film surface: (a) PZT surface on top of opened Pt/Ti bottom electrode gap, with PZT film in contact with SiO_2, (b) PZT surface next to Pt/Ti gap, (c) PZT surface on top of Pt/Ti bottom electrode, (d) schematic of AFM imaging location. AFM imaging and figure construction courtesy of Y.-B. Jeon.

The deposited and annealed PZT film is then wet-etched in a diluted HF:HCL solution [101] with the detailed conditions described in Appendix A.1. A diluted $HF:HNO_3$ solution is also possible [162]. The resultant actuator is shown in Figure 3-6. A SEM cross-section of the etched structure, with photoresist, is performed to assess the undercut. As shown in Figure 3-7, there is approximately 690 nm undercut for a PZT layer that is 250 nm thick, which is acceptable for our device design which has 300 μm wide and at least 200 μm long PZT actuators. The 5 μm resist used is AZ 4620. A different resist material for thin coatings, OCG 825, was also used for a 1 μm resist and tested for wet-etching. The result gives large undercuts on the order of 50 μm, as shown in Figure 3-8. Electrical characterization of the completed PZT film, with top and bottom electrodes, is discussed in Section 3.2.

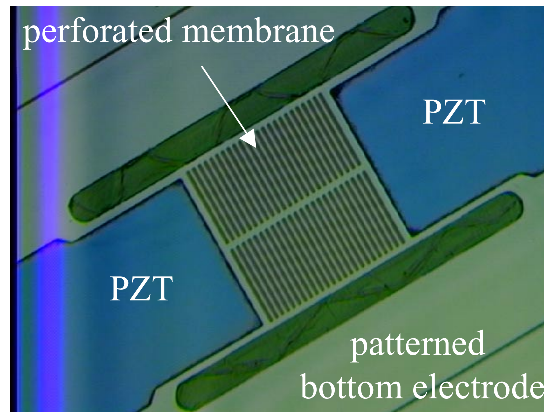

Figure 3-6: Wet-etched PZT on patterned bottom electrode.

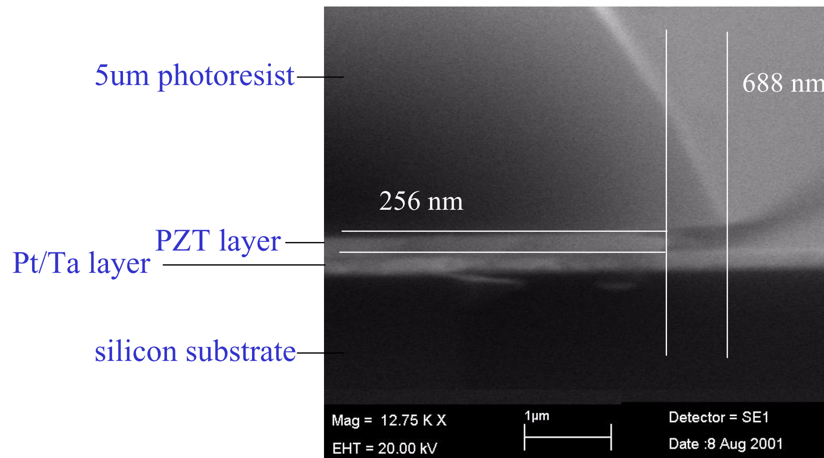

Figure 3-7: SEM cross-section of wet-etched PZT profile, showing undercut.

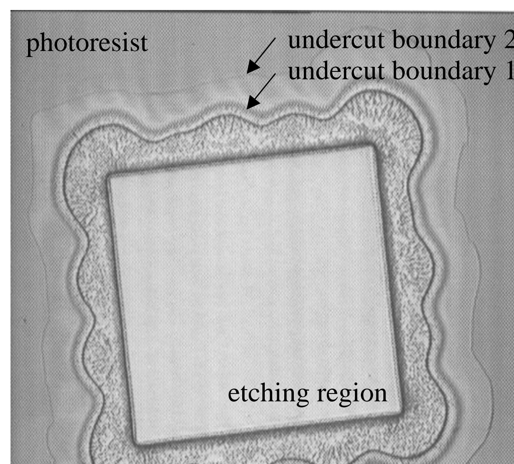

Figure 3-8: Top optical microscope view of wet-etched PZT shape, with thin 1 μm OCG 825 resist. The undercut is on the order of 50 μm.

3.1.4 Diffractive gratings

The minimum linewidth of the diffractive gratings is chosen at 2 μm, and fabricated via platinum lift-off. Figure 3-9 shows an SEM of the fabricated binary phase grating for use in reflection mode. The grating depth measures at 190 $\pm$ 5 nm (20.1% more than $\frac{\lambda}{4}$ of a 632.8 nm HeNe laser) and the fill factor is estimated at 42 $\pm$ 2% (instead of 50%), with 1.7 μm ridge and 2.3 μm groove. As mentioned in Section 2.3.2, these deviations from the ideal dimensions decreases the theoretical first-order diffraction efficiency for a binary phase grating in reflection mode to 21.5%.

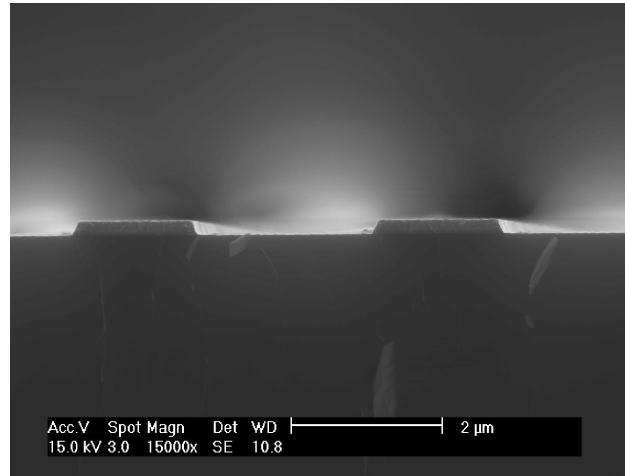

Figure 3-9: SEM of fabricated binary diffractive grating. SEM courtesy of Y.-B. Jeon and A. Garratt-Reed.

The completed thin-film processing of the devices, prior to KOH release, is shown in Figure 3-10. The design of these devices were suggested and discussed in Section 2.1 (Figure 2-2 and Figure 2-3).

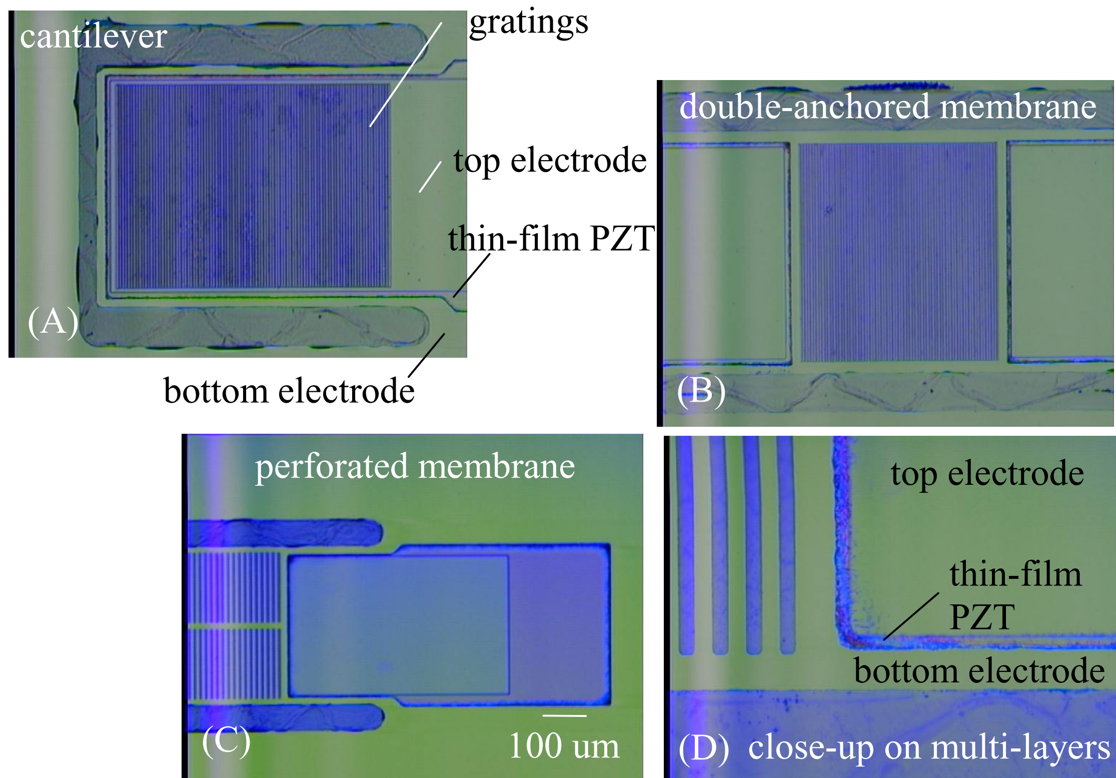

Figure 3-10: Top-view of completed thin-film processing of devices, prior to KOH release: (A) cantilever design, (B) double-anchored membrane design, (C) perforated membrane design, (D) close-up on the multi-layer structure.

3.1.5 Device release

The membrane is released from the backside via a combined KOH wet-etch and a final RIE dry-etch. The fabricated device is first placed in a 20% KOH solution at 75°C for 6.5 hrs, followed by a slower KOH etch at 65°C for approximately 1.5 hrs. Wax protection is used on the frontside to protect the PZT/Pt/Ti device layers. The final minutes of the timed KOH etch is crucial: due to non-uniformity in the KOH etch across the wafer, an over-etch in the KOH will lead to removal of the oxide barrier (especially with the elevated temperatures), with the KOH solution attacking the PZT and lifting-off the Pt/Ti electrode. Hence, the KOH etch is stopped with approximately 5 μm of Si remaining before it reaches the oxide barrier. Detection is made possible with an optical microscope, viewed from the frontside, wherein the remaining few microns of Si becomes translucent in the gap regions. The wax is then removed with a trichloroethylene solvent and a Si RIE dry-etch performed from the backside to release the membrane.

Membrane bow, both along membrane length and width, is expected from the thin-film residual stresses. After backside RIE release of the membrane, we observed bow along the membrane edges. This is shown in Figure 3-11, where most of the membrane is in focus, with the out-of-focus regions confined to the membrane edges (approximately 20 μm into the membrane). The magnitude of out-of-plane deflection is estimated on the order of 10 μm across the 330 μm wide membrane, from microscope depth-of-view measurements. Subsequent profilometries to detail the edge bow proved difficult for optical non-contact profilometers (due to the sharp rise of the edges) and surface contact profilometers (due to mechanical fragility of the released membrane).

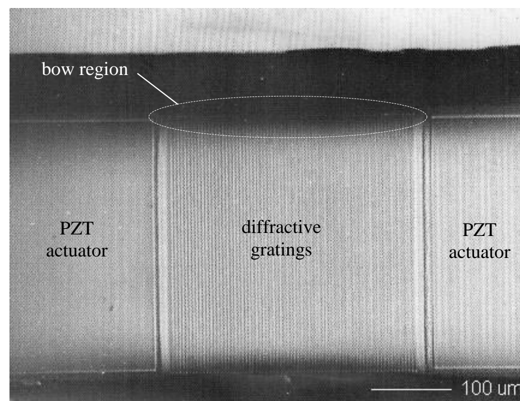

Figure 3-11: Released membrane after KOH bulk micromachining and RIE release. The bow at the membrane edges is observable from the out-of-focus regions, extending approximately 20 μm into the membrane.

We were, however, able to measure the membrane bow profile before final RIE release in more detail. This is shown in Figure 3-12, where there is approximately 5 μm of Si remaining underneath the membrane. There is a deflection of 1 μm downwards, with the typical tensile residual stress of PZT and compressive stress of SiO_2 causing the membrane to bow upwards.

The bow in the grating region is, however, hard to ascertain due to either in-plane resolution limit of the measurement instruments or the grating diffraction effects interfering with the Michelson setup of the instrument.

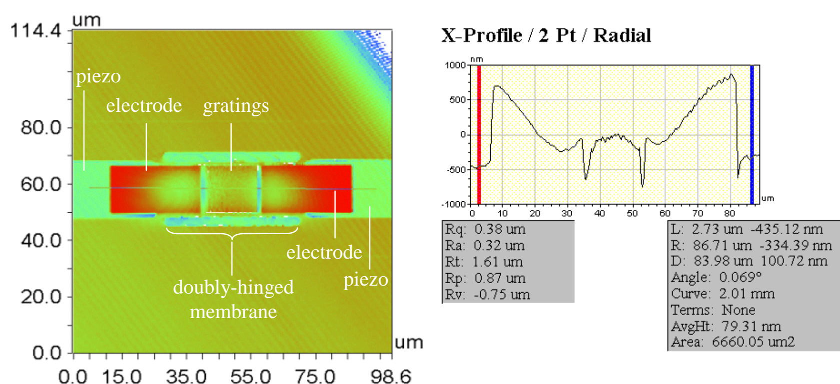

Figure 3-12: Optical profilometry on membrane before RIE release and after KOH bulk micromachining, depicting membrane profile before final release.

3.2 Electrical Characterization

The completed device shows excellent ferroelectric properties. Figure 3-13 shows the polarization against electric field hysteresis characterization. The saturation polarization is 67 μC/cm^2 while the coercive field is 38 kV/cm (corresponding to 1.9 V). The measured dielectric constant, after device completion, is unaffected by the backside bulk KOH and surface RIE etch release, and is about 1200 on our completed device. Figure 3-14 shows the dielectric constant against excitation frequency, with the dielectric constant dropping off at approximately more than 30 kHz. The dielectric loss is estimated at below 0.1 and has a corresponding response with the dielectric constant. The actual estimate of d_{31} value is detailed in Section 3.3.2, wherein the measured mechanical motion is used to indirectly gauge the d_{31} coefficient and an independent direct d_{33} measurement result is discussed. The measured power consumption at 10 V DC is 30 nW from current measurements.

Fatigue analysis of the PZT film, on an unreleased membrane, was investigated. Figure 3-15 shows the cycling results under a 5 V 19.6 μs rectangular pulse. While piezoelectric actuators are generally used at $\pm\frac{1}{3}$ E$_c$, the 5 V amplitude corresponds to 1.8 E$_c$ and brings about the possibility of residual charge built up. However, the effect is not serious as shown in the fatigue cycling up to at least 1.5×10^{10} rectangular-waveform cycles. Figure 3-15 shows the polarization change – specifically, the difference between saturation polarization at maximum voltage and remnant polarization at negative maximum voltage – for two consecutive sets of cycling on the same device. The second fatigue cycling is done a few days after stopping of the first fatigue cycling.

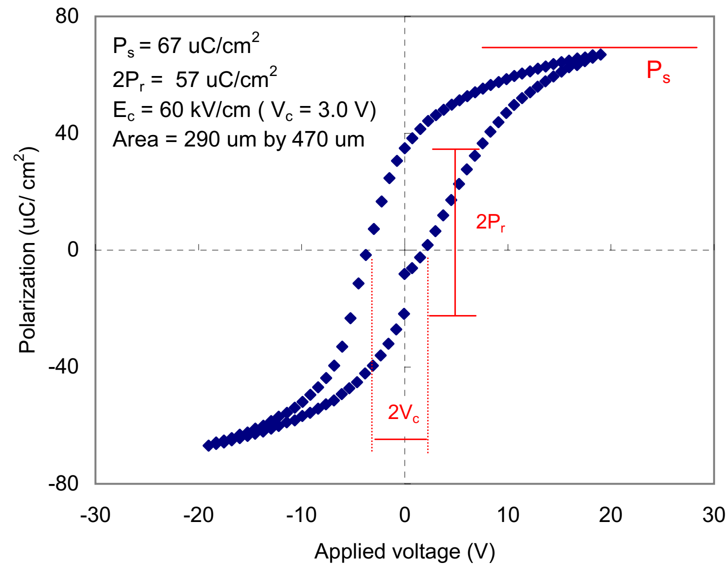

Figure 3-13: Polarization electric field (expressed as applied voltage) hysteresis curve for completed device. Ferroelectric properties were unaffected after KOH bulk micromachining and RIE release.

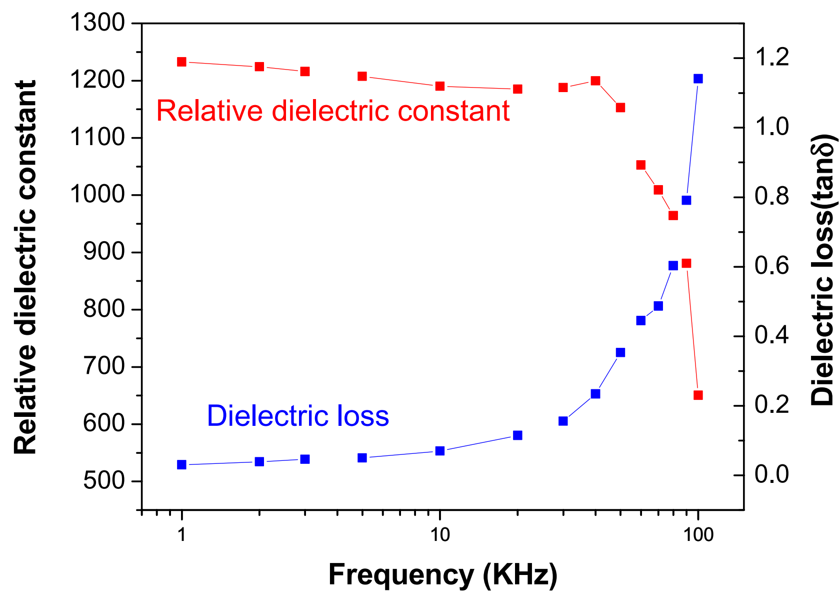

Figure 3-14: Dielectric constant and dielectric loss frequency response of PZT film in completed device.

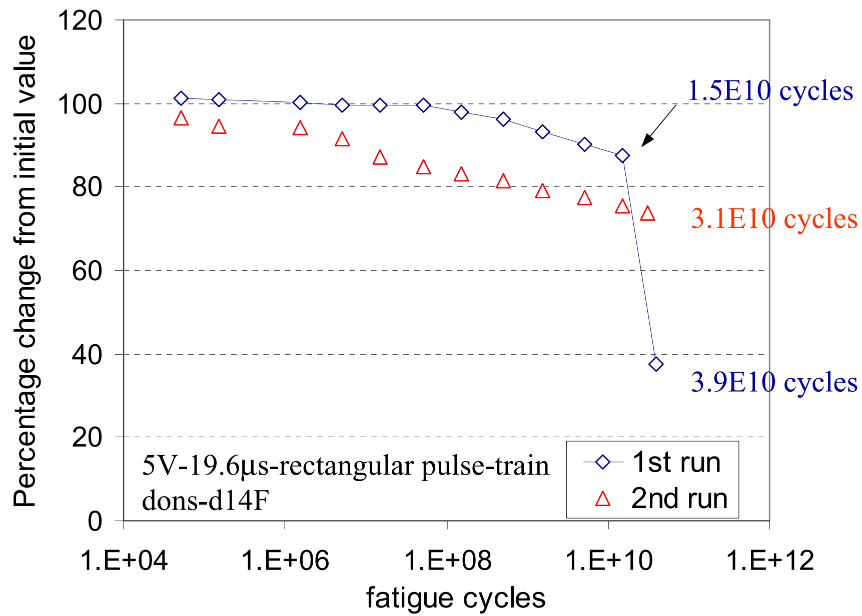

Figure 3-15: Fatigue cycling results of PZT film, under a 5 V 19.6 μs rectangular pulse. The second set of cycling is done on the same device and polarization is the value investigated.

3.2.1 Variation of electrode sizes

Different electrode sizes, consisting of different PZT lengths and contact pad sizes, were included in the design matrix. Figure 3-16 shows the dielectric constant against various electrode sizes for a single wafer. Included in Figure 3-16 are also water-immersible cantilever devices and devices where the bottom electrode is patterned for contact pad separation. It is observed that the PZT quality decreases with increasing electrode size - a reasonable explanation would be increasing particle contamination with increasing electrode size.

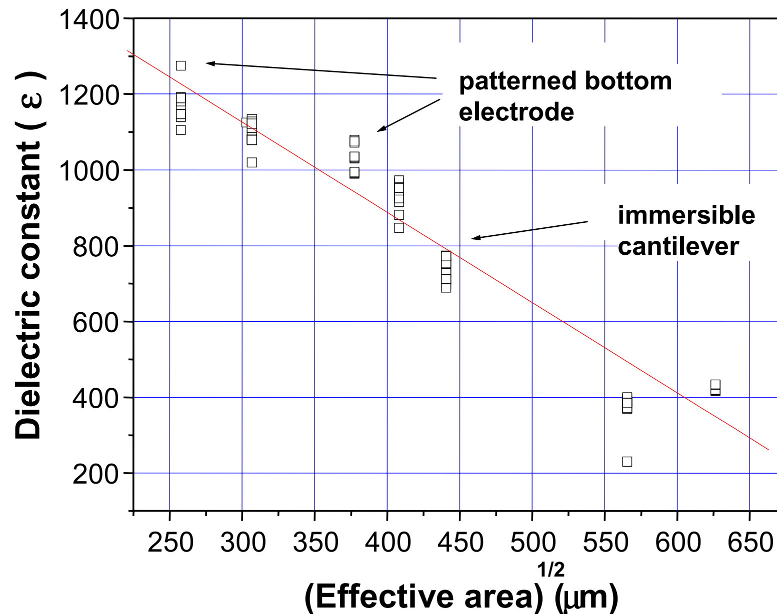

Figure 3-16: Measured dielectric constant for various electrode sizes for a single wafer. Figure courtesy of Y.-B. Jeon.

3.2.2 Water-immersible active cantilever characterization

A design with water-immersible piezoelectric cantilevers was included in the fabrication. To protect electrical short between the top and bottom electrodes in a liquid, an encapsulated design for the PZT is used as illustrated in Figure 3-17. In this design, the top electrode and a segmented portion of the bottom electrode encapsulate the PZT film area (as shown in the top view with the dotted lines). Thus, water is not in contact with the PZT film nor the bottom electrode.

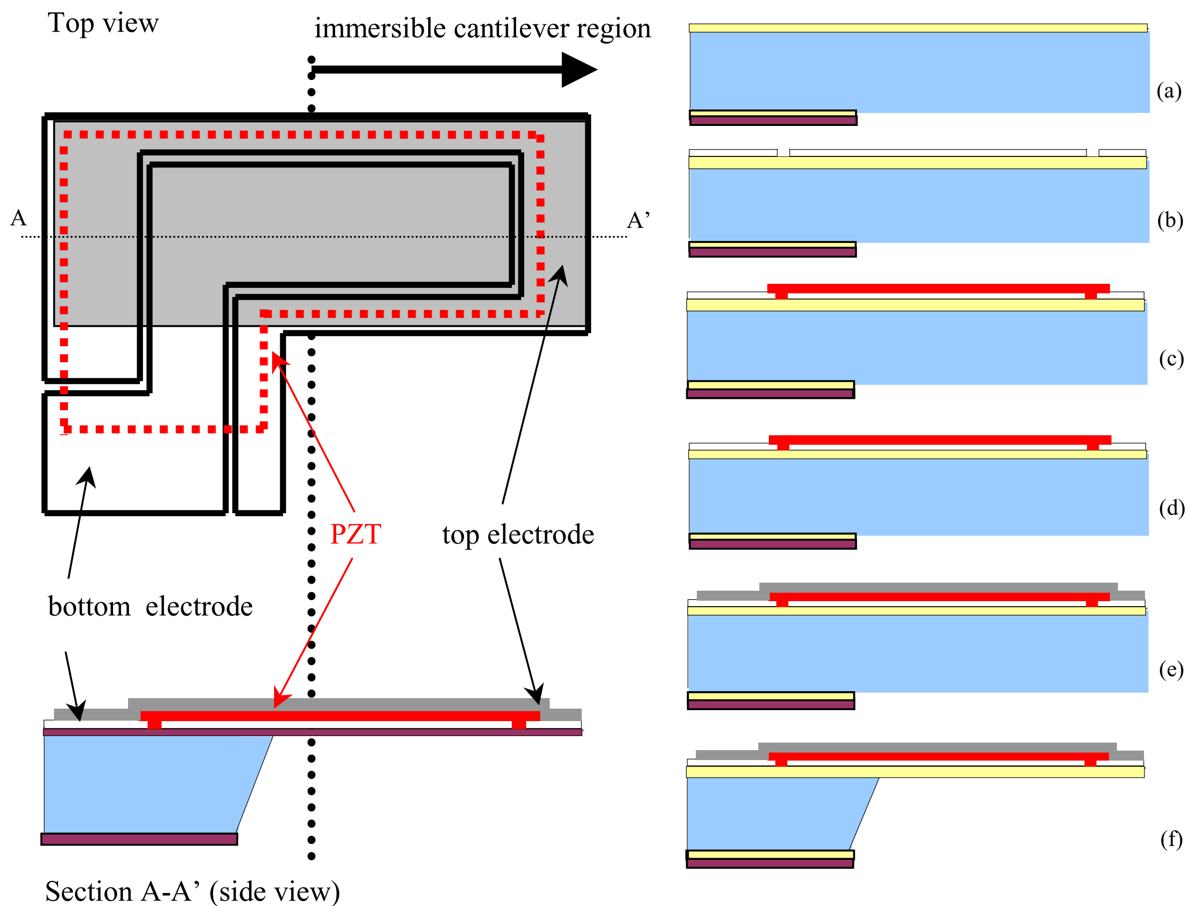

Figure 3-17: Left: Design schematic of water-immersible piezoelectric cantilever. Right: Side profile of fabrication process. Figure courtesy of Y.-B. Jeon.

The fabrication process is identical to that illustrated in Figure 3-1, although the side profiles are different. In this process, the regions where the bottom electrode is opened with 2 μm gaps (such that PZT is in direct contact with the diffusion barrier) have different material properties after annealing due to inter-diffusion of Si into the PZT. An AFM image of this region was shown previously in Figure 3-5a. Nonetheless, the overall electrical properties of the PZT film is excellent. This is shown in Figure 3-18. The saturation polarization, remnant polarization, coercive field and dielectric constant are 54 μC/cm^2, 15 μC/cm^2, 60 kV/cm and 1200 respectively. The properties are almost the same in air and water. The polarization properties of the PZT film dropped to approximately 72% of its initial value after 2 $\times 10^{10}$ cycles at 5 V (with each cycle a 19.6 μs rectangular pulse). In water, however, the PZT film degraded earlier, dropping to approximately 80% of its initial value after 1.5 $\times 10^9$ cycles and failed after 5.1 $\times 10^9$ cycles. A reasonable cause of failure is the diffusion of wafer through the 200 nm Pt layers to the PZT, causing electrical short between the encapsulated top and bottom electrodes.

Underwater applications following this proof-of-concept include water-immersible pressure sensors, water-immersible cantilever actuators for Scanning Transmission Microscopy

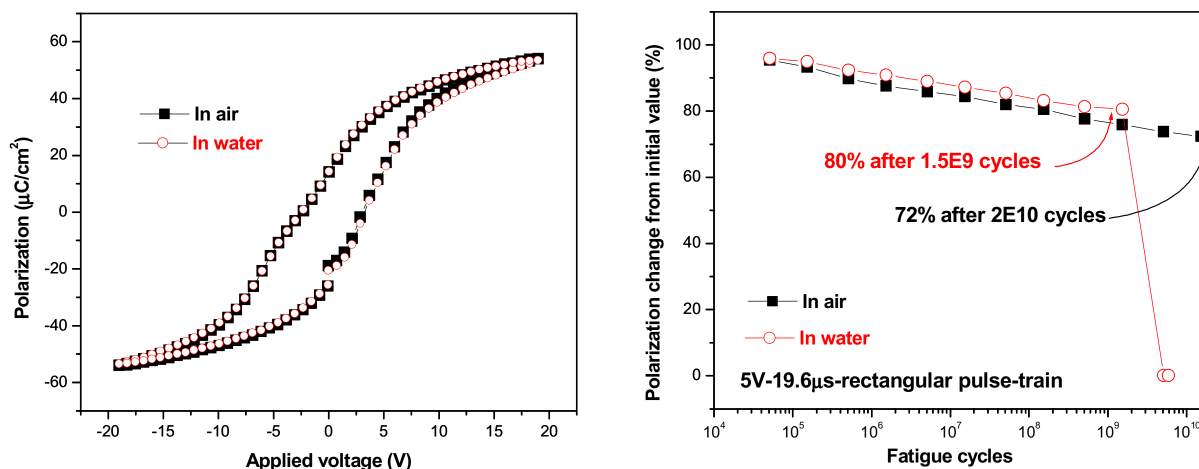

Figure 3-18: Polarization properties of PZT film in air and water: (a) hysteresis characterization, (b) fatigue analysis. Figure courtesy of Y.-B. Jeon.

and biomedical devices. Packaging in this device is more involved so as to prevent water leakage to the contact pad regions of the cantilever. Future development on this work involves modifications to the current design to improve actuator lifetime in water.

3.3 Device Demonstration - Mechanical

For nanometer measurements of the double-anchored membrane mechanical motion, the Computer Microvision [34] metrology tool is used. A laser vibrometer is used to characterize mechanical resonance and noise. The deflection of the membrane is also visually observed under bright-field illumination of an optical microscope.

3.3.1 Membrane and cantilever deflections

Under a 120X optical microscope, deflections of the double-anchored membrane and free cantilever can be visually noticed for different actuation voltages. The probe station setup with a double-anchored membrane design is illustrated in Figure 3-19. The bright region in the center of the figure is the diffractive grating region. Figure 3-20 shows the setup with a free cantilever, where unbalanced residual stresses resulted in uneven flatness at the gratings region.

Multiple-cycle experiments were also performed on the double-anchored membrane to test for fatigue failure. The devices were tested up to 4.52×10^9 cycles and showed no mechanical fracture. The applied voltage was cycled at 8 kHz, below the first modal resonance, and with a 5 V peak-to-peak amplitude.

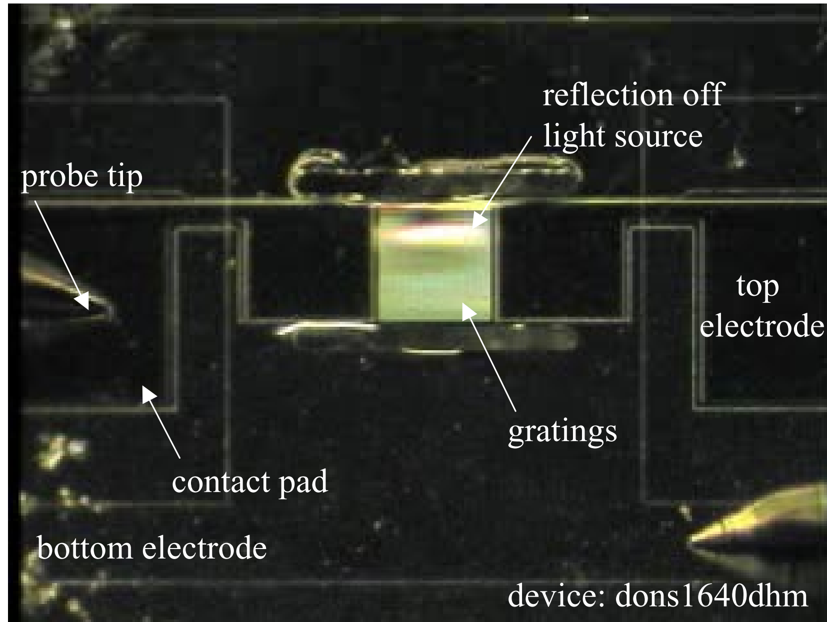

Figure 3-19: Probe station setup with a completed double-anchored membrane design. The bright region in the center of the figure is the diffractive grating region.

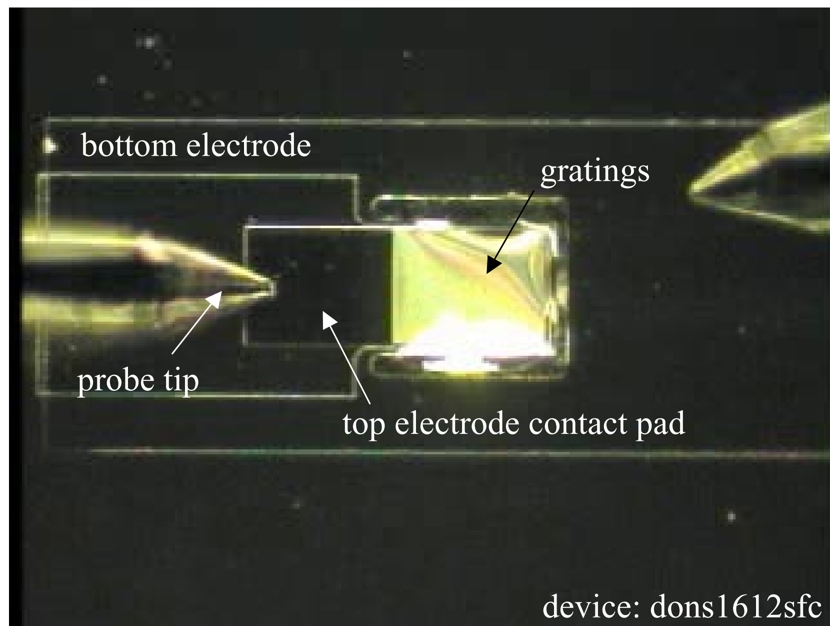

Figure 3-20: Probe station setup with a completed free cantilever. Uneven flatness in the gratings region, due to unbalanced residual stresses, can be visually observed.

Geometry	*Design I*	*Design II*
PZT length, L (μm)	450	200
PZT thickness, t_{pzt} (μm)	0.51	
grating aperture length, L_a (μm)	300	
membrane thickness, t_{mem} (μm)	0.4	
membrane width (μm)	300	
Performance		
d_{31} coefficient, inferred (pC/N)	-100 $\pm$ 15	
d_{33} coefficient, direct measurement (pC/N)	275.4	
ε_r relative dielectric constant	1200	
minimum resolvable grating period change (nm)	0.6	
grating period change (nm)	8.3 at 9 V	4.9 at 10 V
membrane strain	0.21% at 9 V	0.12% at 10 V
diffracted angular change at 10 V (μrads)	486	154

Table 3.1: Analog Piezoelectric Tunable Grating Parameters.

3.3.2 Microvision analysis

Direct measurement of the membrane strain deformation when actuated by the thin-film PZT microactuators require an instrument with nanometer resolution. A metrology tool developed at MIT for MEMS devices – the Computer Microvision system [34] at the Freeman lab – has such capabilities. This instrument reconstructs three-dimensional images of microscopic targets using the optical sectioning property of a light microscope. Interferometry capability with coherent laser illumination is also possible. The collected images are post-processed and combined to analyze the target in all six degrees of freedom, with nanometer resolution for displacements.

Measurement of a device, with Design I (450 μm PZT length), demonstrated a 229 $\pm$ 2 nm total membrane displacement at 9 V. By tracking the displacements of individual grating beams, an average period change of 8.3 nm (0.21% membrane strain) at 9 V actuation is observed. This translates into an expected diffracted angular change of 328 μrads for our fabricated device parameters. A device, with Design II (200 μm PZT length), shows a 4.9 nm period change at 10 V (corresponding to 0.12% membrane strain and an expected 194 μrads diffracted angle change). The period change at 1 V for both devices is approximately 0.6 nm, calculated from total membrane displacement. As summarized in Figure 3-21, both experimental device measurements are in good agreement (correlation coefficient $\rho \sim 0.9$) with a single analytical formulation for a d_{31} coefficient of approximately -100 $\pm$ 15 pC/N. A

consistent set of material properties is used in the analytical model to define both theoretical plots of Figure 3-21. In addition, an independent measuring method – using the pneumatic loading method [72] – is carried out by Dong-Guk Kim[3] to characterize the PZT film. The measured d_{33} value is 275.4 pC/N. While the exact d_{31} is uncertain from the pneumatic loading method, taking typical ratios between d_{33} and d_{31} in PZT materials, we estimate a d_{31} of approximately -115.7 pC/N from the d_{33} value. This falls within our estimate of the d_{31} from analytical modeling and Computer Microvision measurements. These results are summarized in Table 3.1.

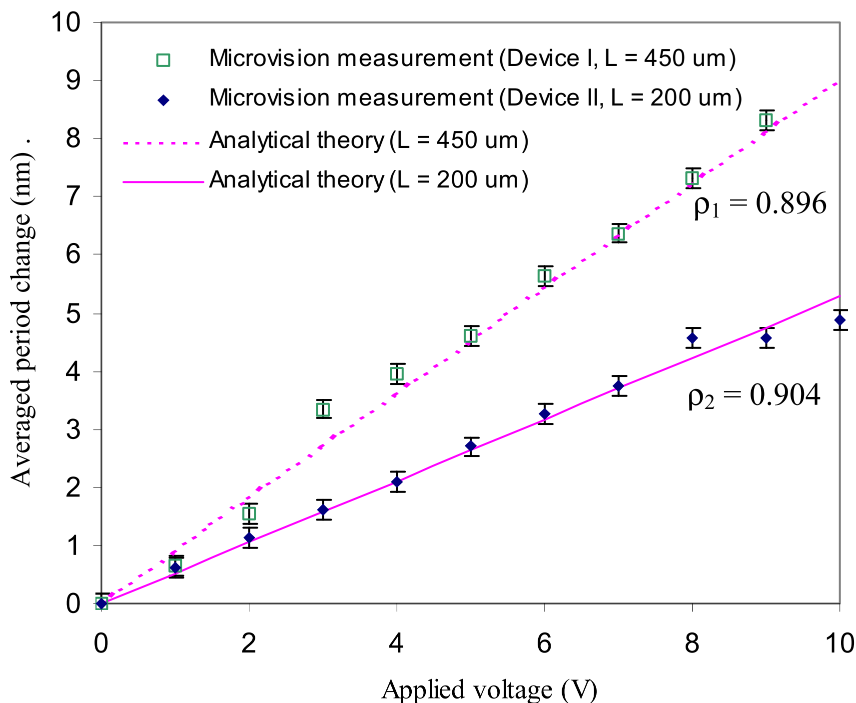

Figure 3-21: Measured period change against applied voltage for two different device designs. Both results match with the analytical model for a single set of material properties and with a single fitted d_{31} coefficient at -100 pC/N.

The membrane strain demonstrates an average uniformity percentage of 16%, calculated as the ratio of the standard deviation of the membrane strain to the average membrane strain, over 40 measurements in different regions of the grating. This is shown in Figure 3-22, with the error bars depicting the maximum and minimum values. The uniformity variation is due to membrane thickness variation and anchor asymmetry in the double-anchored structure, after membrane release. This mechanical non-uniformity is averaged out in the diffracted optical spectrum, although there is a corresponding spatial spreading of the energy in each diffracted order. In designing specific optical systems, therefore, the angle of acceptance

[3] At the Korea Advanced Institute of Science and Technology.

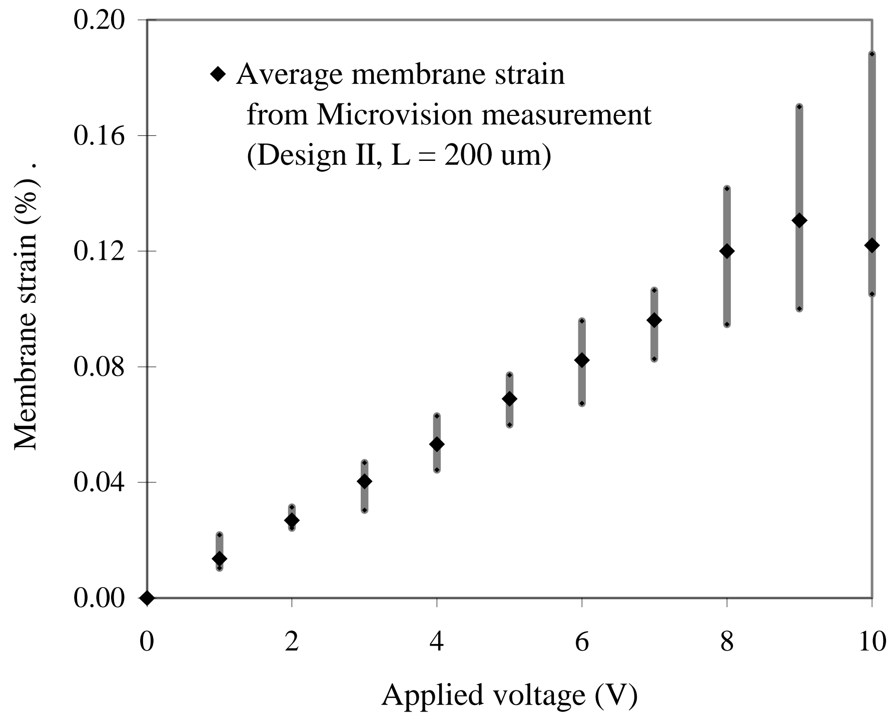

Figure 3-22: Uniformity of membrane strain under actuation. A uniformity variation of 16% (defined as the standard deviation over the averaged value) is measured. The error bars depict the maximum and minimum values of the measurements.

should be sufficiently large so that the bulk of the diffracted order of interest is captured.

The PZT polarization-electric field hysteresis response, due to domain reorientations, is observed during -10 V to +10 V actuation, with a non-zero membrane displacement at 0 V. The result matches the PZT film electrical characterizations. For compensating hysteresis and piezoelectric strain drifts, a mechanical latching mechanism or an active feedback control loop would prove useful.

3.3.3 Vibration and noise characterization

Dynamic response of the double-anchored membrane is measured [139] with a laser Doppler vibrometer which conceptually operates by detecting the frequency shift of the back-scattered laser to determine the velocity of a vibrating object. The device chip is placed on a piezo-shaker and the frequency response is illustrated in Figure 3-23. The first modal resonance, out-of-plane bending, is determined at 14.1 kHz. The low quality factor Q [131] is due to the large membrane area (widths of 300 μm and lengths of either 800 or 1200 μm). The membrane displacements under a 14.1 kHz excitation frequency is shown in Figure 3-24. The figure segments show the displacements for different time-steps of one oscillation.

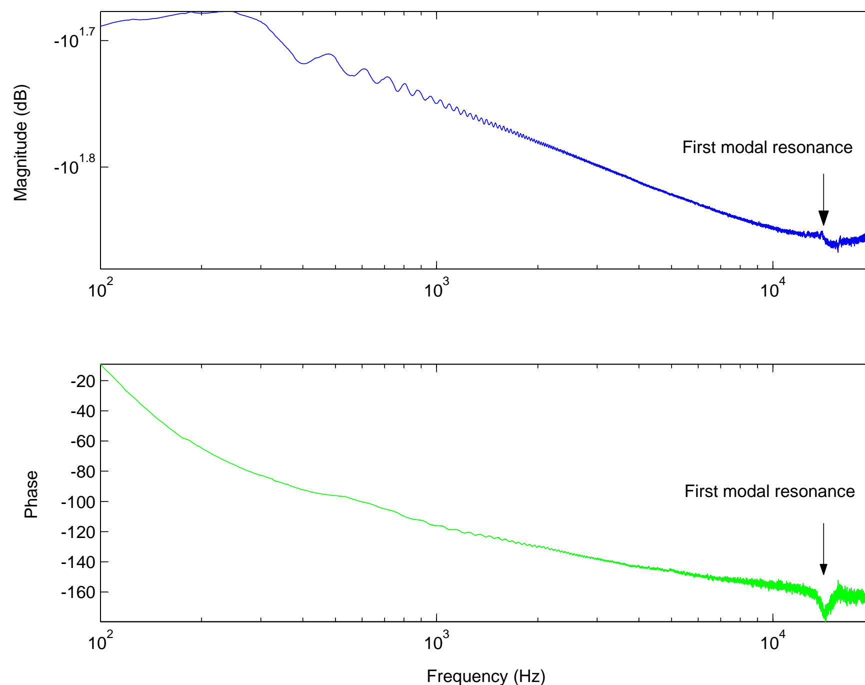

Figure 3-23: Dynamic response of double-anchored membrane, with first modal (out-of-plane bending) resonance at 14.1 kHz.

In addition, we compared the frequency response between a released membrane and an unreleased membrane with the laser vibrometer. Figure 3-25 shows the responses for the devices, where Device 1 and 2 are released membrane devices and the static grating device similar to Device 1 and 2, except that it is not released by KOH etching. Up to the first modal resonance, there is no discernable difference within the resolution of the instrument.

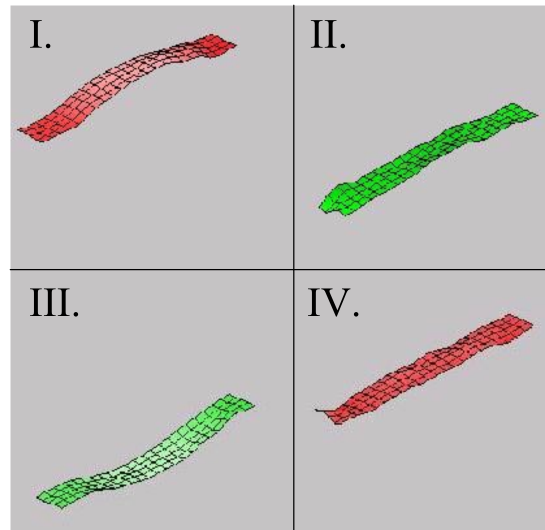

Figure 3-24: Double-anchored membrane displacement under 14.1 kHz excitation. The figure segments show the displacements for different time-steps of one oscillation.

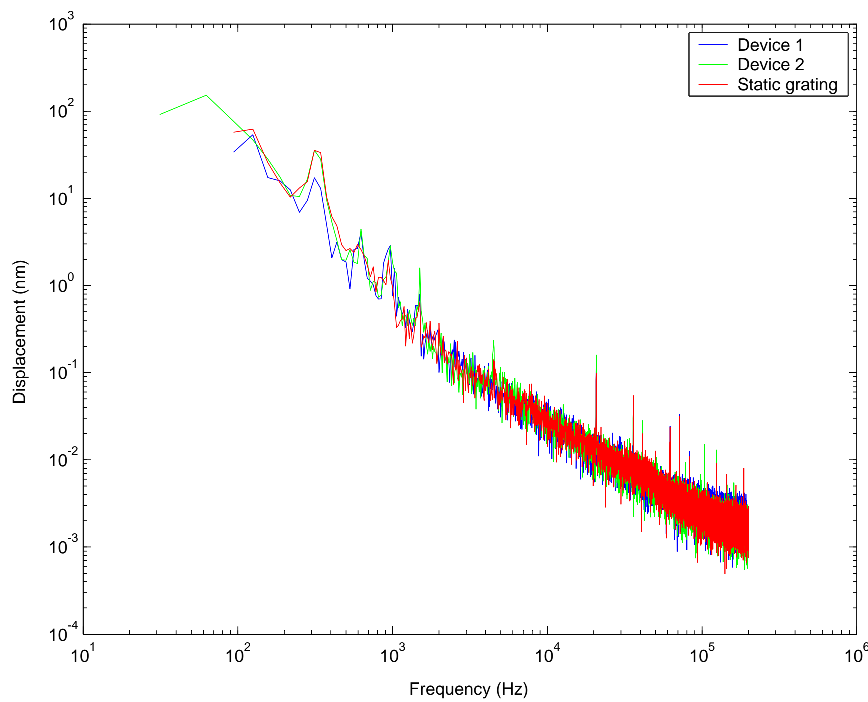

Figure 3-25: Comparison of deformable membrane against an unreleased grating device, for characterization of ambient noise floor effects. Up to the first modal resonance of 14.1 kHz, there is no discernable difference within the resolution of the instrument.

3.4 Device Demonstration - Optical

For optical measurements, the device is either packaged by wire-bonding onto a pin grid array chip (such that the chip can be placed perpendicular to the optical bench) or mounted horizontally onto a probe station with optical beam deflected down towards the probe station. A schematic of the setup is depicted in Figure 3-26. A 632.8 nm HeNe laser was utilized as the illumination source and the diffracted order imaged onto a CCD camera. A telescope can be included to magnify the diffracted angular change. To determine shift of the diffracted order for various actuation voltages, an image centroid method is used, where the centroid X_c and Y_c of the tracked image distribution is computed simply as:

$$X_c = \frac{\sum_i x_i I_i}{\sum_i I_i} \tag{3.1}$$

$$Y_c = \frac{\sum_i y_i I_i}{\sum_i I_i} \tag{3.2}$$

where x_i and y_i are spatial coordinates of intensity profile I_i. Thresholding is used to improve the image tracking[4]. Fourier correlation could also be used to differentiate between image shifts [4].

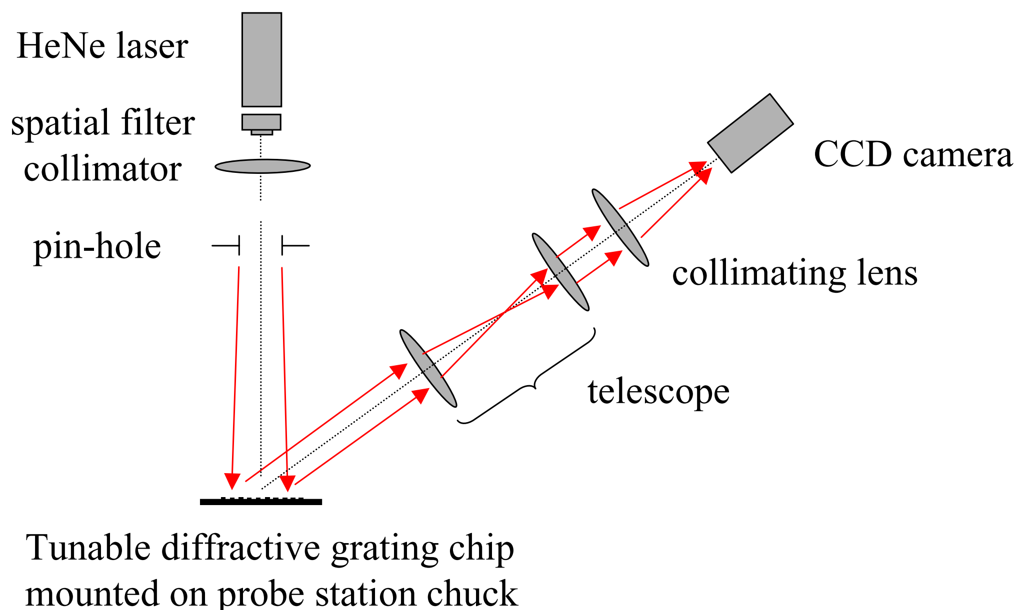

Figure 3-26: Schematic of setup for optical centroid measurements.

[4]A more formal thresholding method involves searching through all available threshold-levels and looking for minimal centroid variance [2].

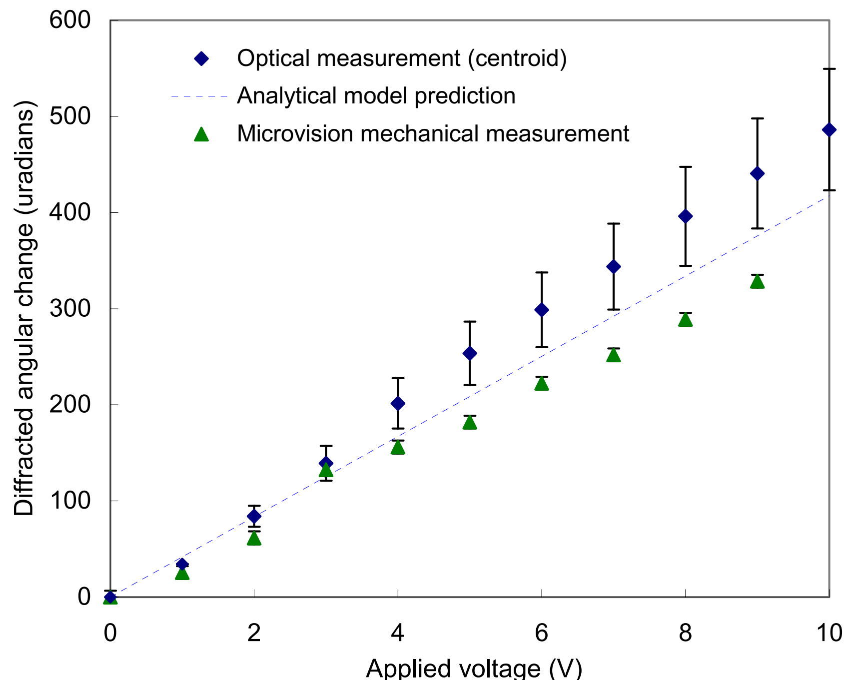

Figure 3-27: First order diffracted angular change against applied voltage obtained by optical image centroid processing and mechanical motion measurements. The optical measurement is corrected for tilt in the membrane through the finite-element mechanical model and is the main source of uncertainty.

Figure 3-27 shows the first diffracted order angular change by applying voltage to one of the two device actuators, for a device with Design I parameters. This angular change is then corrected for tilt in the membrane, via the matched finite-element model described in Section II, when only one of the two actuators is employed. Uncertainty in the optical measurement is largely due to numerical accuracy of the finite-element model correction. This is calculated to be a fixed percentage – at 13% – for a 1% uncertainty in the finite-element model. Other sources of uncertainties, such as membrane rotation due to asymmetrical membrane lengths from device release and thermal disturbances, also contribute to the error bars shown in Figure 3-27.

Comparisons between the optical image centroid processing, mechanical membrane deformation measurements, and theoretical predictions show agreement within 15%. At 10 V, the angular change is estimated at 486 μrads for this device. A device of Design II shows a correspondingly scaled diffracted angular change of 154 μrads at 10 V. The systematic error between the optical and mechanical measurements is due to uncertainty in the finite-element results; a more computational expensive finite-element model could conceivably reduce this systematic variation. This comparison between the mechanical experiments, optical measurements and theory, nonetheless, shows the fine control of the diffracted angles at low actuation voltages and suggests possibilities for implementation towards specific

applications, such as discussed earlier in Section 2.4.

Future work includes microfabrication control of the residual stress in the thin-film piezoelectric and diffusion barrier materials to reduce out-of-plane motion and tilt, and the introduction of mechanical latches to maintain fixed displacements over time. Further possibilities in the optical detection techniques involve: (1) an interferometric setup with two frequencies onto the grating to detect shifts in the fringe pattern when the device is actuated, (2) simultaneous capture of first and second order diffraction images to eliminate tilt effects by taking the difference between the two orders.

3.5 Summary

This chapter begins with the thin-film piezoelectric microfabrication and the integrated process flow for the analog tunable gratings. This is followed by electrical measurements – which shows an excellent dielectric constant of 1200 – of the film, including a characterization for water-immersible active cantilevers. The released double-anchored membrane is characterized mechanically for its grating period displacement under actuation and its frequency response. The device is then characterized optically to infer the motion of the first diffracted order under actuation. Future work is discussed, such as thin-film residual stress control or the introduction of mechanical latches to maintain fixed displacements over time. Applications of this demonstration of analog tunable gratings include dispersion compensation, miniaturized spectrometry and tunable external cavity lasers amongst the many.

Chapter 4

Design Of Strain-Tunable Photonic Band Gap Microcavity Waveguide

You might discover after a bit, for example,
that when there's only one bishop around on the board
that the bishop maintains its color. Later on you might
discover the law for the bishop as it moves on the diagonal
which would explain the law you understood before...
Then things can happen, everything's going good,
you've got all the laws, it looks very good,
and then all of a sudden some strange phenomenon occurs in some corner.
–R. Feynman, The Rules of The Game (1981).

4.1 Background

The ability to mold the flow of light [62] with photonic band gaps was first suggested in 1987 [161, 63] and has since seen numerous work and applications. These spatially periodic structures consist of high dielectric contrast media, wherein absorption is minimized and scattering designed at the interfaces, to produce many of the same phenomena for photons as the atomic potential does for electrons. These characteristics are theoretically captured exactly through Maxwell's equations. Such structures can be broadly categorized into one-dimensional, two-dimensional and three-dimensional structures.

One-dimensional photonic crystals have current implications in both research and industry. An interesting example is an all dielectric coaxial hollow waveguide that, through light confinement with a photonic band gap in a one-dimensional dielectric reflector [18], can overcome the problems of polarization rotation and pulse broadening in optical light transmission [58]. A schematic of the design was illustrated earlier in Figure 1-3a. Two-dimensional photonic crystals, typically consisting of holes or rods in a plane with index-guiding in the

third dimension, have applications such as channel add/drop filters for wavelength division multiplexing communications, zero-loss waveguide bends, low-loss waveguide crossings, or low-threshold microlasers (Figure 1-3b). Three-dimensional photonic crystals, typically in a face-centered cubic diamond lattice (till date), have been designed and experimentally demonstrated. They have band gaps at 10 μm and 1.5 μm wavelengths, and have been made in both high contrast dielectric material (usually) and metal [97, 31, 114, 30]. A particular three-dimensional structure has been designed (Figure 1-3c shows a schematic of the structure) and fabricated [120] at MIT.

Our interest is in a low-dimensional photonic crystal – the microcavity waveguide, as shown in Figure 4-1 – that rests on the foundations first reported by Foresi, Fan and Lim [33, 27, 94]. The periodic structure, in this case circular holes, is embedded within a dielectric slab waveguide. This periodic array not only limits the wavevector to π/a, where a is the spatial period, but also folds the dispersion relation of the waveguide and splits the lowest-order mode. This splitting produces a band gap. The size of the band gap is dependent on the dielectric contrast; for an air-cladded Si waveguide on a SiO_2 layer, the band gap is $\sim 27\%$ of the midgap frequency. A defect, termed the "microcavity", is then created by increasing the distance between two holes at the center of this periodic structure. This allows localized states to be supported in the photonic band gap. It is also this break in periodicity, rather than a break in the vertical mirror symmetry, that causes radiation losses (in $\hat{x}$) at the defect. The set of holes on each side of the microcavity effectively forms a Bragg mirror. Its response is analogous to a Fabry-Perot resonator or tunneling through a double potential barrier, although its strong field confinement gives a cavity modal volume of 0.055 μm^3 [33], less than half a cubic half-wavelength ($\frac{1}{2}\left(\frac{\lambda}{2}\right)^3$).

Applications for the microcavity waveguide include new photonic chip architectures and devices, such as filters, signal routers and all-optical gallium arsenide[1] switches. In particular, we are interested in a silicon implementation[2] for integration ease with current integrated circuit foundries.

The motivation for a strain-tunable silicon microcavity waveguide, as first described in Chapter 1 (Section 1.1), can be briefly summarized here as follows:

1. The demonstration of strain-tunability in silicon microphotonics, which has vanishingly small electro-optic nonlinearities for modulation.

2. The demonstration of tunability with low power requirements, on order of 10 nW and 5 V, with use of piezoelectric actuators for strain-tuning.

3. The demonstration of strain-tunability[3] in silicon photonic crystals.

[1] Requiring galliuim arsenide, an all-optical reflection switch for ultrashort pulses has been proposed theoretically for a similar structure to the microcavity waveguide discussed here, but with a asymmetrically confined defect [86].

[2] Will silicon show stimulated emission and optical gain sufficient for a silicon laser? There is an elusive possibility [38, 118].

[3] Other general methods for tunability in photonic crystals were described in Section 1.3.

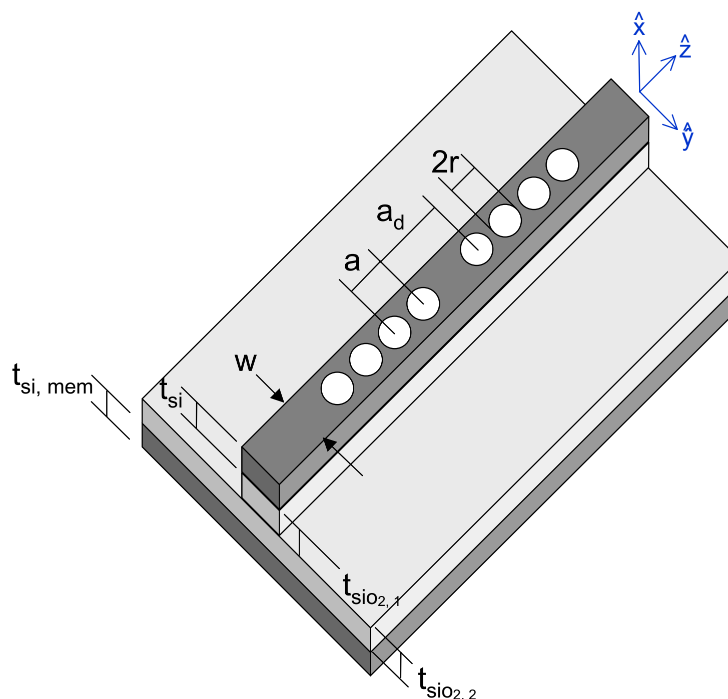

Figure 4-1: Schematic of microcavity waveguide.

4. The possibility of modulation frequencies on order of MHz and device-level localization of tunability, in comparison with current techniques of thermal tuning and compensation.

Specific applications for the tunable microcavity waveguide range from dynamic reconfiguration of the resonant optical filters to correction of fabrication mismatches in optical communication devices.

4.2 Strain-tuning Platform For Microphotonics

The conceptual design consists of a deformable double-anchored membrane supporting optical elements, as illustrated in Figure 4-2. This strain-tuning platform is general for microphotonic components. The membrane itself is actuated with thin-film piezoelectric actuators and is previously described in Section 2.1 and 2.2 for analog tunable diffractive gratings. The thin-film piezoelectric actuators could operate in d_{31} mode (which would consist of a tri-level of Pt top electrode, PZT film and Pt bottom electrode) or d_{33} mode with a inter-digitated Pt top electrode, PZT film and ZrO_2 tri-layer. The membrane is on order of thickness as the PZT film, a micron or less, and made up of material[4] with sufficient limiting strain

[4]Examples of membrane material explored here are Pt, Si, or a Si and SiO_2 combination.

in the desired spatial modulation range. Possible microphotonics components include microcavity waveguides, microring resonators, arrayed waveguide gratings, and Bragg grating waveguides.

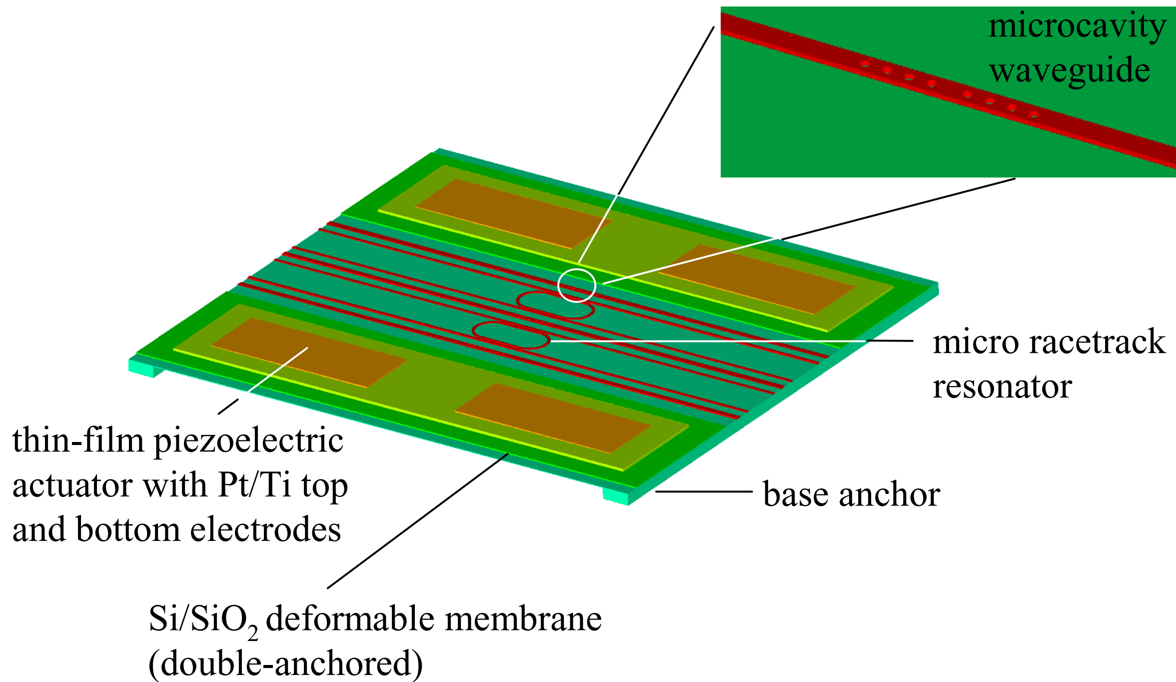

Figure 4-2: Strain-tuning platform for microphotonics. Consisting of thin-film piezoelectric actuators and a double-anchored membrane, this design is general for various microphotonic components of interests.

The in-plane membrane strain, in the direction along the length of PZT, is profiled in Figure 4-3a. In particular, the strain distribution illustrated is for a design with PZT length, L_{pzt}, of 250 μm and total membrane thickness of 0.5 μm, comprising of 0.1 μm Si ($t_{Si,mem}$) and 0.4 μm thermal oxide ($t_{SiO_2,2}$). For an actuation voltage of 10 V in this design, the strain at the center of the membrane is 0.12%. Figure 4-3b shows the membrane strain against varying total membrane ($t_{Si,mem} + t_{SiO_2,2}$) thickness. The strain decreases with increasing total membrane thickness and asymptotes around 0.04% for a 2 μm thick membrane.

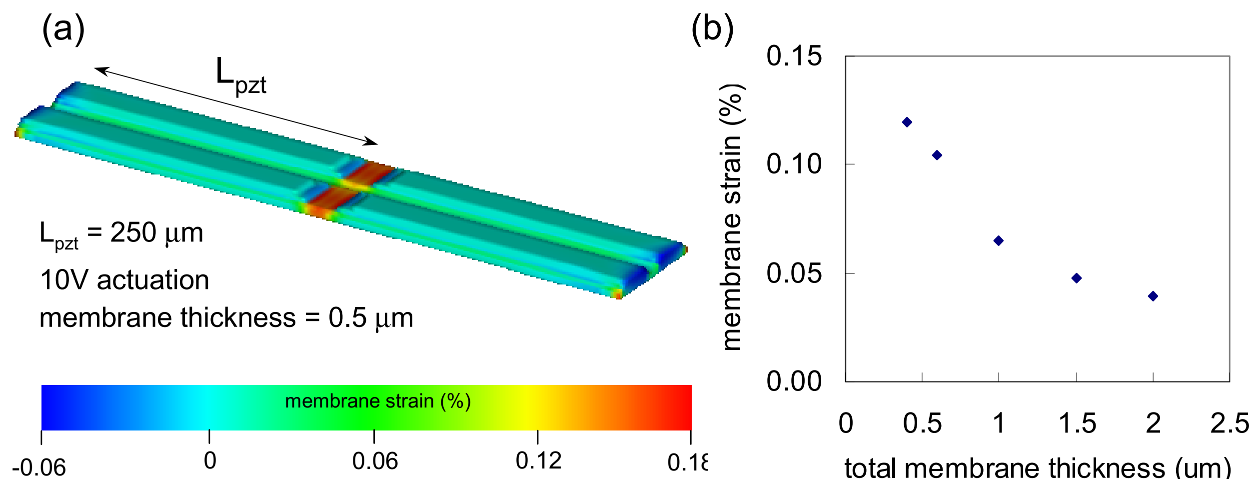

Figure 4-3: Finite-element model of membrane strain: (a) in-plane strain profile, along length of PZT, (b) variation of membrane strain against Si membrane thickness.

4.3 Concept And Design Of Microcavity Waveguide

Microcavities with photonic band gaps have been studied in literature. Microcavities using distributed Bragg reflectors and distributed feedback Bragg gratings have been reported [163], although they typically have a larger modal volume and require large numbers of grating periods for cavity confinement due to the weak index modulation. Deep gratings for cavity confinement have also been analyzed and demonstrated, with lower transmission and larger modal volume [82, 153] than the microcavity waveguide.

In contrast, the microcavity waveguide design permits: (1) modal volumes less than half of a cubic half-wavelength, (2) high Q resonance on order of hundreds to a thousand, (3) significant enhancement of spontaneous emission with the high Q and small modal volume [61], and (4) total physical size of defect and holes on order of 4 μm for possible high-density optical circuits. To understand the microcavity waveguide design, we begin with a discussion of the dielectric slab waveguide.

4.3.1 Dielectric slab waveguide

To find the guided modes in a dielectric slab waveguide, we require: (1) Maxwell's equations (specifically the derived Helmholtz wave equation) and, (2) matching boundary conditions. Maxwell's equations, in complex time-harmonic form, are [109] :

$$\vec{\nabla} \times \vec{E} = -j\omega\mu\vec{H} \tag{4.1}$$
$$\vec{\nabla} \times \vec{H} = j\omega\varepsilon\vec{E} + \vec{J} \tag{4.2}$$
$$\vec{\nabla} \cdot \varepsilon\vec{E} = \rho_e \tag{4.3}$$
$$\vec{\nabla} \cdot \mu\vec{H} = 0 \tag{4.4}$$

where $\vec{E}$ is the electric field, $\vec{H}$ the magnetic field, ω the time-harmonic wave frequency, μ the medium permeability, and ε the medium permittivity. $\vec{J} = 0$ and $\rho_e = 0$ in the absence of current sources and charges in our waveguide.

Taking the curl of Equation 4.1 and substituting into Equation 4.2 with $\vec{J} = 0$, we obtain a single equation for $\vec{E}$ as[5]

$$\vec{\nabla} \times \left(\vec{\nabla} \times \vec{E}\right) = \omega^2\mu\varepsilon\vec{E} \tag{4.5}$$

which can be quantized as an eigenproblem. Or expressed for the magnetic field $H(\vec{r})$, where we explicitly include the position dependence $\vec{r}$, as

$$\vec{\nabla} \times \left(\frac{1}{\varepsilon(\vec{r})}\vec{\nabla} \times H(\vec{r})\right) = \left(\frac{\omega}{c}\right)^2 H(\vec{r}) \tag{4.6}$$

And with $\vec{\nabla} \cdot \vec{E} = 0$ for piece-wise isotropic media or slowly varying ε, the following Helmholtz wave equation results from Equation 4.5

$$(\vec{\nabla}^2 + \omega^2\mu\varepsilon)\vec{E} = 0 \tag{4.7}$$

In particular, for wave guidance in a dielectric slab, we have from Equation 4.7 the following dispersion relations

$$\beta^2 - \alpha_y^2 = \omega^2\mu\varepsilon_{outside} \tag{4.8}$$
$$\beta^2 + k_y^2 = \omega^2\mu\varepsilon_{inside} \tag{4.9}$$

where β is the propagation constant in the waveguide, α_y the decay constant in the evanescent field outside the waveguide, k_y the wave number in $\hat{y}$, and $\varepsilon_{outside}$ and ε_{inside} the permittivity outside and inside the waveguide medium respectively. Equation 4.9 is used to derive the dispersion diagram – frequency against wave vector – if k_y is known for each frequency ω.

To find k_y for each ω, we need to match the boundary conditions. The dielectric slab is symmetric in the x-z plane[6], as was illustrated in Figure 4-1. The transverse electric field[7] solutions (electric field polarized along x̂ and transverse to direction of propagation ẑ) are

[5] In a periodic media, however, it turns to be more convenient to use the magnetic field formulation as described in Equation 4.6 [62].

[6] A general model for asymmetric waveguides is found in Kogelnik and Ramaswamy [78].

[7] The Goos-Hänchen phase shift at total internal reflection is larger for TM modes than TE modes [80],

either symmetric or antisymmetric. Following discussions by Haus [44] or Kong [80], the symmetric solution can be described as

$$E_x = A\, cos\, k_y y\, e^{-j\beta z}, \qquad |y| < \frac{w}{2} \tag{4.10}$$

$$E_x = B\, e^{-\alpha_y y}\, e^{-j\beta z}, \qquad y > \frac{w}{2} \tag{4.11}$$

$$= B\, e^{\alpha_y y}\, e^{-j\beta z}, \qquad y < \frac{w}{2} \tag{4.12}$$

where w is the waveguide width. The respective magnetic fields can be found from Faraday's law (Equation 4.1). With symmetry in x-z plane, we need only to match boundary conditions at y = $\frac{w}{2}$. Continuity of E_x/H_z at y = $\frac{w}{2}$ gives the following transcendental equation

$$tan\, k_y d = \frac{\alpha_y}{k_y} \tag{4.13}$$

Solutions for k_y can either be found graphically or numerically. When the k_y solutions are combined with Equation 4.9, the dispersion diagram for a dielectric slab waveguide is obtained.

4.3.2 The microcavity waveguide

The dispersion diagram for a microcavity waveguide, however, is more difficult to attain analytically. However, the dispersion diagram, or band structure, of the microcavity waveguide follows the same asymptotes as a dielectric slab waveguide. In the presence of the periodic structure, the dispersion diagram could be thought of being folded at specific k-points (due to repetition of k outside the Brillouin zone [77]). We refer to the MIT Photonic Bands package [68] for a numerical calculation, which computes the definite-frequency fully-vectorial eigenstates of Maxwell's equations in periodic dielectric structures for arbitrary wavevectors. The microcavity waveguide band structure in the first Brillouin zone, is computed by Johnson [65] with the software and illustrated in Figure 4-4 for a structure without defect. In the design of the band structure, we can employ the scale-invariance of Maxwell's equations which results from Equation 4.6. To illustrate this, we perform a change of variables $\vec{r}\,' = s\vec{r}$ and $\vec{\nabla}\,' = \vec{\nabla}/s$ [62, 128]

$$\vec{\nabla}\,' \times \left(\frac{1}{\varepsilon'(\vec{r}\,')} \vec{\nabla}\,' \times \vec{H}(\vec{r}\,'/s) \right) = \left(\frac{\omega}{cs} \right)^2 \vec{H}(\vec{r}\,'/s) \tag{4.14}$$

resulting in less confinement for the TM mode. In our waveguides, we are particularly interested in TE-like modes.

where s is a scaling factor. Because k and ω have inverse dimensions of $\vec{r}$ and time t respectively, they are transformed back to real space by the following

$$\vec{k}\,' = \frac{ka}{2\pi} \quad \text{and} \quad \omega\,' = \frac{\omega a}{2\pi c} \tag{4.15}$$

With Equation 4.15, the band structure is plotted as a non-dimensional frequency ($\omega a/2\pi c$) and non-dimensional k-vector ($ka/2\pi$) with respect to lattice constant a. For operation at 1.55 μm wavelengths, a is on order of 0.5 μm; for operation at 5 μm wavelengths, a is on order of 2 μm.

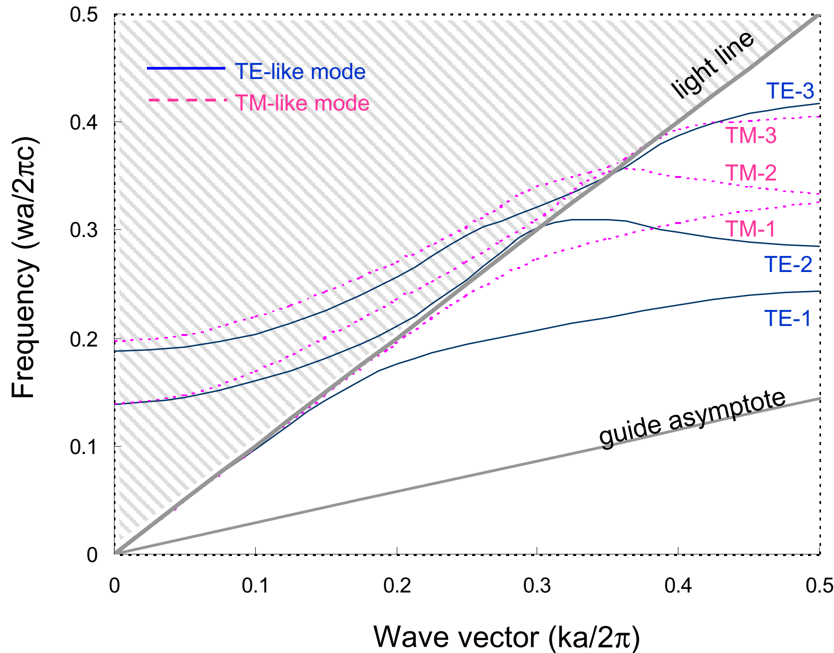

Figure 4-4: Band structure of dielectric slab waveguide with embedded holes. Computation courtesy of Johnson [65, 68].

States above the light line are not index-guided by the dielectric waveguide, and form a continuum of radiated modes. States below the guide asymptote are not allowed in the waveguide. Selected states in-between these two asymptotes are guided – shown in Figure 4-4 as TE-like (electric field mostly in yz plane) or TM-like modes – and evanescent in $\hat{x}$ and $\hat{y}$. A band gap can be observed between the first and second TE-like modes. The introduction of a defect in the periodicity (such as increasing the amount of dielectric between two selected sets of holes, breaking the translational symmetry) permits a localized state to exist in the photonic band gap. This state is pulled down from the second TE-like mode into the band gap. Conversely, reducing the amount of dielectric between two selected sets of holes will push a state up from the lower band. Section 4.3.3 discusses the design of various parameters in the microcavity waveguide.

Device parameter	*Design dimension*
waveguide width	1.19a
waveguide height	0.44a
defect length a_d	1.50a
hole diameter	0.46a
oxide insulator thickness	0.44a
number of holes on each side of microcavity	4
refractive index silicon	3.48
refractive index silicon oxide	1.44

Table 4.1: Microcavity Waveguide Design Parameters.

The design parameters of our microcavity waveguide follows that suggested in Fan [27] and Foresi [32] and are summarized in Table 4.1. The device structure is similar to that of a hybrid between a "monorail" and an "air-bridge". A "monorail" structure consists of a microcavity waveguide on an oxide ridge, with the oxide fixed to the substrate; an "air-bridge" structure has the microcavity waveguide cladded by air all around the waveguide and is only suspended by two fixed ends of the waveguide. The transmission spectra of both devices differ by less than 10%. The resulting transmission for a "monorail" structure, computed by Johnson [65], is shown in Figure 4-5.

The peak transmission is 0.68 with resonance frequency at 0.2625 c/a. The transmission has a first-order Lorentzian response, characteristic of a Fabry-Perot cavity in quarter-wave shifted distributed feedback (DFB) resonators. To achieve desired Butterworth band pass ("flat-top") filter [110] characteristics, cascaded microcavity resonators can be considered, such as developed for cascaded DFB resonators using coupled-mode theory in time [45]. The total Q, as further described in Section 4.3.3, is computed to be 180. Moreover, the ripples in the calculated stop band is postulated to be from reflections off the waveguide input port (at the computational boundary), output port, and the effective dielectric mirrors from the two set of holes. At the band edges, there are larger numerical errors but we also expect Fabry-Perot oscillations due to the low group velocity at the edges [65].

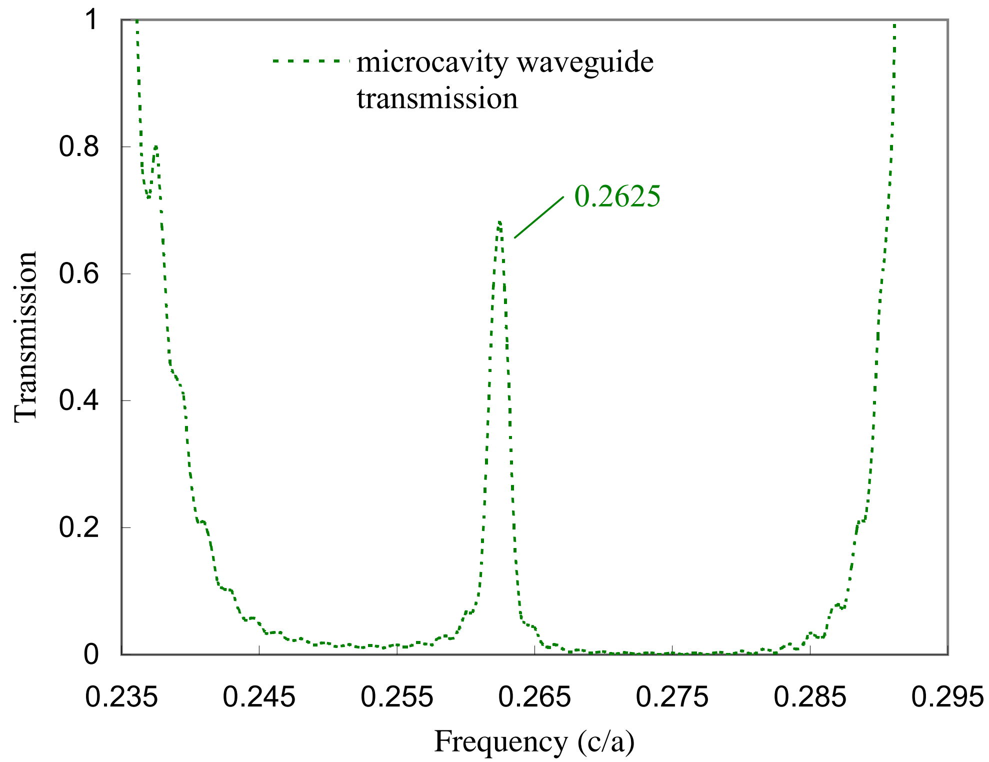

Figure 4-5: Photonic band gap transmission spectrum of microcavity waveguide. Computation courtesy of Johnson [65].

4.3.3 Design thoughts

The theoretical design and experimental demonstration is first discussed in detail by Fan [27], Foresi [32] and Lim [94]. We summarize here the design considerations for reference.

Effect of geometry variations [27, 32]

a_d/a **ratio** A quarter-wave phase shift with a_d at $1.5a$ gives the strongest resonant mode confinement. This is analogous to a Fabry-Perot resonator, although the resonance does not appear in the middle of the band gap (as in a Fabry-Perot) but displaced towards the lower frequency band edge. Increasing the defect size, for a constant lattice constant a, increases the resonant wavelength.

Number of holes Increasing the number of holes will increase reflectivity of the Bragg-like mirrors; however, coupling into the cavity will also be reduced. It is also suggested, by Foresi, that the increased microcavity radiation with increased number of holes saturates after approximately four holes. A comparison of Q against the number of holes is discussed in Fan, and reiterated in Appendix B.2.

Having asymmetrical number of holes on both sides of the microcavity will affect the input and output coupling into the waveguides. A reflection all-optical switch have been proposed theoretically, employing this concept [86].

r/a **ratio** The size of the band gap depends on the ratio of the hole radius r to lattice constant a, and also the dielectric constant of the waveguide material. For our waveguide, the band gap is approximately 28% of the midgap frequency (taken at starting of band edges[8]) for a r/a ratio of 0.46.

Reducing hole radius r will also increase the effective index of the photonic crystal. This reduces radiation losses, though confinement in the microcavity is also reduced. The number of holes can be increased for better confinement, although radiation will yet again increase. There exists therefore a trade-off on microcavity confinement and radiation losses.

Furthermore, reducing the hole radius r, or in general reducing the amount of lower dielectric material (in this case air) with respect to the higher dielectric material, will shift spectrum to lower frequencies. One can think of this as an "effective" refractive index – with less lower dielectric material, the effective refractive index increases, pulling down the guide asymptote in Figure 4-4 and correspondingly pulls down the defect state frequency.

[8]Taken at end of band edges, nearer to the resonance, the band gap is approximately 20% of midgap frequency.

Changes in the waveguide width w can be thought of along the same lines as the r/a ratio. Reducing the width decreases the ratio of higher dielectric material to lower dielectric material. The operating spectrum shifts to a higher frequency.

Waveguide thickness t_{Si} The transmission spectrum is strongly dependent on the waveguide thickness t_{Si}. A 15% increase in thickness increases the resonance wavelength by 50 nm, and shifts the spectrum on the same order of magnitude. Again, one can use an effective index concept to predict the trend. An increase in thickness increases the effective index of the photonic crystal (for a microcavity waveguide made of higher dielectric material than its surroundings). Referring to Figure 4-4, the "guide asymptote" line shifts down for a higher effective index, and the states correspondingly shifts downwards. The result is a lower frequency, or a longer wavelength, transmission.

Total Q and radiation Q

The total quality factor Q is a measure of the losses in a resonator cavity – in general terms, it is the power stored in a cavity divided by the power dissipated from the cavity. This is described as [164]

$$Q = \frac{\omega_o E}{P} \tag{4.16}$$

where ω_o is the center resonance frequency, E the stored energy in the cavity, and $P = \frac{dE}{dT}$ is the dissipated power. This translates to a resonator supporting Q oscillations before its energy decays by a factor of $e^{-2\pi}$ ($\sim 0.2\%$) of its original value. It is a measure of the total lifetime at which light leaks out of a cavity. For a Fabry-Perot, Q is represented as [44]

$$Q_{Fabry-Perot} = \frac{2\pi\sqrt{R}nl\cos\theta}{(1-R)\lambda} = \frac{\lambda}{\delta\lambda} \tag{4.17}$$

where R is the mirror reflectivity, l the cavity length, θ the incidence angle with respect to mirror normal, λ the center wavelength, and $\delta\lambda$ the full width wavelength at half-maximum (FWHM). The definition of Q as the ratio of center wavelength λ and FWHM $\delta\lambda$ is convenient in experimental characterization (with Q on order of several hundreds), given the high resolution in wavelength measurements for $\delta\lambda$. We will use this method for experimental determination of Q, as measured in Section 5.2.4 (page 120).

Light in the microcavity can leak into air or into the waveguide, and hence Q is related to its subcomponents by

$$\frac{1}{Q} = \frac{1}{Q_r} + \frac{1}{Q_w} \tag{4.18}$$

where radiation Q_r is the lifetime for light leaking into air and waveguide Q_w is the lifetime for light leaking into the waveguide. Q_r is an intrinsic property of the structure geometry, affected primarily by the broken translational symmetry rather than the broken mirror symmetry. In analogy with a Fabry-Perot, Q increases exponentially with increased number of

holes (which increases the reflectivity R). In addition, the peak transmission T at resonance is described by

$$T = \left(\frac{Q}{Q_w}\right)^2 = \left(1 - \frac{Q}{Q_r}\right)^2 \tag{4.19}$$

For high T (and low loss), therefore, Q_r must be $\gg Q$, or in other words, $Q \sim Q_w$. For the microcavity waveguide, Q is computed to be 180 [65].

Other thoughts

The microcavity waveguide is designed such that there is a large separation between the fundamental resonant mode and higher order modes. Using the Fabry-Perot analog, the small physical size of the microcavity (on the order of 0.6 to 0.7 μm for operation at 1.55 μm wavelengths) pushes the frequency separation of the modes up to 60 - 70 THz or free spectral range at 0.49 - 0.57 μm for normal incidence [44].

To further improve on the Bragg-like mirror reflectivities (and hence the Q), the oxide is further etched to extend the holes beyond the Si waveguide layer [27, 32]. This improves the field overlap with the holes. This thickness, denoted as $t_{SiO_{2,1}}$ in Figure 4-1, is on order of 0.3 μm.

In addition, absorption and scattering losses from actual waveguide material and fabrication are important considerations. Single-crystal silicon waveguides have the lowest losses (order of 10 - 30 dB/cm, depending on the Silicon-On-Insulator material and fabrication conditions) compared to poly-silicon or nitride waveguides [93, 32]. The waveguide sidewall roughness and top surface roughness are pertinent to determining the scattering losses in the dielectric waveguide.

4.4 Perturbation Theory On Maxwell's Equations For Shifting Material Boundaries

General perturbation theory for electromagnetism can be found in literature [136, 107]; perturbation on the medium permittivity ($\delta\varepsilon$) and/or permeability ($\delta\mu$) can be found in [142]. However, perturbation on the step-wise linear dielectric surface boundaries suffers from the following difficulties [66, 47]:

1. Since ε is a step function, the electric field perpendicular to the interface is discontinuous such that the first-order expansion of the electric field is finite even for an infinitesimal perturbation parameter $\Delta\alpha$.

2. Casting the problem in the magnetic field formulation, where magnetic fields are continuous, however, encounters another issue. The operation $\nabla \times \vec{H}$ is also discontinuous and not first-order in $\Delta\alpha$.

3. We can finally transform the coordinate system such that the boundary moves; however, such transforms are cumbersome to apply for arbitrary surfaces.

The perturbation analysis in this Section is anchored from a general method proposed by Johnson *et. al.* [66] – using a limit of systems with anisotropic smoothed boundaries. We summarize here the derivation and methodology before presenting our perturbation results.

The single formulation for electric field, Equation 4.5, can be thought of as an eigenproblem with basis-independent ket states $|E>$ following Dirac's notation [24]. For a small perturbation $\Delta\alpha$, we expand eigensolutions $|E>$ as $|E>=\sum_{n=0}^{\infty}\ |E^{(n)}>$ and ω as $\omega=\sum_{n=0}^{\infty}\ \omega^{(n)}$ [19], where $|E^{(0)}>$ and $\omega^{(0)}$ is the unperturbed eigensolution. The first-order perturbation in the limit of infinitesimal $\Delta\alpha$ is expressed in the below exact expression

$$\frac{d\omega}{d\alpha}=-\frac{\omega^{(0)}}{2}\frac{\left\langle E^{(0)}\left|\frac{d\varepsilon}{d\alpha}\right|E^{(0)}\right\rangle}{\langle E^{(0)}\mid\varepsilon|\,E^{(0)}\rangle} \tag{4.20}$$

This is the Hellman-Feyman theorem [19]. Taking higher-order derivatives of both the eigenvalue and eigenfields, we can similarly extract exact expressions for higher-order perturbation. The top integral on the right-hand side of Equation 4.20 is a surface integral over the interface (including the perturbation) described as

$$\left\langle E^{(0)}\left|\frac{d\varepsilon}{d\alpha}\right|E^{(0)}\right\rangle=\int dA\frac{dh}{d\alpha}(\varepsilon_1-\varepsilon_2)|\vec{\mathrm{E}}^{(0)}|^2 \tag{4.21}$$

The bottom integral is a surface integral on the unperturbed solution.

To evaluate the top integral for step-wise dielectric boundaries, however, the discontinuities mentioned above appears. To get around this problem, Johnson *et. al.* proposed a *smooth* transition between boundary of the two materials, ε_1 and ε_2, and then taking the infinitesimal limit of the smoothing transition. The smoothing is anisotropic (following the idea of an "effective" medium) and described by an dielectric tensor

$$\varepsilon_s(x)\equiv\begin{pmatrix}\tilde{\varepsilon}(x) & & \\ & \bar{\varepsilon} & \\ & & \bar{\varepsilon}\end{pmatrix} \tag{4.22}$$

where $\bar{\varepsilon}$ is from an isotropic smoothing for $\vec{\mathrm{E}}_{||}$ (in-plane of interface) and $\tilde{\varepsilon}$ a harmonic mean smoothing for $\vec{\mathrm{E}}_{\perp}$ (perpendicular to interface plane). $\bar{\varepsilon}$ is defined as [66]

$$\bar{\varepsilon}(x)\equiv\int g_s(x-x')\ \varepsilon(x')dx' \tag{4.23}$$

where g_s is a smoothing function around $x=0$ that goes to a Dirac delta function as $s\rightarrow 0$. This gives $d\bar{\varepsilon}/dh=(\varepsilon_1-\varepsilon_2)g_s(x-h)$. In addition, $\tilde{\varepsilon}$ is defined as

$$\tilde{\varepsilon}(x)^{-1}\equiv\int g_s(x-x')\ \varepsilon(x')^{-1}dx' \tag{4.24}$$

This gives $d\tilde{\varepsilon}/dh = -\tilde{\varepsilon}(x)^2(\varepsilon_1^{-1} - \varepsilon_2^{-1})\ g_s(x-h)$. The combined contribution of both $\bar{\varepsilon}$ and $\tilde{\varepsilon}$ for $\left\langle E^{(0)} \left| \frac{d\varepsilon}{d\alpha} \right| E^{(0)} \right\rangle$ gives, after some algebra, the following

$$\left\langle E^{(0)} \left| \frac{d\varepsilon_s}{d\alpha} \right| E^{(0)} \right\rangle = dA\ \frac{dh}{d\alpha} \int dx \left[\ \Delta\varepsilon_{12} \left|\vec{\mathrm{E}}_{||}^{(0)}\right|^2 - \Delta(\varepsilon_{12}^{-1}) \left|\tilde{\varepsilon}\vec{\mathrm{E}}_{\perp}^{(0)}\right|^2\ \right] g_s(x-h) \tag{4.25}$$

where $\Delta\varepsilon_{12} \equiv \varepsilon_1 - \varepsilon_2$ and $\Delta(\varepsilon_{12}^{-1}) \equiv \varepsilon_1^{-1} - \varepsilon_2^{-1}$. The fact that $\tilde{\varepsilon}\vec{\mathrm{E}}_\perp$ ($= \vec{\mathrm{D}}_\perp$) is continuous now gives a well-defined result for $s \to 0$. Taking this limit, we have

$$\left\langle E^{(0)} \left| \frac{d\varepsilon}{d\alpha} \right| E^{(0)} \right\rangle = \int dA\ \frac{dh}{d\alpha}\ \left[\ \Delta\varepsilon_{12} \left|\vec{\mathrm{E}}_{||}^{(0)}\right|^2 - \Delta(\varepsilon_{12}^{-1}) \left|\vec{\mathrm{D}}_{\perp}^{(0)}\right|^2\ \right] \tag{4.26}$$

This permits us to evaluate first-order perturbation on shifting material boundaries, given that we know: (i) $\vec{E}_{||}^{(0)}$ and $\vec{D}_{\perp}^{(0)}$ at every location of interest and, (ii) $dh/d\alpha$ at the interface of interest. We proceed to derive the fields at every location of interest (Section 4.4.1), and compute $dh/d\alpha$ analytically as described in Section 4.4.2. An overview of the computational scheme is illustrated in Appendix B.3 (Figure B-3). For higher-order perturbation and non-waveguide problems, careful selection of the basis expansions are required [66]. This first-order perturbation method is general and can be applied to cases such as adiabatic coupling, surface roughness and tapered waveguide geometries.

4.4.1 Finite-difference time-domain results

The general procedure for finite-difference time-domain computations involves approximating Maxwell's equations in real space using finite difference discretization, imposing appropriate boundary conditions, and then explicitly stepping forward in time [85]. While this method tends to be more numerically accurate than an effective index [142] or beam propagation method [54], it is typically computationally expensive. We thus employ a relatively coarse[9] 3D FDTD computation performed by Johnson [65] and interpolate the fields between the calculated nodes. Moreover, with the interpolated FDTD, we can now find the E-fields at specific locations, such as along the circular hole boundary, as required by Equations 4.20 and 4.26. An example of the interpolation is shown in Figure 4-6 for five interpolated points between the FDTD calculated nodes. This example is also on one unit cell of the photonic crystal waveguide for $\mathrm{E}_{real,\hat{z}}$, the E-field (real) in the $\hat{z}$ direction (along waveguide propagation). When repeated for the whole photonic crystal and using 40 interpolated points between the FDTD calculated nodes, the $\mathrm{E}_{real,\hat{z}}$ is illustrated in Figure 4-7. There is strong confinement at the cavity – the modal volume is 0.055 μm^3 [33], less than half a cubic half-wavelength ($\frac{1}{2}\left(\frac{\lambda}{2}\right)^3$). There is also a node at the center of the cavity, as expected from the pulling down of the state from the second band.

[9] Discretization is at 10 pixels per lattice constant a.

This result is then used to find the $E_{||}$ and $D_{\perp}$ profiles along the circular hole boundaries, as illustrated in Figure 4-8. The horizontal axis is the discretized points (total of 360) along the hole circumference. These profiles are then used to compute the first-order perturbation from shifting material boundaries, with the results summarized in Section 4.4.3. We now proceed to determine the shift in the material boundary for a given perturbation: $dh/d\alpha$.

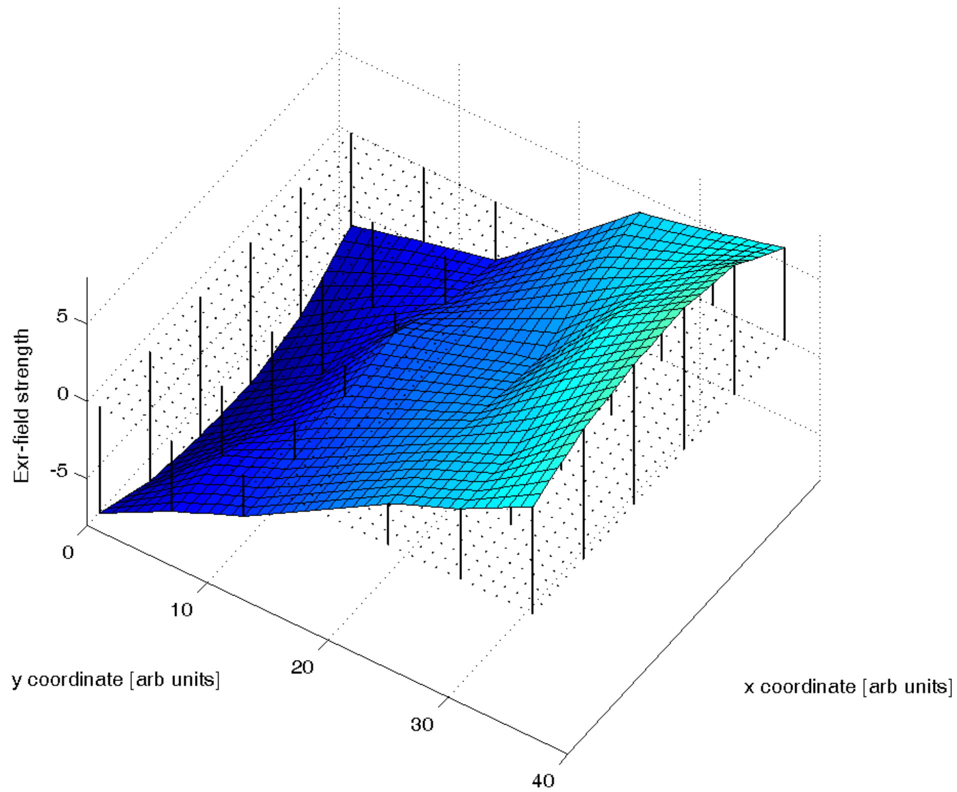

Figure 4-6: Interpolated $E_{real,\hat{z}}$ field for one unit cell of the photonic crystal waveguide. The columns are from a coarse 3D FDTD computation by Johnson [65]. The interpolated result is the surface defined by the columns.

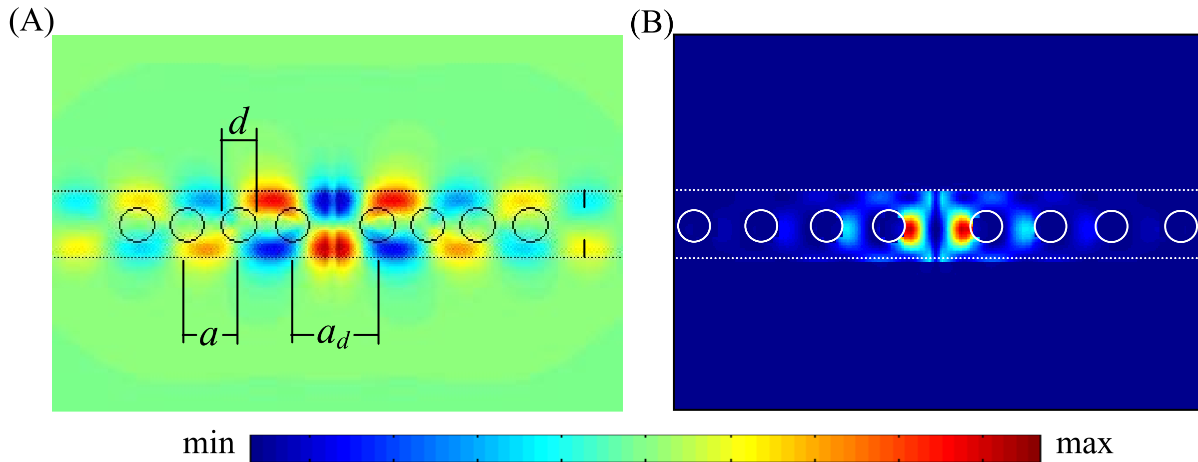

Figure 4-7: (A) Unperturbed interpolated $E_{real,\hat{z}}$ field (color plot) at middle slice of waveguide, (B) Energy density distribution (color plot) at same middle slice. Design parameters are $a_d = 1.50a$, $w = 1.19a$, $t_{Si} = 0.44a$, air-cladded Si "air-bridge" waveguide, and with 4 holes on each side of cavity. Resonance found at 0.2625 c/a and Q at 180.

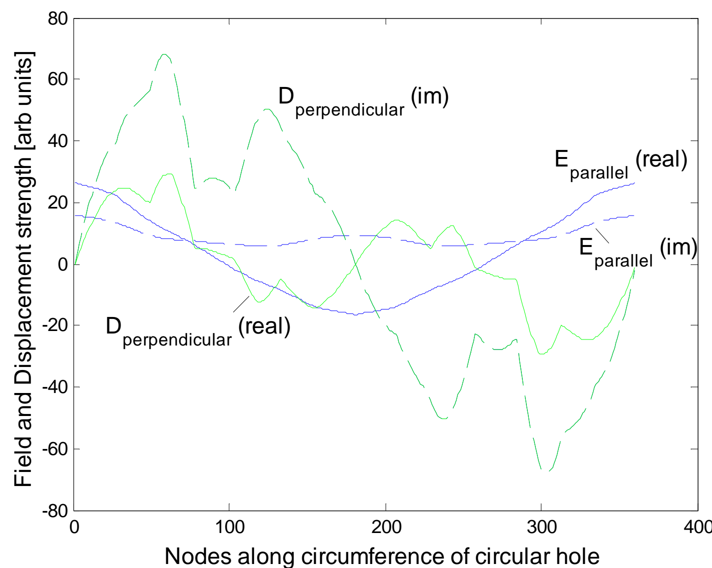

Figure 4-8: Example of interpolated $E_{||}$ and $D_{\perp}$ profiles along one hole circumference of the photonic crystal waveguide. The x-axis is the discretized points (total of 360) along the hole circumference.

4.4.2 Mechanics of circular hole deformation

To determine $dh/d\alpha$ we require the material displacements (dh) for each applied perturbation ($d\alpha$). Our problem resembles the hole-in-a-plate scenario in elasticity theory. Beginning with the stress components reported in literature, we will derive the material displacements from material compatibility and Hooke's constitutive equations for elastic plane stress.

Specifically, the stress function in polar coordinates is of the following form for circular holes in plates [145]

$$\phi = \left(Ar^2 + Br^4 + C\frac{1}{r^2} + D\right)\cos 2\theta \tag{4.27}$$

where A, B, C and D are integration constants determined from boundary conditions, and r the radial location from hole center. We note that the stress function is assumed free from discontinuities. The stress function provides the following normal and shear stress components when the integration constants are determined

$$\sigma_r = \frac{1}{r}\frac{\partial\phi}{\partial r} + \frac{1}{r^2}\frac{\partial^2\phi}{\partial\theta^2} = \frac{S}{2}\left(1-\frac{a^2}{r^2}\right) + \frac{S}{2}\left(1+\frac{3a^4}{r^4}-\frac{4a^2}{r^2}\right) \tag{4.28}$$

$$\sigma_\theta = \frac{\partial^2\phi}{\partial r^2} = \frac{S}{2}\left(1+\frac{a^2}{r^2}\right) - \frac{S}{2}\left(1+\frac{3a^4}{r^4}\right)\cos 2\theta \tag{4.29}$$

$$\tau_{r\theta} = \frac{1}{r^2}\frac{\partial\phi}{\partial\theta} - \frac{1}{r}\frac{\partial^2\phi}{\partial r\,\partial\theta} = -\frac{S}{2}\left(1-\frac{3a^4}{r^4}+\frac{2a^2}{r^2}\right)\sin 2\theta \tag{4.30}$$

where σ_r is the normal stress in the radial direction $\hat{r}$ as illustrated in Figure 4-9, σ_θ the normal stress in the circumferential direction $\hat{\theta}$, $\tau_{r\theta}$ the shear stress, S the uniformly applied tension magnitude, and a the hole radius.

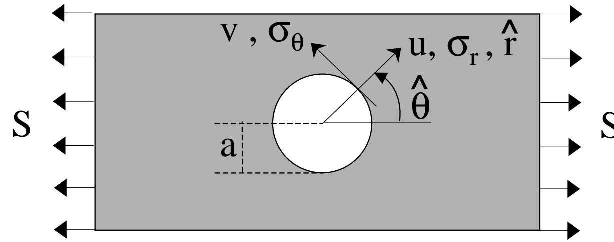

Figure 4-9: Nomenclature of circular hole deformation.

The above stress components are related to strain components through Hooke's constitutive equations for plane stress. The strain components, in turn, gives us the material displacements (through the compatibility equation for elastic deformation within a body, i.e. without cracks or overlaps) as

$$\frac{\partial u}{\partial r} = \varepsilon_r = \frac{1}{E}\left(\sigma_r - \nu\sigma_\theta\right) \tag{4.31}$$

$$\frac{u}{r} + \frac{\partial v}{r\partial\theta} = \quad \varepsilon_\theta \quad = \frac{1}{E}\left(\sigma_\theta - \nu\sigma_r\right) \tag{4.32}$$

$$\frac{\partial u}{r\partial\theta} + \frac{\partial v}{\partial r} - \frac{v}{r} = \quad \gamma_{r\theta} \quad = \frac{1}{G}\,\tau_{r\theta} \tag{4.33}$$

where u is the material displacement normal to interface, v the material displacement tangential to interface, ε_r the $\hat{r}$ strain, ε_θ the $\hat{\theta}$ strain, $\gamma_{r\theta}$ the shear strain in $\hat{r}\hat{\theta}$, E the Young's modulus, G the shear modulus, and ν the material Poisson ratio.

We substitute Equations 4.28 – 4.30 into the above equations. After some algebra, we simplify the resulting second-order ordinary differential equation (that has 40^+ terms) taking the hint that the material displacements should be free from discontinuities. Boundary conditions of $v = 0$ at $\theta = 0$ and $u = 0$ at $\theta = \pi/4$ are used. The solution of the material displacements u and v is derived to be of the following form

$$u = \frac{1}{E}\left[\frac{S}{2}\left(1 - \frac{a^4}{r^3} + \frac{4a^2}{r}\right)\cos 2\theta + \frac{\nu S}{2}\left(1 - \frac{a^4}{r^3}\right)\cos 2\theta\right] \tag{4.34}$$

$$\begin{aligned} v = & \frac{r}{E}\left[\frac{S}{2}\left(1 + \frac{3a^4}{r^4}\right)\frac{\sin 2\theta}{2} + \frac{\nu S}{2}\left(1 + \frac{3a^4}{r^4} - \frac{4a^2}{r^2}\right)\frac{\sin 2\theta}{2}\right] + \\ & \frac{1}{E}\left[\frac{S}{2}\left(1 - \frac{a^4}{r^3} + \frac{4a^2}{r}\right)\frac{sin2\theta}{2} + \frac{\nu S}{2}\left(1 - \frac{a^4}{r^3}\right)\frac{\sin 2\theta}{2}\right] \end{aligned} \tag{4.35}$$

u and v from Equations 4.34 and 4.35 are partial components of h in Equation 4.26 at each applied perturbation S (or α in Equation 4.26) for every location (r,θ) in each unit cell of the photonic crystal waveguide. (To find h completely for the entire photonic crystal waveguide, we also included translation at each of the holes and at the defect to get the final results of Section 4.4.3.) While our scenario would be most accurately described with a possible "hole-in-a-bar" model due to the width of the waveguide approximately three times the hole diameter, the hole-in-a-plate scenario provides an estimate with discrepancies expected on order of ten percent [10]. The discrepancies can also be thought of being reflected in the numerical coefficients of the stress function (Equation 4.27), while the general form of the stress function is preserved.

Figure 4-10 shows the resulting shape of the hole under a non-dimensional (S/E) applied stress of 0.2; Figure 4-11 shows displacements u and v for the same applied stress. With the hole displacements obtained, we can thus proceed with computing the effect of strain perturbation on the microcavity waveguide.

[10] With a width four times of the hole diameter, Timoshenko estimates an error of 6% using the hole-in-a-plate scenario [143]. The error is because the boundary conditions are based on Saint-Venant's principle that the change is negligible at distances large compared to the hole radius.

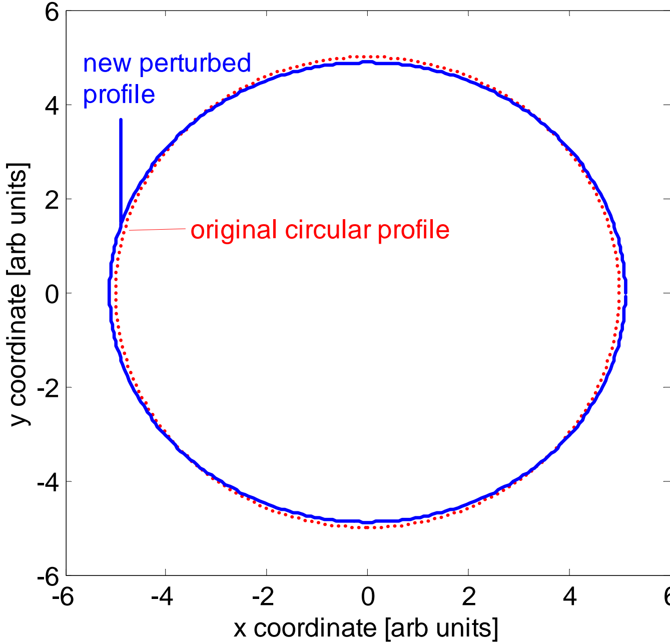

Figure 4-10: Shape profile of holes under perturbed non-dimensional stress (S/E) of 0.2 .

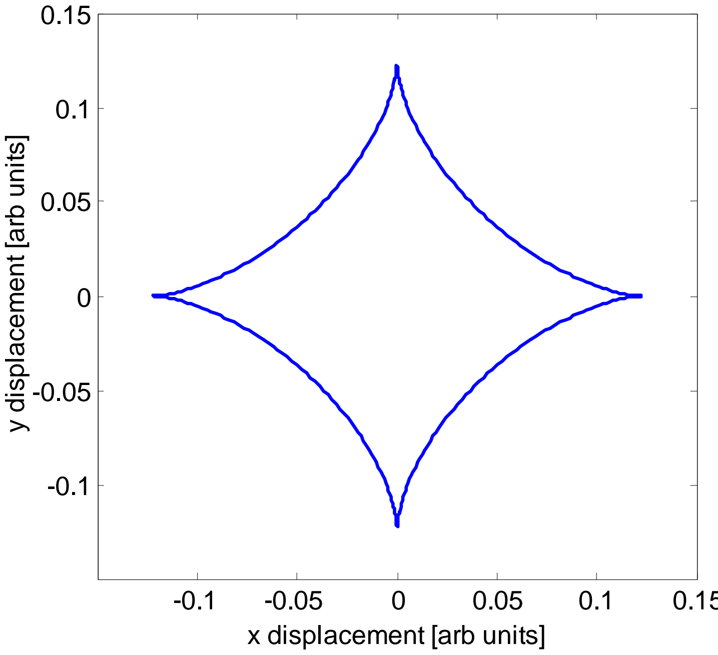

Figure 4-11: Hole material displacements for perturbed non-dimensional stress (S/E) of 0.2 .

4.4.3 Perturbation analysis

We started by computing the top integral described by Equation 4.26 : the interpolated $E_{||}$ field and $D_{\perp}$ FDTD profiles along the circular hole interface is described in Section 4.4.1, and the material displacements on a hole for a given perturbation α (or applied stress S) is analyzed in Section 4.4.2. To account for the entire photonic crystal waveguide, we include translation, in addition to ellipticity, of the microcavity and holes with zero displacement at the center of the microcavity due to symmetry. This is evident in Figure 4-12. h is thus found. $dh/d\alpha$ is then obtained by taking the numerical derivative at each α. We now include both $dh/d\alpha$ and the interpolated $E_{||}$ and $D_{\perp}$ profiles through Equation 4.20 to compute $d\omega/d\alpha$.

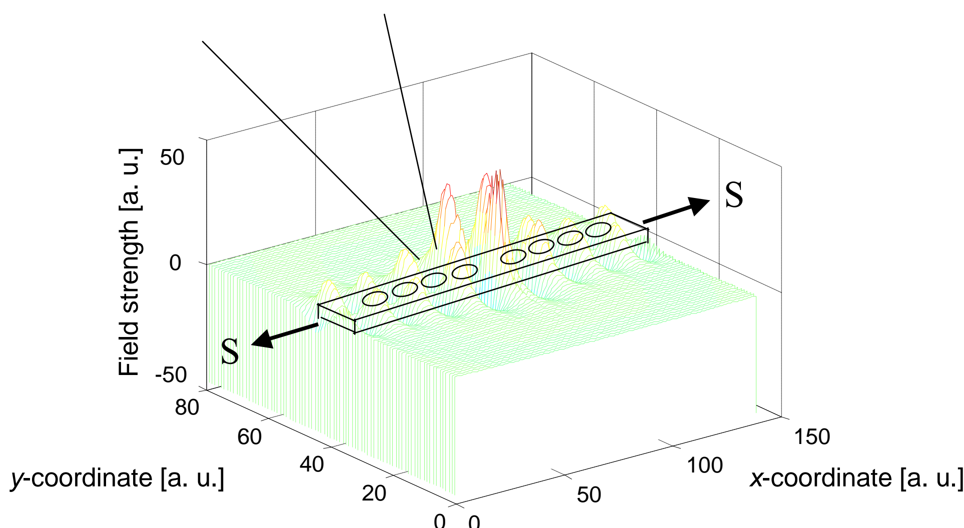

Figure 4-12: Schematic depicting the summation over the entire photonic crystal waveguide. Translation and ellipticity effects of the microcavity and holes are both required. The field plotted is $E_{x,}$ (real) at the middle slice of the waveguide.

2D computation The change in the resonant wavelength against the mechanical strain, for the various mechanical strain effects, is summarized in Figure 4-13 for a 2D computation. Positive strain denotes tension in the photonic crystal. The 2D computation is taken at the middle slice (in the $\hat{x}$ direction) of the microcavity waveguide. The change in resonant wavelength is divided into the mechanical strain effects due to: (1) change in defect size, (2) change in lattice constant (hole position shift), and (3) ellipticity of the holes. Both changes in the defect size and the lattice constant contribute positively to the change in resonant wavelength. The elliptical nature of the holes contributes negatively to the net wavelength

shift. Moreover, as expected, the wavelength change is linear with respect to the applied strain due to the small perturbation of less than 0.5%. For a +0.2% strain (tensile), a 6.50 nm (0.56%) increase in the wavelength is expected for resonance at 1.55 μm.

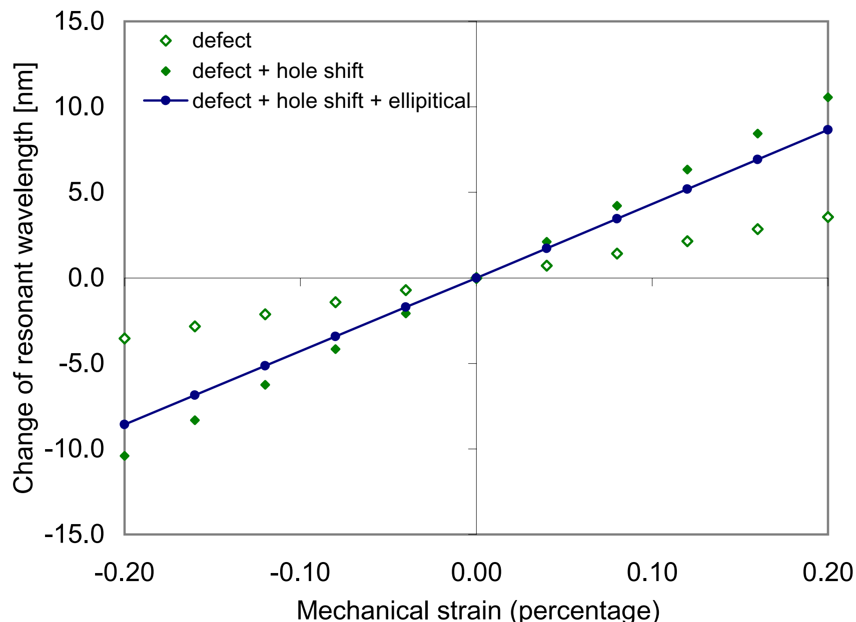

Figure 4-13: Change in resonant frequency against mechanical strain for 2D perturbation computation. The mechanical strain effects is divided into: (1) change in the defect size, (2) change in the lattice constant, and (3) ellipticity of the holes. For a +0.2% strain (tensile), a 8.67 nm (0.56%) increase in the resonance wavelength is expected.

3D computation A full 3D computation is next performed. Likewise, both changes in defect size and lattice constant contributes positively to the resonant wavelength change, while ellipticity reduces the net effect. For a +0.2% strain (tensile), a 8.46 nm (0.55%) increase in wavelength is expected for resonance at 1.55 μm. Comparison between the 2D and 3D computations has only a 2.4% difference in the net resonant wavelength change, although the contributions by each of the mechanical strains effects are different. In the 2D computation, change in the lattice constant is a large contributing factor; in the 3D computation, the strain at the defect plays a major role as expected from a Fabry-Perot analogy. As expected from the Fabry-Perot analogy[11], the resonance changes to longer wavelengths for positive (tensile) strain since the major effect is from the defect length.

[11]Another way to think about the increase in defect length is the addition of higher refractive index material to the cavity, resulting in lower frequency and higher wavelength resonances.

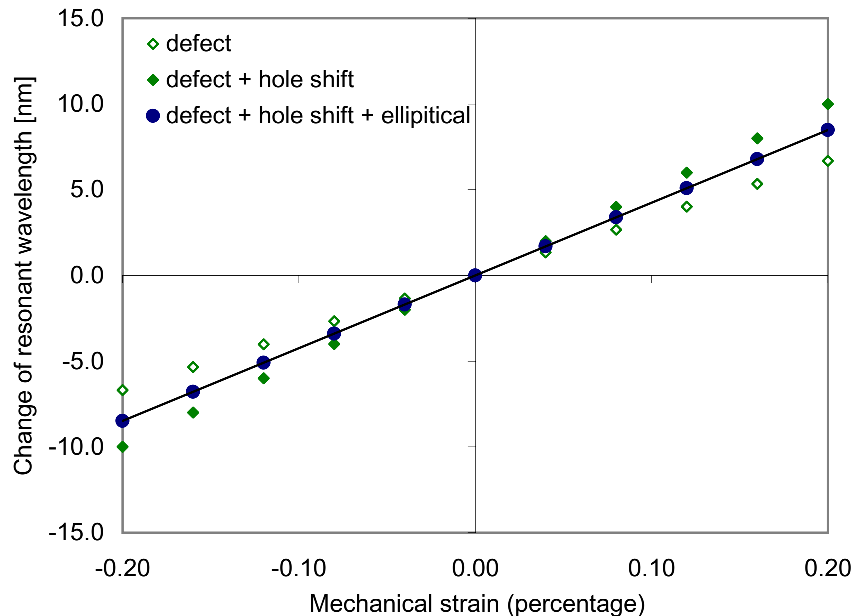

Figure 4-14: Change in resonant frequency against mechanical strain for a 3D perturbation computation. For a +0.2% strain (tensile), a 8.46 nm (0.55%) increase in the resonance wavelength is computed.

Numerics The fineness of the interpolation was tested by continually decreasing the mesh size, until an asymptotic limit of the final result is observed. For the integral of Equation 4.26, mesh sizes between 360 and 1080 were used in the circumference, with the maximum disparity at 0.25% fractional difference. For the bottom integral on the right-hand side of Equation 4.20, interpolation nodes between 5 nodes to 40 nodes were used (between the FDTD results), with final results differing by less than 2.5% fractional difference.

Tuned spectra The tuning of the resonant frequency is summarized in Figure 4-15, where both the original and perturbed transmission spectra under 0.2% mechanical strain are plotted. Only the perturbed transmission near resonance is shown because the FDTD fields employed in the perturbation theory ($\vec{E}_{||}$ and $\vec{D}_{\perp}$) are calculated at the resonant frequency. Perturbation at the band edges can also be found if the fields at the band edges can be found with certainty.

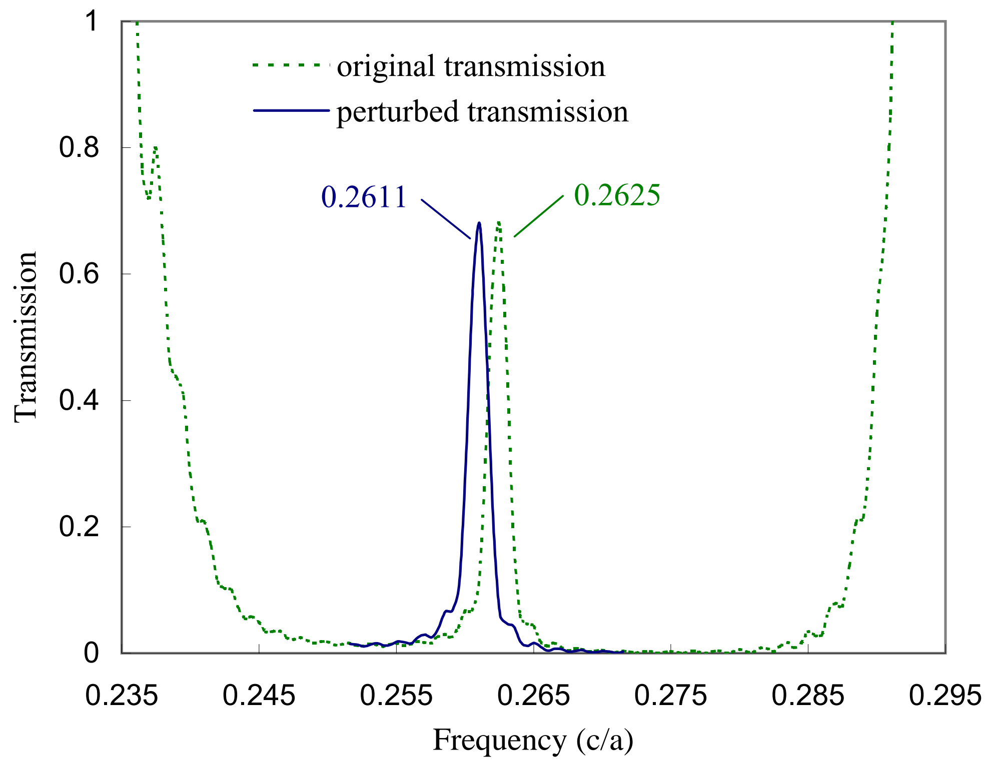

Figure 4-15: Perturbed transmission from 0.2% applied strain in comparison with the original transmission.

4.5 Other Considerations

4.5.1 Photoelastic Pockels effect

Changes in the refractive index δn for an applied strain ε (or stress) is described through the photoelastic Pockels effect or stress birefringence as [129]

$$\delta n = -\frac{1}{2}\, \wp\, n^3 \varepsilon \tag{4.36}$$

where $\wp$ is the photoelastic coefficient and n the refractive index (at 3.48 for silicon at 1.552 μm wavelength). The photoelastic coefficient for <100> silicon is found as $2.89 \times 10^{-5}\ E\varepsilon$ where E is the Young's modulus [36]. Combining this with Equation 4.36, δn therefore scales as ε^2. Moreover, for a small index change δn the frequency shift δf is described by [27]

$$\delta f = \left(\frac{1}{1 + \frac{\sigma \delta n}{n}} - 1 \right) f^{(o)} \tag{4.37}$$

where $f^{(o)}$ is the unperturbed resonant frequency and σ the fraction of the mode located inside the higher dielectric of the microcavity waveguide. For small $\delta n/n$,

$$\frac{\delta f}{f^{(o)}} = -\frac{\delta \lambda}{\lambda^{(o)}} \sim -0.8\ \frac{\delta n}{n} \tag{4.38}$$

for σ estimated at 0.80 [27]. Therefore, for an applied strain ε of +0.1%, δn is -9.78×10^{-5} which gives $\delta\lambda$ at -0.04 nm. For ε of 0.3%, $\delta\lambda$ is -0.32 nm. This shift in wavelength is small compared to strain perturbation computed in Section 4.4. We also note that Equation 4.37 describes the changes in resonant frequency for electro-optic effects: with $\delta n/n$ on order of 0.1%, $\delta f/f^{(o)}$ is estimated at -0.08%.

4.5.2 Bending losses in waveguide

Losses associated with bends in waveguides are important considerations for integrated optics, arising from a phase mismatch between the E-field in the core and the E-field in the cladding [106, 93, 32]. In our device, the bow in the membrane when the piezoelectric material is actuated results in an out-of-plane bend of the waveguide. This bend has a radius of curvature of order 5000 μm. This is illustrated in the finite-element ADINA model of Figure 4-16, wherein the bow is amplified for visual clarity. For a loading stress of 140 MPa (0.1% strain), there is a 16 nm relative (from one side to the other side of waveguide) out-of-plane displacement for the 8 μm region of waveguide investigated.

The loss through waveguide bends, α, for the fundamental TE mode, can be described with [88]

$$\alpha = \frac{\alpha_x^2 \lambda_1}{\pi(\alpha_x d + 2)} \cos^2\left(\frac{k_{2x} d}{2}\right)\ e^{\alpha_x d}\ e^{-2\alpha_x (k_z - k_1) R / k_1} \tag{4.39}$$

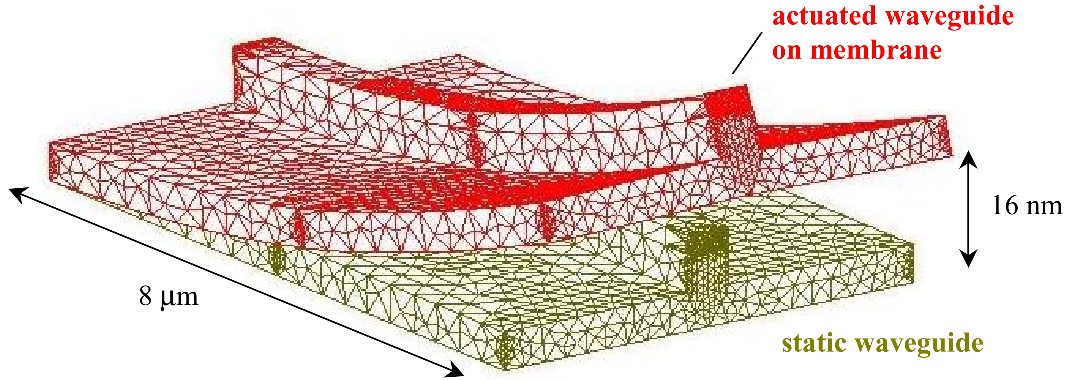

Figure 4-16: Finite-element mesh of microcavity waveguide, showing bow in the waveguide. For a loading stress of 140 MPa (0.1% strain), there is a 16 nm relative out-of-plane displacement for the 8 μm region of waveguide investigated. Displacement is amplified for visual clarity.

where the subscripts 1 denote the cladding region and 2 the waveguide core respectively, R the radius of curvature, d the waveguide width, and $\alpha_x d$ related as

$$\alpha_x d = \sqrt{v^2 + 1} - 1 \tag{4.40}$$

with $v^2 = k_1^2 d^2 (\frac{n_2^2}{n_1^2} - 1)$. The wavenumbers k_1 and k_2 and absorption α_x is found from dispersion relations

$$k_1 = \omega \sqrt{\mu \varepsilon_1} \tag{4.41}$$

$$\alpha_x = \sqrt{k_x^2 - \omega^2 \mu \varepsilon_1} \tag{4.42}$$

$$k_{2x} = \sqrt{\omega^2 \mu \varepsilon_2 - k_z^2}. \tag{4.43}$$

The result is an exponential dependence of α on radius of curvature R. With the predicted radius of curvature on the order of 5000 μm, the loss is significantly less than 0.01 dB in high-index contrast Si waveguides, negligible compared to roughness scattering losses [90] as expected. The bend in our microcavity photonic crystal waveguide, however, could conceivably increase the coupling to the radiation modes.

4.5.3 Limiting strain and stress concentration

Limiting strain Applied strain on the microcavity waveguide leads to increased stresses on the single-crystal silicon material, both at the holes and the interface between the silicon

and the buried oxide. The fracture toughness of silicon is low (less than 1 MPa·m$^{1/2}$ [17]) which implies strong sensitivity of strength to processing-induced flaws or cracks [127]. The limiting strain is thus a concern. The limiting strain at room temperature is largely defined by the material surface roughness in the region of the largest applied stresses. As is conventional for brittle materials, the strength is reported in terms of Weibull statistics. For micromachined structures, Chen [16, 15] reports the Weibull reference strength of 4.6 GPa for surface roughness of 0.3 μm and 1.2 GPa for surface roughness of 3 μm. For roughness on order of 0.1 μm, Chen reports the strength greater than 4 GPa, limited by the measurement range of the test setup. Our estimated roughness for our microcavity waveguide is on order of 20 nm for the sidewalls and 1 nm for the top surface. With an applied strain of 0.1% (limited by the current piezoelectric actuator design), the applied stress at the holes is $\sim$ 200 MPa (depending on the material properties and crystalline orientation) and therefore below the Weibull reference strengths reported. The appropriate limiting strain for the device, however, is strongly dependent on any sharp corners (such as through anisotropic KOH etching on the wafer backside) or cracks that might result from device processing.

Materials other than single-crystal silicon are also possible for the microcavity waveguide, although the index contrast and optical losses needed to be considered in the selection. The use of polysilicon will allow a yield strain on order of 0.7% [133], while the use of polymer waveguides (such as poly(p-phenylenevinylene)-silica composites or polyalkylsilyne) will permit an estimated strain up to a few percent [48, 51].

Stress concentration at interface The applied stress on the microcavity waveguide also induces an increased interface stress between the Si waveguide and the oxide insulator ridge. Figure 4-17 shows the finite-element modeling on the microcavity waveguide on an oxide "ridge" under 200 MPa loading stress (0.12% strain). The maximum interface stress is $\sim$ 810 MPa, located at the interface between the two layers. The minimum stress is located at the center of the microcavity. It is difficult, however, to gauge the possibility of delamination of the thin-film Si waveguide, as the specific experimental data is highly dependent on the presence of cracks[12]. The double-anchored membrane is therefore designed such that the input and output facets of the waveguides, a source of cracks during sample cleaving, are placed away from stress concentration regions such that no additional stress is observed at the facets during piezoelectric actuation.

[12]On the contrary, bond toughness data is readily available.

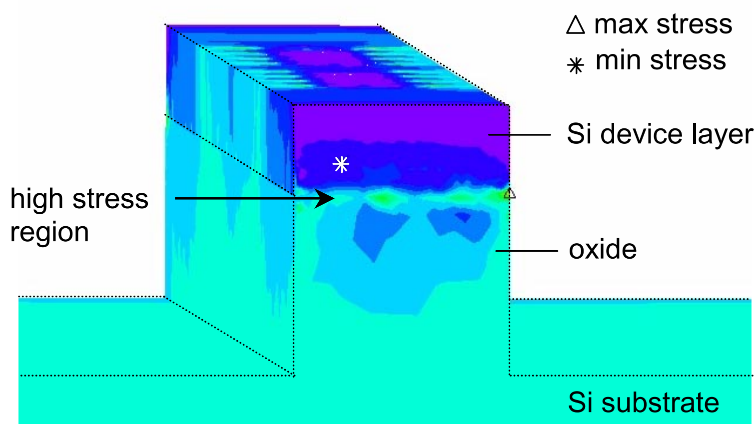

Figure 4-17: Finite-element mesh of microcavity waveguide, under 200 MPa loading stress. The maximum interface stress, between the Si device layer and oxide, is ∼ 810 MPa.

4.6 Summary

We began this chapter by describing the strain-tuning platform for microphotonics, along with a review of the concept and design of the microcavity waveguide. First-order semi-analytical perturbation theory is then employed to compute the changes in the transmission spectrum for an applied strain to the microcavity. This required fields along specific boundaries and regions derived from an initial FDTD computation, and analytical material displacements of circular holes derived from classical mechanics. From a full 3D computation, the perturbation shift in the resonance wavelength is predicted at 0.82% for a 0.3% mechanical strain. We also considered photoelastic effects, limiting strain, bending losses in the device design. The next chapter discusses the physical realization of the device, along with experimental comparisons to theory.

Chapter 5

Nanofabrication And Experiment Of Strain-Tunable Photonic Band Gap Microcavity Waveguide

If a man will begin with certainties,
he shall end in doubts;
but if he will be content to begin with doubts
he shall end in certainties.
– Sir Francis Bacon (1561 - 1626).

This chapter presents the detailed fabrication and experimental results of the strain-tunable microcavity waveguide. Device fabrication incorporates nanolithography of the photonic crystal with thin-film piezoelectric microactuators, while optimizing the process for high-transmission silicon waveguides and good-quality piezoelectric films. Experimental characterization demonstrates, for the first time, the dynamic tuning of microcavity resonances in response to an applied strain. This suggests the generalization to tunable silicon microphotonic devices, based on the concept of the deformable membrane platform.

5.1 Nanofabrication

The scale-invariance of Maxwell's equations suggest that a microcavity waveguide with lattice constant a at 2 μm gives a resonance wavelength on order of a few μm. This microwave regime is more difficult for measurement compared to the optical regime. Instead, if a is on order of 400 nm, resonance will be around 1.55 μm optical telecommunication wavelengths where detectors and sources are more readily available[1]. To achieve a on order of

[1] In a sense, choosing the smaller length-scale of a few hundred nanometers shifts the burden of difficulty to the device fabrication instead of device measurement, with the current technologies available.

several hundred nanometers, the minimum feature size is approximately 130 nm. Fabrication schemes possible to reach this length-scale include: deep-ultraviolet optical lithography, direct electron-beam writing, extreme-ultraviolet, ion beam lithography, or X-ray lithography. We employ the X-ray and electron-beam lithography tools available at the MIT Nanostructures Systems Laboratory of Prof. H. I. Smith. In this section, we discuss the overall fabrication process of the device strain-tunable microcavity waveguide, X-ray and electron-beam lithography results, a new PZT process, and a Si membrane release procedure.

5.1.1 Overall process flow and integration considerations

The fabrication process has three major milestones: (1) aligned X-ray lithography along with waveguide processing for optical resonance detection with low transmission losses (Section 5.1.3, (2) integrated thin-film PZT processing with repeatable results given the high material cost of specialized wafers for optical waveguides (Section 5.1.2), (3) high yield membrane release with Si on top of membrane (Section 5.1.4). PZT processing is designed before the X-ray lithography so that any yield issues with PZT processing will be shifted upstream and dealt with before X-ray waveguide processing and membrane release. This however requires etching of the PZT before annealing, as PZT cannot be annealed on top of a bare Si layer nor is there a reliable protective layer[2] which can be cleanly removed without attacking the 200 nm Si device layer. Membrane release possibilities include front-side XeF_2 etching or bulk KOH micro-machining from the backside. A combination of these two can be used to release a membrane with remaining Si for structural support against the oxide. Figure 5-1 diagrams the fabrication process.

The beginning substrate is a Silicon-On-Insulator Unibond wafer from SOITEC, chosen for low-loss transmission [93, 32]. The desired silicon device thickness is 184 nm, for resonance at 1.55 μm. Given the specialized wafers are single-side polished, we begin with a chemical mechanical processing step on the backside. PECVD silicon nitride is then deposited and patterned on the backside to permit the possibilities of using KOH bulk micromachining. The silicon device layer on the frontside is then etched to form the trenches for the thin-film PZT actuators. Subsequently, the bottom electrode is deposited with evaporation and lift-off processing. Thin-film PZT is then coated, dried and heated at 350 C for pyrolysis, but left unannealed. Wet-etching is then employed to pattern the PZT before annealing at 650 C. A Pt/Ti top electrode is then deposited with evaporation and lift-off processing. Oxide is reactive ion etched away at selective areas to permit a XeF_2 release later in the processing. X-ray nanolithography is then employed to pattern PMMA with 130 nm minimum features. Cr is evaporated and lift-off to form a hard mask for silicon etching to define the microcavity waveguide. After the silicon etching, the hard mask is removed with a Cr etchant. Resist is patterned above the waveguide to protect it from an eventual XeF_2 etch. The wafer is

[2]The most possible candidate is silicon nitride to protect the Si when annealing PZT; however, dry or wet etches to remove the nitride will attack the 200 nm Si device layer, wherein the thickness is crucial to the guided mode wavelength.

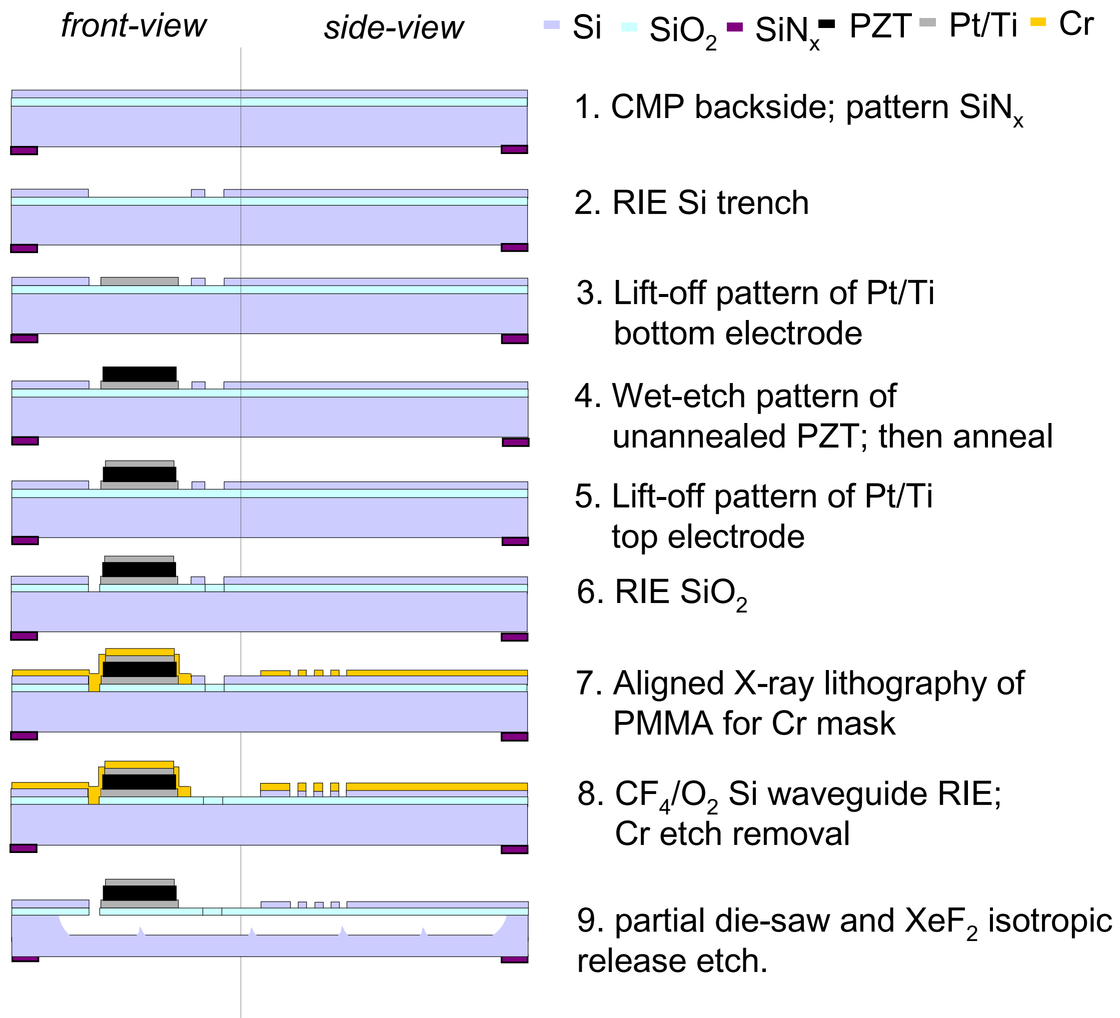

Figure 5-1: Fabrication process flow schematic of strain-tunable photonic crystal waveguide.

then partially die-sawed to allow eventual easy cleaving without breaking the membranes. A XeF_2 dry-etch is used to release the membrane, and the wafer cleaved to access the waveguide facets. Processing details are listed in Appendix C.1. We describe results of PZT processing, X-ray lithography, and membrane release in the following sections.

5.1.2 PZT processing for integrated microactuators

We develop a new processing technology – that of etching the PZT film before annealing – in order to satisfy the process flow requirements that the PZT processing does not affect the 200 nm Si device layer on the SOI wafer. The electrodes are evaporated, instead of sputtered, and patterned with lift-off instead of reactive ion etching. We also employ wet-etching for a quick turn-around time and which does not require extensive equipment as in the case of dry etching. However, wet etching might lead to large undercuts beneath the resist. The undercut issue is solved with proper selection and processing of the resist, and optimizing different etch times and solution concentrations. We also note that the unannealed PZT film does not adhere to non-platinum surfaces during wet-etching, permitting the film to be removed easily. The process details are given in Appendix C.1. The resist used is $\sim 5\ \mu$m of AZ 4620 from Hoechst Celanese Corporation, and approximately 5 sec etching time in 63% DI (200 ml)/ 32% HCl / 5% BOE solution.

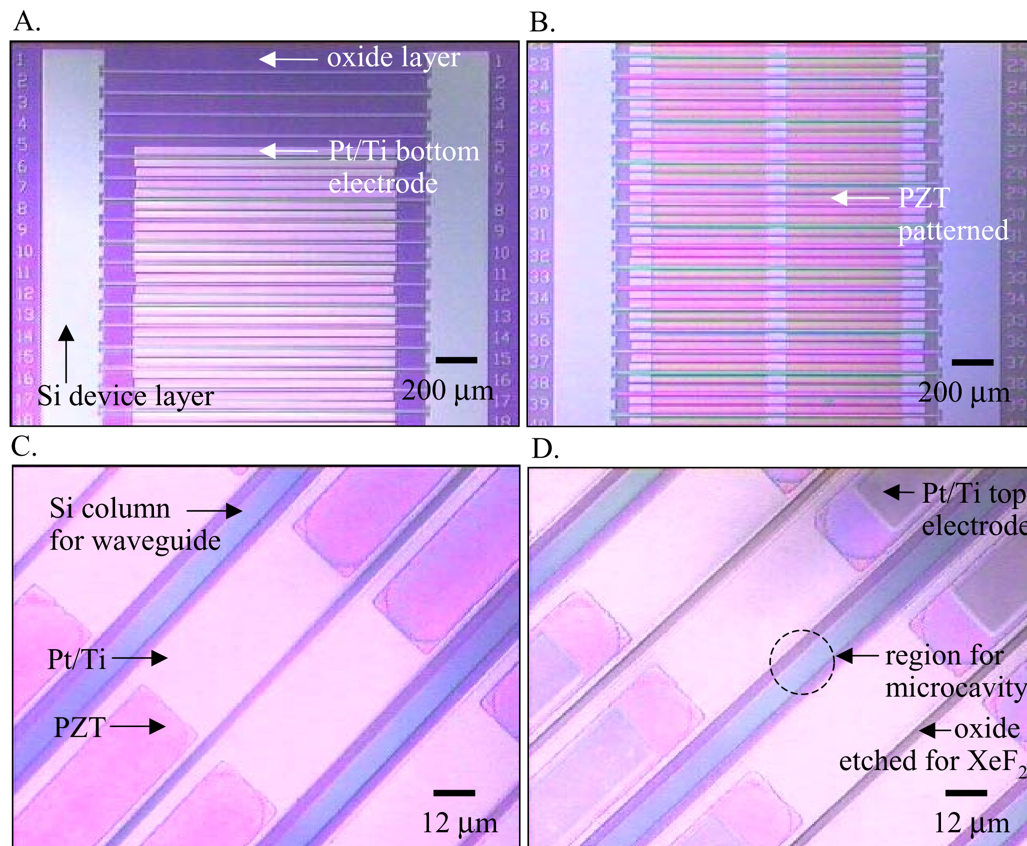

Figure 5-2: Topview of processed results for defining thin-film piezoelectric actuators: (a) Pt/Ti bottom electrode patterned with lift-off, (b) wet-etched patterned PZT, (c) wet-etched patterned PZT (annealed) at higher magnification, and (d) Pt/Ti top electrode patterned with lift-off and oxide layer etched in preparation for XeF_2 etching to release membrane.

Figure 5-2 shows the top-view of PZT processing at the various steps: (A) patterned

Pt/Ti bottom electrode with lift-off, (B) wet-etched PZT, (C) wet-etched PZT after annealing (at higher magnification), and (D) patterned Pt/Ti top electrode on completed PZT actuator. The silicon column (or mesa) in-between the actuators will subsequently form the waveguides and the microcavities. With a linewidth of 30 μm in the PZT actuators, the expected undercut needs to be tightly controlled, especially when the PZT film is etched before annealing. (An annealed PZT film is more dense and will have less undercut when etched after annealing.) We therefore diluted the etchant and kept the etch times on the order of seconds. The completed 23 μm PZT "strips" demonstrate good polarization versus electric field hysteresis properties, as illustrated in Figure 5-3. The saturation polarization measures at 59 μC/cm^2, the coercive field at 127 kV/cm (corresponding to 3.8 V), and the remnant polarization, 2P$_r$, at 62 μC/cm^2, comparable to properties from conventional PZT[3] processing. The measured resistances range from 6×10^8 to 2×10^{10} Ω, which translates to resistivities of 2×10^7 to 8×10^8 Ω·m, as expected from the thin-film PZT material.

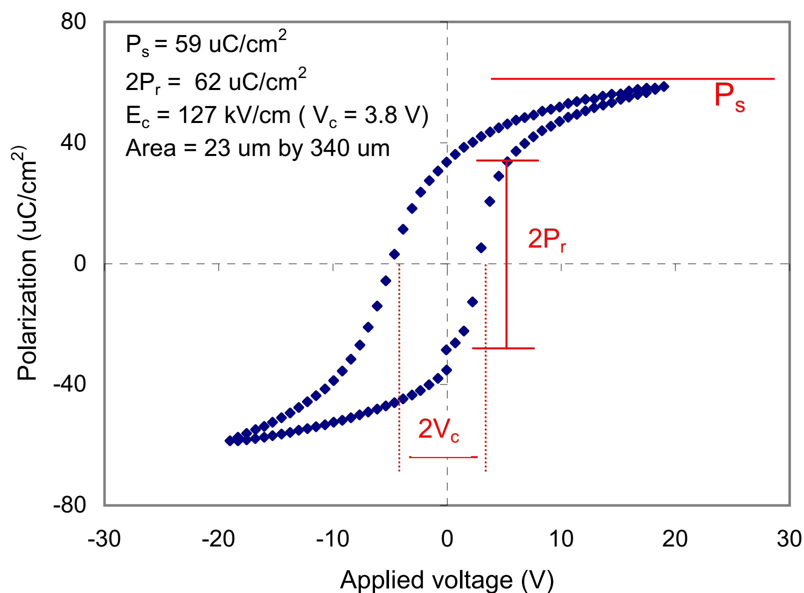

Figure 5-3: Polarization electric field (expressed as applied voltage) hysteresis curve for completed actuators for the microcavity waveguide. The PZT film was etched before annealing in a wet-etchant.

[3]Reactive-ion-etching is typically, at this point of writing, used to etch the PZT film and the Pt/Ti electrodes. Sputtering is commonly used to deposit the bottom electrode. PZT is either spun on with a sol-gel material or sputtered.

5.1.3 X-ray nanolithography for microcavity waveguide

We use X-ray nanolithography with Cu L-line source of λ at 1.32 nm (940 eV) in the NanoStructures Laboratory (NSL) of MIT under the direction of Prof H. I. Smith. Features as small as 20 nm can be replicated in a practical manner with this process. First, to create an X-ray mask, the pattern is written by electron-beam lithography into 240 nm PMMA (poly-methyl-methacrylate, 3% 950K) on a SiN_x membrane. The PMMA is then developed, with a methyl-isobutyl-ketone in isopropanol (1:2 buffering) solution, and gold is electroplated into the PMMA mold. This is typically the "mother" mask. The mother mask is written by Juan Ferrara of NSL. A negative image of the pattern, or a "daughter" mask, is created by exposing with the mother mask using soft-contact X-ray nanolithography. The mother-daughter mask procedure is used as X-ray masks could break easily.

The daughter mask is then exposed onto 240 nm PMMA on a SOI device substrate, with alignment of the mask with respect to the piezoelectric actuators. The Si column, shown earlier in Figure 5-2c, is designed to be sufficiently wide so that the resist thickness is uniform (in order for proper exposure and development) even when spun onto a wafer with etched features. Lift-off of 50 nm Cr is then used to create a hard-mask [4] for Si waveguide etching. We note, in this case, the mother mask is of the same image polarity as the final Cr hard-mask. Depending on control of the resist development time and the X-rays exposure time, variation of the hole diameters and waveguide widths is on order of 10%. Figure 5-4 shows the SEM of the exposed PMMA and subsequent lift-off for the Cr mask.

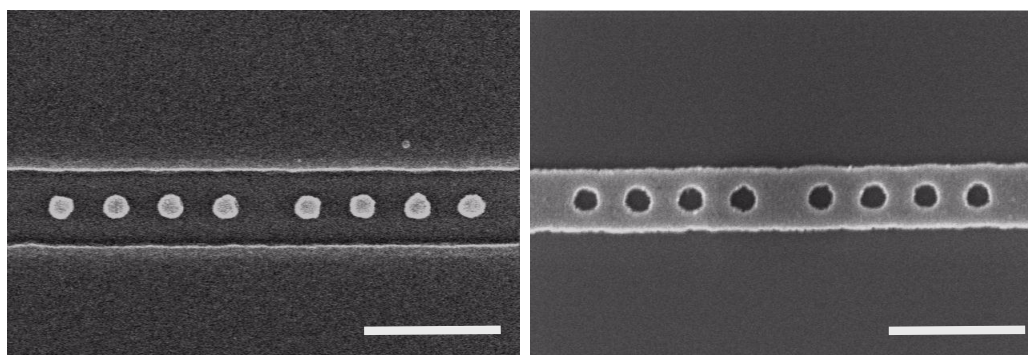

Figure 5-4: Intermediate steps of X-ray processing: (a) transfer of pattern from mask into PMMA, (b) Cr lift-off to form hard mask for Si plasma etching.

Alignment of the mask to the substrate is made more difficult because the mask is dark-field; that is, most of the region of interest is Au so that any structures directly beneath the

[4] Using PMMA as a direct mask for Si RIE etching is not feasible, as the O_2 in the RIE plasma will remove PMMA – through ashing and heating – very quickly. PMMA as a direct mask for SiO_2 etching is possible, although a CHF_3 etchant needs to be used and the substrate kept cool through chamber venting every minute [121].

mask cannot be observed. To get around this issue, the waveguides on the mask is aligned to test structures on other locations of the substrate. Figure 5-5 shows the integrated results of X-ray nanolithography with the piezoelectric microactuators. Rotational alignment is essential due to the length of the waveguide and has to be made within ~ 0.3 degrees. $\hat{y}$ alignment is also essential due to the need to locate the waveguides and microcavities on the previously defined Si column. $\hat{z}$ alignment is more relaxed.

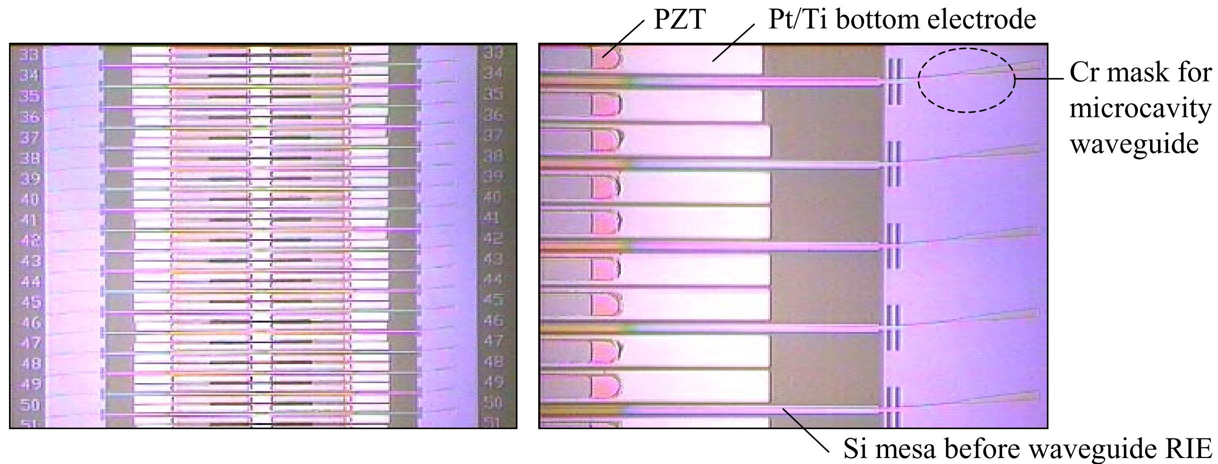

Figure 5-5: Aligned X-ray nanolithography with Cr hard-mask defined on Si mesa before waveguide etch.

With the Cr hard mask created, the Si is etched in a 13.5 sccm CF_4 / 1.5 sccm O_2 plasma at 10 mtorr and 300 V DC bias with power $\sim$ 190 W. The etch rate is $\sim$ 20 - 26 nm/min. The Si etch is optimized to achieve vertical (and straight) sidewalls to reduce transmission losses and such that the optical response will be at the wavelengths of interest. Appendix C.3 shows the SEM cross-sections of different etch recipes. The lower pressure (10 mTorr) and lower DC bias recipe gives a slower etch rate, but results in the more vertical and straight sidewalls. In this process, sidewall roughness, on order of 20 nm, is the largest contributing factor for transmissions losses[5].

The Cr mask is then removed with a wet etchant (perchloric acid, $HClO_4$, with ceric ammonium nitrate, $Ce(NH_4)2(NO_3)_6$). The Cr etchant does not attack the completed PZT actuators. Next, for some wafers, we also performed a short Si etch, without the Cr mask, to trim down the Si waveguide thickness [6] as the beginning specialized Unibond SOI wafers had device layer thickness $\sim$ 5% more than desired in the design. The top surface roughness

[5]Top surface roughness on the Si device layer is on order of 1 nm from AFM measurements, significantly smaller than sidewall roughness.

[6]The waveguide thickness is essential for operation at the desired optical wavelengths of 1.55 μm. Increasing the thickness decreases the operating frequency of the microcavity waveguide, as discussed in Section 4.3.3, page 90.

increased from $\sim$ 0.6 nm to 1.4 nm after this etch, but is still smaller than the roughness from the sidewalls.

A completed microcavity waveguide is illustrated in Figure 5-6. The lattice constant a is 425 nm, defect size a_d at 655 nm, waveguide width w at 490 nm, with 4 holes on each side of the microcavity. The waveguide thickness is kept at $\sim$ 190 nm.

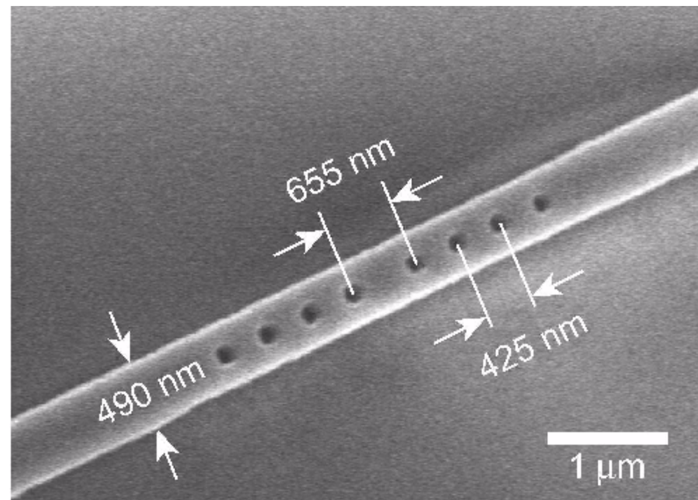

Figure 5-6: SEM of completed microcavity waveguide under 20,000X magnification.

Stitching errors of electron-beam lithography Both direct electron-beam writing and X-ray nanolithography (with the electron-beam written masks) are prone to stitching errors from an electron beam lithography system. The particular electron-beam system we used is integrated from IBM gifts VS-2A and VS-6 [7]. To write the 2000 μm (in length) waveguides, the electron-beam field – which is approximately 102.5 to 125 μm in size – has to be translated multiple times to complete the writing layout. Translation is done by moving the sample stage. Positional errors in the field stitching are therefore observed as kinks in the waveguide, as shown in Figure 5-7, leading to scattering losses in transmission at each of these stitches. In this particular SEM, the stitching error is approximately 125 nm. Development of a positional feedback system with fiducial grids – such as the Spatial-Phase-Locked E-Beam Lithography system – has improved stitching accuracies to a nanometer standard deviation [43].

Direct electron-beam writing We also used direct electron-beam writing for the microcavity waveguide. In this process, control of the exposure dosage (by controlling the

[7]The pixel size of the system ranges from 6.25 to 7.0 nm.

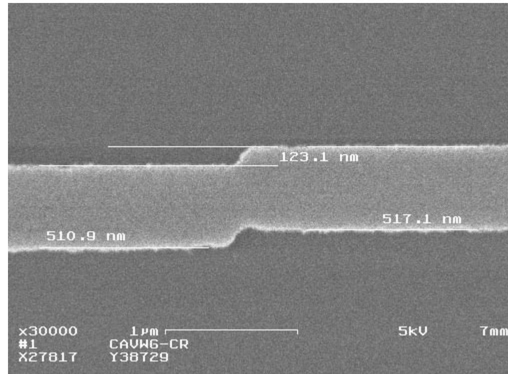

Figure 5-7: Stitching error in electron-beam writing of X-ray mask, as reflected in discrete kinks in resultant waveguide. In this particular SEM, the stitching error is approximately 125 nm.

scanning speed of the beam) is pertinent to achieve the designed device dimensions. Resist development time and thickness considerations are secondary compared to the exposure dose. Figure C-11 of Appendix C shows the effect of different doses (between 330 $\mu C/cm^2$ to 446 $\mu C/cm^2$): for $\sim 21\%$ increase in dose, the features can vary by $\sim 9\%$, such as for the hole diameter. The design configurations in the electron-beam writing layout are listed in Figure C-12 of Appendix C (page 159), wherein we include variations such as defect length, width of waveguide, number of holes and overall physical size of the device. This process was eventually not used, at the time of writing, due to availability issues of the electron-beam equipment.

5.1.4 Tunable membrane platform release

There are two main methods to release the membrane platform. For a Si/SiO_2 membrane, a combination of KOH bulk micromachining, Si backside RIE and XeF_2 dry release from the front-side is necessary. For a SiO_2 membrane (without Si), we only require XeF_2 etching from the front-side. Without Si in the membrane, there is concern of whether the double-anchored oxide membrane will survive under residual stress and piezoelectric actuation. We demonstrate for our device dimensions – 600 to 1000 μm length and 100 μm wide – that the double-anchored oxide membrane is sufficiently robust for oxide thickness of both 0.4 μm and 3 μm. Figure 5-8 shows the top view micrograph of the 0.4 μm oxide membranes released by front-side XeF_2 dry etching. The curved shadows on the length-wise sides of the membranes are due to out-of-plane bow from residual stresses in the oxide and PZT films. The chirped dark (short) lines in each membrane are indicative of the out-of-plane membrane bow. The membranes are tested under PZT actuation up to 20 V and they do not fracture.

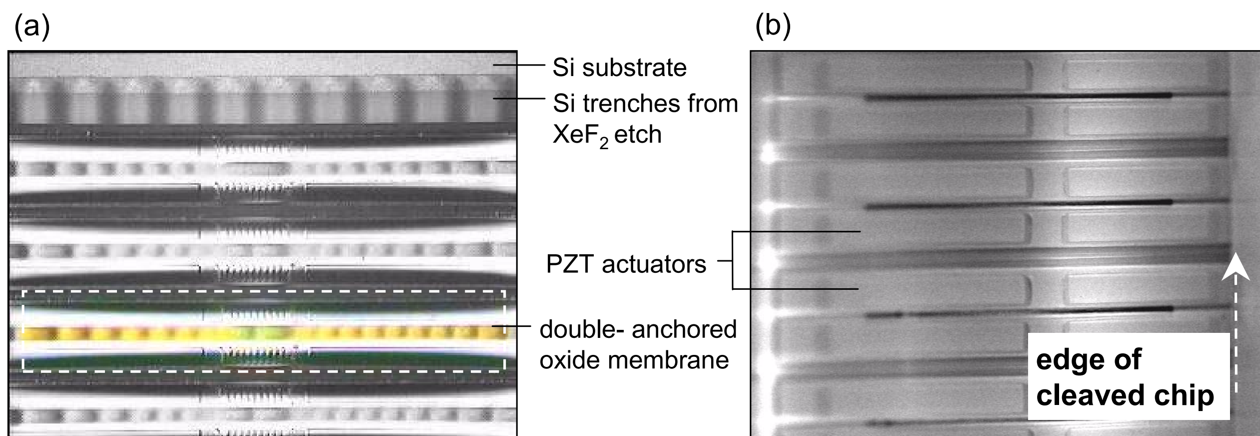

Figure 5-8: Double-anchored oxide membranes released by front-side XeF_2 isotropic etching: (a) optical micrograph, (b) SEM image.

5.2 Experiment

And then there was light.

This section describes the microcavity experiments, on both a "static" microcavity (without the integrated microactuators) and a tunable microcavity. Laser diode sources, through coupled lensed fibers, are used to determine the photonic band gaps and cavity resonances.

5.2.1 Measurement setup

Device characterization is performed at the MIT Optics and Quantum Electronics Group of Prof E. P. Ippen and H. A. Haus. The measurement setup schematic for characterizing optical waveguides is illustrated in Figure 5-9. The apparatus is managed by P. T. Rakich [124]. With two Santec tunable laser diodes, the measurement window is from 1430 to 1610 nm. The setup also permits full polarization control, 10 nm sample stage resolution with bulk piezoelectric actuators, and high resolution confocal signal collection. Imaging cameras in the setup also permit detection of proper coupling into the waveguides (for guidance instead of oxide cladding modes). Figure 5-10 shows: (a) exit view of waveguide depicting proper coupling into waveguide and low-loss transmission through waveguide, and (b) top view of guidance into a waveguide with radiation losses from the holes and at the microcavity. Direct imaging of the output facet and scattering from the waveguide stitching errors permit practical determination of waveguide coupling.

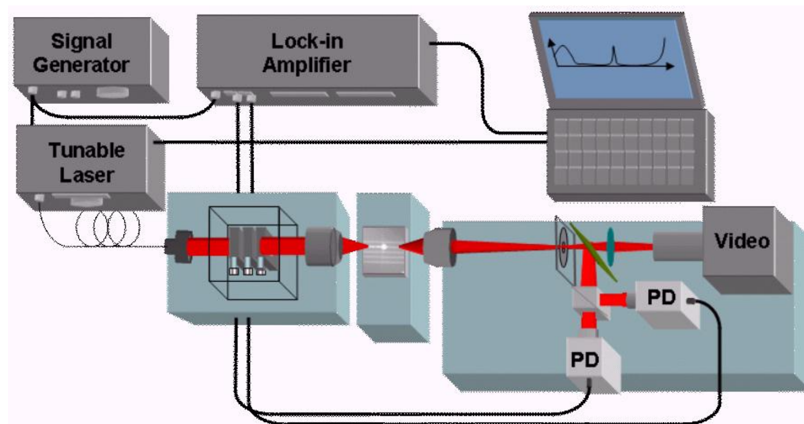

Figure 5-9: Schematic of waveguide characterization setup in the MIT Optics and Quantum Electronics Group. Setup permits measurement range from 1430 to 1610 nm with laser diodes, full polarization control, 10 nm sample stage resolution, and high resolution confocal signal collection. Figure courtesy of P. T. Rakich [124].

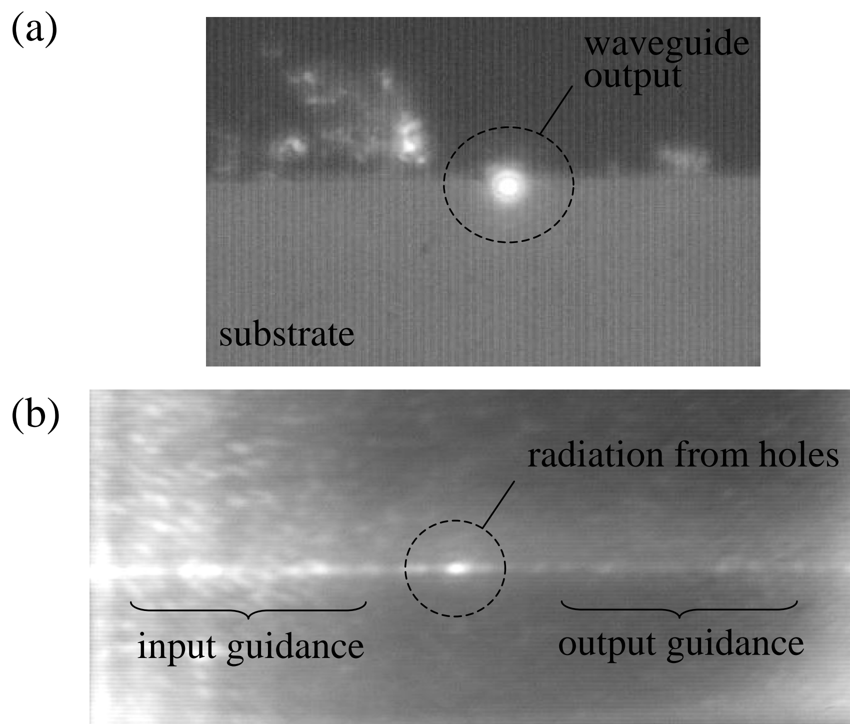

Figure 5-10: Imaged views of microcavity waveguide in operation: (a) exit view of waveguide depicting proper coupling into waveguide and low-loss transmission through waveguide, and (b) top view of guidance into a waveguide with radiation losses from the holes and at the microcavity.

5.2.2 Waveguide loss characterization

A widely used methodology to measure waveguide transmission losses is through the cut-back method [55]. This simply involves measuring the transmission, destructively removing some of the waveguide, and re-measuring the transmission to determine the loss. Other methods include photo-thermal deflection [46], or inclusion of a "paper-clip"-like structure to vary the waveguide length (much like the cutback method, except that it is non-destructive) in a single chip with similarly-prepared facet qualities [93]. We employ here the Fabry-Perot resonance method [126, 146] which is a convenient single-step method for high-contrast waveguides. The input and output facets act as effective mirrors to form a Fabry-Perot cavity, with reflectivities R given as

$$R = \left(\frac{n_o - n_{eff}}{n_o + n_{eff}} \right)^2 \tag{5.1}$$

where n_o is the refractive index of the medium adjacent to the waveguide and n_{eff} the effective refractive index for the waveguide. Equation 5.1 assumes vertically-cleaved facets. While a a mode solver can be used to find n_{eff}, we use here an analytical solution for a good approximation. For a three-layer structure consisting of top cladding, guidance layer, and

bottom cladding, n_{eff} can be found from the following [93]

$$k_o d\sqrt{n_2^2 - n_{eff}^2} = v\pi + tan^{-1}\left[\sqrt{\frac{n_{eff}^2 - n_1^2}{n_2^2 - n_{eff}^2}}\right] + tan^{-1}\left[\sqrt{\frac{n_{eff}^2 - n_3^2}{n_2^2 - n_{eff}^2}}\right], \text{for TE waves} \quad (5.2)$$

$$k_o d\sqrt{n_2^2 - n_{eff}^2} = v\pi + tan^{-1}\left[\frac{n_2}{n_1}\sqrt{\frac{n_{eff}^2 - n_1^2}{n_2^2 - n_{eff}^2}}\right] + tan^{-1}\left[\frac{n_2}{n_3}\sqrt{\frac{n_{eff}^2 - n_3^2}{n_2^2 - n_{eff}^2}}\right], \text{for TM waves} \quad (5.3)$$

where k_o is the wavevector in air, d the thickness of the guidance layer, n_1 the top cladding index, n_2 the guidance layer index, n_3 the bottom cladding index, and v an integer. The rectangular waveguide can be divided into three-layer sections horizontally (in the plane of waveguide) or vertically. The effective indices are found for each horizontal slice and then the effective index method used again to sum up the three horizontal slices to get n_{eff}. n_{eff} is found to be 2.4737 for air-cladded silicon (n_{Si} of 3.48) on thermal oxide (n_{SiO_2} of 1.44), giving facet reflectivity R of 0.18.

With n_{eff} and R determined, the waveguide loss, or absorption, coefficient α is described as

$$\alpha = \frac{1}{L}\, ln\, \left(R\, \frac{1+\sqrt{\frac{P_{min}}{P_{max}}}}{1-\sqrt{\frac{P_{min}}{P_{max}}}}\right) \quad (5.4)$$

For R of 0.18, α is thus estimated to be between 5 - 7 dB/cm.

Total loss between the input and output fibers, including fiber-to-waveguide coupling, is estimated to be on order of 30 dB. Most of this loss is in the fiber-to-waveguide coupling, due to the poor mode overlap between the launch fiber and the waveguide facets[8]. An integrated spot size converter [148] or an anti-reflective coating evaporated on the waveguide facets could decrease coupling loss.

[8]For photonic crystal waveguides formed from line defects in a 2D photonic crystal, the coupling is made worse with an impedence mismatch between the linear dispersion in the fiber and the nonlinear dispersion in the photonic crystal waveguide.

5.2.3 Membrane mechanical measurements

Direct measurements of the membrane displacement was performed with the Computer Microvision system [34] in the Freeman lab, as was used with the tunable grating measurements and briefly described earlier in Section 3.3.2. The experiments were performed by probing two of the four integrated microactuators, requiring four individual 3-axis probes. As the contact area has 22 μm widths, probes with 2.4 μm tips are used to contact the electrodes. Wire-bonding cannot be performed as the contact area is limited by the pre-determined length of the waveguides in the X-ray masks. DC-biased voltages, up to order 10 V, are applied to one of each pair of probes.

As with the Microvision experiments performed on the tunable gratings (Section 3.3.2), the displacements are converted in membrane strain, with strain of 0.022% estimated at 10 V. This numbers are plotted against finite-element (FE) models performed in Coventorware^{TM}, as illustrated in Figure 5-11. The strain measurements are in good agreement, although there is large uncertainty in the FE estimates due to the high sensitivity of the strain to the membrane location.

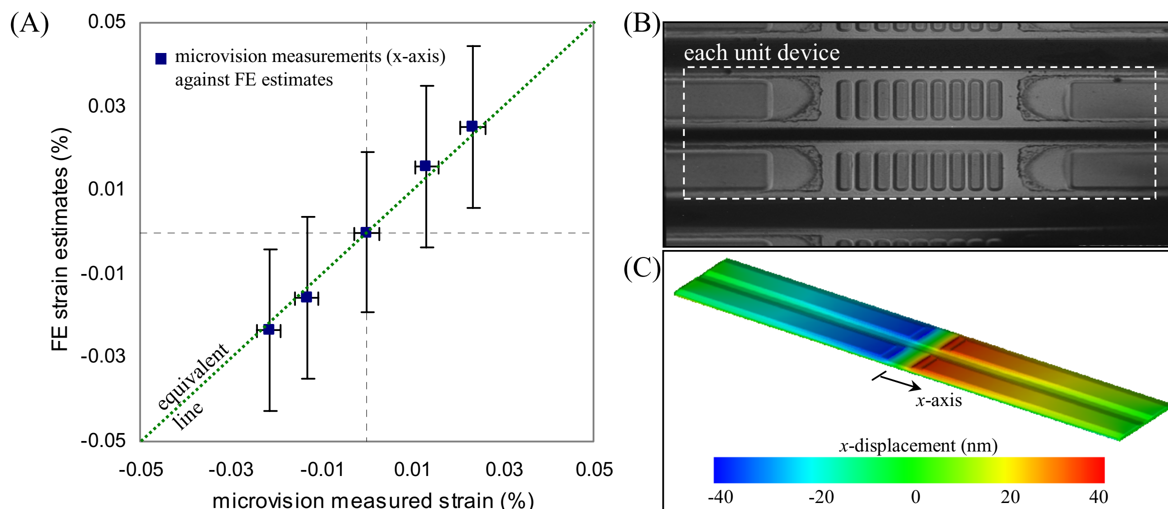

Figure 5-11: (A) Comparison of Microvision [34] measured strain against FE model estimates, (B) top view of deformable membrane under the Microvision system, (C) x-axis displacement estimates under the FE model.

5.2.4 Static microcavity measurements

Laser diode measurements The observation of the microcavity resonance is illustrated in Figure 5-12, with dimensions of the specific device (Design I) detailed in Table 5.1. The peak transmission is at 1555.2 nm. Q, as described in Section 4.3.3 on page 90, is determined

to be 159 ± 10 for the static microcavity waveguide with a FWHM of 9.8 nm[9]. This is in agreement with theoretical predictions of Q_{FDTD} at 180 by Johnson [65] and 172 by Fan [27].

For this particular device (Design I), the waveguide thickness is trimmed down to 176 nm. In addition, the oxide layer is 3 μm thick, effective separating any field overlap with the Si substrate. Figure 5-12 also shows a higher frequency signal convolved with the Lorentzian of the microcavity resonance. This higher frequency signal has a periodicity of $\sim$ 5 nm, which corresponds to a larger Fabry-Perot of $\sim$ 70 μm length in the waveguide. This is from the e-beam lithography field stitching errors that occurs every 60 - 100 μm along the waveguide.

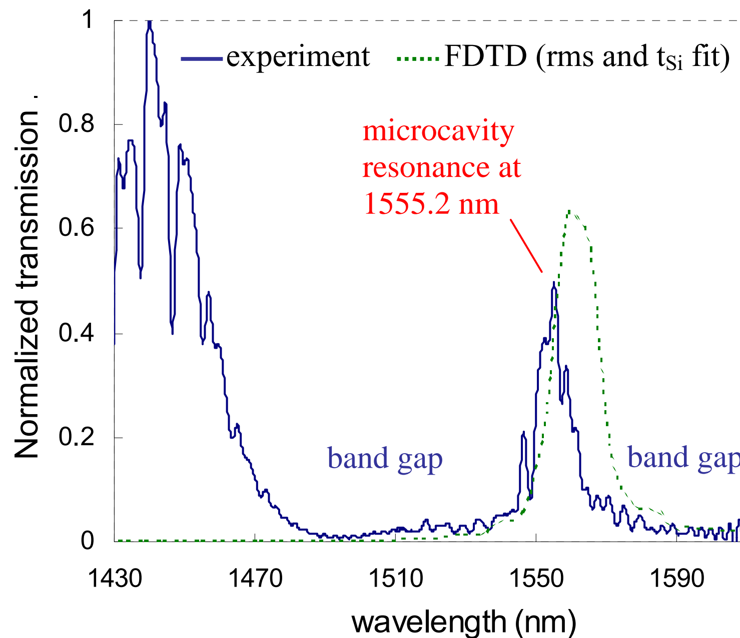

Figure 5-12: Normalized transmission of static microcavity waveguide. The measured spectrum is low-pass filtered to remove high frequency measurement noise. Measured device dimensions are listed in Table 5.1.

The finite-difference time-domain prediction, shown as the dotted (green) line in Figure 5-12, is corrected for the 5 nm SEM measurement resolution of the microcavity waveguide dimensions. This 5 nm measurement resolution translates to a 3% root-mean-square error – with measurements of the lattice constant a, defect length a_d, diameter of holes $2r$, and width of waveguide w – in the device physical dimensions. It is also corrected for a waveguide thickness of 176 nm instead of the 190 nm used in the original computations. It

[9] Q is determined directly from the measured FWHM since the spectrum resolution is 0.1 nm or less. Another method to determine Q is by varying the Q of a theoretically generated first-order Lorentzian and gauging the best fit with the experimental measurement. The goodness-of-fit can be determined with a correlation coefficient $\rho = \frac{Cov(measurement, generatedLorentzian)}{\sqrt{Var(measurement)\ Var(generatedLorentzian)}}$, or a cross-correlation technique.

Device parameter	*Measured dimension*	*% design variation*
spatial period a	429 nm	+3%
waveguide width w	1.26a	+ 6%
waveguide height t_{Si}	0.41a	-8%
defect length a_d	1.50a	+1%
hole diameter $2a$	0.44a	-5%
oxide ridge thickness $t_{SiO_{2,1}}$	0.69a	-
oxide layer thickness $t_{SiO_{2,2}}$	6.22a	-
depth of holes into oxide	0.70a	-
number of holes on each side of microcavity	4	-
refractive index of silicon	3.48	-
refractive index of silicon oxide	1.44	-

Table 5.1: Specific measured dimensions of microcavity waveguide with transmission spectrum shown in Figure 5-12.

is also reported that simulations show that the longer wavelength band edge does not shift appreciably with dimensional variations, while the resonance and shorter wavelength band edge is more sensitive [33]. The predicted transmission peak at 1558 nm compares well with the measurement of 1555.2 nm, a 0.2% fractional difference.

Comparison of measured resonances for two device geometries – Design I and II – is shown in Figure 5-13. Design II has a defect length a_d 14 nm longer than Design I, with a similar lattice constant a (within SEM measurement uncertainty). The longer defect length leads to a longer resonant wavelength as observed and as can be expected from the Fabry-Perot analogy. The shift is smaller than expected due to the devices of Design II having smaller waveguide widths and larger holes than Design I[10]. In the particular device of Design II, Q is estimated at 280 with a FWHM of 5.6 nm.

[10]In the particular fabrication of devices of Design I, the PMMA is over-exposed and over-developed in order to safely clear the holes. This results in larger waveguide widths and smaller holes, leading to a higher dielectric material ratio in the device and hence a longer resonant wavelength.

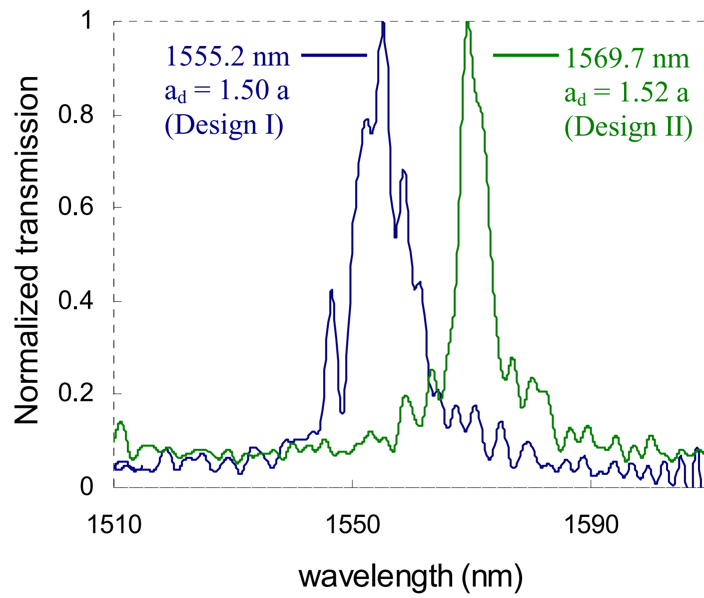

Figure 5-13: Measured resonances for microcavity waveguides with different defect length a_d. Design I has $a_d = 1.50a = 648$ nm. Design II has $a_d = 1.52a = 662$ nm.

5.2.5 Dynamic strain-tunable microcavity measurements

Tunable microcavity setup The experimental setup, including the probes, is shown in Figure 5-14. Lensed fibers are used to couple light into and out of the microcavity waveguides. Imaging of the chip is performed by looking vertically down onto the chip and at an angle, to position the probe tips and also to observe proper coupling into and out of the waveguides. Two probes are required for each PZT actuator, for the top and bottom electrodes. The probe setup is similar to the ones used for the microvision measurements, as described in Section 5.2.3. A DC-biased voltage, up to 16 V, is applied to one of each pair of probes.

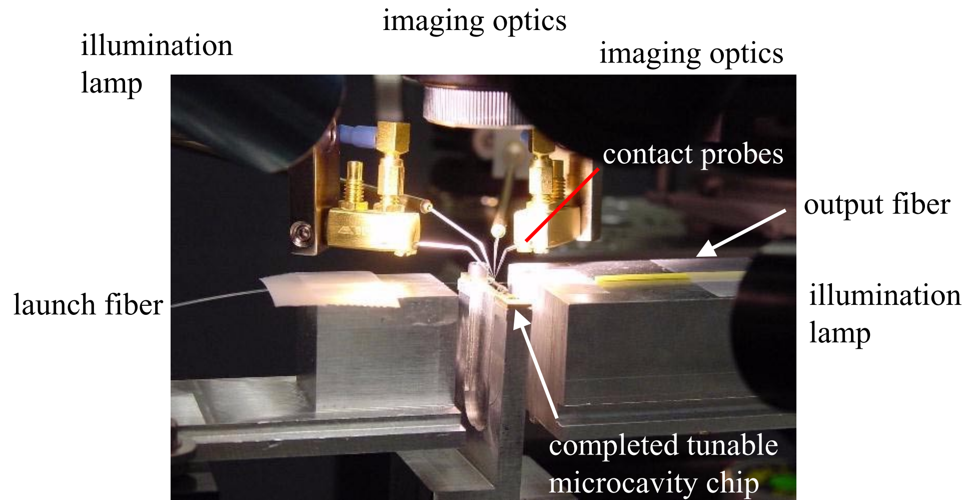

Figure 5-14: Experimental setup with positioned lensed fibers for input and output coupling, imaging optics, and electrical probes for the integrated PZT microactuators.

Tunable microcavity experiments When a DC-bias is applied, the shift in resonance, $\Delta\lambda$, is determined to be -0.91 nm at 15 V (compression) and +0.63 nm at 16 V (tension). Figure 5-15 shows the tuned resonances between 0 V and 16 V (tension) applied voltages to two of the four actuators. This, to our knowledge, is the first report of active strain to dynamically tune the responses of silicon photonic crystals. The spectrum shown for each applied voltage is averaged over multiple measurements, with the wavelength resolution determined to be 0.02 nm from multiple measurements.

The fitted Lorentzians are generated with a Trust-Region[11] nonlinear least squares algorithm which uses an iterative approach to minimize the residuals [8]. Only the data at the main peak is analyzed, as the "side"-ripples might give systematic errors to the fitting algorithm. The R^2 values involved in the fitted first-order Lorentzians are 0.94 ± 0.03 with

[11] This algorithm [8] is employed with the Matlab 6.1 Curve Fitting Toolbox. Other nonlinear least squares algorithms are the Levenberg-Marquardt or Gauss-Newton algorithms.

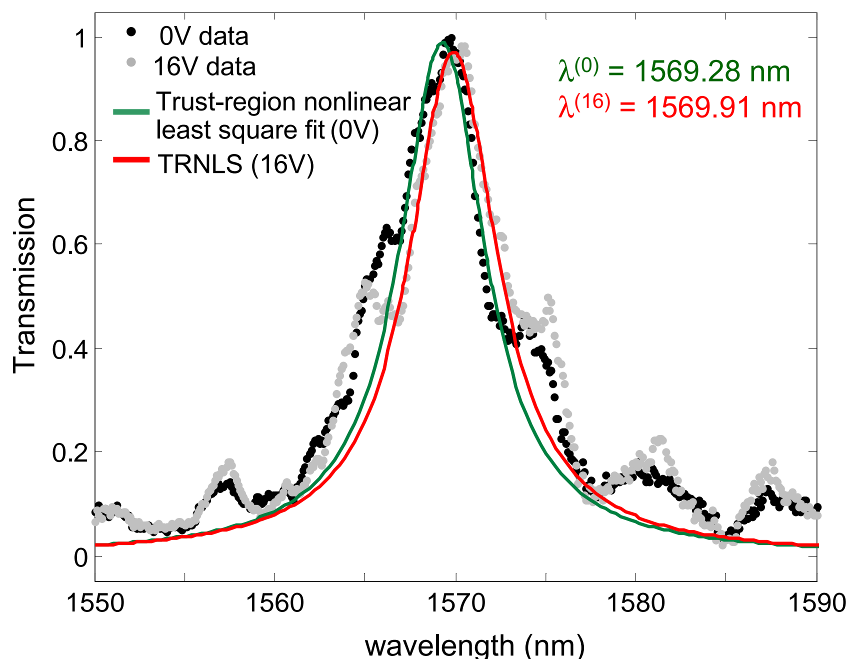

Figure 5-15: Strain-tuned resonance of the microcavity waveguide at 0 V and 16 V, in tension. A trust-region nonlinear least squares fit is used to generate the Lorentzians.

sum-squares-error at 0.28. Third-order Lorentzians and first-order Lorentzians with sinusoids are also explored to determine the shift in resonance, with $R^2 \sim 0.99$ and residuals at $\sim$ 0.01. Intensity-weighted mean, mode and median calculations are also used to determine the resonance shift. All these methods show the same directional shift for various applied voltages; the first-order fitted Lorentzian is selected as the one with the theoretically-expected transmission response and with the most certainty.

Both compression and tension are possible to be applied to the microcavity because the microcavity is located off the mid-plane of the double-anchored membrane during actual device fabrication. That is, during alignment of the X-ray mask to the completed microactuators, the microcavity is physically translated in the $\hat{z}$-direction (along the waveguide direction, as first denoted in Figure 4-1) to be aligned beside a pair of PZT actuators. This allows compression when those actuators are activated and tension when the opposite, on the other side of the membrane, pair of actuators are involved.

Tunable microcavity analysis There is an observed increase in Q for shorter resonant wavelengths, from the decrease in cavity lengths, on order of a few percent fractional difference. This suggests stronger localization of the fields with a shorter cavity length for this particular device. This effect is similar to the fractional edge dislocation discussed by Vuckovic *et. al.* [155] where there is a maximum Q for an appropriate cavity length, as the cavity length is progressively scanned. The explanation could be thought of as follows [65]: initially, as a state is pulled down into the band gap (by adding dielectric material between

the holes to create the defect), the fields become more localized[12] and there is less coupling into waveguides. Total Q increases. As the state is further pulled into the gap, localization get stronger but peaks near the mid-gap, as is Q. As the state continues to be pulled further down towards the lower frequency band edge, the fields become less localized until the state eventually disappears. There is more coupling into the waveguide, and Q decreases back down. Our measurements, therefore, suggest this particular device has a defect size such that the localization (and total Q) is past its maximum. Full simulations would be needed to determine the specific location of the strongest localization with respect to the device defect size.

Figure 5-16 summarizes the measured tuned resonances in comparison with the perturbation analysis described in Section 4.4. The applied strain, on the horizontal axis of Figure 5-16, is estimated through the Computer Microvision [34] measurement system as described previously in Section 3.3.2. The error bar in the horizontal axis is from Microvision measurement uncertainties; the error bar in the vertical axis is from various fitting algorithms to the Lorentzian response. The theory predicts the experimental results well, without any fitted coefficients. This validates the developed perturbation numerical model in predicting changes in resonant frequency for a given applied strain.

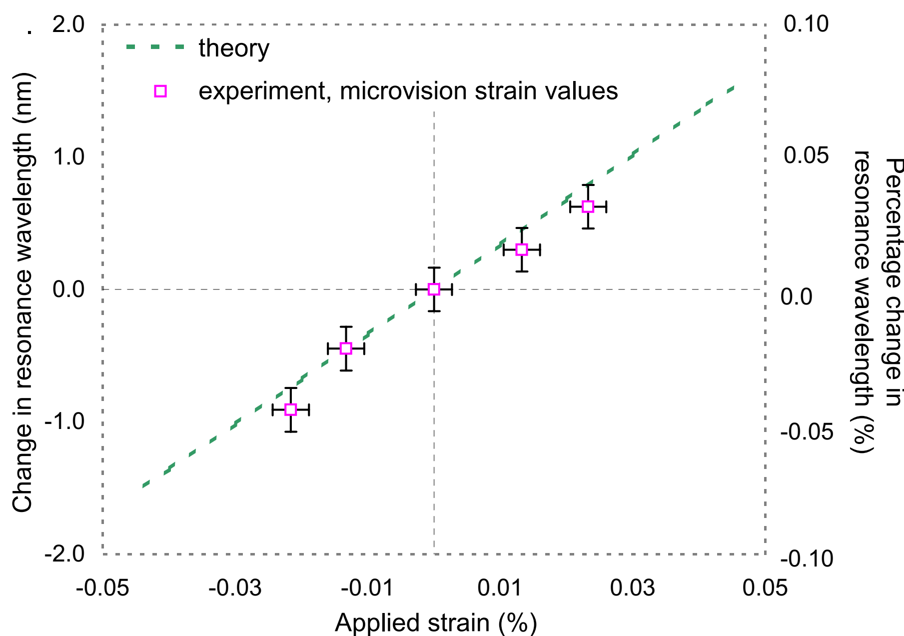

Figure 5-16: Comparison of strain-tuned microcavity resonance against modeling predictions.

[12]Only in the band gap are the fields localized; as the state enters or leaves the band gap, it becomes delocalized and eventually disappears.

The total applied strain is at $\sim 0.04\%$ and is smaller than the 0.21% strain reported for the tunable gratings (in Section 3.3.2) due to smaller force delivered to the microcavity. This is because of (1) the thicker membrane, and (2) the small linear length amplification factor (as described in Section 2.2.2, page 34) in the double-anchored membrane for the microcavity waveguide. The thicker membrane is due to the thick oxide (1 - 3 μm) needed to insulate the mode from the substrate. The small linear length amplification factor is due to the constrained design space of the microcavity waveguide from the nanolithography X-ray mask.

To increase the maximum applied strain, we can therefore: (1) reduce the membrane thickness, (2) increase the linear length amplification factor given more flexibility in the microcavity waveguide design, and (3) reduce the residual stress in the membrane. Reducing the membrane thickness will, to first-order, result in a linear increase in applied strain, as described in the elastic energy variational approach of Section 2.2.4 (Equation 2.24). The reduction from the current 3 μm oxide, constrained by the availability of the Unibond SOI wafers, to a 1 μm oxide will give an estimated factor of three improvement. Reduction in residual stress will lead to a linear increase in maximum applied strain, with most of the elastic energy in our specific double-anchored membrane dominated by residual stress (Section 2.2.4). The residual stress could be reduced by using a different material for the membrane, such as a variable Si ratio SiN_x material. Using a SiN_x membrane, however, leads to additional processing steps and the need to deposit and define a low-loss dielectric material for the waveguide, instead of using the single-crystal Si in the SOI wafer as is currently.

Evaluation of technology The currently demonstrated dynamic tuning range of 1.54 nm in passive silicon microphotonics at optical frequencies is significant compared to tuning ranges achieved with electro-optics (as mentioned in Section 1.1, in III-V materials, $\Delta\lambda$ is typically on order of 0.05 nm [99] and, in polymeric electro-optic materials, up to 6.6 pm/V [123]). The application is particularly significant in two targeted areas: (1) post-device fabrication trimming, or relaxation of tight production tolerances, in DWDM optical telecommunications, (2) active compensation against external disturbances for high-density integrated optics. First, based on a projected 200 DWDM channels, the C and L band (1525 - 1565 nm and 1575 - 1608 nm respectively) bandwidth translates to ~ 0.4 nm wavelength spacing per channel. If we assume, to first-order, we can resolve two spectra at the Rayleigh's resolution and translate this to device dimensional tolerances, a ~ 0.28 nm dimensional tolerance is needed. This is difficult to achieve with current nanofabrication technologies. Taking current abilities to resolve device dimensions on order of a nanometer, this translates back into an uncertainty, from device fabrication, in wavelength resolution of ~ 2 nm. The currently demonstrated tuning range with piezoelectric strain-tuning is thus immediately significant as a post-device fabrication trimming technology for DWDM optical networks.

Second, current methods for trimming or compensation against external disturbances in optical telecommunication devices typically involves thermal-related effects. However, thermal methods typically require high power (order mW per active device), has response times

on order of kHz, and might be difficult to achieve localized tuning within order 10 μm spatial dimension. Moreover, to achieve a temperature-controlled environment, power dissipation through natural convection gives an estimate of 0.3 W for a 5 ^{o}C differential temperature. The high-power density of piezoelectric actuators, and hence the low power consumption, translates to power requirements on order of nW per active device. In addition, response times are possible up to MHz and discrete localized tuning can performed on each device. If, for example, 10^5 individual devices are required on a chip for active trimming or compensation, piezoelectric tuning requires order 10 mW while thermal methods require 100 W. This immediately suggests scalability for piezoelectric tuning in replacement of current thermal methods.

In terms of actively switching channels, however, the currently demonstrated 1.54 nm range has less implications. For 200-channel DWDM networks, this range translates to switching of a few channels. For the same tuning range, thermal methods would be required to achieve on order of a 15 ^{o}C differential temperature, with a sensitivity of $\sim$ 0.1 nm/K [59]. We project the piezoelectric tuning range could be quickly extended up to order 8 nm, through described suggestions on page 127. This corresponds to a strain of $\sim$ 0.2%, for tuning 10 - 20 channels. For a tuning range larger than order 10 nm, some designs suggestions, described in Section 6.2.3, can be implemented.

5.3 Summary

This chapter began with discussing the micro- and nano-fabrication of the strain-tunable silicon microcavity waveguide. The overall processing flow, integrating thin-film piezoelectric microfabrication and X-ray nanolithography, is described. Results from a new PZT processing method – that of PZT wet-etching before annealing – are demonstrated. The nanostructures are then defined on the resulting substrate, and successfully released with a XeF_2 isotropic dry etch.

The experimental results show a photonic band gap on order of 300 nm, with cavity resonances at 1555.2 and 1569.7 nm. Total Q is found to be between 160 and 280 for different geometries. Waveguide losses is estimated to be between 5 - 7 dB/cm. The dynamic tunable microcavity shows a tuning of 1.54 nm for both tension and compression applied through the integrated PZT microactuators at 16 V and 15 V respectively. This is the first demonstration of strain-tunability on photonic crystals to our knowledge, and is a general method – with targeted applications – towards strain-tuning of silicon microphotonic devices.

Chapter 6

Conclusions

Day after day he appeared before us incomparably faithful to the illusions of the stage,
and at sunset the night descended upon him quickly, like a falling curtain.
The seamed hills became black shadows towering high upon a clear sky;
above them the glittering confusion of stars resembled a mad turmoil stilled by a gesture;
sounds ceased, men slept, forms vanished–and the reality of the universe alone
remained—a marvellous thing of darkness and glimmers.
–J. Conrad, Heart of Darkness (1990 ed.).

This chapter highlights the major developments and accomplishments in this thesis. Beginning with the generalized concept of strain-tuning of periodic microphotonic devices, we describe two specific implementations: the fundamental diffractive grating and the photonic band gap microcavity waveguide. The theoretical formulations and concepts, the integrated device fabrication processes and results, and the experimental demonstrations and analyses of each device is recapitulated. Recommendations for future explorations are presented.

6.1 Looking Back

The concept of strain-tuning of periodic microphotonic devices is generalized, in this thesis, to the fundamental diffractive grating element, and the photonic band gap microcavity waveguide. The motivation for active tuning of network components is based on the following immediate demands, as first presented in Section 1.1:

I. usage-based reconfiguration of network components for overall network adaptivity and reliability,

II. active compensation against external disturbances such as thermal and stress-induced fluctuations, material dispersions and absorptions, and

III. device trimming to achieve or relax tight production tolerances in high bandwidth optical and optoelectronic devices.

Piezoelectric strain-tuning is selected, in contrast to electro-optic or thermal tuning, due to

the advantages of low power and voltage requirements, ultra-fine control with MHz dynamic response times, localized tuning in high-density integrated optical chips, and compact integration of microactuators. The cost is the added microfabrication complexity to include the integrated actuators. The demonstration of the analog tunable diffractive gratings and the tunable microcavity waveguide is based on the piezoelectric-enabled deformable membrane platform.

Analog Tunable Gratings In contrast and complementary to the state-of-the-art "digitally" tunable diffractive gratings developed for high-resolution projection displays and miniaturized spectrometry [1, 49], we presented, in Chapter 2 and 3, in-plane strain to diffractive gratings for continuous control of the grating period and diffraction angles. An analytical piezoelectric membrane model is employed to explore the mechanical design space. Moreover, finite-element modeling is pursued to investigate out-of-plane displacements and resonance modes. The effects in the optical domain is modeled through Fourier optics to estimate deviations from the ideal binary phase reflection grating. The microfabrication process involves bulk and surface micromachining for various device designs. The completed thin-film PZT demonstrated an excellent dielectric constant of 1200 with a d_{31} of -100 $\pm$ 15 pC/N. The released double-anchored membranes show grating period displacements up to 8.3 nm (0.21% strain for a 4 μm period) at 9 V, in agreement with theory. The devices are also characterized optically to infer the motion of the first diffracted order under actuation, with a diffracted angular change estimated at up to 486 μrads at 10 V. The responses, in both theory and experiment, are linear with respect to the applied voltages, due to the small-amplitude displacement. This analog tuning of the diffracted angles suggests immediate applications towards tunable optical network components – such as wavelength add/drop filters, dispersion compensators and external cavity lasers – and miniaturized spectrometers.

Strain-Tunable Photonic Band Gap Microcavity Waveguide The concept of strain-tuning of periodic microphotonic devices is extended to the photonic band gap microcavity waveguide. In Chapter 4, design analyses are pursued through perturbation theory on the finite-difference time-domain numerical experiments, in order to resolve the small-amplitude perturbation with certainty. The design of the piezoelectric deformable membrane is strongly aided with earlier developments on the tunable diffractive gratings. Other considerations such as stress birefringence and bending losses are brought to bear. Process flow design, detailed in Chapter 5, involves integration of micro- and nano-fabrication methods. To improve the processing yield, thin-film sol-gel piezoelectric processing is pushed before X-ray nanolithography of the photonic crystal. This necessitates the new process development of sol-gel PZT wet-etching before annealing, to preserve the Si device layer quality of the SOI wafer for the waveguide. Aligned X-ray nanolithography and waveguide process optimization is also demonstrated. Experimental results demonstrate photonic band gaps on order 300 nm ($\sim$ 19% mid-gap frequency) and resonances at 1.55 μm wavelengths with Q on order of 160 - 280 for various device geometries. The waveguides, coupled through lensed fibers with

laser diode sources, demonstrated optical intensity losses of 5 - 7 dB/cm. Dynamic tuning of the resonances through strain perturbation is reported for the first time, to our knowledge. The experimental results are in good agreement with theory, and suggests implications for tunable photonic crystals, tunable filters for high-density optical integration, and tunable low-threshold lasers.

6.2 Looking Forward

In this section, we present selected possibilities for future explorations, divided into three sections: (1) tunable diffractive gratings, (2) other microphotonic elements for the strain-tuning deformable membrane platform, and (3) tunable microcavity waveguide explorations.

6.2.1 Tunable diffractive gratings explorations

Future work for the tunable gratings include control of the residual stress in the thin-films during device fabrication to reduce out-of-plane deflections. In addition, the introduction of mechanical latches could be explored. This could consist of sinusoidal-like gears at the membrane edges to maintain fixed displacements over time without the need for an external applied voltage, or a mechanical ledge over the deformable membrane to constrict out-of-plane deflections.

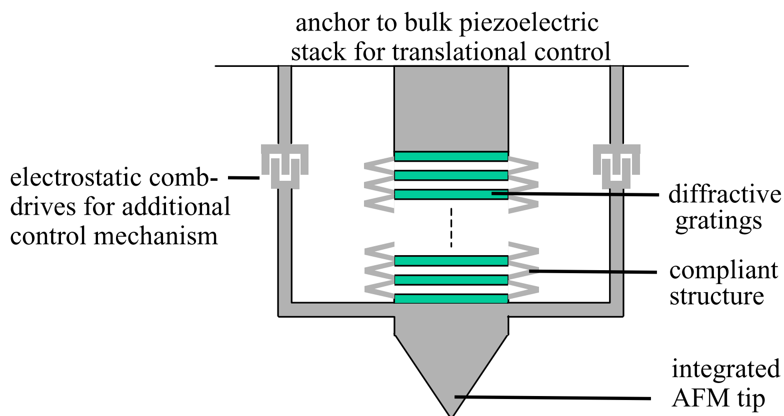

Figure 6-1: Inclusion of the diffractive grating with an atomic force microscopy tip for metrology applications. Top-view schematic shown.

A few applications for the tunable grating towards telecommunication networks were investigated in more detail earlier in Section 2.4. These included dynamic dispersion – chromatic and polarization – compensation, wavelength-selective switching, and thermal compensation. In addition, the concept of a deformable grating can be explored towards metrology with sub-nanometer resolution, such as: (1) inclusion into an atomic force microscope as shown in Figure 6-1, or (2) as optical strain gauges [9, 13, 132]. The inclusion of

inter-digitated gratings has been successfully demonstrated towards arrayed scanning probe microscopy [104]; the illustration in Figure 6-1 shows an alternate design for inclusion of the gratings *in-plane* with the atomic force microscope tip. Compared to the current atomic force microscope cantilevers, in-plane actuation mechanisms can now easily be included, perhaps to serve as an additional control parameter. Moreover, the use of interference patterns with two input wavelengths will improve the detection resolution of the grating displacements.

6.2.2 Microphotonic elements for the strain-tunable platform

Tunable microring resonators The strain-tunable platform could also be implemented for tuning microring resonators. Tuning of a microring resonator through vertical dielectric slab perturbation on top of the microring has been demonstrated in the microwave regime, such as by Yun [166]. The perturbation of the field at the microring in the optical regime, however, requires vertical position control on the order of $\dot{A}$. Closed-loop feedback control with electrostatic capacitance sensing [112] or 0.1 $\dot{A}$ displacement[1] sensing with tunneling tips [100] are possibilities to implementation. Alternatively, for the fine displacement control, we could employ a bulk piezoelectric stack following Yun or thin-film piezoelectrics. The piezoelectric stack could provide the displacement range required, while with thin-film piezoelectrics, we could design a bimorph (or multimorph) structure to achieve the displacements necessary.

Another possibility, in the near term, would be to employ strain-tuning to the microring (or micro racetrack) resonators with the strain-tuning platform as previously illustrated in Figure 4-2. Trade-offs, subjected to design improvements, include tuning range, response times, system level integration, tuning uniformity and repeatability. For strain-tuning, the tuning in the optical response can be described simply as

$$\frac{\Delta\lambda}{\lambda} = n_{eff}\frac{\Delta L}{L} \tag{6.1}$$

where L is the resonator total round-trip physical length, ΔL the change in L with strain-tuning, n_{eff} the effective index [105], λ the resonant wavelength, and $\Delta\lambda$ the change in resonant wavelength. With n_{eff} order unity, the same fractional change in physical length is reflected in the resonant wavelength. This contrasts to strain-tuning in the photonic band gap silicon microcavity waveguide, as the strain is amplified mechanically through the stress concentration at the holes, resulting in larger optical fractional changes (order 2 - 3 times) for the same strain. For +0.1% strain (in the direction of the input and output bus waveguides) on a micro racetrack resonator, the majority of the change in length ΔL will be along the coupling length region. That is, $\frac{\Delta L}{L}$ will be less than, but close to, 0.1%. From Equation 6.1, this gives a $\Delta\lambda$ is approximately +1 nm for operation at 1.55 μm wavelengths.

[1]This high resolution is possible through the exponential dependence of the field on the gap between the tip and substrate.

This is comparable with thermal effects where a sensitivity of +0.11 nm/^{o}C is reported in GaAs [59]; that is, a 10 ^{o}C temperature increase gives approximately 1.1 nm increase in resonant wavelength. In Si, the change in refractive index through the thermo-optic effect $\frac{\Delta n}{\Delta T}$ is estimated to be 2×10^{-4} /^{o}C [29], which gives an estimate of $\Delta\lambda$ of +0.9 nm for a 10 ^{o}C temperature rise. In comparing piezoelectric strain-tuning and thermal tuning for micro racetrack resonators, the same evaluation (as mentioned in Section 1.1 and also on page 5.2.5) is valid: piezoelectric strain-tuning has a scalability advantage given each active device requires only on order nW power consumption, has faster time response on order MHz, and is able to achieve localized tuning below 10 μm spatial separation. The trade-off is the increased fabrication complexity, which includes thin-film PZT processing and microfabrication to define a floating membrane, which must be overcame. In the case of the micro racetrack resonators, the tunable range using either methods is about the same. For small number of tunable devices on an optical chip, thermal tuning is therefore probably sufficient; for high-density integrated optics with individual tuning of active devices required, piezoelectric strain-tuning is the better candidate.

Tunable Q for a 2D photonic band gap defect mode laser The strain-tunable platform could also be implemented for a defect mode laser microcavity. A laser microcavity with peak emission at 1.55 μm, modal volume of 0.03 μm^3 and Q of 250 was reported by Painter *et. al.* [117]. By elongating a line of holes (or fractional edge dislocation), Q can be tuned to above 1×10^4 [155], starting from a Q of $\sim 2 \times 10^3$. We can apply the strain-tuning concept for dynamic tuning of the laser microcavity Q, to compensate for fabrication mismatches in the elongated line of holes. In this example, the strain needs to be localized at the line of holes; a possible design is illustrated in Figure 6-2. The schematic is not drawn-to-scale: L_1 is $\gg$ than L_2, with L_2 on the order of 2 - 4 μm. A challenge to overcome in this particular pursuit is the need for strains to be on the order of a few percent for the modulation of Q. Large displacement and large force actuators would be necessary in this particular implementation.

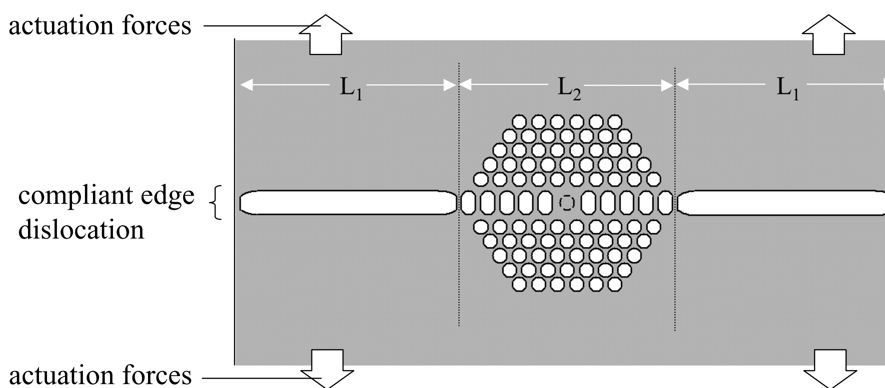

Figure 6-2: Design concept for localized strain, to perturb the elongated holes for dynamic tuning of Q for a 2D photonic band gap defect mode laser.

6.2.3 Tunable microcavity waveguide explorations

Dielectric slab perturbation for the microcavity waveguide Phase shifters, based on the vertical mechanical control of a dielectric slab to change the effective index, have been reported in the microwave and optical regimes [22, 91, 7, 73, 166]. This dielectric slab perturbation, at the time of writing, is actively pursued for tuning of microring and micro-racetrack resonators. This concept could also be applied to the microcavity waveguide. The trade-offs between the vertical and in-plane perturbation are as follows:

1. For vertical perturbation, there is the need for accurate vertical positional control of the dielectric slab due to the exponential dependence of gap separation.

2. For in-plane perturbation, there is the need to define the membrane and also physical deformation of the optical structure itself.

We illustrated in Figure 6-3 such a concept for the microcavity waveguide in the near term. The perturbed response is expected to have an exponential dependence on the gap between the waveguide and the dielectric slab. This is due to the evanescent field of the guided mode in the waveguide. This necessitates tight position control ($\sim \dot{A}$) at the smaller gap ($\sim$ 60 nm) distances. Electrostatic capacitance plates with feedback control can be used for actuation and sensing, in addition to the possibility of tunneling tips for displacement measurements. Piezoelectric transducers, either as a stack or in a bimorph structure, could also be used to achieve the fine gap control.

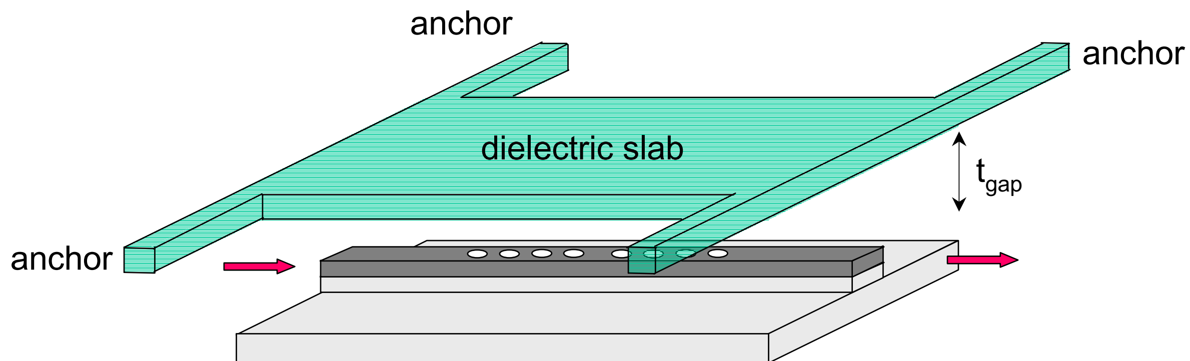

Figure 6-3: Vertical displacement of dielectric slab to perturb the field at the microcavity. Electrostatic capacitors plates with feedback control or piezoelectric actuators could be used to control the displacement.

The benefits of using dielectric slab perturbation with electrostatic capacitance plates control, compared to the developed piezoelectric strain-tuning design, are the following:

i. a possible larger tuning range, together with binary on/off switching,

ii. no necessity to strain actual device structure, nor a need for a floating membrane structure,

iii. immediate compatibility with Si processing (although piezoelectric aluminum nitride may be feasible in Si processes).

The disadvantages are mainly in the needed positional control of the slab, listed as follows:

i. a need for tight vertical displacement control (order $\dot{A}$) due to exponential dependence of the perturbed response on the gap

ii. a need for tight in-plane "parallel" motion – no out-of-plane tilt – to reliably control the effective index.

There is also the requirement to fabricate two layers, the dielectric slab and a sacrificial layer, although piezoelectric processing is arguably more difficult. A decision to choose dielectric slab perturbation would therefore, in my opinion, shift the uncertainty in successful device operation over to *control* of the dielectric slab, rather than fabrication of the piezoelectric material. In summary, under the current piezoelectric strain-tuning design, strain-tuning should be chosen if a reliable tuning range of order 10 nm is desired. For a wider tuning range (expected on order of 30 - 40 nm), dielectric slab perturbation should be attempted.

Large strain actuators and devices For large strain tunability on order of 1% (which corresponds to order 50 nm tuning range at 1.55 μm wavelengths), two variations could be included: (1) the use of integrated microscale strain-amplifiers with thin-film sol-gel PZT[2], and (2) the use of a polymer material as the optical confining medium and the deformable membrane for a large strain limit. In the first variation, the strain-amplifiers could be of geometry such as the moonie/bow/cymbal actuators reported [150, 20]. In the second variation, the use of a polymer might lead to a lower index contrast. Δn for polymer waveguides is typically on order of 0.6 reported at UV wavelengths [51], although Δn on order of 1.7 have been developed for polymer optoelectronics [48]. The latter index contrast is sufficient for modal localization of a possible resonance cavity.

The Haus hitless design for dynamic tuning of microcavity waveguides In addition to large strain tunability and dielectric slab perturbation possibilities, dynamic tuning of the microcavity resonance as an optical filter for demand-based reconfiguration would lead to optical signal losses during the tuning from one desired wavelength to the other. This requires a by-pass or "hitless" switch such that the signals would be transferred to another signal bus, during the filter reconfiguration. An invention by Professor H. Haus permits a "hitless" design during dynamic reconfiguration. Another possibility is to employ a $\Delta\beta$ waveguide optical switch that consists of two cascaded waveguide couplers, such as reported by Kogelnik and Schmidt [79]. The propagation constants in the waveguides, β_1 and β_2, are trimmed with an external applied electric field to effect power transfers between one or the other waveguide. For example, the cascaded couplers can be designed with length l and zero mismatch δ ($= \frac{\beta_1-\beta_2}{2}$) such that there is complete power transfer when there is no applied

[2]While single-crystal PZT will permit strains up to $\sim$ 1%, there is a practical issue on the process integration of such crystals with optical elements.

electric field. When an electric field is applied such that $\delta = \frac{\sqrt{3}}{2}\frac{\pi}{l}$, there is no power transfer between the two waveguides. These "by-pass" switches are explorations in the near term to enable the capabilities of the tunable microcavity optical filter.

Possible explorations with the static microcavity waveguide There are also possible future explorations with the static microcavity waveguide. A possible all-optical reflection switch with low switching energies on order of femtojoules was theoretically proposed with an asymmetrical microcavity waveguide [86]. Using GaAs material (or $In_yGa_{1-y}As$) for the defect and $Al_xGa_{1-x}As$ (or InP) for the waveguide, the authors suggested a reflection switch through absorptive (or dispersive) nonlinearities with an extinction ratio of $\sim$15 dB. Issues arises, however, on how to reduce reflection between the nonabsorptive-absorptive interface and the two orders of magnitude change in the absorption required. There exists the possibilities to pursue various geometries and materials.

In addition, the development of the microcavity towards waveguide intersections for virtually negligible cross-talk is a possibility. Reported in Johnson et. al. [69], the addition of a resonant cavity that respects the symmetry of two intersecting waveguides increases the throughput from 75% to 90%, when compared with a conventional waveguide intersection. The crosstalk decreases from 7% to 0.08%. The throughput is not unity, due to radiation losses at the intersection and direct coupling from the input port into the transverse ports. Intersecting waveguides with low cross-talk is a step towards the development of high-density integrated optical circuits.

6.2.4 Summary

In this section, we described future possibilities for strain-tuning, both for other microphotonic devices and for derived applications on the demonstrated tunable diffractive grating and the tunable photonic band gap microcavity waveguide. These illustrations show the wide-range applicability of strain-tuning, towards specific applications such as miniaturized spectrometry, dispersion compensators and tunable filters in DWDM optical networks, and integrated tunable filters and lasers in microphotonics platforms. In the latter application, the possibility of post-fabrication trimming relaxes the fabrication tolerances and the use of low-power piezoelectric microactuators allow for scalability in dynamic tuning to individual active devices on a high-density integrated optical chip. Though challenges remain for microphotonics to be as prevalent as microeletronics, piezoelectric strain-tuning is a meaningful step towards the physical realization of microphotonics platforms.

Appendix A

Fabrication Details Of Analog Tunable Gratings

This appendix describes the microfabrication process flow of the analog tunable piezoelectric-actuated gratings in detail. In addition, the mask layout for a single chip and a summary of the designs across the wafer are illustrated.

A.1 Detailed process of analog tunable gratings

DONS-15 Fabrication Process Flow

Version 1.15: December 06, 2001

Beginning substrate:
N-type <100> 4” Silicon wafers
Double-side polished, 425-475um thickness, TTV<3um, Bow&Wrap<10um, 1-50 Ω-cm

Step 1: **Create alignment and die-saw marks**

- Standard 1um resist (coater, TRL)
- Standard pre-bake (30mins, 90°C, prebake oven, TRL)
- Standard thin photo (EV1, ~3s, front-front, TRL)
- Standard post-bake (20min, 120°C, postbake oven, TRL)
- Standard 1um resist (backside resist protection, coater, TRL)
- Standard post-bake (20min, 120°C, postbake oven, TRL)
- 1-2um Si etch (AME5000 “Undoped-Poly-Etch”, ~80A/sec, ICL)
- Standard piranha (acid-hood, TRL)
- Standard RCA clean (rca, TRL)

Figure A-1: Detailed process conditions for analog tunable gratings (I).

Step 2: **Diffusion Barrier deposition**

Split process (**A**): Si-rich Silicon Nitride (VTR SiNx)
- Target deposition: 2000A, LPCVD
- Location: ICL VTR

Split process (**B**): Wet SiO_2 (thermal)
- Standard wet oxide growth.
- Target thickness: 2000A.
- Process time: ~**20 ± 1** mins. Total: ~2.5 hrs (including tube ramp up).
- Location: ICL oxidation tube

Step 3: **Create KOH backside mask**
- PECVD SiNx deposition on backside (for Split Process (B) wafers with SiO2)
  - Target deposition: 2000A (still just okay after 8hrs KOH) or more
  - Location: ICL Concept1 (or TRL Plasmaquest)
- Frontside resist protection (for the AME5000): 1um thin resist.
- RIE backside nitride
  - Location: ICL AME5000 (Chamber A and B: both **~40A/s**)
  - Note: for Split process (B), also need to etch $Si0_2$ layer (2000A) together. SiO2 etch rate ~30A/s. Over-etch.
- Standard piranha clean (acid-hood, TRL)

Step 4: **Ti/Pt Bottom Electrode Deposition and Lift-off**
(Gold-contaminated after this)
- Image Reversal photo and develop with AZ 5214
  - After HMDS, spin coat recipe: 6sec@0.5krpm, 6sec@0.75krpm, 30sec@5krpm to get ~1.8um photoresist.
  - Prebake (30min, 90°C)
  - Expose (EV1 with mask; 1.0 to 1.4sec; **1.0sec** preferred for DSP wafers)
  - Flat bake on hot plate in post-bake oven: (65 to 90sec, 120°C; **65sec** preferred for DSP wafer as better conduction)
  - Flood exposure without mask: (60sec on EV1)
  - Develop (MIF 422, ~**6-9mins** for perforated gratings) – no post-bake required
  - Target Linewidth: 2um
  - Location: TRL, coater / oven / EV1
- Standard e-beam deposition
- Target deposition: 200A Ti (Deposition rate: 1A/s) and <500°C substrate temperature
- Target deposition: 2000A Platinum (Deposition rate: 2A/s)
- Note: Use planetary plates for less contamination issues, though poorer lift-off profile.
- Note: Very clean surface needed. Ensure beam is centered by pushing cover to the side when loading wafers initially.
- Location: TRL e-beam
- Acetone lift-off on bottom electrode; followed by methanol and 2-propanol for cleaning.
- Ultrasonic ~2-3mins for quicker lift-off and clearing lift-off residues.
- Cleaning of solvents and contaminants with: acetone / methanol / 2-propanol and **multiple** rinse dumps.

Figure A-2: Detailed process conditions for analog tunable gratings (II).

Step 5: **PZT Deposition and anneal**

- Spin-coat Mitsubishi PZT sol-gel: Pb(Zr,Ti)O3 -- 15% PZT(118/52/48) A6 Type
- Location: new MTL PZT dedicated spin-coater in TRL

- PZT 1st deposition: spin-co at 500rpm for 3s, 1500rpm for 30s, hot plate drying (pyrolysis) at 350-400C for 5mins
    - Note: for 0.25um PZT layer, use 4 separate coatings, each ~0.06um
- Box furnace 1st Annealing: at 700C for 1min
- PZT 2nd deposition: spin-co at 500rpm for 3s, 1500rpm for 30s, hot plate drying (pyrolysis) at 350-400C for 5mins
- Box furnace 2nd Annealing: at 700C for 15min
    - Note: under 0.25um PZT layer, use just one time annealing at 700C for 15min

- Location: TRL PZT dedicated box-furnace

Step 6: **PZT Wet Etch Pattern**

- Pattern resist profile with 5um thick resist. 1um resist gives severe undercut.
- Wet etchant: 206 DI + 100 HCl + 16 BOE (7:1)
- Etching time: 90sec for 0.25um PZT layer. **~1min 50sec to 2mins 5sec** (max) for 0.5um PZT layer.

- Note: Wet etchant of HNO3 and BOE (for the HF) is also possible, though reagent and etch rate not characterized. Benefit is the HNO3 should not be attacking Ti, though BOE (with the HF) still does.
- Note: BOE in etchant also removes the PZT residue in the free space areas and the oxide, though PZT crack features engrained into Si substrate.

- Note: If dry etching of PZT:
    - (1) Cl2/BCl3=10/30 sccm ratio; 150W RF power; etch rate expected: 0.15um/min; resist etch: 0.27um/min
    - (2) Cl2/Ar=21/129 sccm ratio; 150W RF power; etch rate expected: 0.123um/min; resist etch: 0.47um/min
    - Location: EML Plasmatherm

Step 7: **Ti/Pt Top Electrode Deposition and Lift-off**

- Image reversal photo and develop
- Note: Standard lift-off procedures as for bottom electrode, though not as stringent, as much larger features. Developing time ~2-3mins

- Target deposition: 200A Ti (Deposition rate: 1A/s) and <500°C substrate temperature
- Target deposition: 2000A Platinum (Deposition rate: 2A/s)
- Note: Use planetary plates for less contamination issues, though poorer lift-off profile.
- Note: Very clean surface needed to match bottom electrode.
- Note: Ensure beam is centered by pushing cover to the side when loading wafers initially.
- Location: TRL e-beam

- Acetone lift-off on bottom electrode; followed by methanol and 2-propanol for cleaning.
- Ultrasonic ~2-3mins for quicker lift-off and clearing lift-off residues. Check for possible peel-off.
- Cleaning of solvents and contaminants with: acetone / methanol / 2-propanol and **multiple** rinse dumps.

Figure A-3: Detailed process conditions for analog tunable gratings (III).

Step 8: **Pt Gratings Deposition and Lift-off**

- Image reversal photo and develop
  - After HMDS, spin coat recipe: 6sec@0.5krpm, 6sec@0.75krpm, 30sec@6krpm to get ~1.8um photoresist.
  - Prebake (30min, 90°C)
  - Expose (EV1 with mask; 1.0 to 1.2sec; **1.0sec** preferred for DSP wafers)
  - Flat bake on hot plate in post-bake oven: (65 to 90sec, 120°C; **65sec** preferred for DSP wafer as better conduction)
  - Flood exposure without mask: (60sec on EV1)
  - Develop (MIF 422, ~**6-9mins** for perforated gratings) – no post-bake required
  - Target Linewidth: 2um
  - Location: TRL, coater / oven / EV1
  - Note: be sure to try DSP/diffusion barrier/Pt/Ti dummy wafers before real device.
- Standard e-beam deposition
- Deposition rate: 2A/s for device uniformity and <500°C substrate temperature
- Target deposition: 1580A +/- 10A Platinum (aim for 1500A as TRL e-beam might over-deposit.)
- Location: TRL e-beam

- Acetone lift-off at TRL, SolventHood; followed by methanol and 2-propanol and multiple rinse dumps for cleaning.
- Ultrasonic ~1-2mins for quicker lift-off and clearing lift-off residues, not more in case of peeling off.

Step 9: **Si backside KOH etch**
(Performed at Schmidt Group laboratory)

- Etchant: 20% KOH (3litre DI and 750g KOH pellets)
- Target etch depth: wafer etch-through of measured thickness (450 +/- 25um)
- Apiezon Wax W (black wax) protection, with quartz wafer or glass mask.
  Heat quartz/glass up to ~200F before applying thin wax layer vertically onto quartz/glass.
  Extend wax cover over edge of quartz/glass so that it will be fine after 8hr KOH etch.
  Place wafer / wafer part with device side to wax. Press softly on wafer part to remove air pockets on frontside.
  Seal carefully wafer edges with thick layer of wax.
  Cool down combined part slowly for good adhesion of wax to key regions of device.
- Etch condition: **6hrs 32mins at 75C** (etch rate: 1.06um/min to 1.10um/min; etches about 395um)
  (Break interval at about 3.5hrs to check adhesion of black wax and to wash under DI water. Re-strengthen black wax is necessary.)
  Followed by **~73-95mins at 65C** (etch rate: 0.6um/min). Approximated etch time is ~83mins.

- Note: To leave several microns of silicon remaining for RIE to release structure.
  Detection possible via Schmidt Group microscope under which the silicon punch-through areas become translucent. With PZT above, it actually fluoresces with a pink color.
- Note: Allow KOH bath to reach 75C before adding wafer. And allow bath to reach 65C before placing wafer in again.
- Removal of Apiezon Wax W with Xylene, trichloroethylene (TCE), or Toluene.
- Location: Schmidt Group KOHhood

Step 10: **Si backside RIE release etch**
(Performed at EML)

- Si etchant gases to remove remaining silicon layer.
- Note: place new clean wafer on device side (when device is flipped over) to prevent contamination.
- Note: if TRL Plasmaquest under etch recipe "Sietch.rcp", etch time is about 10 to 30mins. Do 5min stepwise check after the first 10mins.
- Location: EML Plasmatherm

Figure A-4: Detailed process conditions for analog tunable gratings (IV).

A.2 Mask layout and design summary of analog tunable gratings

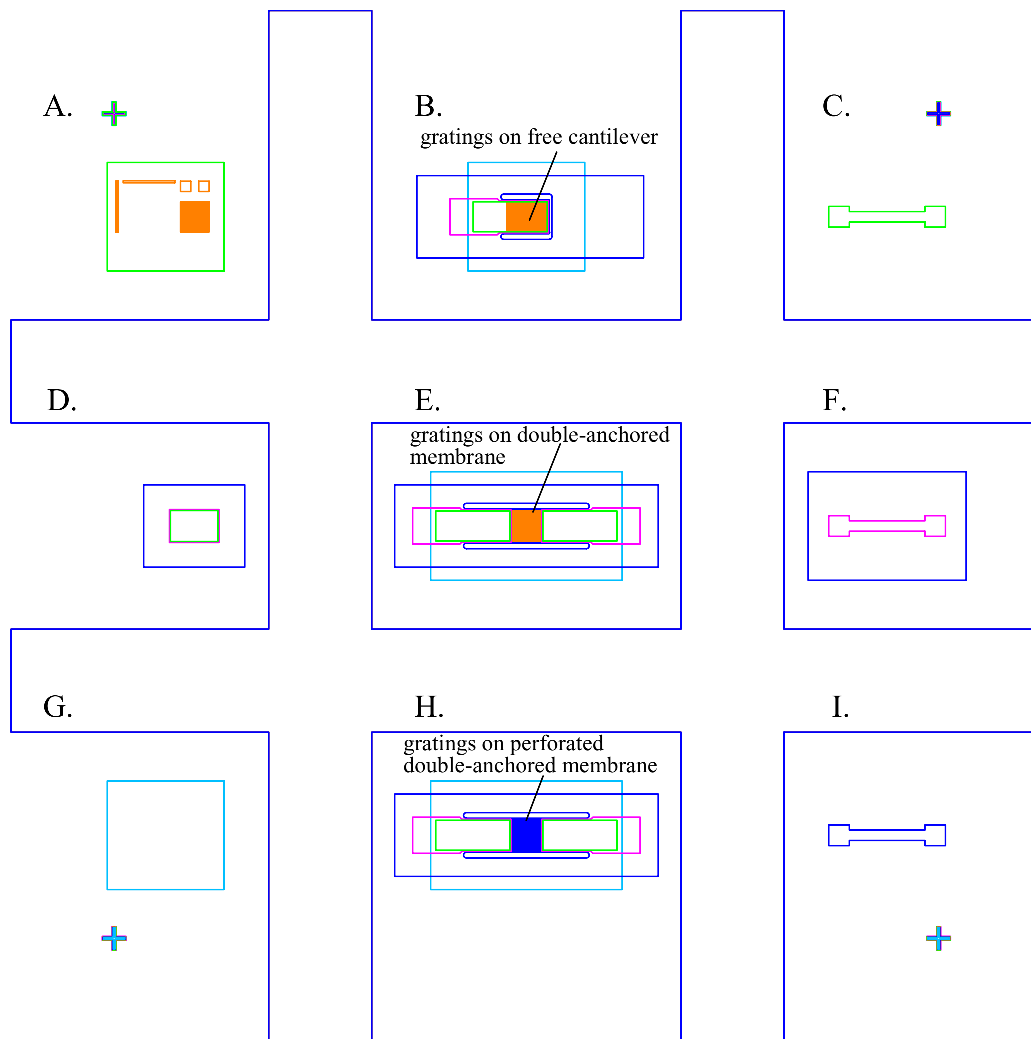

Figure A-5: Mask layout for a single chip with analog tunable gratings: (A) Test element for 2 μm diffractive gratings lift-off, (B) Device: free cantilever with gratings, (C) Test element for Pt top electrode, (D) Test element for Pt-PZT-Pt structure, (E) Device: double-anchored membrane with gratings, (F) Test element for PZT-Pt structure, (G) Test element for backside KOH, (H) Device: perforated double-anchored membrane with gratings, (I) Test element for Pt bottom electrode.

June 3, 2001

DONS-14 Mask Set Summary

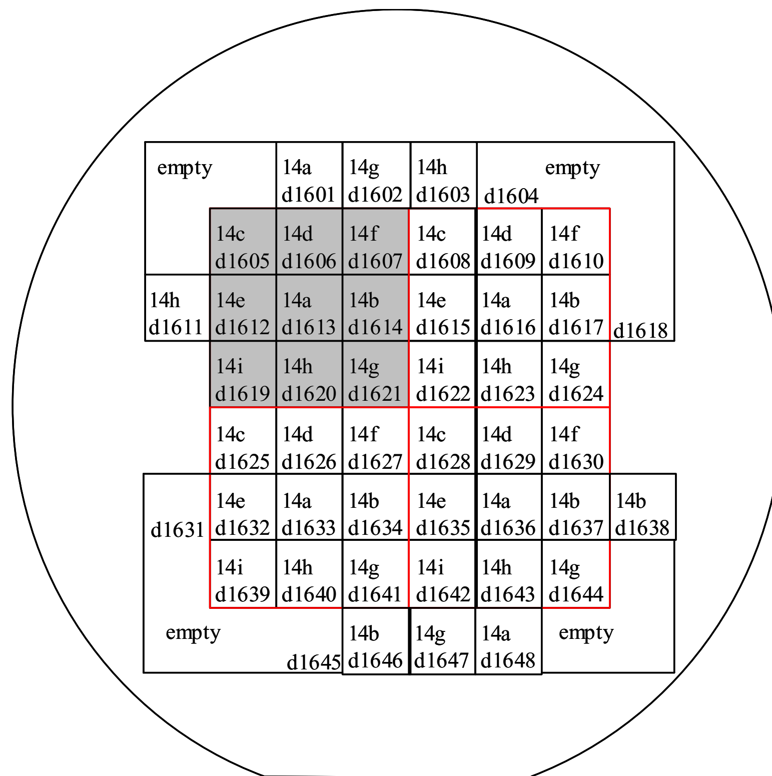

DONS-14a: - Primary structure
- 2 µm grating
- 450 µm PZT length
- 150 µm contact pad
- separated perforated membrane

DONS-14b: - like primary structure, but with separated contact pads
- separation gap: 10 µm

DONS-14c: - like primary structure, but with crab-like perforated membrane
- 6 µm period grating, instead of 2 µm, for more mechanical strength

DONS-14d: - water-immersible active cantilevers

DONS-14e: - like primary structure, but with 500 µm contact pads

DONS-14f: - like primary structure, but with 200 µm PZT length

DONS-14g: - like primary structure, but with 200 µm PZT length and 500 µm contact pads

DONS-14h: - like primary structure, but with 200 µm PZT length and 500µm contact pads
- and with separated contact pads

DONS-14i: - like primary structure, but with 200 µm PZT length and 150 µm contact pads
- and with 4 µm grating period

Figure A-6: Summary of design matrix for analog tunable gratings. Shown also are the locations of the chips on a wafer. A water-immersible active cantilever is also included in the design and fabrication.

Appendix B

Other Design Considerations Of The Photonic Band Gap Microcavity Waveguide

This appendix reiterates and highlights design considerations on the high-contrast dielectric waveguide, as analyzed by Foresi, Lim and Lee *et. al.* [32, 93, 90], and the microcavity photonic crystal as analyzed by Fan [27] – two of the building blocks of the tunable microcavity waveguide.

B.1 Design considerations on high-contrast dielectric waveguide losses

The waveguide primary design has an index contrast of ~ 2.0, 200 nm thickness and 500 nm width. This cited thickness permits only the fundamental TE (electric field in horizontal plane of waveguide) mode to be guided. The TE mode profile, as illustrated by Foresi [32], is well-confined although more so vertically than horizontally. With the higher mode amplitude at the sidewalls than the top interface, thus, sidewall roughness is pertinent to determining waveguide losses in this primary design.

Sidewall losses were considered with the following three effects: (1) roughness amplitude and auto-correlation length [90], (2) cladding index, and (3) wavelength dependences. For a root-mean-square sidewall roughness of 1 nm and a auto-correlation length of 10 nm, a loss of 0.1 dB/cm is theoretically estimated by Lee [89]. Sidewall roughness also accounts for polarization dependent losses, with preferential attenuation in the TE mode [93].

The buried oxide insulator layer strongly defines the waveguide losses. As shown in Figure B-1 from Foresi's work [1], an oxide thickness of order 700 nm is needed to limit losses,

[1] The losses are calculated with the Beam Propagation Method [54] where the eigenmodes are first found from a waveguide without the substrate.

due to extension of the mode into the substrate, to less than 1 dB/cm.

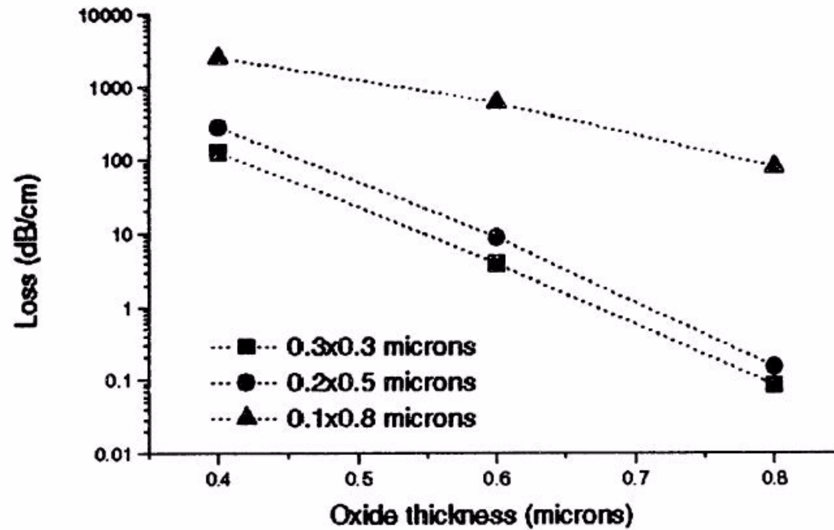

Figure B-1: Waveguide losses, from mode extension into substrate, against buried oxide insulator thickness for various waveguide geometries as calculated by Foresi [32].

The device material is also selected, from the currently available technologies, to minimize losses. The possibilities are Unibond (hydrogen implantation and wafer bonding), PolySi (amorphous silicon deposition and annealing), BESOI (wafer bonding and etch back) and SIMOX (oxygen ion implantation) substrates. The following effects are considered in the device layer for low losses: (1) top surface roughness, (2) thickness uniformity, and (3) defect and doping levels. SIMOX wafers typically have thinner oxide thickness – below the 700 nm desired – due to the direct oxygen implantation technique. BESOI wafers typically have thicker device layers than required, with large thickness variations (on order of 10%). They also have high free carrier concentrations on order of 10^{18} cm^{-3}, leading to higher losses. PolySi, annealed after deposition to produce a lower surface roughness, has a lower crystallinity than single-crystal Unibond and thus higher losses, although it has the advantage of being able to contribute in multi-layer device structures. Unibond wafers are capable to reach the desired device layer and oxide layer thickness, with low free carrier (10^{15} cm^{-3}) and defect concentrations (10^{5} cm^{-2}). With these considerations, Unibond wafers are chosen for initial concept demonstration. The wafers are chosen with device layer thickness close to 200 nm, oxide thickness at least 1 μm, top surface roughness controlled to less than 1 nm, and low free carrier and defect concentrations.

B.2 Effects of variation on primary photonic crystal design

The effects of random disorder on the microcavity waveguide is briefly discussed by Joannopoulos [61]. The disorder could arise in the device fabrication, such as the Cr lift-off or reactive ion etching steps. For disorders at 5% waveguide width (or 23 nm of a 468 nm width), there is still little effect on the resonance Q. This is due to: (1) the small fraction of the disorder length compared to the wavelength, and (2) the concentration of the energy at the middle of the cavity and hence little effects from variation at boundaries.

Q, as described in Section 4.3.3, is dependent on the number of holes on each side of the microcavity. In the Fabry-Perot analogy, as the number of holes increases, the effective dielectric mirror reflectivity increases and thus the resonance finesse increases. In the double potential barrier tunneling analogy, as the number of holes increases, the potential barrier increases. The Q increase together with the number of holes is seen in a computation by Fan [27], as reiterated in Figure B-2. In this particular plot, Q is found to be 271 for three holes on each side of the microcavity[2]. As even more holes are added (more than six on each side), there is more significant coupling to the continuum modes and there will be light leaking outwards. Therefore, there is an optimal number of holes for the microcavity waveguide.

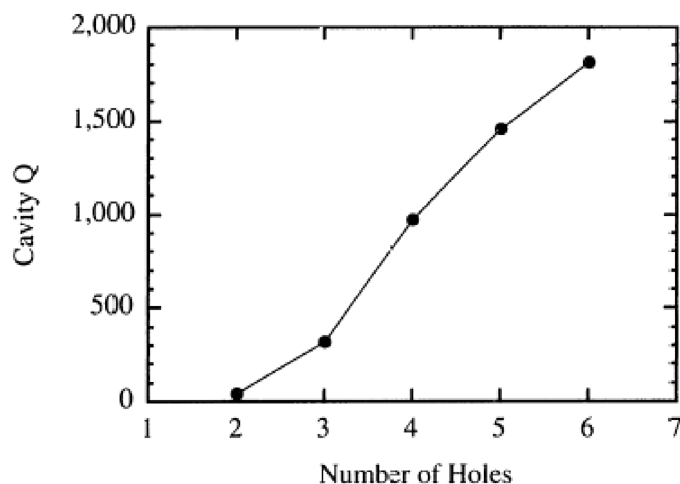

Figure B-2: Quality-factor Q against the number of holes on each side of the microcavity, as calculated by Fan [27].

A design for a TM-like mode in the microcavity is also suggested in Fan [27]. Essentially, this consists of rotating the microcavity waveguide by 90°. The electric fields are now predominantly in the vertical direction, with the first band (lowest frequency mode)

[2]This Q is computed for an air-bridge design. Q computed for a monorail is cited as 172 [27].

concentrated in the dielectric (just as before). To ease planar fabrication of the TM-like microcavity, the holes, standing on its side, could be replaced with vertical rods from reactive ion etching. With such rods, the dielectric material will be disconnected and the band gap smaller, although TM-like resonant modes are now possible.

B.3 Computational scheme for strain-perturbation on microcavity waveguide

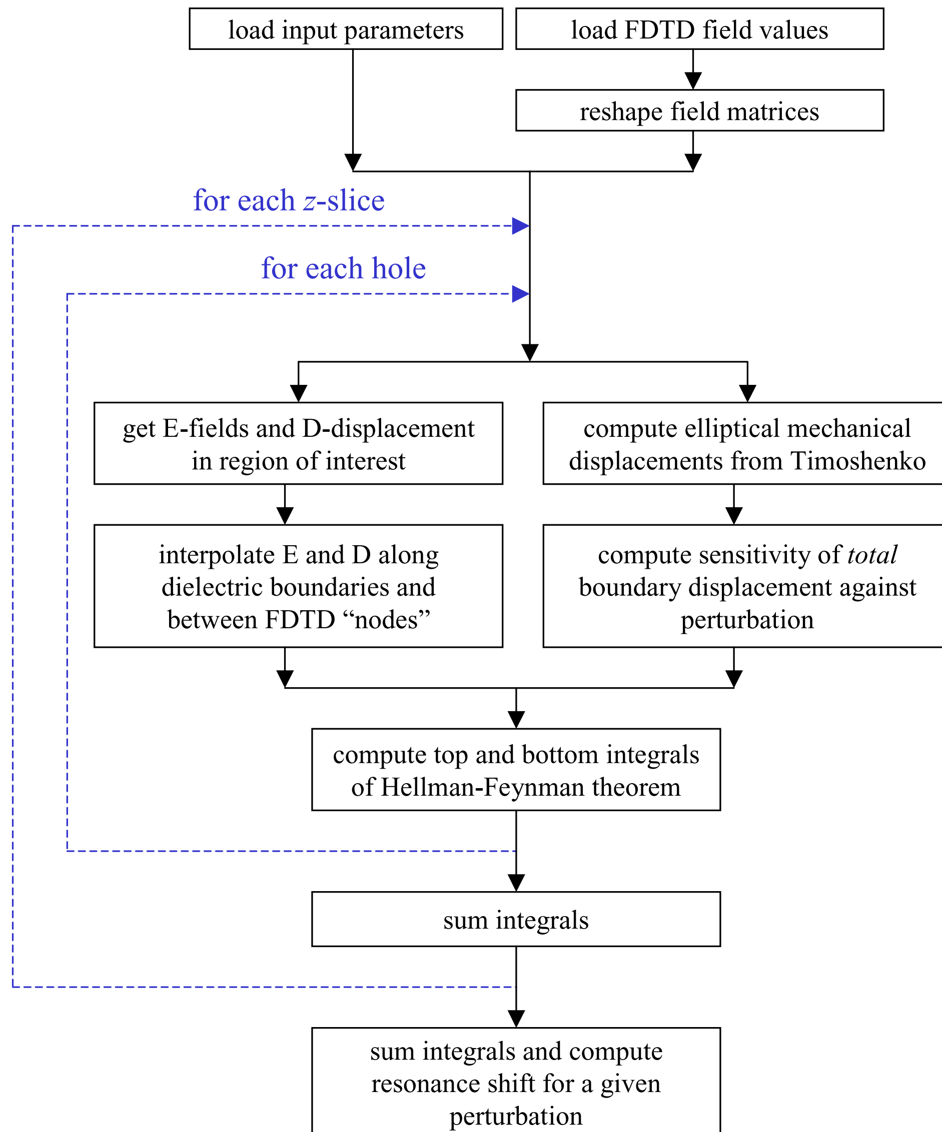

Figure B-3: Summary of computation scheme for strain-perturbation on microcavity waveguide for a given perturbation.

Appendix C

Fabrication Details Of Photonic Band Gap Microcavity Waveguide

This appendix describes the micro- and nano-fabrication processing of the strain-tunable photonic crystal in detail, along with considerations in process integration. The contents of this appendix are:

1. Detailed process flow of strain-tunable photonic crystal. The process to create X-ray masks is briefly mentioned.
2. Mask layout for a single chip, depicting locations on the chip.
3. Optimized etch results for high-contrast dielectric waveguides.
4. Electron beam lithography dosage variation and design matrix for microcavity waveguides.

C.1 Detailed integrated process flow of strain-tunable photonic band gap microcavity waveguide

ATPC-1-11 Fabrication Process Flow

Version 1.3: Jun 27, 2002	Version 1.4: Jul 22, 2002	Version 1.5: Sep 12, 2002
Version 1.6: Oct 04, 2002	Version 1.7: Dec 25, 2002	Version 1.8: Dec 27, 2002
Version 1.9: Feb 14, 2003	Version 1.10: Feb 22, 2003	Version 1.11: March 22, 2003 (final)

Beginning substrate: Unibond 4" SOI wafers from SOITEC, 2000A FZ active Si material (surface roughness RMS <2A and max-min <15A); 10,000A buried oxide; 525µm CZ <100> SSP P-type substrate with <100 dislocations/cm^2

Stage A: Substrate preparation

Step 1: **CMP polishing of backside SOI**

- 5um AZ 4620 thick resist deposition on front-side as protection during CMP (coater, TRL)
- CMP polishing of backside (CMP, ICL)
- Double-piranha after CMP for entry back into TRL

Step 2: **Create Si trench for PZT and alignment marks** – mask: atpc18trench

- Standard 1um OCG 825 resist (coater, TRL)
- Standard pre-bake (1 hr, 90 °C, prebake oven, TRL)
- Standard thin photo (EV1, ~20 s, front-front, TRL)
- Standard post-bake (30 min, 110 °C, postbake oven, TRL)
- Standard 1um resist (backside resist protection, coater, TRL)
- Standard post-bake (30 min, 110 °C, postbake oven, TRL)
- at least 0.2 µm Si etch (STS1 "stshallo.set" recipe, etch rate ~ 0.2 µm/min: do two minutes for over-etch)
- Standard asher (asher, TRL)
- Note: Si trenches are for PZT to be in contact with SiO_2 membrane

Step 3: **Create SiN_x backside mask for KOH** – mask: atpc18koh

- PECVD SiNx deposition on backside
  - Target deposition: 3000 A (okay for 8hrs KOH)
  - Location: ICL Concept1 (or TRL Plasmaquest)
- Frontside resist protection (for the AME5000): 1um thin resist.

Figure C-1: Detailed process conditions for strain-tunable photonic band gap microcavity waveguide (I).

Process is Au-contaminated after this step

- RIE backside nitride
  - Location: TRL Plasmaquest ("etchSiN.rcp": etch rate **~ 5 – 10 A/s**)
- Standard piranha clean (acid-hood, TRL)

Stage B: Create thin-film PZT actuators

Step 4: **Patterning of Pt bottom electrode** – mask: atpc18bte (use backside alignment)

- Image-reversal photoresist development (per Endnote)
- Standard E-beam deposition
- Deposition rate: 1 A/s for device uniformity and <500 °C substrate temperature
- Target deposition: 2000 A Pt and 200 A Ti
- Location: TRL, Ebeam
- Note: use aluminum foil and drop of resist to protect alignment marks so that no overlap of alignment marks.
- Note: place Pt bottom electrode close to waveguide to reduce amount of oxide etching in membrane. Pt bottom electrode should not be too close to waveguide, to prevent coupling between metal and dielectric.
- Note: use Pt/Ti target source each time for excellent bottom electrode quality

Step 5: **PZT deposition**

- Spin-coat Mitsubishi PZT sol-gel: $Pb(Zr,Ti)O_3$
- Location: TRL PZT dedicated spin-coater
- PZT deposition: spin-coat at 500 rpm for 3 s, 1500 rpm for 30 s, hot plate pyrolysis at 350 C for 5 mins
- Note: ~ 0.2 μm PZT layer per coat (thick sol)
- Location: TRL PZT dedicated coater

Step 6: **PZT patterning** – mask: atpc18pzt (use backside alignment)

- Pattern AZ 4620 resist profile with 5 μm thick resist. 1 μm resist gives severe undercut.
- Wet etchant: 200 DI + 100 HCl + 15 BOE (7:1)
- Etching time: ~ 5 sec for 0.3 μm unannealed PZT
- Note: depending on the sol and conditions, some wafers require up to 90 sec for 0.25 μm PZT layer. **~2 min** (max) for 0.5 μm PZT layer.
- Note: Wet etchant of HNO_3 and BOE (for the HF) is also possible, though reagent and etch rate not characterized. Also HNO_3 / HF / CH_3COOH solution is an isotropic etching solution for Si [Robbins and Schwartz].
- Benefit is the HNO_3 should not be attacking Ti (HCl does), though BOE (with the HF) still does slightly.
- Note: the diluted BOE etches ~ 10 – 20 nm of oxide.
- Note: use acetone / methanol / iso-propanol to remove photoresist, though asher is possible (though unsure of effect on PZT)
- Note: after DI water wash, dry on hot plate at 100C for about 15 mins to remove any possible solvent.

Step 7: **PZT annealing**

- Place wafer on annealing boat, and both on hot plate at 350 C for 5 mins, as intermediate heat-up step.
- Box furnace annealing: at 650 C for 30 mins (or 700 C for 15 mins, with larger thermal shock).
- After annealing, open furnace and move boat out onto opened furnace door and leave it there for ~ 1 min.
- Then place on 350 C hot plate for 5 mins, as intermediate cool-down step.
- Then place on 75 C hot plate for 5 mins, to step down cooling.
- Note: 15 min thermal oxidation at 700 C has ~5.5 nm oxide growth on Si waveguide
- Location: TRL PZT dedicated furnace

Figure C-2: Detailed process conditions for strain-tunable photonic band gap microcavity waveguide (II).

Step 8: **Patterning of Pt top electrode** – mask: atpc18tope (use backside alignment)

- Image-reversal photoresist development (per Appendix)
- Standard E-beam deposition
- Deposition rate: 1 A/s for device uniformity and <500 °C substrate temperature
- Target deposition: 2000A Platinum and 200 A Ti
- Location: TRL, Ebeam

Step 9: **RIE Patterning of SiO_2 membrane** – mask: atpc18oxide (use backside alignment)

- Standard photoresist development
- Thickness of SiO_2 membrane is ~ 200 nm
- Recipe: "etchSiO2.rcp" (CF_4/ He/ H_2 / 100W); etch rate: ~ 5A/s.
- Location: TRL, Plasmaquest
- Note: SiO_2 etching only now instead of before bottom electrode deposition, so as to prevent step-height in image reversal resist during bottom electrode processing. But should be okay for before bottom electrode deposition too.
- Note: SiO_2 area is covered under PMMA during X-ray lithography so the area will not be covered by Cr.
- Cleave wafer into quarters for usage with NSL X-ray Head5; target mount on 3" handle wafer with thick resist.

<u>Stage C: in Nanostructures Laboratory to create photonic crystal waveguide</u>

Step 10: **Creation of Cr mask through X-ray lithography of PMMA** – PBG v2.1 X-ray mask

- PMMA (positive resist) spun onto SOI wafer - 3krpm 60sec coating for 230nm PMMA
- "Mother" and "daughter" mask created in NSL, see Appendix
- Daughter mask brought into close contact with substrate, with Al studs for separation
- Under 20x objective for alignment (+/- 2-3 µm needed) done with X-ray Head5: 20x used for sufficient magnification and sufficient depth-of-view
- X-ray exposure of PMMA: ~21.5 hrs on Head5 with piezoelectric z-control stage; source-to-substrate distance is ~ 12 cm; O_2 ppm ~ 200; vacuum < 1 x 10^{-6}; 27 – 30 hrs in X-ray Head1
- PMMA developed in methyl-isoButane-ketone:iso-propanol (1:2) at 21°C for 20 – 90 sec; monitor PMMA development with AFM
- 500A Cr evaporated onto sample
- Lift-off of Cr, through 1-methyl-2-pyrrolidinone dissolving of PMMA at 90°C, to form Cr mask. Ultrasound in lift-off for ~ 2 mins, while holding on beaker.
- Location: NSL X-ray Head 5, NSL evaporator, NSL flow hood

- Note: PMMA developer does not affect PZT properties as it is a solvent.
- Note: PMMA covers top electrode region so there is no adhesion of Cr to Pt area.
- Note: 10dB Au absorption above PZT actuators to prevent any damage to PZT
- Note: 500nm PZT will lead to increase separation, but will not affect X-ray fidelity on waveguide width and holes
- Note: After PMMA exposure and also after Cr lift-off, check alignment before Si etch.

Figure C-3: Detailed process conditions for strain-tunable photonic band gap microcavity waveguide (III).

Step 11: **Si waveguide RIE** – Cr hard mask, inverse of PBG v2.1 X-ray mask

- Etch plasma: CF_4 / O_2 (13.5 sccm / 1.5 sccm) with 10 mtorr pressure and 300 V DC bias
- Power, though not controllable, is ~ 120 W.
- Etch time: ~ 15 mins. This is longer than test structure as Si etch is highly non-uniform with Pt electrodes near to Si waveguide. This extra-timed etch is to make sure the Si is etched distinctly.
- On test structures (without Pt electrodes beside waveguide) etch rate: ~ 19 – 26 nm / min, with total etch time of ~ 478 – 660 sec (depending on power) for 212 nm waveguide
- Follow up with a SiO_2 etch, using CHF_3. Etch rate: ~ 50 nm / min. Etch about 3 - 5 mins for 0.3 µm deep into oxide.
- SiO_2 etch recipe: 300V (controlled), 138W, 15 sccm CHF_3, 10 mTorr.
- If necessary to do a trim etch (to thin down the Si waveguide thickness), do it after the Cr mask removal, for not more than 1 min. Etch rate is ~ 19 – 26 nm / min for our etch recipe.
- Location: NSL Plasmatherm

- Note: place thick photoresist with cotton swabs on alignment marks to prevent them from getting etched away.
- Bake thick resist for 60 mins at 90C.
- Note: CF_4 / O_2 RIE for 15mins in Plasmatherm did not affect any of the PZT properties. There seems to be a deposition over the PZT (resulting in different visual color of the PZT), but electrical properties after CF_4 / O_2 RIE still fine. Substrate temperature should be kept low for precaution. Also, Cl_2/BCl_3 (20/20 sccm) is used as plasma-etch for PZT.

Step 12: **Removal of Cr mask**

- Wet-etch removal of Cr mask
- Etchant: perchloric acid (HClO4) and ceric ammonium nitrate Ce(NH4)2(NO3)6
- Do "descum.rcp" in NSL Plasmatherm for 4 mins before the Cr etch, in order to wet-etch remove the Cr cleanly.
- With "descum.rcp", Cr etch takes about 2 mins. Without "descum.rcp", Cr does not etch cleanly and takes at least 15 mins.
- Location: NSL flow hood
- Note: PZT etchant is HCL/BOE or HNO_3/BOE.
- Note: etchant does not attack PZT / Pt / Ti films after placing it in for 15 mins.

Figure C-4: Detailed process conditions for strain-tunable photonic band gap microcavity waveguide (IV).

Stage D: Creation of thin-membrane and cleaving of Si waveguides

Step 13: **Pattern** photoresist for XeF2 protection – mask: atpc18oxide
- Note: photoresist work is done before die-saw and XeF2 to have rigid substrate to work on
- Note: pattern resist by mounting quarter wafer (with tape) on full wafer chuck, so that vacuum still okay!
- Note: use sectional alignment marks for quarter-wafer alignment.
- Only 5 µm thick resist to be used because of contour profile in device. (Thin resist is attempted but does not develop away in the oxide trench region.) Develop time of thick resist not more than 2 mins, as uneven resist profile will be remove for longer than 2 mins development time.
- Photoresist **must** cover input/output faucets of Si 2000A waveguide (as protection and for XeF2 release etch)
- Photoresist **must** cover top *and* bottom electrode so that XeF_2 does not attack Ti layer of top *and* bottom electrodes, causing separation
- 5 µm standard photoresist development (5 µm resist is able to withstand a 4 hr XeF_2 etch)
- Location: TRL, EV1

Step 14: **Partial die-saw for aligned wafer cleaving**
- Partial depth die-saw to allow easy cleaving as the final step, especially with membrane already released in final step. Cleave in the other direction before die-saw in orthogonal direction. Die-saw through full-length of device.
- Flip substrate upside-down to allow backside to be reached. Use three UV tape (each 268 µm) to create physical separation between the substrate and the die-saw chuck.
- Single wafer die-saw (mode C), with 176 µm Si depth remaining after die-saw. Do not blow air-gun into substrate as this will cleave substrate.
- Note: cleaving must be final step, so that photoresist will be protecting entrance of waveguide during XeF_2 release.
- Location: ICL die-saw

(Step 14b: **Polish waveguide facet**)
- Waveguide polishing performed with vertically mount for polishing
- Protect with resist against residue on waveguide and photonic crystal holes
- Location: Akinwande group
- Note: yield possibly low with breaking of thin membranes, even with photoresist support.
- Wafer cleaving with partial die-saw produces sufficient clean cleavage for coupling into waveguide.

Step 15: **XeF_2 dry-release of membrane, dry-ash of resist and cleave**
- Etch-rate for release of membrane: ~ 10 µm / min.
- Note: use 10 sec for XeF_2 transfer time and 60 sec for etching time, with 120 sec venting time.
- Note: do Plasmaquest oxide RIE of ~ 10 mins to remove any native oxide before XeF_2 etch.
- Note: ~ 6 – 10 cycles to release structure.
- Note: Etch-rate depends on open surface area, and can be anywhere between 1 – 15 µm/min.

- use TRL asher to remove resist. Ashing time for 5 µm thick resist: 60 mins removes resist.
- Note: do not over-ash (i.e. not more than 60 mins), as over-ash might etch away the Si waveguide.
- Option 2 to remove resist - O_2 plasma at NSL Plasmatherm. Possibility of burning resist, affecting waveguide facet, and unsure of resist removal in sub-micron holes of waveguide.
- Option 3 to remove resist – Wet removal with acetone / methanol / iso-propanol. Possibility of breaking fragile membrane and remaining solvent on waveguide facet. Surface tension at sub-micron holes should not result in solvent remaining (as wet-etch used to remove Cr in X-ray litho).

- Cleave partially die-sawed chip, using glass slides and tweezers.

Figure C-5: Detailed process conditions for strain-tunable photonic band gap microcavity waveguide (V).

Endnotes

Image Reversal photo and develop (with AZ 5214E)

- Standard 1um coating line (after HMDS)
- Prebake (30min, 90°C)
- Expose (EV1 with mask)
- Flat bake (90sec, 120°C)
- Flood exposure (60sec on EV1)
- Develop (MIF 422, 1min until clear) – no post-bake required
- Target Linewidth: 2um
- Location: TRL, coater / oven / EV1

X-ray "mother" mask creation

- 3.0 um thick SiN_x membrane supported on pyrex ring
- Spin-coat 2500A PMMA mask mask (3krpm spinning of 3% PMMA with ~ 230nm PMMA thickness)
- Direct write e-beam to create *negative* feature in PMMA

- (Field size of e-beam is ~ 125um with pixel sizes of 7.0nm)
- (Length of waveguide ~ 2.0mm; with facet (7um at opening end) and 6° tilt)
- (Mask layout consists of straight WG, PBG WG and microcavity PBG WG)
- Control of field stitching is important for features greater than field size.

- Develop of PMMA
- Thin-layer of metallization on SiN_x membrane to provide contact for electroplating
- Resulting features filled with 2000A Au by electroplating (NSL, ~ 20nm / min plating rate)
- Au provides ~10dB of absorption for incident x-rays from Cu source

X-ray "daughter" mask creation

- 3.0 um thick SiN_x membrane supported on pyrex ring
- Aluminum studs evaporated onto daughter mask (after completion of PMMA / electroplating development)
- PMMA spun onto daughter mask (2.5krpm spinning of 3% PMMA with ~ 250nm PMMA thickness)
- Mother mask brought into close proximity to daughter mask

- Exposure of PMMA, though mother mask, with x-ray to transfer pattern
- Daughter mask developed and electroplated to form the correct polarity for pattern transfer

Figure C-6: Detailed process conditions for strain-tunable photonic band gap microcavity waveguide (VI).

C.2 Mask layout of strain-tunable photonic band gap microcavity waveguide

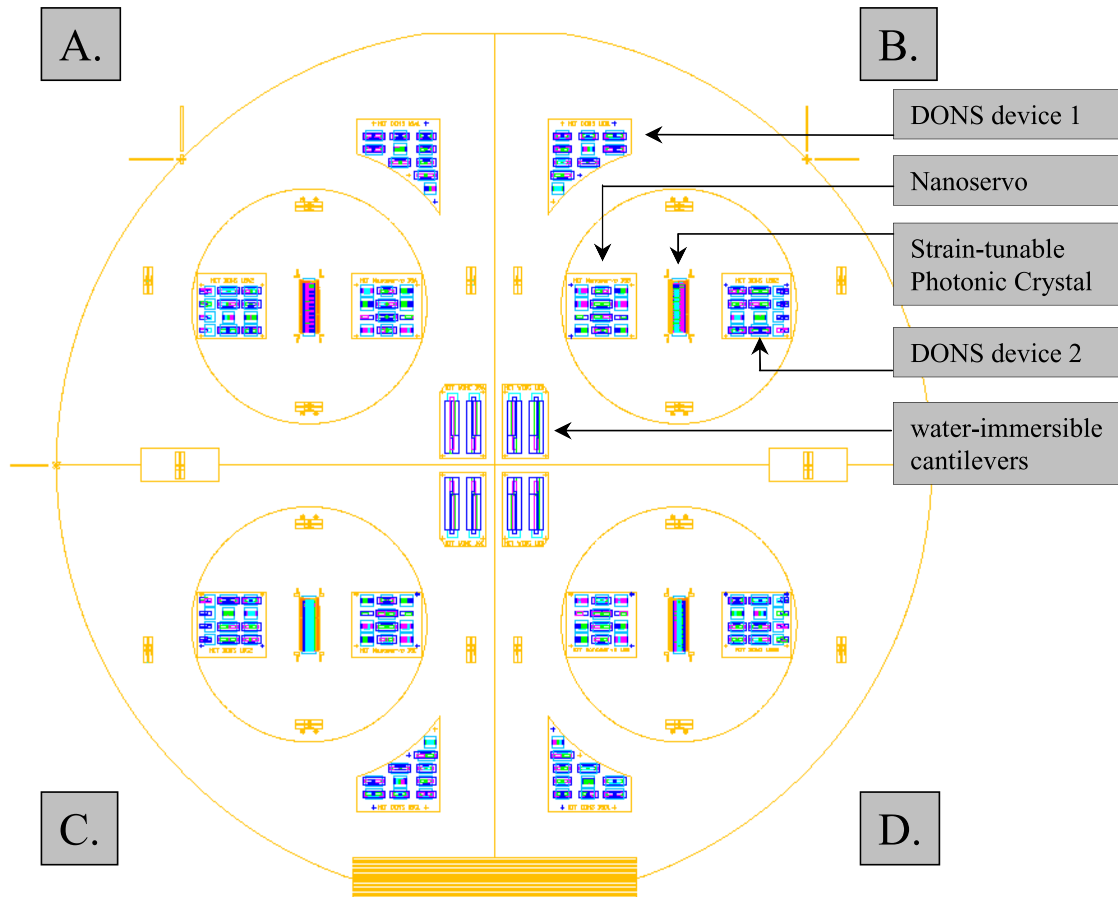

Figure C-7: Mask layout with mirror-symmetrical (horizontal and vertical) segments A,B,C, and D on the wafer. The five different chips in each segment, as labeled, are: (a) strain-tunable photonic crystal, (b) DONS device 1, (c) DONS device 2, (d) Nanoservo, and (e) water-immersible cantilever. The space layout on the mask is designed to be compatible with the X-ray masks.

C.3 Optimized RIE conditions for high-contrast dielectric waveguide

200 sec, with 393 V and 265 W

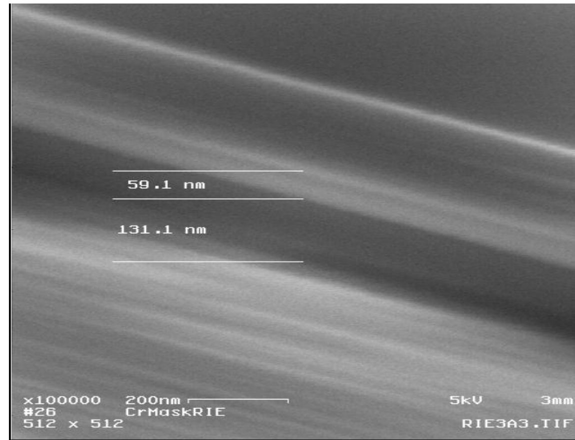

340 sec, with 393 V and 267 W

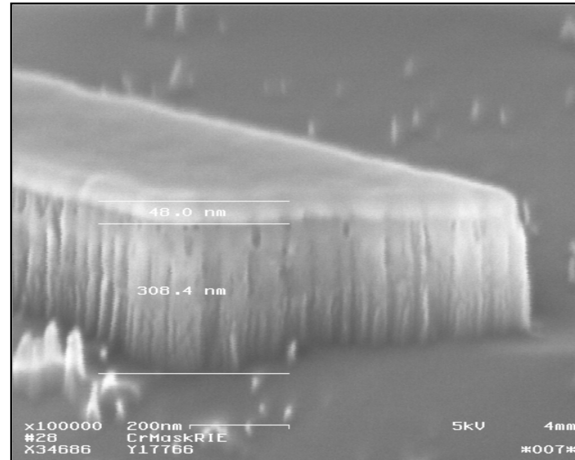

Figure C-8: Etch conditions: CF_4 / O_2 at 13.5 / 1.5 sccm ; 20 mtorr; 400 V DC bias. Etch rate: 52 nm/min.

200 sec, with 294 V and 194 W

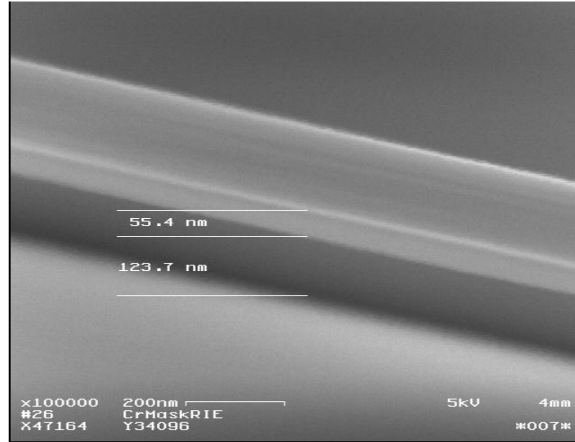

340 sec, with 293 V and 195 W

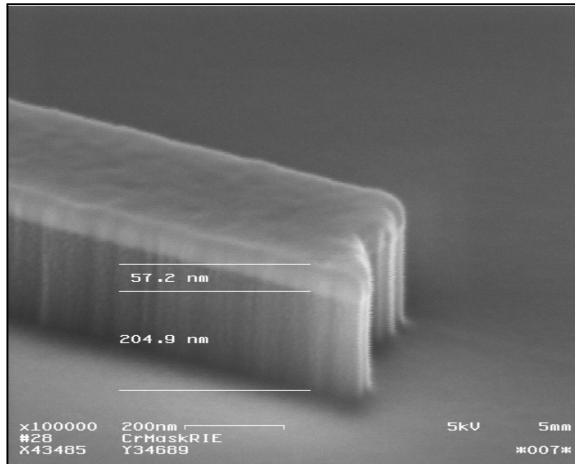

Figure C-9: Etch conditions: CF_4 / O_2 at 13.5 / 1.5 sccm ; 20 mtorr; 300 V DC bias. Etch rate: 36 nm/min.

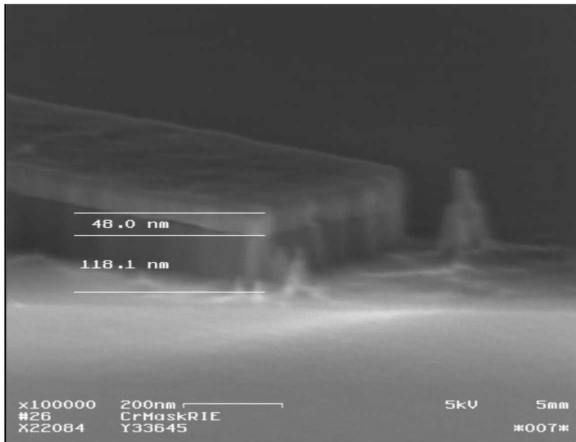

200 sec, with 295 V and 191 W

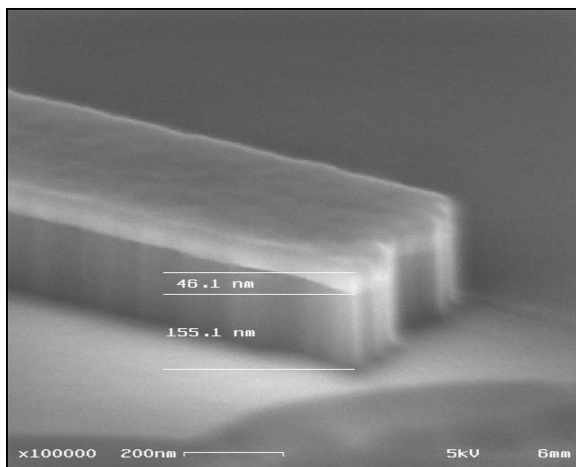

340 sec, with 293 V and 189 W

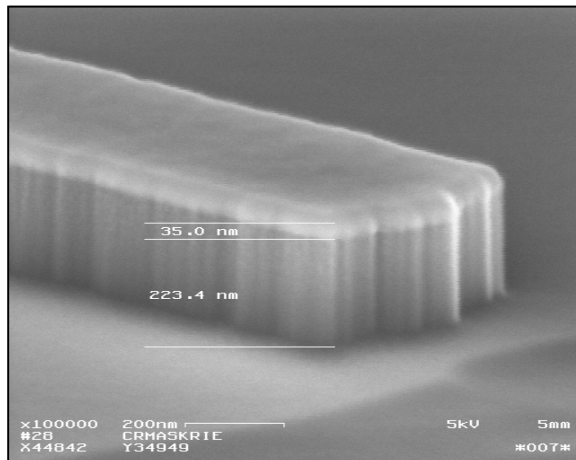

520 sec, with 294 V and 193 W

Figure C-10: Etch conditions: CF_4 / O_2 at 13.5 / 1.5 sccm ; 10 mtorr; 300 V DC bias. Etch rate: 20 -26 nm/min.

C.4 Electron beam lithography for microcavity waveguides

A. 446 μC/cm² (430 KHz)

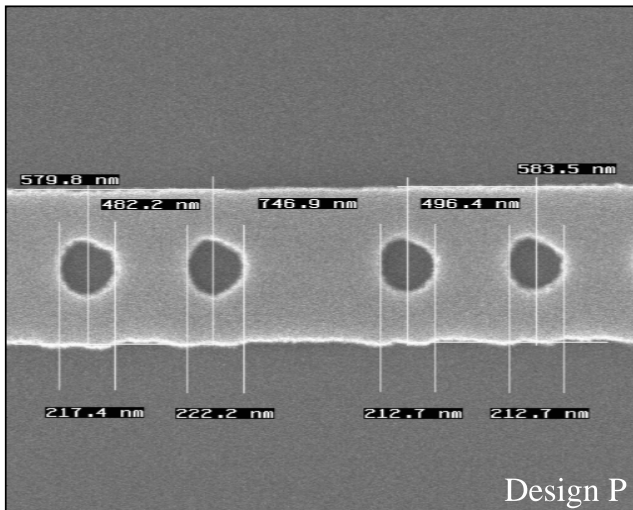

B. 400 μC/cm² (480 KHz)

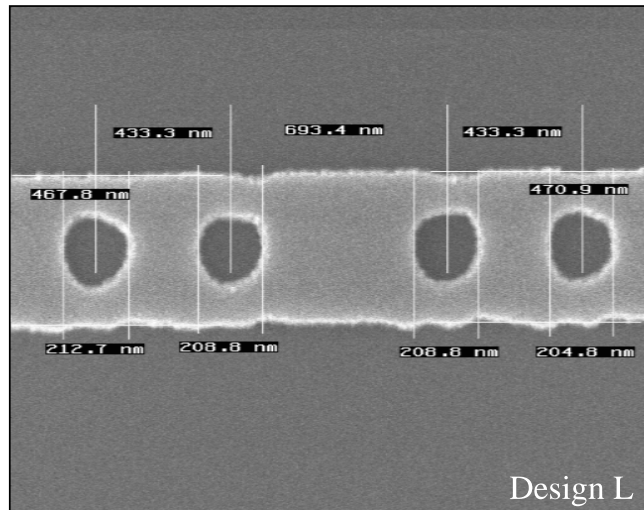

C. 362 μC/cm² (530 KHz)

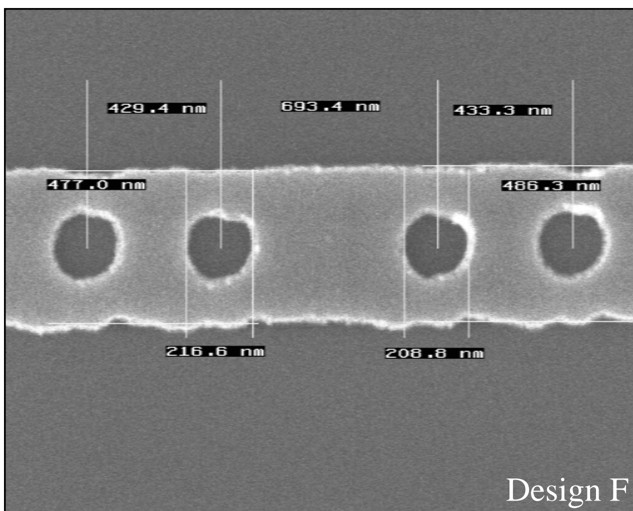

D. 330 μC/cm² (580 KHz)

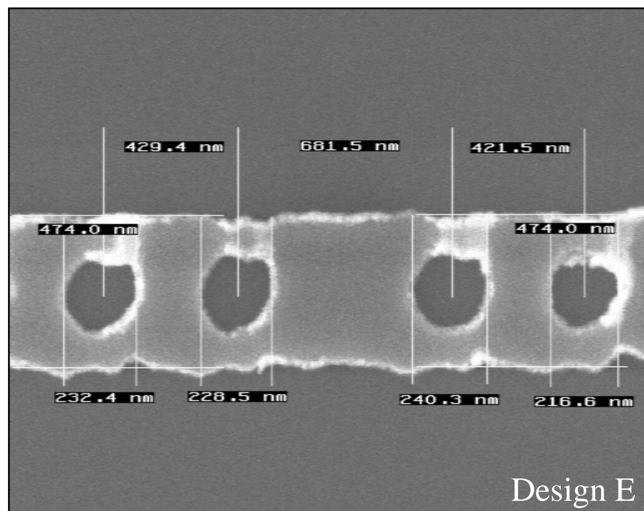

Figure C-11: Variation in electron beam exposure dose, through different beam scanning frequencies, on the microcavity waveguide geometry. SEM shows profile after Cr lift-off with PMMA. Design details in the electron beam layout are listed in Figure C-12, page 159.

Design nomenclature	waveguide	a_defect (nm)	w (nm)	Comments
Design A	1	589.4	468	
	2		468	
	3		468	
Design B	4	610.5	468	
	5		468	
	6		468	
Design C	7	626	468	
	8		468	
	9		468	
Design D	10	631.5	468	
	11		468	
	12		468	
Design E	13	652.6	468	
	14		468	
	15		468	
Deisgn F	16	662.5	468	
	17		468	
	18		468	
Design G	19	673.6	468	
	20		468	
	21		468	
Design H	22	694.7	468	
	23		468	
	24		468	
Design I	25	715.7	468	
	26		468	
	27		468	
Deisgn C	28	626	468	
	29		468	
	30		468	
Design F	31	662.5	468	
	32		468	
	33		468	
Design J	34	712.5	440	
(same as Design C, but smaller width)	35			
	36			
Design K	37	525	440	
(same as Design F, but smaller width)	38			
	39			
Design L (same as Design F, but with three holes)	40	662.5	468	
Design M	41	667.5	555	*a* = 439 nm
	42			
	43			
Design N	44	630	497	*a* = 439 nm
	45			
	46			
Design O	47	662.5	468	2 holes on one
(same as Design F, but asymmetrical holes)	48			side ; 4 holes on
	49			the other side
Design P (14% increased physical size)	50	712.5	525	*a* = 475 nm
	51			*r* = 119 nm
	52			
Design Q (16% decreased physical size)	53	525	388	*a* = 350 nm
	54			*r* = 87.5 nm
	55			
Design R (transmission waveguides)	56	-	468	
	57	-	468	
	58	-	468	
	59	-	468	
	60	-	468	

Note: Lattice constant *a* fixed at 421 nm; hole radius *r* at 106 nm; waveguide thickness *t* at 200 - 212 nm.

Figure C-12: Design matrix of microcavity waveguide for electron beam lithography.

Bibliography

[1] R.B. Apte, F. Sandejas, W. Banyai, and D. Bloom. Deformable Grating Light Valves for High-Resolution Displays. In *Solid-State Sensor and Actuator Workshop*, pages 1–6, Hilton Head Island, SC, June 1994.

[2] J. Arines and J. Ares. Minimum variance centroid thresholding. *Optics Letters*, 27(7):497 – 499, April 2002.

[3] D.K. Armani, T.J. Kippenberg, S.M. Spillane, and K.J. Vahala. Ultra-high-Q toroid microcavity on a chip. *Nature*, 421:925–928, 2003.

[4] George Barbastathis. MIT, personal communication.

[5] R.H. Baughman, L.W. Shacklette, R.L. Elsenbaumer, E.J. Plichta, and C. Becht. *Micro electromechanical actuators based on conducting polymers*, pages 267–289. Molecular Electronics. Kluwer, Netherlands, 1991.

[6] D.J. Bishop and R. Giles. Silicon micromechanics takes on light-wave networks. *The Industrial Physicist*, pages 39–42, 1998.

[7] A. Borgioli, Y. Liu, A.S. Nagra, and R.A. York. Low-Loss Distributed MEMS Phase Shifter. *IEEE Microwave And Guided Wave Lett.*, 10(1):7–9, 2000.

[8] M.A. Branch, T.F. Coleman, and Y. Li. A Subspace, Interior, and Conjugate Gradient Method for Large-Scale Bound-Constrained Minimization Problems. *SIAM Journal on Scientific Computing*, 21(1):1–23, 1999.

[9] Stuart B. Brown. United States patent number 4,939,368 titled "Polychromatic optical strain gauge", 1989.

[10] D.M. Burns and V.M. Bright. Micro-Electro-Mechanical Variable Blaze Gratings. In *Proc. 1997 IEEE Micro Electro Mechanical Systems Workshop*, pages 55–60, Nagoya, Japan, January 1997.

[11] K. Busch and S. John. Liquid-Crystal Photonic-Band-Gap Materials: The Tunable Electromagnetic Vacuum. *Phys. Rev. Lett.*, 83(5):967–970, 1999.

[12] W. G. Cady. *Piezoelectricity*. McGraw-Hill, New York, 1964. Revised edition by Dover Publications.

[13] D.R. Cairns, C.C. Bowley, S. Danworaphong, A.K. Fontecchio, G.P. Crawford, L. Li, and S.M. Faris. Optical strain characteristics of holographically formed polymer-dispersed liquid crystal films. *Appl. Phys. Lett.*, 77(17):2677–2679, 2000.

[14] C.J. Chang-Hasnain. Tunable VCSEL. *IEEE Jour. of Selected Topics in Quantum Electronics*, 6:978–987, 2000.

[15] K.-S. Chen. *Materials Characterization And Structural Design Of Ceramic Micro Turbomachinery*. PhD dissertation, Massachusetts Institute of Technology, Department of Mechanical Engineering, 1998.

[16] K.-S. Chen, A. Ayon, and S.M. Spearing. Controlling and Testing the Fracture Strength of Silicon on the Mesoscale. *J. Am. Ceram. Soc.*, 83(6):1476–1484, 2000.

[17] P. Chen and M.H. Leipold. Fracture toughness of Silicon. *Am. Ceram. Soc. Bull.*, 59:469–472, 1980.

[18] D.N. Chigrin, A.V. Lavrinenko, D.A. Yarotsky, and S.V. Gaponenko. All-Dielectric One-Dimensional Periodic Structures for Total Omnidirectional Reflection and Partial Spontaneous Emission Control. *Journal of Lightwave Technology*, 17(11):2018–2024, November 1999.

[19] C. Cohen-Tannoudji, B. Din, and F. Laloë. *Quantum Mechanics*. Hermann, Paris, 1977. Vol. 1 Chap. 2, Vol.2 Chap. 11 and Chap. 13.

[20] N.J. Conway. MEMS amplification of piezoelectric strain for in-plane actuation. Master's thesis, Massachusetts Institute of Technology, Department of Mechanical Engineering, 2003.

[21] P. Currie and J. Currie. Development by pressure of polar electricity in hemihedral crystals with inclined faces. *Bull. Soc. Min. de France*, 3:90, 1880.

[22] R. Dangel and W. Lukosz. Electro-nanomechanically actuated integrated-optical interferometric intensity modulators and 2×2 space switches. *Optics Communications*, 156:63–76, 1998.

[23] D.L. DeVoe and A.P. Pisano. Modeling and Optimal Design of Piezoelectric Cantilever Microactuators. *Jour. of Micromechanical Systems*, 6(3):266–270, September 1997.

[24] P.A.M. Dirac. *Principles of Quantum Mechanics*. Clarendon, Oxford, 1982.

[25] N.E. Dowling. *Mechanical Behavior of Materials*. Prentice Hall International Editions, Singapore, 1997.

[26] X. Duan, Y. Huang, R. Agarwal, and C.M. Lieber. Single-nanowire electrically driven lasers. *Nature*, 421:241–244, 2003.

[27] S. Fan. *Photonic Crystals: Theory and Device Applications*. PhD dissertation, Massachusetts Institute of Technology, Department of Physics, 1997.

[28] A. Figotin, Y.A. Godin, and I. Vitebsky. Two-dimensional tunable photonic crystals. *Phys. Rev. B*, 57:2841–2848, 1998.

[29] U. Fischer, T. Zinke, B. Sch́uppert, and K. Petermann. Singlemode optical switches based on SOI waveguides with large cross-section. *Electron. Lett.*, 30(5):406–408, March 1994.

[30] J.G. Fleming and S.Y. Lin. Three-dimensional photonic crystal with a stop band from 1.35 to 1.95 um. *Optics Letters*, 24(1):49–51, January 1999.

[31] J.G. Fleming, S.Y. Lin, I. El-Kady, R. Biswas, and K.M. Ho. All-metallic three-dimensional photonic crystals with a large infrared bandgap. *Nature*, 417:52–55, 2002.

[32] J.S. Foresi. *Optical Confinement and Light Guiding in High Dielectric Contrast Materials Systems*. PhD dissertation, Massachusetts Institute of Technology, Department of Materials Science and Engineering, 1997.

[33] J.S. Foresi, P.R. Villeneuve, J. Ferrera, E.R. Thoen, G. Steinmeyer, S. Fan, J.D. Joannopoulos, L.C. Kimerling, H.I. Smith, and E.P. Ippen. Photonic-bandgap microcavities in optical waveguides. *Nature*, 390:143–145, 1997.

[34] D.M. Freeman, A.J. Aranyosi, M.J. Gordon, and S.S. Hong. Multidimensional Motion Analysis of MEMS using Computer Microvision. In *Solid-State Sensor and Actuator Workshop*, pages 150–155, Hilton Head Island, SC, 1998.

[35] B. Gisin, N. Gisin, and F. Cochet. Transmission gratings for chromatic dispersion compensation. *Optics Letters*, 21(9):686 – 688, May 1996.

[36] K. Gomi and Y. Niitsu. Effect of crystalline orientation on photoelastic constant of Si single crystal. *Int. Symp. on Polarization Analysis and Applications to Device Technology*, 2873:238–1241, June 1996.

[37] J.P. Gordon and H. Kogelnik. Pmd fundamentals: Polarization mode dispersion in optical fibers. *Proc. of the Nat. Aca. of Sci.*, 97(9):4541–4550, 2000.

[38] M.A. Green, J. Zhao, A. Wang, P.J. Reece, and M. Gal. Efficient silicon light-emitting diodes. *Nature*, 412:805–808, 2001.

[39] N.W. Hagood, W.H. Chung, and A. von Flotow. Modelling of Piezoelectric Actuator Dynamics for Active Structural Control. *Jour. of Intell. Mater. Syst. and Struct.*, 1:327–354, July 1990.

[40] P. Halevi and F. Ramos-Mendieta. Tunable Photonic Crystals with Semiconducting Constituents. *Phys. Rev. Lett.*, 85(9):1875–1878, 2000.

[41] W. G. Hankel. . *Abh. Sachs*, 12:457, 1881. ; Ber. Sachs. 33, p. 52, 1881.

[42] G. Harsanji. *Polymer films in Sensor Applications*. Technomic Publishing Co., Lancaster, PA, 1995.

[43] J.T. Hastings. *Nanometer-precision pattern placement and applications in integrated optics*. PhD dissertation, Massachusetts Institute of Technology, Department of Electrical Engineering and Computer Science, 2003.

[44] H. A. Haus. *Waves and Fields in Optoelectronics*. Prentice Hall, October 1983.

[45] H.A. Haus and Y. Lai. Theory of Cascaded Quarter Wave Shifted Distributed Feedback Resonators. *IEEE Jour. of Quantum Electronics*, 28(1):205–213, 1992.

[46] R.K. Hickernell, D.R. Larson, R.J. Jr. Phelan, and L.E. Larson. Waveguide loss measurement using photothermal deflection. *Appl. Opt.*, 27:2636–2638, 1988.

[47] N. R. Hill. Integral-equation perturbative approach to optical scattering from rough surfaces. *Phys. Rev. B*, 24:7112–7120, 1981.

[48] P.K.H. Ho, S. Thomas, R.H. Friend, and N. Tessler. All-Polymer Optoelectronic Devices. *Science*, 285:233 – 236, 1999.

[49] G.B. Hocker, D. Younger, E. Deutsch, A. Volpicelli, S. Senturia, M. Butler, M. Sinclair, T. Plowman, and A.J. Ricco. The Polychromator: A Programmable MEMS Diffraction Grating for Synthetic Spectra. In *Solid-State Sensor and Actuator Workshop*, pages 89–91, Hilton Head Island, SC, June 2000.

[50] R. Holland. *Design of Resonant Piezoelectric Devices*. M.I.T Research Monograph No. 56, Cambridge, Massachusetts, first edition, 1969.

[51] L.A. Hornak, T.W. Weidman, and E.W. Kwock. Polyakylsilyne photodefined thin-film optical waveguides. *J. Appl. Phys.*, 67(5):2235 – 2239, 1990.

[52] L.J. Hornbeck. Deformable-Mirror Spatial Light Modulator. *Spatial Light Modulators and Applications III, Proc. Of SPIE*, 1150:86–102, August 1989.

[53] M.H. Huang, S. Mao, H. Feick, H. Yan, Y. Wu, H. Kind, E. Weber, R. Russo, and P. Yang. Room-Temperature Ultraviolet Nanowire Nanolasers. *Science*, 292:1897–1899, June 2001.

[54] W. Huang, C. Xu, S.T. Chu, and S.K. Chaudhuri. The finite-difference vector beam propagation method. *J. Light. Tech.*, 10(3):295–305, 1992.

[55] R.G. Hunsperger. *Integrated Optics: Theory and Technology.* Springer-Verlag, New York, third edition, 1991.

[56] I.W. Hunter and S. Lafontaine. A Comparison Of Muscle with Artificial Actuators. In *Proc. 1992 IEEE Micro Electro Mechanical Systems Workshop*, pages 178–185, Travemunde,Germany, February 1992.

[57] I.W. Hunter, S. Lafontaine, J.M. Hollerbach, and P.J. Hunter. Fast reversible NiTi fibers for use in microrobotics. In *Proc. 1991 IEEE Micro Electro Mechanical Systems Workshop*, pages 166–170, Nara, Japan, January 1991.

[58] M. Ibanescu, Y. Fink, S. Fan, E.L. Thomas, and J.D. Joannopoulos. An All-Dielectric Coaxial Waveguide. *Science*, 289:415–419, July 2000.

[59] T.A. Ibrahim, V. Van, and P.-T. Ho. All-optical time-division demultiplexing and spatial pulse routing with a GaAs/AlGaAs microring resonator. *Optics Letters*, 27(10):803–805, May 2002.

[60] S. Jin, H. Mavoori, R.P. Espindola, L.E. Adams, and T.A. Strasser. Magnetically Tunable Fiber Bragg Gratings. In *24th Conference on Optical Fiber Communication*, page ThJ2, San Diego, CA, February 1999.

[61] J.D. Joannopoulos. The Almost-Magical World of Photonic Crystals. *Brazilian J. of Phys.*, 26(1):58–67, 1996.

[62] J.D. Joannopoulos, R.D. Meada, and J.N. Winn. *Photonic Crystals: Molding the Flow of Light.* Princeton University Press, Princeton, New Jersey, 1st edition, 1995.

[63] S. John. Strong Localization of Photons in Certain Disordered Dielectric Superlattices. *Phys. Rev. Lett.*, 58:2486–2489, 1987.

[64] S. John and T. Quang. Collective Switching and Inversion without Fluctuation of Two-Level Atoms in Confined Photonic Systems. *Phys. Rev. Lett.*, 78(10):1888–1891, 1997.

[65] S.G. Johnson. MIT, personal communication.

[66] S.G. Johnson, M. Ibanescu, M.A. Skorobogatiy, O. Weisberg, J.D. Joannopoulos, and Y. Fink. Perturbation theory for Maxwell's equations with shifting material boundaries. *Phys. Rev. E*, 65, June 2002.

[67] S.G. Johnson and J.D. Joannopoulos. Three-dimensionally periodic dielectric layered structure with omnidirectional photonic band gap. *Appl. Phys. Lett.*, 77:3490–3492, 2000.

[68] S.G. Johnson and J.D. Joannopoulos. Block-iterative frequency-domain methods for Maxwell's equations in a planewave basis. *Optics Express*, 8(3):173–190, 2001.

[69] S.G. Johnson, C. Manolatou, S. Fan, P.R. Villeneuve, J.D. Joannopoulos, and H.A. Haus. Elimination of cross talk in waveguide intersections. *Optics Lett.*, 23:1855–1857, 1998.

[70] I.P. Kaminow and T.L. (editors) Koch. *Optical Fiber Telecommunications IIIA*. Academic Press, Boston, first edition, 1997.

[71] H. Kawai. The piezoelectricity of poly(vinylidene fluoride). *Jpn. J. Appl. Phys.*, 8:975–976, 1969.

[72] D.-K. Kim and H.-G. Kim. A New Characterization of Piezoelectric Thin Films. *Proc. of 11th IEEE Int. Symp. on Appl. of Ferroelectrics*, 24:65–68, 1998.

[73] H.-T. Kim, J.-H. Park, Y.-K. Kim, and Y.-W. Kwon. Millimeter-wave Micromachined Tunable Filters. *IEEE MTT-S Int. Microwave Symp. Digest*, pages 1235–1238, 1999.

[74] S. Kim and V. Gopalan. Strain-tunable photonic band gap crystals. *Appl. Phys. Lett.*, 78(20):3015–3017, 2001.

[75] S.-G. Kim and K.-H. Hwang. Thin-film micromirror array (TMA) for large information display systems. *Journal of the Society for Information Display*, 8(2):177–181, 2000.

[76] S.Y. Kim, S.B. Lee, S.W. Kwon, S.S. Choi, and J. Jeong. Channel-switching active add/drop multiplexer with tunable gratings. *Electronics Letters*, 34(1):104, January 1998.

[77] C. Kittel. *Solid State Physics*. John Wiley and Sons, New York, 1986.

[78] H. Kogelnik and V. Ramaswamy. Scaling rules for thin-fiber optical waveguides. *Appl. Opt.*, 8:1857, 1974.

[79] H. Kogelnik and R.V. Schmidt. Switched directional couplers with alternating $\Delta\beta$. *IEEE J. Quantum Electronics*, QE-12(7):396–401, 1976.

[80] J.A. Kong. *Electromagnetic Wave Theory*. EMW Publishing, Cambridge, MA, 2000.

[81] G.T.A. Kovacs. *Micromachined Transducers Sourcebook*. McGraw-Hill, 1st edition, 1998.

[82] T.F. Krauss, B. Vogele, C.R. Stanley, and R.M. De La Rue. Waveguide microcavity based on photonic microstructure. *IEEE Photonics Tech. Lett.*, 9(2):176 – 178, 1997.

[83] W.P. Krug. Nanophotonics for Mobile Platforms. In *Conf. on Lasers and Electro-optics*, Baltimore, MD, June 2003. The conference talk on DARPA-funded Optics Overview (Boeing Phantom Works) reports a tuning sensitivity of 0.26 nm per 0.1% change in refractive index.

[84] P. Krulevitch, A.P. Lee, P.B. Ramsey, J.C. Trevino, J. Hamilton, and M.A. Northrup. Thin Film Shape Memory Alloy Microactuators. *Jour. of Micromechanical Systems*, 5(4):270–282, December 1996.

[85] K.S. Kunz and R.J. Luebbers. *The Finite Difference Time Domain Method for Electromagnetics*. CRC Press, Boca Raton, 1993.

[86] S. Lan and H. Ishikawa. High-efficiency reflection-type all-optical switch for ultra-short pulses based on a single asymmetrically confined photonic crystal defect. *Optics Letters*, 27(14):1259–1261, July 2002.

[87] C.-K. Lee and F. C. Moon. Model sensors / actuators. *Journal of Applied Mechanics*, 57:434–441, 1990.

[88] D.L. Lee. *Electromagnetic Principles of Integrated Optics*. Wiley and Sons, New York, 1986.

[89] K.K. Lee. *Transmission and routing of optical signals in on-chip waveguides for silicon microphotonics*. PhD dissertation, Massachusetts Institute of Technology, Department of Materials Science and Engineering, 2001.

[90] K.K. Lee, D.R. Lim, A. Agarwal, K. Wada, and L.C. Kimerling. Scattering losses in a high Δn waveguide system for silicon microphotonics. *Mat. Res. Soc. Symp. Proc.*, 637:E3.4.1–E3.4.7, 2001.

[91] M.-Y. Li. New Tunable Phase Shifters Using Perturbed Dielectric Image Lines. *IEEE Trans. Microwave Theory and Tech.*, 46(10):1520–1523, 1999.

[92] S.-K. Liaw, K.-P. Ho, and S. Chi. Dynamic Power-Equalized EDFA Module Based on Strain Tunable Fiber Bragg Gratings. *IEEE Photonics Technology Letters*, 11(7):797, July 1999.

[93] D.R. Lim. *Device Integration for Silicon Microphotonic Platforms*. PhD dissertation, Massachusetts Institute of Technology, Department of Electrical Engineering and Computer Science, 2000.

[94] K.-Y. Lim. *Design and fabrication of one-dimensional and two-dimensional photonic bandgap devices*. PhD dissertation, Massachusetts Institute of Technology, Department of Electrical Engineering and Computer Science, 1999.

[95] L.Y. Lin, E.L. Goldstein, and R.W. Tkach. Free-Space Micromachined Optical Switches for Optical Networking. *IEEE Journal of Selected Topics in Quantum Electronics*, 5(1):4–9, 1998.

[96] P. Lin and S.D. Senturia. The in-situ measurement of biaxial modulus and residual stress of multi-layer polymeric thin films. *Thin Films: Stresses and Mechanical Properties II*, 188:41 – 46, 1990. Materials Research Society Symposium Proceedings.

[97] S.Y. Lin, J.G. Fleming, D.L. Hetherington, B.K. Smith, R. Biswas, K.M. Ho, M.M. Sigalas, W. Zubrzycki, S.R. Kurtz, and J. Bur. A three-dimensional photonic crystal operating at infrared wavelengths. *Nature*, 394:251–253, 1998.

[98] B.E. Little, J.S. Foresi, G. Steinmeyer, E.R. Thoen, S.T. Chu, H.A. Haus, E.P. Ippen, L.C. Kimerling, and W. Greene. Ultra-Compact Si-SiO2 Microring Resonator Optical Channel Dropping Filters. *IEEE Photon. Tech. Lett,*, 10:149–151, 1998.

[99] B. Liu, A. Shakouri, and J.E. Bowers. Wide Tunable Double Ring Resonator Coupled Lasers. *IEEE Photon. Tech. Lett.*, 14(5):600–602, May 2002.

[100] C.-H. Liu, A.M. Barzilai, J.K. Reynods, A. Partridge, T.W. Kenny, J.D. Grade, and H.K. Rockstad. Characterization of a high-sensitivity micromachined tunneling accelerometer with micro-g resolution. *J. Microelectromechanical Systems*, 7:235–244, 1999.

[101] W. Liu, J.S. Ko, and W. Zhu. Preparation and properties of multi-layer $Pb(Zr,Ti)O_3$ / $PbTiO_3$ thin films for pyroelectric application. *Thin Solid Films*, 371(1 - 2):254, 2000.

[102] C. Luo, S.G. Johnson, J.D. Joannopoulos, and J.B. Pendry. All-angle negative refraction without negative effective index. *Phys. Rev. B.*, 65:201104(R), 2002.

[103] M.J. Madou. *Fundamentals of Microfabrication: The Science of Miniaturization*. CRC Press, 2nd edition, 2002.

[104] S.R. Manalis, C.F. Quate, and S.C. Minnie. *Bringing Scanning Probe Microscopy Up To Speed*. Kluwer Academic Press, Boston, first edition, 1999.

[105] E.A.J. Marcatili. Dielectric rectangular waveguide and directional coupler for integrated optic. *Bell Syst. Tech. J.*, page 2071, 1969.

[106] D. Marcuse. Bending losses of the asymmetric slab waveguide. *Bell Syst. Tech. J.*, 50(8):2551, 1971.

[107] D. Marcuse. *Theory of Dielectric Optical Waveguides*. Academic Press, San Diego, 1991.

[108] K.W. Markus. Commercialization of optical MEMS - volume manufacturing approaches. In *Optical MEMS, 2000 IEEE/LEOS International Conference*, pages 7–8, Kauai, Hawaii, August 2000.

[109] J. C. Maxwell. A dynamical theory of the electromagnetic field. *Philosophical Transactions of the Royal Society of London*, 155:459 – 512, 1865.

[110] G.S. Mosehytz and P. Horn. *Active Filter Design Handbook*. Wiley, New York, 1st edition, 1981.

[111] D.T. Neilson, *et. al.* Fully provisioned 112x112 micro-mechanical optical cross connect with 35.8Tb/s demonstrated capacity. In *25th Conference on Optical Fiber Communication*, Baltimore, MD, March 2000.

[112] Gregory N. Nielson. MIT, personal communication.

[113] T. Niino, S. Egawa, N. Nishiguchi, and T. Higuchi. Development of an electrostatic actuator exceeding 10N propulsive force. In *Proc. 1992 IEEE Micro Electro Mechanical Systems Workshop*, pages 122–127, Travemunde, Germany, February 1992.

[114] S. Noda, K. Tomoda, N. Yamamoto, and A. Chutinan. Full three-dimensional photonic bandgap crystals at near-infrared wavelengths. *Science*, 289:604–606, 2000.

[115] S. Noda, M. Yokoyama, M. Imada, A. Chutinan, and M. Mochizuki. Polarization Mode Control of Two-Dimensional Photonic Crystal Laser by Unit Cell Structure Design. *Science*, 293:1123–1125, August 2001.

[116] O. Painter, R.K. Lee, A. Scherer, A. Yariv, J.D. O'Brien, P.D. Dapkus, and I. Kim. Two-Dimensional Photonic Band-Gap Defect Mode Laser. *Science*, 284:1819–1821, 1999.

[117] O. Painter, R.K. Lee, A. Scherer, A. Yariv, J.D. O'Brien, P.D. Dapkus, and I. Kim. Two-dimensional Photonic Band-Gap Defect Mode Laser. *Science*, 284:1819–1821, June 1999.

[118] L. Pavesi, L. Dal Negro, C. Mazzoleni, G. Franzò, and F. Priolo. Optical gain in silicon nanocrystals. *Nature*, 408:440–444, 2000.

[119] D.A. Pommet, E.B. Grann, and M.G. Moharam. Effects of process errors on the diffraction characteristics of binary dielectric gratings. *Applied Optics*, 34(14):2430, May 1995.

[120] M. Qi. PhD dissertation, Massachusetts Institute of Technology, Department of Electrical Engineering and Computer Science, 2003 (expected).

[121] Minghao Qi. MIT, personal communication.

[122] L. Quetel, L. Rivoallan, E. Delevaque, H. Poignant, M. Monerie, and T. Georges. Programmable fiber grating based wavelength multiplexer. In *21st Conference on Optical Fiber Communication*, page WF6, San Jose, CA, February 1996.

[123] P. Rabiei, W. Steier, C. Zhang, and L.R. Dalton. Polymer Micro-Ring Filters and Modulators. *Jour. of Lightwave Tech.*, 20(11):1968–1975, November 2002. The high quality polymer electro-optic effect is reported in Y. Shi et. al. *Science* **288**, pp. 119-122, 2000.

[124] Peter Thomas Rakich. MIT, personal communication.

[125] Lord Rayleigh. *Phil. Mag.*, 5(8):261,1879.

[126] R. Regener and W. Sohler. Loss in low-finesse Ti:LiNbO_3 optical wave resonators. *Appl. Phys. B*, 36:143–147, 1985.

[127] S.G. Roberts. Fracture and brittle-ductile transition in si. In R. Hull, editor, *Properties of crystalline silicon*, pages 144–148. INSPEC, the Institution of Electrical Engineers, London, 1999.

[128] K. Sakoda. *Optical Properties of Photonic Crystals*. Springer, New York, 2001.

[129] B.E.A Saleh and M.C. Teich. *Fundamentals of Photonics*. Wiley, New York, 1st edition, 1991.

[130] D.E. Sene, J.W. Grantham, V.M. Bright, and J.H. Comtois. Development and Characterization of Micro-Mechanical Gratings for Optical Modulation. In *Proc. 1996 IEEE Micro Electro Mechanical Systems Workshop*, pages 222–227, San Diego, CA, February 1996.

[131] Stephen D. Senturia. *Microsystem Design*. Kluwer Academic Publishers, Boston, Massachusetts, 1st edition, 2001.

[132] W.N. Sharpe, B. Yuan, and R.L. Edwards. A New Technique for Measuring the Mechanical Properties of Thin Films. *Appl. Phys. Lett.*, 6(3):193–199, 1997.

[133] W.N. Jr. Sharpe, B. Yuan, R. Vaidyanathan, and R.L. Edwards. Measurements of Young's modulus, Poisson's ratio and tensile strength of polysilicon. In *Proc. 1997 IEEE Micro Electro Mechanical Systems Workshop*, pages 424–429, Nagoya, Japan, 1997.

[134] W.-C. Shih, C. W. Wong, Y. B. Jeon, S.-G. Kim, and G. Barbastathis. Electrostatic and Piezoelectric Analog Tunable Diffractive Gratings. In *Proc. of Conference on Lasers and Electro-Optics*, page CMP4, Long Beach, CA, May 2002.

[135] M.B. Sinclair, M.A. Butler, A.J. Ricco, and S.D. Senturia. Synthetic Spectra: A Tool for Correlation Spectroscopy. *Applied Optics*, 36(15):3342, May 1997.

[136] A.W. Snyder and J.D. Love. *Optical Waveguide Theory*. Chapman and Hall, London, 1983.

[137] O. Solgaard, F. Sandejas, and D. Bloom. A Deformable Grating Optical Modulator. *Optics Letters*, 17:688, May 1992.

[138] M. Soljačić, M. Ibanescu, S.G. Johnson, Y. Fink, and J.D. Joannopoulos. Optimal bistable switching in nonlinear photonic crystals. *Phys. Rev. E*, 66:055601(R), 2002.

[139] Lodewyk Jasper Steyn. MIT, personal communication.

[140] T. Storgaard(U.S. Patent number (reference)) Larsen, S. Bouwstra, and O. Leistiko. Opto-mechanical accelerometer based on strain sensing by a Bragg grating in a planar waveguide. *Sensors and Actuators A*, 52:25–32, 1996.

[141] Y. Sugarawa, *et. al.* Metal-ceramic composite actuators. *Journal of the American Ceramic Society*, 75(4):996–998, 1992.

[142] T. Tamir, editor. *Springer Series in Electronics and Photonics 26*. Springer-Verlag, New York, second edition, 1990. Perturbation method found in pp. 30-31.

[143] S. Timoshenko. Bull. Polytech. Inst., Kiew, 1907.

[144] S. Timoshenko. *Theory of Plates and Shells*. McGraw-Hill, New York, 2nd edition, 1959.

[145] S. Timoshenko. *Theory of Elasticity*. McGraw-Hill, New York, 3rd edition, 1971.

[146] G. Tittlebach, B. Richter, and W. Karthe. Comparison of three transmission methods for integrated optical waveguide propagation loss measurements. *Pure and Appl. Opt.*, 2(6):683–700, 1993.

[147] E.B. Treacy. Optical pulse compression with diffraction gratings. *IEEE J. Quantum Electron.*, QE-5:454–459, 1969.

[148] T. Tsuchizawa, T. Watanabe, E. Tamechika, T. Shoji, K. Yamada, J.-i. Takahashi, S. Uchiyama, S.I. Itabashi, and H. Morita. Fabrication and Evaluation of Submicron-Square Si Wire Waveguides with Spot Size Converters. In *15th Annual Meeting of the IEEE Lasers and Electro-optics Society*, Glasgow, Scotland, November 2002. Paper TuU2.

[149] K. Uchino. Electrostrictive actuators: materials and applications. *Ceramic Bulletin*, 65:647–652, 1986.

[150] K. Uchino. *Piezoelectric Actuators and Ultrasonic Motors*, pages 78–83. Electronic Materials: Science and Technology. Kluwer, Boston, MA, 1997.

[151] D. Vakhshoori, P.D. Wang, M. Azimi, K.J. Knoop, and M. Jiang. MEMs-Tunable Vertical-Cavity Surface-Emitting Lasers. In *26th Conference on Optical Fiber Communication*, page TuJ1, Anaheim, CA, March 2001.

[152] P.F. Van Kessel, L.J. Hornbeck, R.E. Meier, and N.R. Douglass. A MEMS-based projection display. In *Proc. of the IEEE*, volume 86, pages 1687–1704, August 1998.

[153] P.R. Villeneuve, S. Fan, S.G. Johnson, and J. D. Joannopoulos. Three-dimensional photon confinement in photonic crystals of low-dimensional periodicity. *IEE Proc. Optoelectron.*, 145(6):384 – 309, December 1998.

[154] Y.A. Vlasov, X.-Z. Bo, J.C. Sturm, and D.J. Norris. On-chip natural assembly of silicon photonic bandgap crystals. *Nature*, 414:289–293, November 2001.

[155] J. Vučković, M. Lončar, H. Mabuchi, and A. Scherer. Design of photonic crystal microcavities for cavity QED. *Phys. Rev. E*, 65, June 2002.

[156] C. Warde, J. McCann, V. Shrauger, H. Ieong, A. Ersen, X.-Y. Wang, and J. Hubbard. Membrane Mirror Light Modulator Technology. *Diffractive/Holographic Technologies and Spatial Light Modulators, Proc. Of SPIE*, 3951:191–199, 2000.

[157] M.S. Weinberg. Working Equations for Piezoelectric Actuators and Sensors. *Jour. of Micromechanical Systems*, 8(4):529–533, December 1999.

[158] A.M. Weiner, D.E. Leaird, J.S. Patel, and J.R. Wullert. Programmable femtosecond pulse shaping by use of a multielement liquid-crystal phase modulator. *Opt. Lett.*, 15(6):326–328, 1990.

[159] C. W. Wong, W.-C. Shih, Y. B. Jeon, S. Desai, D. Freeman, S.-G. Kim, and G. Barbastathis. Analog Tunable Gratings With Nanometer Resolution. In *Solid-State Sensor, Actuator, and Microsystems Workshop*, pages 342–345, Hilton Head Island, SC, June 2002.

[160] B. Xu, L.E. Cross, and J.J. Bernstein. Ferroelectric and antiferroelectric films for microelectromechanical systems applications. *Thin Solid Films*, 377-378:712–718, 2000.

[161] E. Yablonovitch. Inhibited spontaneous emission in solid state physics and electronics. *Phys. Rev. Lett.*, 58:2059–2062, 1987.

[162] K. Yamashita. High-Directivity Array of Ultrasonic Micro Sensor Using PZT Thin Film on Si Diaphragm. In *11th Int. Conf. on Solid-State Sensors and Actuators, Transducers'01*, pages 114–117, Munich, Germany, June 2001.

[163] A. Yariv. *Quantum Electronics*. Wiley and Sons, New York, 1975.

[164] A. Yariv. *Optical Electronics*. Saunders, Philadelphia, PA, 1991.

[165] K. Yoshino, Y. Shimoda, Y. Kawagishi, K. Nakayama, and M. Ozaki. Temperature tuning of the stop band in transmission spectra of liquid-crystal infiltrated synthetic opal as tunable photonic crystal. *Appl. Phys. Lett.*, 75(7):932–934, 1999.

[166] T.-Y. Yun. *One-dimensional Photonic Bandgap (PBG) Structures And Piezoelectric Transducer (PET) Controlled Devices For Microwave Applications*. PhD dissertation, Texas, A & M University, Department of Electrical Engineering, 2001.

[167] X.M. Zhang and A.Q. Liu. A MEMS Pitch-tunable Grating Add/Drop Multiplexers. In *Optical MEMS, 2000 IEEE/LEOS International Conference*, pages 25–26, Kauai, HI, August 2000.